

© Copyright 2015

Carly Ann Holstein

Development of a Novel Paper-Based Flu Test for Improved Diagnosis at the Point of Care

Carly Ann Holstein

A dissertation
submitted in partial fulfillment of the
requirements for the degree of

Doctor of Philosophy

University of Washington

2015

Reading Committee:

Paul Yager, Chair

David Baker

Elain Fu

Program Authorized to Offer Degree:

Bioengineering

University of Washington

Abstract

Development of a Novel Paper-Based Flu Test for Improved Diagnosis at the Point of Care

Carly Ann Holstein

Chair of the Supervisory Committee:

Professor Paul Yager

Bioengineering

The development of paper-based diagnostics has surged in recent years, due to the suitability of these tests for use at the point of care. Paper-based diagnostics offer the ability to perform relatively sophisticated chemical processing, but in an automated device that is low in cost, generates a result in a matter of minutes, and can be operated by untrained users in clinics and homes around the world.

Influenza infection, or the flu, is one illness that stands to benefit greatly from the improved point-of-care testing afforded by paper-based diagnostics. This commonly occurring infection results in millions of illnesses and thousands of deaths in the U.S. each year, many of which could be prevented or mitigated by timely and effective diagnosis and disease management. Improved point-of-care flu testing could also help reduce inefficient and wasteful healthcare spending, as well as the economic burden of flu due to lost productivity.

To this end, we have developed a novel paper-based assay for influenza, based on the detection of the surface protein hemagglutinin. This assay was made possible by the use of novel, recombinant affinity proteins for influenza hemagglutinin, developed by collaborators of the project. Since these “flu binders” represent a significant departure from the mainstay of IgG capture molecules for

traditional paper-based assays, the use of these affinity proteins required the in-depth study of protein adsorption to paper and the development of novel immobilization methods. Using the combination of the recombinant flu binders and the immobilization and assay strategies developed herein, we demonstrated a novel paper-based assay for influenza detection that is more sensitive than a traditional lateral flow immunoassay. Additionally, since this assay targets the hemagglutinin protein of influenza, it allows for the possibility for influenza subtyping, which is not available for any influenza rapid diagnostic test on the market. Overall, this work represents a significant development towards improved influenza diagnosis and disease management at the point of care.

Table of Contents

Table of Contents.....	i
List of Figures.....	v
List of Tables.....	x
Acknowledgements	xi
Dedication.....	xiii
1. Introduction	1
1.1. Significance of Problem	1
1.2. Proposed Solution.....	1
1.3. Summary of Thesis	2
2. Background	5
2.1. Point-of-Care Diagnostics	5
2.1.1. Need for Point-of-Care Diagnostics.....	5
2.1.2. Current Point-of-Care Diagnostics.....	6
2.2. Paper Microfluidics.....	11
2.2.1. Principles of Paper Microfluidics	11
2.2.2. Current Paper-Based Diagnostic Platforms.....	16
2.3. Influenza.....	18
2.3.1. Biology of Influenza	18
2.3.2. Influenza Infection	23
2.3.3. Current Influenza Diagnostics.....	24
2.3.4. Next-Generation Influenza Diagnostic.....	26
2.4. Paper-Based Assay Development Considerations.....	27
2.4.1. Assay Substrates	27
2.4.2. Affinity Reagents.....	29
2.4.3. Immobilization Techniques.....	36
3. Protein Adsorption.....	41
3.1. Motivation	41
3.2. Common Methods	42
3.2.1. Lateral Flow Challenge Method	42
3.2.2. Full Protein Spot Analysis Method	44
3.3. Initial Exploration of Protein Adsorption.....	46

3.3.1. Methods	46
3.3.2. Results and Discussion	47
3.4. Solution Depletion	52
3.4.1. Methods	53
3.4.2. Results and Discussion	56
3.5. IgG Adsorption to Nitrocellulose	64
3.5.1. Methods	65
3.5.2. Results and Discussion	65
3.6. pH Dependence of Protein Adsorption.....	70
3.6.1. Methods	70
3.6.2. Results and Discussion	72
3.7. Identification of Nitrocellulose-Binding Proteins.....	85
3.7.1. Methods	85
3.7.2. Results and Discussion	85
3.8. Conclusions.....	92
4. Flu Binder Immobilization	94
4.1. Motivation	94
4.2. Common Methods	95
4.2.1. Lateral Flow Challenge	95
4.2.2. Flu Hemagglutinin Assay	97
4.2.3. Signal Quantification	98
4.3. Immobilization by Direct Adsorption	98
4.3.1. Methods	99
4.3.2. Results and Discussion	100
4.4. Immobilization by Covalent Attachment.....	103
4.4.1. Methods	104
4.4.2. Results and Discussion	107
4.5. Immobilization by Streptavidin-Biotin Anchoring.....	123
4.5.1. Methods	124
4.5.2. Results and Discussion	125
4.6. Immobilization by Nitrocellulose-Binding Anchor Protein.....	129
4.6.1. Methods	130
4.6.2. Results and Discussion	130

4.7. Comparison to Standard IgG Immobilization	132
4.7.1. Methods	133
4.7.2. Results and Discussion	133
4.8. Conclusions	134
5. Flu HA Assay Development.....	136
5.1. Motivation	136
5.2. Common Methods	136
5.2.1. Flu Hemagglutinin Assay	136
5.2.2. Signal Quantification	137
5.3. Stem Region Flu Binders Fail to Capture Whole Virus	137
5.3.1. Methods	138
5.3.2. Results and Discussion	138
5.4. Head Region Flu Binder for Whole Virus Capture	141
5.4.1. Methods	141
5.4.2. Results and Discussion	142
5.5. Final Assay Characterization	154
5.5.1. Methods	154
5.5.2. Results and Discussion	154
5.6. Conclusions	157
6. Limit of Detection Analysis.....	159
6.1. Motivation	159
6.2. Novel Method for Statistically Robust Limit of Detection Analysis.....	161
6.2.1. Method Description	161
6.2.2. Method Illustration with Example Assay Data	168
6.2.3. Comparison to Standard Method	172
6.3. Conclusions	175
7. Towards Improved Flu Testing.....	176
7.1. Motivation	176
7.2. User Assessment.....	176
7.2.1. Methods	176
7.2.2. Results and Discussion	178
7.3. 2DPN Folding Card Development.....	178
7.3.1. Methods	178

7.3.2. Results and Discussion	179
7.4. Demonstration of Improved Paper-Based Flu Assay	180
7.4.1. Methods	181
7.4.2. Results and Discussion	183
7.5. Conclusions	185
8. Conclusions and Future Work	187
8.1. Overall Summary and Conclusions	187
8.2. List of Contributions from Work	189
8.3. Future Work	190
References	192
Appendix A: List of Abbreviations	207
Appendix B: MATLAB Program <i>quantifyColorimetricSignal.m</i>	209
B.1. Description	209
B.2. Code	222
Appendix C: MATLAB Program <i>analyzeProteinSpots.m</i>	245
C.1. Description	245
C.2. Code	249
Appendix D: MATLAB Program <i>LODanalysis.m</i>	275
D.1. Description	275
D.2. Code	275
Appendix E: MATLAB Program <i>LODcomparison.m</i>	280
E.1. Description	280
E.2. Code	280

List of Figures

Figure 1. Health spending in the United States.....	5
Figure 2. The evolution of the “mChip” microfluidic ELISA system by Sia and colleagues.....	9
Figure 3. Illustration of a typical lateral flow test (LFT).....	10
Figure 4. Multi-analyte detection afforded by μ PADs.	16
Figure 5. Multi-step reagent delivery afforded by a 2DPN.....	17
Figure 6. Phylogenetic description of the orthomyxoviridae family of viruses.....	19
Figure 7. Model structure of the influenza A virus.	19
Figure 8. Cellulose and nitrocellulose.....	27
Figure 9. SEM of nitrocellulose membrane.....	28
Figure 10. Structure of an IgG antibody.....	30
Figure 11. Antibody-derived proteins.....	31
Figure 12. Aptamer structure.....	32
Figure 13. Illustration of the hemagglutinin (HA)-binding “flu binders.”	33
Figure 14. Theoretical model of protein adsorption to nitrocellulose.....	38
Figure 15. Anchoring through the cellulose binding domain.....	39
Figure 16. Illustration of the protein spot analysis method for evaluating protein adsorption.....	45
Figure 17. Protein adsorption for proteins ranging in size.....	48
Figure 18. Comparison of IgG and BSA adsorption.....	50
Figure 19. Comparison of streptavidin vs. IgG adsorption.....	51
Figure 20. Standard curve for biotin-BSA-FITC quantification in solution depletion experiments....	57

Figure 21. FITC-BSA solution depletion, log scale.	57
Figure 22. FITC-BSA solution depletion, linear scale.....	57
Figure 23. Nitrocellulose membranes after FITC-BSA solution depletion.....	58
Figure 24. Adsorption models for FITC-BSA solution depletion.....	59
Figure 25. Standard curves for non-labeled protein solution depletion.	61
Figure 26. IgG and BSA solution depletion, 1.5 hours.	62
Figure 27. IgG and BSA solution depletion, 6 hours.....	62
Figure 28. IgG and BSA solution depletion, 96 hours.	63
Figure 29. IgG orientation and its fragments.	64
Figure 30. Adsorption of IgG and its fragments, full results.	66
Figure 31. Comparison of protein adsorption speed for IgG and fragments.	67
Figure 32. Comparison of protein adsorption strength for IgG and fragments.....	69
Figure 33. Schematic of the IEF system.....	71
Figure 34. BSA adsorption to nitrocellulose as a function of the pH of the spotting buffer.	73
Figure 35. Quantification of signal intensity for BSA adsorption vs. pH.	73
Figure 36. Initial testing of streptavidin adsorption vs. pH.	75
Figure 37. Initial testing of streptavidin adsorption vs. pH, signal intensities.	76
Figure 38. Protein adsorption for the streptavidin/avidin protein series.	79
Figure 39. Protein adsorption for the streptavidin/avidin protein series, signal intensities.....	79
Figure 40. IEF gel, in grayscale.....	81
Figure 41. IEF gel, in false color.....	81

Figure 42. Mapping of IEF gel standard markers.....	82
Figure 43. IEF gel for the analysis of streptavidin/avidin protein pIs.	82
Figure 44. Full protein spot analysis for streptavidin adsorption vs. pH.....	84
Figure 45. Adsorption screening of DI-V globular proteins.....	87
Figure 46. Adsorption screening of 3-helix protein.	89
Figure 47. Full protein spot analysis for 3-helix adsorption vs. pH.....	90
Figure 48. Comparison of DI, 3-helix, and IgG adsorption to nitrocellulose.....	91
Figure 49. Illustration of the four immobilization strategies developed herein.....	94
Figure 50. Test line pattern created with the piezoelectric spotter.....	95
Figure 51. Methods used to assess each immobilization strategy.....	96
Figure 52. Dipstick format.....	97
Figure 53. Protein fouling characterization of different nitrocellulose membranes.....	101
Figure 54. Flu binder immobilization by direct adsorption.....	102
Figure 55. Flu binder functionality when immobilized by direct adsorption.....	103
Figure 56. Covalent attachment of thiolated flu binders to functionalized nitrocellulose.....	104
Figure 57. Flu binder HA-binding analysis by SPR.....	105
Figure 58. Reducing agents for thiolated flu binder.....	107
Figure 59. Optimization of reducing agent for cys-HB80.4 immobilization to FF60-GMA.....	108
Figure 60. Immobilization of thiolated flu binder to NC-GMA.....	109
Figure 61. Functionality of thiolated flu binder immobilized to NC-GMA.....	110
Figure 62. Illustration of flu binder immobilization with and without linker.....	111

Figure 63. Stem region flu binders with polypeptide linkers.	112
Figure 64. Functionality of flu binders with thiolated linkers immobilized to NC-GMA.	113
Figure 65. SPR results comparing HA-binding of HB80.4 and HB36.5 flu binder variants.	115
Figure 66. Functionality of cys-HB36.5 flu binder variants immobilized to NC-GMA.	116
Figure 67. Comparison of NC-GMA and NC-maleimide.	118
Figure 68. Comparison of assay signal on NC-GMA and NC-maleimide membranes.	119
Figure 69. Effect of added TCEP on cys-HB36.5 performance.	121
Figure 70. Fluorothiol assay for quantification of reduced thiol content in flu binder samples.	122
Figure 71. Immobilization of regular vs. NC-binding mutant streptavidin.	125
Figure 72. Regular vs. mutant streptavidin anchoring of b-HB80.4.	127
Figure 73. Effect of biotin-BSA wash on mutant SA anchor system.	128
Figure 74. Performance of DI-HB36.6 fusion proteins.	131
Figure 75. Mut. SA + b-HB36.5 outperforms standard Ab capture.	133
Figure 76. Anchor-based stem region binder systems fail to capture whole virus.	139
Figure 77. Thiolated stem region binder systems fail to capture whole virus.	140
Figure 78. Immobilization of head region binders by direct adsorption.	142
Figure 79. Functionality of head region binders for HA capture by direct adsorption.	143
Figure 80. Trimer 11 capture of recombinant HA and whole virus.	144
Figure 81. Performance of head region binder-based assay with and without lysis.	147
Figure 82. Experimental design for the PCR analysis of flu assay test strips.	149
Figure 83. Results from the PCR analysis of flu assay test strips.	151

Figure 84. All-flu-binder assay for influenza virus detection.....	153
Figure 85. Analytical sensitivity of the novel flu HA assay with Trimer 11 capture.	156
Figure 86. Analytical sensitivity of novel flu HA assay with biotin-HB36.5 anchored by mut. SA. ..	157
Figure 87. Illustration of the how the L_C and L_D values are determined for LOD analysis.....	161
Figure 88. Description of the dataset used to demonstrate the LOD analysis method herein.....	168
Figure 89. Variance check for example data.....	169
Figure 90. Results from the LOD analysis method.....	170
Figure 91. Visual comparison of LOD estimates for two different versions of the flu HA assay.	172
Figure 92. Comparison of 4PL calibration curve to linear calibration curves.	174
Figure 93. 2DPN prototype kits for user assessment.	177
Figure 94. Demonstration of the flu HA assay in a 2DPN folding card.....	180
Figure 95. Traditional immunoassay for HA.....	182
Figure 96. Correlations between different units of virus concentration.....	183
Figure 97. Analytical sensitivity of traditional immunoassay.....	184

List of Tables

Table 1. List of the RNA segments and encoded proteins of the influenza A viral genome.....	20
Table 2. Description of influenza virus nomenclature.....	22
Table 3. List of flu binders used in the flu HA assay development herein.....	35
Table 4. Power supply protocol used to perform the isoelectric focusing.....	71
Table 5. Proteins evaluated as part of the streptavidin/avidin protein series.....	77
Table 6. Buffer set used to achieve an extended pH range.....	78
Table 7. Comparison of reported and experimental isoelectric points.....	83
Table 8. Five globular proteins (DI-V) screened for nitrocellulose binding.....	86
Table 9. 3-helix protein screened for nitrocellulose binding.....	88
Table 10. SPR run procedure for each sample cycle.....	106
Table 11. LOD analysis method results.....	171
Table 12. Comparison of the LODs for two different influenza HA assays.....	171
Table 13. Comparison of the 4PL-based LOD method to standard $3\sigma/m$ method.....	175
Table 14. Summary of flu HA assay performance.....	185

Acknowledgements

This work would not have been possible without the vision and guidance of Professor Paul Yager, who was the principal investigator of the overarching flu project and the primary supervisor for the work herein. It has been a pleasure to work with Professor Yager, to learn from his scientific prowess, and to be inspired by his earnest curiosity and desire to make an impact on the world. I am especially grateful for his support of my professional development and allowing me the freedom to explore my own path toward making an impact.

I am also appreciative of my supervisory committee members, Professors Elain Fu, David Baker, and Michael MacCoss, for their time and support throughout this process. Professor Fu and Professor Baker were also instrumental collaborators of the work herein and provided critical guidance to the project.

I would like to thank the many collaborators with whom I had the pleasure of working on this project. Dr. Aaron Chevalier and Dr. Eva-Maria Strauch developed the many variants of flu binders that were used for assay development, in addition to helping guide the influenza capture and detection strategies used herein. More recently, Jorgen Nelson and Dr. Franziska Seeger have also contributed to the flu binder development. Undergraduate students Steven Bennett and Karen Keniston were also critical collaborators on this work, running many of the flu assay and protein adsorption experiments described herein. I am grateful for their contributions and the opportunity not only to mentor them, but to learn from them as well. Dr. Gina Fridley was a key collaborator on the protein adsorption work, especially the development of the protein spot analysis method. She was also an invaluable colleague, supporter, mentor, and friend. Finally, I am indebted to graduate student Caitlin Anderson for providing unwavering support and help in running final experiments as I prepared this thesis. I am grateful to be leaving the project in her very capable hands.

I would also like to thank all members of the Yager, Lutz, and Fu labs for the many years of support, collaboration, and friendship. I am particularly grateful for those who have provided guidance and support related to this work: Samantha Byrnes, Joshua Buser, Koji Abe, Tinny Liang, Dr. Shichu Huang, Dr. Paula Ladd, Peter Kauffman, Sujatha Ramachandran, Dr. Jen Osborn, and Dr. Dean Stevens. Finally, this group would not function without the support of Chelsea Musick, who runs all of the behind-the-scenes operations of the administrative, purchasing, and financial aspects of the lab.

This work was supported by the National Science Foundation Graduate Research Fellowship Program under Grant No. DGE – 0718124, by the National Institute of Allergy and Infectious Diseases of the National Institutes of Health under award number R01AI096184, and by the University of Washington Department of Bioengineering. The content is solely the responsibility of the author and does not necessarily represent the official views of the National Institutes of Health.

Finally, I could not have completed this thesis work without the abounding love and support of my friends and family. I am incredibly thankful for all of you. Most of all, I am deeply grateful for my husband, Tyler Holstein, who has experienced the highs and lows of this process with me and has offered nothing but support and encouragement. Words do not adequately express my gratitude.

Dedication

For my loving husband, Tyler. Thank you for being my biggest supporter.

1. Introduction

1.1. Significance of Problem

While lateral flow tests have made point-of-care (POC) testing possible, their performance is often severely deficient, especially compared to their gold standard, laboratory-based counterparts. One test that has particularly suffered in the lateral flow format is the influenza rapid diagnostic test (RDT). Common influenza RDTs have been found to have sensitivities as high as 70% and as low as 10% when tested in mixed-age populations [1]. Given that a coin flip can achieve 50% sensitivity, the performance of these influenza RDTs leaves much room for improvement. Since influenza is such a commonly occurring infection, affecting 5-20% of the population [2] and costing tens of billions of dollars [3] in the U.S. annually, improved diagnosis would make a significant impact on the management of this disease, both clinically and economically.

1.2. Proposed Solution

Given the poor performance of influenza RDTs, our laboratory aims to develop a higher-sensitivity paper-based influenza diagnostic using a combination of our laboratory's existing two-dimensional paper network (2DPN) platform and the novel methods developed herein. While this diagnostic will test for multiple influenza targets, the focus of my work has been on the influenza hemagglutinin (HA) protein, which can be used for subtyping the influenza virus. This subtyping would provide clinicians with important diagnostic information about the virus that could be used both for clinical action and epidemiological surveillance [4]. Moreover, viral subtyping is not currently available in any influenza RDT on the market [4], further motivating our choice to target this important surface protein.

To develop improved diagnostic capability for flu, we utilized novel protein affinity reagents for influenza HA, called flu binders, and both traditional and novel nitrocellulose membranes as the assay substrate. The flu binders were designed in the laboratory of our collaborator Dr. David Baker, who is in the Department of Biochemistry at the University of Washington and is a member of the supervisory committee for this work. The novel nitrocellulose membranes were created by collaborators at the General Electric (GE) Global Research Center (GRC), who work from base nitrocellulose membranes manufactured by the GE subsidiary Whatman. The use of these novel

materials allowed us to investigate two targeted areas for assay improvement: novel immobilization strategies and novel virus detection strategies using recombinant affinity proteins.

The flu binder immobilization effort was divided into two areas of work, one to better understand and command protein adsorption to nitrocellulose and one to investigate other methods of immobilization. The use of flu binders for the development of novel virus detection strategies was explored in order to fully leverage the highly customizable flu binders and determine the optimal assay reagent stack for the capture and detection of HA. We then combined the best methods generated in this work to demonstrate an improved assay for influenza detection relative to standard immobilization and detection techniques.

The outcome of this work is a set of tools and strategies that help enable paper-based diagnostics for protein-based pathogen or biomarker detection. We have demonstrated this work extensively for the detection of influenza virus and HA antigen. This work includes several first-of-their-kind achievements: (1) the first demonstration of computationally designed, recombinant affinity proteins for paper-based diagnostics, (2) the first lateral flow test based on the influenza HA protein, and (3) the first paper-based assay for whole influenza virus detection. While we have not been able to demonstrate subtyping of HA during the timeframe of this work, we expect this work to be directly transferable to other HA subtypes, thereby representing the first step toward and groundwork for HA subtyping. In addition to this practical accomplishment, we also generated a deep base of knowledge about protein immobilization to nitrocellulose and recombinant affinity protein-based assays that can be utilized for the development of future paper-based assays for other disease targets.

1.3. Summary of Thesis

This dissertation is divided into eight chapters. This first chapter introduces the problem and the approach that we have taken herein to contribute to a solution to this problem. Chapter 2 provides a review of key background concepts that are required to understand the significance and scientific approach of the work. These background concepts include point-of-care diagnostics, paper microfluidics, influenza, and current approaches for paper-based assay development. Further background information is also provided in the subsequent chapters as needed to introduce a specific area of work. These chapters describe the five core areas of work performed for this thesis, each of which is summarized below. Each chapter includes the specific motivation for the given

area of work and breaks down the work into various sub-topics for which the detailed methods and results are provided.

The first core area of work, described in chapter 3, is the fundamental understanding and use of protein adsorption to nitrocellulose membranes. Since protein adsorption to nitrocellulose is poorly understood, we have studied the adsorption of several commonly used proteins in order to understand which physical properties most affect the adsorption process. Through this work, we also developed an experimental system for screening and assessing the adsorption of proteins on membranes. We then used this system and our protein adsorption knowledge to identify a nitrocellulose-binding protein unit that can be used as an anchor for the immobilization of recombinant affinity reagents, such as the flu binders.

Chapter 4 builds on the protein adsorption work of chapter 3 by describing the development of novel strategies for the immobilization of recombinant affinity proteins to nitrocellulose membranes. In order to determine the best method for immobilizing recombinant affinity proteins, we characterized four different immobilization strategies for the stem region flu binder: 1) direct adsorption of flu binder to nitrocellulose, 2) covalent attachment of thiolated flu binder to novel modified nitrocellulose membranes from GE GRC, 3) immobilization of biotinylated flu binder through streptavidin anchors, and 4) the use of our novel nitrocellulose-binding protein from chapter 3 as an immobilization anchor for the flu binder through genetic fusion. All methods were assessed in terms of both their immobilization efficiency and the resulting functionality of the flu binder as a capture agent for the flu HA assay.

Chapter 5 focuses on the development of a paper-based assay for influenza using novel detection schemes enabled by our recombinant flu binders, coupled with the immobilization strategies described in chapter 4. Whereas the work in chapter 4 was performed solely with a type of flu binder that targets the stem region of HA, the work in this chapter also included the use of a flu binder that targets the head region of HA. Armed with both the stem region and head region flu binders, we developed and characterized multiple assay stacks for the capture and detection of influenza HA. Some of these stacks detect isolated HA and therefore would require sample pre-processing in order to enable a fully functional flu test, while others detect intact influenza virus, eliminating the need for viral lysis and HA isolation.

Chapter 6 describes a novel statistical method to determine and compare limits of detection of bioassays, which is critical for assessing the assay development work herein, as well as for other

researchers in the field. This method was developed in collaboration with the Department of Statistics at the University of Washington and is meant to fill a need in the field for statistically robust methods to determine the analytical sensitivity of an assay. This method is demonstrated in full using data from a flu assay developed in chapter 5 and is applied to assay development data throughout this thesis.

Chapter 7 describes the work we have done to apply the assay development strategies from the previous chapters towards the development of an improved point-of-care flu test. Specifically, the most promising flu HA assays developed through chapters 4 and 5 were compared to a standard lateral flow test for HA. Through this work, we show that the novel immobilization strategies and detection schemes developed herein using the recombinant flu binder proteins have resulted in a more sensitive paper-based assay for influenza HA and virus. We also describe the work that has been done to begin to translate this assay to a full diagnostic device for point-of-care use.

This thesis concludes in chapter 8 with a summary and significance of the completed work and proposed future steps for researchers who wish to carry on with this line of work. A list of the scientific contributions—in the form of publications and presentations—stemming from this work is also provided.

Appendices are provided at the end of the document. A table of abbreviations is listed in Appendix A. The key MATLAB programs developed throughout this work are described and provided in Appendices B, C, D, and E.

2. Background

2.1. Point-of-Care Diagnostics

2.1.1. Need for Point-of-Care Diagnostics

The ability to diagnose a patient quickly and accurately is paramount to disease management, as the appropriate treatment cannot be administered until the cause has been identified. In many developing countries, point-of-care (POC) diagnostics play a critical role in this process, as clinics often lack the required infrastructure—such as electricity, refrigeration, equipment, and trained personnel—for more advanced testing [5]. The continued need for POC diagnostics for global health applications is therefore significant and is the focus of much POC test development, as I have helped review in the book chapter, “Microfluidic Diagnostics for Low-resource Settings: Improving Global Health without a Power Cord” [6].

There is also a strong need for POC testing in developed countries, however, which is often overlooked. In industrialized countries such as ours, we are afforded many luxuries that make accurate diagnosis possible, especially in hospitals and large clinics where reliable infrastructure, sophisticated equipment, and trained laboratory staff are available [8]. However, the time required to run these laboratory-based tests is often prohibitively long, resulting in the need for patients to return for a second visit or, worse, the missed opportunity for effective treatment [9]. Most significantly, accurate diagnosis often comes at a high expense, contributing to the unsustainable cost of our healthcare system. According to both the World Health Organization (WHO) [10] and detailed reports from the Commonwealth Fund [7,11], the United States spends more on healthcare than any other country in the world, with total expenditure and the expenditure growth rate, as percentages of the gross domestic product

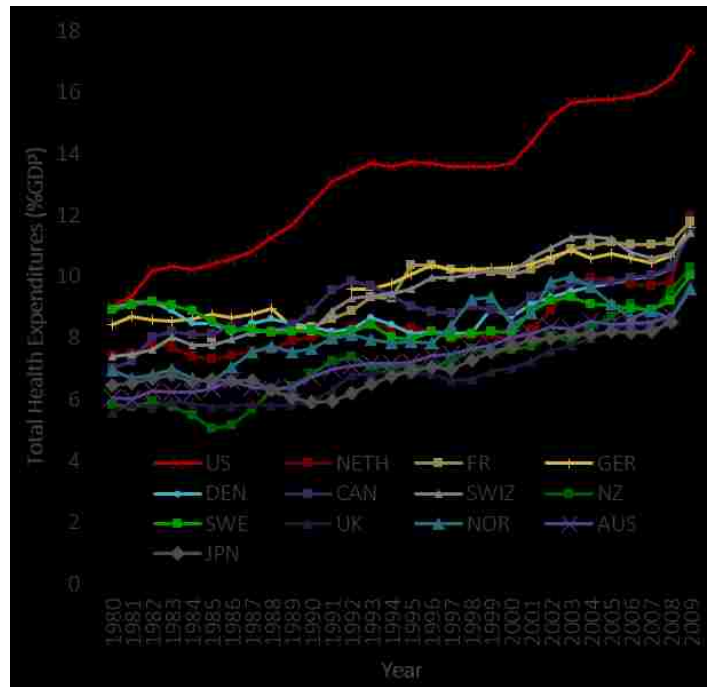


Figure 1. Health spending in the United States.

Total health expenditures in the U.S. (red line) compared to other industrialized countries. Adapted from Squires [7].

(GDP), outpacing all other nations (Figure 1) [7]. In 2009, the U.S. spent 17.4% of its GDP on healthcare [7], and that expenditure is projected to rise to 20% by the year 2020 [12]. Unfortunately, this high healthcare spending does not translate to quality of care, with the U.S. performing worse than many other industrialized countries in several key indicators [7,11]. The combination of this extremely high spending rate and these poor health outcomes makes clear the need for change in our healthcare system, and it is my hope that POC diagnostics and remote medicine will help usher in this type of positive change.

Overall, there is an urgent need for low-cost diagnostics that can be used at the point of care of the patient. The ability to manufacture high-performance diagnostics cheaply would lower one of the critical barriers to their adoption in clinics around the world, thereby increasing access to accurate diagnostic information. This would in turn improve disease management, individual patient outcomes, and even public health outcomes [13–15]. Importantly, this type of proactive healthcare results not only in more effective healthcare, but also in the elimination of downstream costs [13], which is where the bulk of cost savings due to POC diagnostics can be realized. Additionally, as the digital health and remote medicine movement continues to grow [13,16], the at-home use of POC diagnostics is poised to facilitate frequent patient monitoring and preventative medicine, which could reduce overall healthcare costs and improve outcomes even further. It is therefore this need for proactive, accurate, and cost-effective healthcare across the globe that has motivated my work herein.

2.1.2. Current Point-of-Care Diagnostics

Currently, there are many point-of-care diagnostic tests on the market and even more emerging through the research pipeline as the need for these tests becomes increasingly recognized. Current POC tests vary in type, cost, sophistication, and efficacy, leaving much room for improvement in most cases. The two major types of current POC diagnostics are microfluidics-based tests and lateral flow tests, which are reviewed in the following sections.

Traditional Microfluidics-Based Tests

Microfluidics refers to the use of systems that manipulate fluid through channels with at least one dimension less than 1 mm. Microfluidic systems feature several attributes that are ideal for rapid diagnostic testing, including process automation, fast diffusion times, and the need for only small

(microliter) sample volumes [8,17]. For these reasons, several microfluidics-based POC tests have been developed.

The GeneXpert from Cepheid is perhaps the biggest success story in global health diagnostics, as it has greatly aided the diagnosis of tuberculosis (TB), including drug-resistant forms [18]. The GeneXpert MTB/RIF test utilizes microfluidics to perform nucleic acid testing of *Mycobacterium tuberculosis*, obtaining a result within two hours [19]. The GeneXpert system consists of a fairly sophisticated instrument that performs most of the testing functionality and disposable, one-time-use cartridges on which the testing reagents are stored [20]. While the GeneXpert has greatly increased the speed of TB diagnosis, reducing mean testing-to-treatment times from 56 to 5 days in one study [18], the instrument is too expensive and requires too much infrastructure (e.g. electricity) to be used in very remote settings. Even at special negotiated prices for low-resource countries, the instrument still costs \$17k, plus \$10 for every one-time-use cartridge [21]. For these reasons, the GeneXpert is recognized as a solution primarily for centralized laboratories within developing countries [9,15].

The iSTAT from Abbot Diagnostics is a true POC device, serving as a portable analyzer of a panel of common blood analytes used for patient monitoring [15,22]. This hand-held device is based on a microfluidic format that couples the fluid flow to electrochemical detection systems for the measurement of blood chemistries and electrolytes [15,22]. Despite its utility, the iSTAT is still too expensive for many low-resource settings and is rendered useless in settings where maintenance is not possible when it breaks.

Our own group in the Yager laboratory was involved in the development of the DxBox, a small, minimally instrumented device designed to achieve differential diagnosis of fever through a panel of tests for six different fever-causing pathogens [23]. The DxBox system utilizes disposable assay cards controlled by pneumatically driven fluidics provided by the reusable instrument, which also serves as the test reader [23,24]. The DxBox team demonstrated successful multianalyte detection using a flow-through membrane immunoassay card, with all reagents stored dry on the card [24,25]. The team also developed nucleic acid amplification tests (NAATs) [23]. While the DxBox system was never commercialized, the corporate collaborator on the project, Micronics, continues to pursue similar test development as part of the PanNAT Molecular Diagnostic System [26].

Finally, the Sia group has developed a series of iterations on its “mChip” diagnostic system over the past several years (Figure 2), which, in my estimation, has been the best example of a truly low-cost

microfluidic diagnostic system to date. The mChip essentially performs the enzyme-linked immunosorbent assay (ELISA), but in a simple microfluidic format that, in all iterations, includes an automated reader. Originally demonstrated in 2011, the first iteration of the mChip required manual fluid handling and use low-cost materials to achieve a system that comes at one tenth the materials cost (\$0.55/test) of a traditional laboratory ELISA (\$1.80-\$6.20/test) and a fraction of the cost for the equipment (\$75 vs. \$20k) [27]. In particular, the Sia group used injection-molded chips from polystyrene and cyclic olefin copolymer, allowing for significantly reduced cost compared to microfluidic chips created from polydimethylsiloxane (PDMS) via photolithography [27]. During field-testing in Rwanda, the 1st-generation mChip was able to simultaneously detect HIV and syphilis antibodies from 1 μ L of whole blood with sensitivities and specificities comparable to laboratory ELISA [27]. To eliminate the need for pumps, the 1st-generation mChip utilized a simple plastic syringe to drive fluid through the chip [27]. While creative and fairly effective, the manual manipulation of reagents required by this method was not ideal, as it prevents the device from being run by untrained users. In 2013, the group automated the fluid handling into a small device, combined it with the reader, and added cell-phone and satellite communication technologies to synchronize the results with the patient's electronic health record [28]. With this 2nd-generation mChip, the Sia group demonstrated nearly 100% sensitivity and specificity of HIV serodiagnosis from 1 μ L whole blood, combined with real-time communication of results to the patient's cloud-based electronic health record [28]. These advancements for the 2nd-generation, fully automated mChip came at a price, however, with an estimated cost of \$1.00-\$3.00/test and <\$1k for the box [28]. Most recently, the group consolidated all functions onto smartphone dongle device that is powered solely by the battery of the smartphone and is accompanied by an app to run the test [29]. With this dongle-based 3rd-generation mChip, the authors demonstrated a first-of-its kind triplexed immunoassay for HIV antibody and two syphilis antibodies, designed for use in prenatal screening to prevent mother-to-child transmission of these infectious diseases. In field testing by Rwandan healthcare workers, the 15-minute dongle-based test yielded sensitivities of 92% to 100% and specificities of 79% to 100%, with a 97% patient preference for the dongle over laboratory-based tests [29]. This strong performance was also achieved at a low cost, with \$1.44/test in material costs and an estimated \$34 for the dongle. However, the dongle contained substantially less sophistication than the fully automated 2nd-generation device, with the 3rd-generation dongle requiring manual pre-mixing of the sample with diluent, loading of the diluted sample, and actuation of a "one-push vacuum" to initiate fluid flow. Overall, the evolution of these mChip devices, shown in Figure 2, illustrates both the remarkable use of technology to enable

sophisticated diagnostic development and the trade-offs between cost and automation that continue to hinder widespread adoption of traditional microfluidic diagnostics at the point of care.

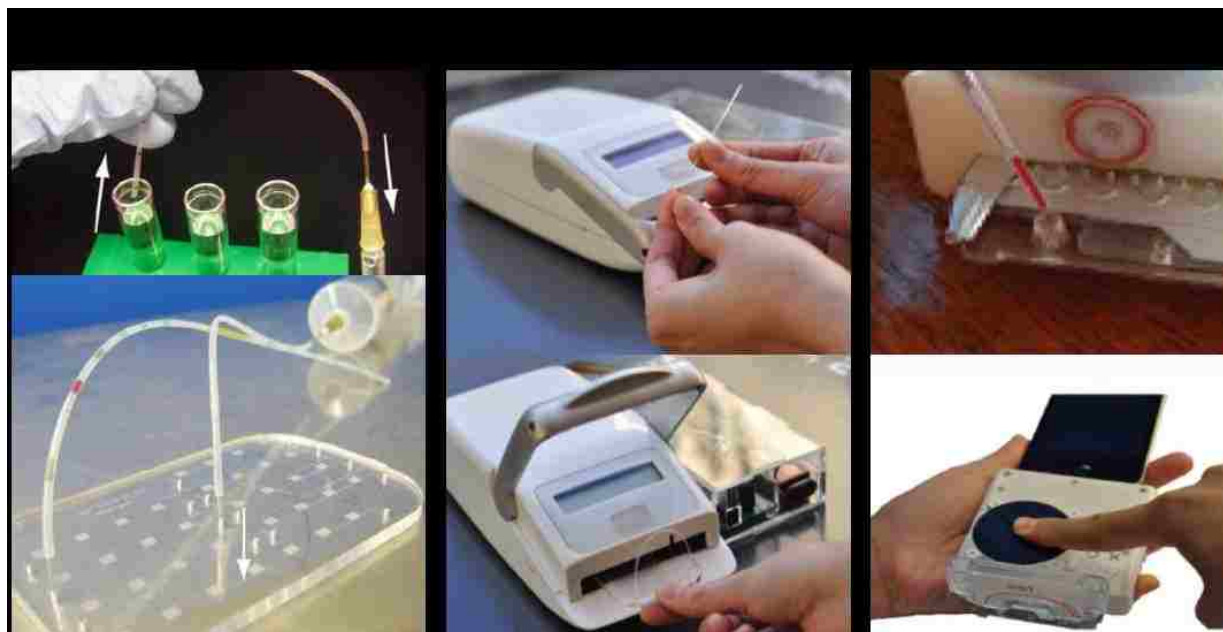


Figure 2. The evolution of the “mChip” microfluidic ELISA system by Sia and colleagues.

The mChip is a low-cost, microfluidic replacement for ELISA testing. Three generations of the mChip have been developed. (A) The 1st-gen mChip is very low in cost (\$0.55/test, \$75 for reader), but requires substantial user manipulation to program fluid flow [27]. (B) The 2nd-gen mChip has a fully automated device for fluid handling, readout, and data communications, at a cost of <\$1k for the box and \$1-\$3/test [28]. (C) The 3rd-gen mChip is run by a smartphone dongle device and accompanying app. It offers high sophistication for the cost (\$34 for dongle and \$1.44/test), but still requires manual sample pre-processing and loading by the user [29].

Despite many sophisticated capabilities of microfluidics-based POC diagnostics and the need for only very low sample volumes, these tests have found limited use in POC settings, mostly due to the high costs and infrastructure requirements associated with the equipment needed to automate the devices. In the case of the mChip, the 1st-generation and 3rd-generation devices are fairly low in cost, but require a level of user manipulation that is non-ideal for POC use. In contrast, lateral flow tests are extremely inexpensive and easy to use and have been widely applied to POC diagnostics. This category of devices is reviewed in the next section.

Lateral Flow Tests

Lateral flow tests (LFTs) are perhaps the most common format for low-cost testing of biological analytes of interest. First introduced in the 1980s for pregnancy testing [30–32], LFTs are now used for testing of many analytes, including disease markers in humans and animals, environmental and agricultural contaminants, drugs of abuse, and biowarfare agents [30,31]. The widespread use of

LFTs has propelled this technology into a \$2.3 billion market, with pregnancy tests still comprising the largest market share [30]. In fact, 10 million lateral flow tests are manufactured each year for pregnancy testing alone [13].

A lateral flow test is based on a simple strip of porous membrane, typically nitrocellulose, which both allows fluid flow through the strip and serves as the substrate on which the detection reaction takes place [31,33] (Figure 3).

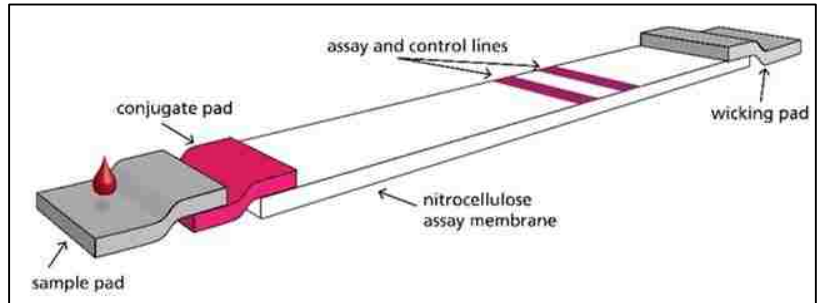


Figure 3. Illustration of a typical lateral flow test (LFT).

A typical LFT contains a sample pad, conjugate pad, nitrocellulose assay membrane, and wicking pad. Image courtesy of Dr. Gina Fridley.

This porous strip is in contact with an absorbent pad on the distal end, which promotes wicking, and a series of sample and conjugate pads on the proximal end, where the assay begins. The conjugate pad contains dried detection antibody for the target analyte that has been conjugated to a visible label, typically gold nanoparticles. Two lines are pre-printed on the porous strip: 1) a test line containing antibody that specifically captures the target analyte of interest and 2) a control line containing antibody that captures excess gold-labeled detection antibody. To start the assay, the user simply applies the patient sample (usually blood, urine, or saliva) to the sample pad, which rehydrates the gold-labeled detection antibody and wicks through the porous membrane, allowing this antibody to bind the target analyte, if present. This antigen-antibody complex (if present) is then bound by the capture antibody at the test line, generating a red color in this region due to the accumulation of gold nanoparticles. The control line also turns red due to the binding of excess gold-labeled antibody, indicating that the test has functioned properly and the reagents have reached the end of the strip.

Due to their low cost and ease of use, lateral flow tests have found utility for diagnostic testing in many POC settings, including doctor's clinics, emergency rooms, ambulances, the battlefield, low-resource clinics in the developing world, and the home [5,30,34,35]. Perhaps most significantly for the future of POC diagnostic testing domestically, the U.S. Food and Drug Administration (FDA) approved an HIV lateral flow test for home use in July 2012 [36], opening the door for at-home testing of infectious and other diseases. Lateral flow tests have therefore played a significant role in establishing POC testing as a valid means of medical diagnosis. Despite this success, LFTs often

suffer from low sensitivity, as compared to gold standard laboratory-based tests [30], driving the need for more accurate POC tests.

2.2. Paper Microfluidics

Based on the continued need for low-cost, easy-to-use POC diagnostics, a new type of test has emerged: the paper-based diagnostic test. These tests, based on the concept of paper microfluidics, combine the simplicity of lateral flow tests with the sophistication of microfluidic-based tests to achieve an intermediate format that is highly suitable for POC use [13,37,38]. The principles of paper microfluidics and current paper-based diagnostic platforms are discussed in the following sections.

2.2.1. Principles of Paper Microfluidics

Attributes of Paper-Based Systems

The hallmark of all paper-based diagnostic systems is the use of “paper” as the primary assay substrate. While paper in the literal sense refers to the everyday writing material made from cellulose pulp, the paper microfluidics community broadly defines “paper” as any porous material that takes the form of a thin sheet [39]. This broad definition of paper will be used herein.

Paper is an ideal substrate for POC bioassays for many reasons. First, paper materials are generally inexpensive, allowing paper-based devices to be widely affordable and accessible [39,40]. Second, paper is highly compatible with biological and chemical reagents and amenable to the storage of such reagents in dry form [39,40]. These features enable long shelf lives for paper-based diagnostics, as have already been demonstrated by lateral flow tests [33]. Third, the porous structure of paper provides both a high internal surface area and short diffusion distances, allowing for high adsorptive capacity and fast reaction times, respectively [39–41]. Finally, and perhaps most importantly, paper affords the passive wicking of fluids by capillary action, eliminating the need for external pumps or power sources and thereby significantly reducing the cost of paper-based systems relative to their microfluidic counterparts [39,40,42]. The physics of this fluid flow in porous media is described next.

Fluid Flow in Porous Media

The flow, or wicking, of fluid through a porous substrate is governed by the capillarity of the system. In a single capillary tube, it is well known that the surface tension of an internal liquid will

cause the liquid to migrate upwards through the tube, until the capillary pressure is balanced by resistive forces [43]. In fact, this passive capillary wicking is the basis for several naturally occurring phenomena, ranging from the transport of water from the roots of a tree to its top-most branches, to the drainage of tears from the eyes [44,45]. In general, the capillary pressure, P_c [N/m²], on a body of liquid in a tube is given by Eqn 1, where γ is the surface tension [N/m], θ is the contact angle between the liquid and the surface, and r is the radius of the tube [m].

$$P_c = \frac{2 \cdot \gamma \cdot \cos\theta}{r} \quad \text{Eqn 1}$$

This pressure constitutes the driving force for fluid flow in the tube, which is governed by the Poiseuille equation given in Eqn 2.

$$Q = \frac{\pi \cdot r^4 \cdot \Delta P}{8 \cdot \mu \cdot L} \quad \text{Eqn 2}$$

In this Poiseuille equation, Q is the volumetric flow rate [m³/s], μ is the viscosity of the liquid [N·s/m²], L is the length of the fluid column [m], and ΔP is the difference in pressure [N/m²] across distance L , which in this case is given by the capillary pressure in Eqn 1.

Based on Poiseuille flow, we can derive an expression for the rate of advancement of the liquid front, as follows. First, we can write the average linear flow velocity, $\langle u \rangle$ [m/s], as the volumetric flow rate divided by the area of the tube ($\pi \cdot r^2$ [m²]), as shown in Eqn 3.

$$\langle u \rangle = \frac{Q}{\pi \cdot r^2} = \frac{1}{\pi \cdot r^2} \cdot \frac{\pi \cdot r^4 \cdot \Delta P}{8 \cdot \mu \cdot L} = \frac{r^2 \cdot \Delta P}{8 \cdot \mu \cdot L} \quad \text{Eqn 3}$$

We can then substitute in the capillary pressure given by Eqn 1 for ΔP , as shown in Eqn 4.

$$\langle u \rangle = \frac{r^2}{8 \cdot \mu \cdot L} \cdot \frac{2 \cdot \gamma \cdot \cos\theta}{r} = \frac{\gamma \cdot \cos\theta \cdot r}{4 \cdot \mu \cdot L} \quad \text{Eqn 4}$$

Since the average linear flow velocity is the rate of change of the length of the fluid column, L , with time, we can write Eqn 4 as this time derivative, given by Eqn 5.

$$\langle u \rangle = \frac{dL}{dt} = \frac{\gamma \cdot \cos\theta \cdot r}{4 \cdot \mu} \cdot \frac{1}{L} \quad \text{Eqn 5}$$

We can then rearrange Eqn 5 and integrate each side, as shown in Eqn 6.

$$\int L \cdot dL = \int \frac{\gamma \cdot \cos\theta \cdot r}{4 \cdot \mu} \cdot dt \quad \text{Eqn 6}$$

This integration yields the expression in Eqn 7.

$$L^2 = \frac{\gamma \cdot \cos\theta \cdot r \cdot t}{2 \cdot \mu} \quad \text{Eqn 7}$$

Taking the square root of each side, we arrive at an expression that describes the position, L , of the end of the fluid column as a function of time, given by Eqn 8.

$$L = \sqrt{\frac{\gamma \cdot \cos\theta \cdot r \cdot t}{2 \cdot \mu}} \quad \text{Eqn 8}$$

This expression is known as the Washburn equation, attributed to Edward Washburn, who published this derivation in 1921 to describe capillary flow [43]. However, Bell and Cameron described the basic form of this equation 15 years earlier [46]. The hallmark of this equation is the square-root dependence of L on time, which means that the advancement of the fluid column slows with time, due to the added resistance of the fluid column itself.

In his paper, Washburn further described the application of Eqn 8 to flow in porous media [43]. Specifically, Washburn postulated that a porous substrate could be approximated as a bundle of n capillary tubes with radii ranging from r_1 to r_n [43]. In this approximation, the total volume of liquid flowed into the porous medium can be described by Eqn 9.

$$V_{total} = \sum_{i=1}^n \pi \cdot r_i^2 \cdot L = \pi \cdot \sqrt{\frac{\gamma \cdot \cos\theta \cdot t}{2 \cdot \mu}} \cdot \sum_{i=1}^n r_i^{5/2} \quad \text{Eqn 9}$$

Although Washburn did not explicitly extend this derivation to describe the average distance of fluid flow in a porous substrate, it follows that this distance, $\langle L \rangle$, can be derived as follows. First, the total distance traveled by fluid in the pores, L_{total} , can be written as the total volume traveled, given by Eqn 9, divided by the sum of the pore areas, as shown in Eqn 10.

$$L_{total} = \frac{V_{total}}{\pi \sum_{i=1}^n r_i^2} = \sqrt{\frac{\gamma \cdot \cos\theta \cdot t}{2 \cdot \mu}} \cdot \sum_{i=1}^n r_i^{1/2} \quad \text{Eqn 10}$$

The average distance traveled, $\langle L \rangle$, can then be written as the total distance traveled, L_{total} , divided by the number of pores, or approximated capillary tubes, n , as shown in Eqn 11.

$$\langle L \rangle = \frac{L_{total}}{n} = \frac{1}{n} \cdot \sum_{i=1}^n \sqrt{\frac{\gamma \cdot \cos\theta \cdot r_i \cdot t}{2 \cdot \mu}} \quad \text{Eqn 11}$$

Finally, the mean pore radius, r_m , can be expressed according to Eqn 12.

$$r_m = \frac{1}{n} \cdot \sum_{i=1}^n r_i \quad \text{Eqn 12}$$

Therefore, it can be seen that Eqn 11 can simply be reduced to Eqn 13.

$$\langle L \rangle = \sqrt{\frac{\gamma \cdot \cos\theta \cdot r_m \cdot t}{2 \cdot \mu}} \quad \text{Eqn 13}$$

Eqn 13 describes the average location of the liquid front as function of the mean pore size. In the paper microfluidics literature, $\langle L \rangle$ is typically replaced with L , which describes the location of the fluid front in a porous substrate, and this equation is referred to as Washburn flow [47–49]. The rate of change of this fluid front can then be written as the derivative of Eqn 13 with respect to time, as shown in Eqn 14, which represents the linear velocity of fluid flow under Washburn flow.

$$\frac{dL}{dt} = u = \sqrt{\frac{\gamma \cdot \cos\theta \cdot r_m}{8 \cdot \mu \cdot t}} \quad \text{Eqn 14}$$

Additionally, from this derivation, it follows that the average capillary pressure felt by liquid in a porous substrate can also be expressed as a function of the mean pore size, given by Eqn 15.

$$P_c = \frac{2 \cdot \gamma \cdot \cos\theta}{r_m} \quad \text{Eqn 15}$$

It should be noted that Washburn cautioned against the general application of his equation to porous media, stating that the relationship only holds for systems that can be approximated as a collection of n cylindrical pores, and that other systems must be tested experimentally [43]. Nevertheless, the paper microfluidics community routinely uses the Washburn equation to describe flow in porous media, and, while the square-root dependence on time has been experimentally verified, the exact form of the coefficient has not [47–49].

In typical paper-based systems, the flow of liquid through the primary assay substrate is aided by the presence of a large absorbent pad, called a wicking pad, which provides a large (negative) capillary pressure to the system. During the initial wet-out of the primary assay substrate, the rate of flow is governed by the Washburn flow equation (Eqn 13), as described above. Once the liquid front has reached the wicking pad, however, the length of the fluid column in the system and the capillary pressure provided by the wicking pad are both approximately constant, resulting in a quasi-steady flow rate. This “fully wetted” flow is described by the Darcy equation of flow, given by Eqn 16.

$$Q = \frac{\kappa \cdot A \cdot \Delta P}{\mu \cdot L} \quad \text{Eqn 16}$$

In this Darcy flow equation, Q is the volumetric flow rate [m^3/s], κ is the permeability of the membrane [m^2], A is the cross-sectional area of the membrane [m^2], μ is the viscosity of the liquid [$\text{N}\cdot\text{s}/\text{m}^2$], L is the length of the fluid column [m], and ΔP is the difference in pressure [N/m^2] across distance L , which in this case is given by the capillary pressure in Eqn 15. This equation was determined empirically by Henry Darcy in 1856 to describe the flow of liquid in soil [50,51], but has since been derived from the Navier-Stokes equation of motion, establishing its theoretical basis as well [52].

In paper-based systems, typical flow rates are on the order of 10^{-4} m/s [47,53]. This characteristic velocity can be combined with the characteristic length scale of the pores, i.e. the average pore diameter (~ 10 μm), to determine the Reynolds number of a typical paper-based device. The Reynolds number (Re), which represents the ratio of the inertial forces to the viscous forces of the system, is given by Eqn 17.

$$Re = \frac{\rho \cdot u \cdot L}{\mu} \quad \text{Eqn 17}$$

In this Reynolds number equation, ρ is the fluid density [kg/m^3], u is the velocity [m/s], L is the characteristic length scale [m], and μ is the fluid viscosity [$\text{kg}/(\text{m}\cdot\text{s})$]. For a paper-based system, where L is approximately 10 μm , the Reynolds number is on the order of 0.001, as shown in Eqn 18.

$$Re = \frac{(1000 \text{ kg}/\text{m}^3) \cdot (10^{-4} \text{ m}/\text{s}) \cdot (10^{-5} \text{ m})}{(8.90 \times 10^{-4} \text{ kg}/(\text{m} \cdot \text{s}))} = 0.001 \quad \text{Eqn 18}$$

Since this Reynolds number is well below unity, the flow in these paper-based systems can be characterized as laminar [54]. Under laminar flow, molecules flow only along their given streamlines, and the only transverse motion that occurs is through diffusion [54,55]. Given this property of laminar flow, paper-based devices have remarkably similar flow characteristics to traditional microfluidic channels, which has allowed many microfluidic tools to be ported to the paper microfluidics field [39,56]. The one exception to this similarity is for the flow of large molecules, which undergo enhanced transverse transport in porous media, presumably due to mechanical interactions with the pore structure of paper substrates [41].

2.2.2. Current Paper-Based Diagnostic Platforms

While paper chromatography, blotting assays, and lateral flow tests have existed for decades, the recent emergence of novel paper-based diagnostic platforms began in the late 2000s with the work of George Whitesides' group [42,57]. Recognizing the benefits of paper-based systems and their suitability for POC use, several different paper-based platforms and subsequent iterations have since been developed. These platforms fall under two main categories: microfluidic paper analytical devices (μ PADs) and two-dimensional paper networks (2DPNs), as reviewed below. All platforms utilize some form of patterning to create flow channels in a porous medium that are hydrophilic relative to a hydrophobic barrier [40].

Microfluidic Paper Analytical Devices (μ PADS)

The original paper-based device of the paper resurgence was the microfluidic paper analytical device (μ PAD), developed in the laboratory of George Whitesides [42,57]. Basic two-dimensional μ PADs feature a flow path consisting of a single inlet channel that diverges into multiple analyte channels, as shown in Figure 4A. These flow paths were initially created using photolithography to pattern hydrophobic channel barriers onto a

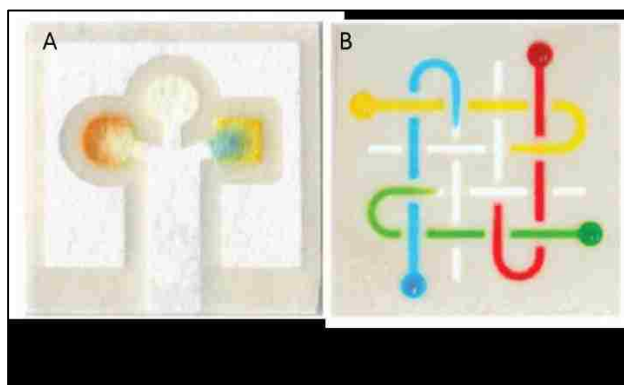


Figure 4. Multi-analyte detection afforded by μ PADs. Examples of (A) two-dimensional [42] and (B) three-dimensional [58] μ PADs.

cellulose substrate, a technique that was carried over from PDMS microfluidics [57]. Since then, most two-dimensional μ PADs have been fabricated using wax printing to deposit the hydrophobic barriers that define the flow channels within the cellulose substrate [59]. Three-dimensional μ PADs have also been developed (Figure 4B), created by the stacking of multiple layers of porous media (typically cellulose) and adhesive material [58,60,61]. The flow channels within each layer are designed to interact strategically with those of the other layers to achieve three-dimensional flow paths that fit compactly into a small material footprint.

Many examples of diagnostic tests have been developed using μ PADs. These tests include the colorimetric detection of total glucose and protein in urine (e.g. urinalysis) [57,58], the fluorescence-based detection of β -galactosidase using a fluidically powered battery [62], and the colorimetric detection of particulate metal in aerosols as a monitoring tool for occupational

exposure [63]. Perhaps the most successful application of μ PADs to date has been the liver enzyme test to monitor the health of patients who are taking combinatorial medications for HIV and/or tuberculosis [64], which is currently in field-testing [65]. Additionally, μ PAD technology is continually being developed, and there is currently a large focus on incorporating printable electronic elements on μ PADs [39,66,67]. Overall, the μ PAD represents a useful paper-based platform, especially when multianalyte detection is desired. However, demonstrations of μ PADs to date have been mostly limited to detection steps that employ simple, single-step chemical or enzymatic reactions. Additionally, current μ PADs generally lack the use of biological affinity reagents, which would likely require the use of porous materials other than cellulose (see section 2.4.1 for further discussion about substrate choice).

Two-Dimensional Paper Networks (2DPNs)

Our own group in the Yager, Lutz, and Fu laboratories pioneered the development of the two-dimensional paper network (2DPN). This paper-based platform utilizes the shape and spatial arrangement of the paper substrate to control fluid flow and achieve automated, multi-step processing. These devices are made from porous nitrocellulose, in which flow paths are physically cut from the parent sheet, typically using a CO₂ laser cutter [69]. This method represents a simple way to create flow paths within the porous substrate and eliminates the need for patterning of additional materials to create hydrophobic barriers.

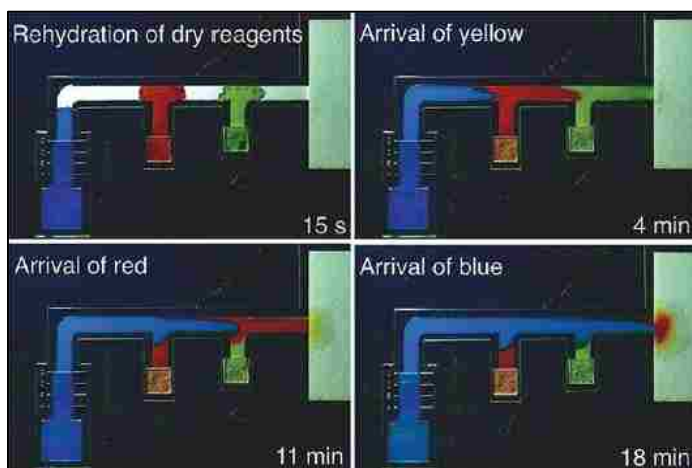


Figure 5. Multi-step reagent delivery afforded by a 2DPN. The multi-step delivery of yellow, red, and blue food coloring is demonstrated by a 2DPN [68].

To date, our group has demonstrated many features of 2DPNs. In particular, Fu *et al.* demonstrated that the timing of fluid delivery could be tuned based on the geometry of the network [48,70]. Importantly, the use of multiple inlet legs and a single outlet leg allows for the delivery of multiple reagents over a given detection region (Figure 5) [49,70]. This multiple input leg format has been used, in combination with a folding-activated card platform, to demonstrate the chemical amplification of gold nanoparticle-based signal [71], the improvement in sensitivity of a lateral flow test for pregnancy [72], and the achievement of a malaria assay with sensitivity comparable to bench-top ELISA [68]. Additional tools have since been demonstrated by our group for use in 2DPN

devices, such as mixing and dilution [56], flow visualization [73], long-term storage of enzymes [74], and controlled rehydration of patterned reagents [75,76]. Fluid tools have been a particular area of focus, with members of our group demonstrating the following fluid metering and valving techniques: the use of sugar barriers to achieve timing delays without the expansion of the 2DPN footprint [70,77], dissolvable sugar bridge for fluid metering [78], the addition of cellulose shunt pads for tunable delays in timing [79], and a comprehensive valving toolkit based on timing wicks that actuate mechanical valves fluidically [80]. Based on these tools, the proof-of-concept malaria PfHRP2 assay has been demonstrated a remarkable six times, each using different features and tools in the 2DPN toolbox [68,74,76,77,79,80].

Other researchers have also made significant contributions to the 2DPN platform. For example, the Richards-Kortum group demonstrated a 2DPN folding card that performs isothermal amplification and subsequent detection of HIV DNA [81]. Apilux *et al.* demonstrated a nitrocellulose-based device for an automated ELISA [82]. As for fluid handling, Chen *et al.* demonstrated an elegant paper-based diode for fluidic valving [83]. Although both Apilux *et al.* and Chen *et al.* employed printing techniques to introduce hydrophobic barriers, instead of laser cutting, the devices primarily utilize the geometry of the paper network to control flow and achieve multi-step processing, making them both prime examples of 2DPN technology.

Overall, the 2DPN format is ideal for bioassays employing biological detection reagents and offers the advantage of multi-step processing, which can be used to achieve sample pre-processing, signal enhancement, and even simple rinsing to improve signal-to-noise ratios. For these reasons, the 2DPN will be used as the platform of choice for the development of the influenza diagnostic herein. Before we discuss the details of the assay development, let us review the basics of influenza, described next.

2.3. Influenza

2.3.1. Biology of Influenza

Influenza Classification

Influenza, or flu, is a commonly occurring set of viruses that have infected humans for at least the past two millennia [84]. The three different types of influenza—A, B, and C—represent three of the five genera of the orthomyxoviridae family of viruses [85] (Figure 6). Each influenza genus consists of a single species of the same name, meaning that influenza A, B, and C are distinct species and

genera of virus. The influenza A virus is further subtyped based on its surface proteins, hemagglutinin and neuraminidase, as described below. The orthomyxoviridae family also contains the isavirus (infecting salmon) and the thogotovirus (infecting ticks), neither of which is antigenically similar to the flu viruses [85,86].

Family	Orthomyxoviridae				
Genus	Influenza A	Influenza B	Influenza C	Isavirus	Thogoto virus
Species	Influenza A	Influenza B	Influenza C	Isavirus	Thogoto/Dhori
Subtype	H 1-16	N 1-9			

Figure 6. Phylogenetic description of the orthomyxoviridae family of viruses.
The orthomyxoviridae family of viruses contains the influenza viruses (A, B, and C).

Influenza Structure

Influenza is an RNA-based virus with a segmented genome [86,88]. The single-stranded RNA segments are packaged with nucleoproteins (NPs), forming the ribonucleoprotein (RNP) structures that are surrounded by the viral envelope [86,88]. Influenza A and B viruses contain eight RNA segments, each of which encodes for one to two viral proteins, with a total of 11 viral proteins for influenza A (Table 1) [86]. Influenza C virus contains only seven RNA segments, as it includes only one type of membrane glycoprotein, the hemagglutinin-esterase-fusion protein, which has functionalities similar to those of both the hemagglutinin and neuraminidase glycoproteins of the influenza A virus [86].

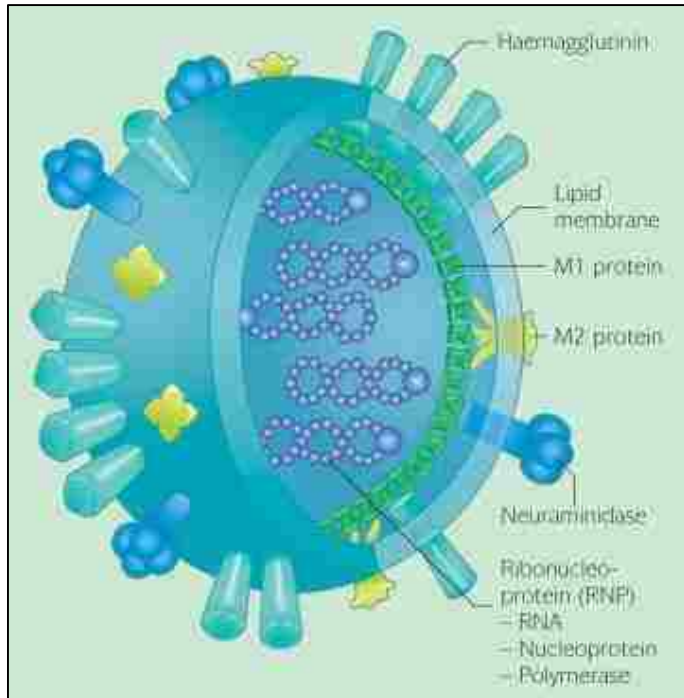


Figure 7. Model structure of the influenza A virus.
From the Rapid Reference to Influenza [87].

Table 1. List of the RNA segments and encoded proteins of the influenza A viral genome.

The ten proteins encoded by the eight RNA segments of the influenza A viral genome. Adapted from [86–88].

RNA Gene Segment	Encoded Protein	Abbr.	Molecules per Virion	Description
1	Polymerase basic 2	PB2	30-60	Component of RNA polymerase; initiation of transcription
2	Polymerase basic 1	PB1	30-60	Component of RNA polymerase; elongation of mRNA
2	PB1-F2	PB1-F2	unknown	Accessory protein from alternate open reading frame; Not present in all influenza A viruses
3	Polymerase acid	PA	30-60	Component of RNA polymerase; protease activity
4	Hemagglutinin	HA	500	Membrane glycoprotein, trimer; receptor binding
5	Nucleoprotein	NP	1000	Internal protein associated with RNA
6	Neuraminidase	NA	100	Membrane glycoprotein, tetramer; virion release
7	Membrane protein 1	M1	3000	Major membrane component that supports lipid bilayer
7	Membrane protein 2	M2	20-60	Membrane ion channel, tetramer
8	Non-structural protein 1	NS1	n/a	Secreted protein; interferon antagonist
8	Non-structural protein 2	NS2	130-200	Nuclear export of viral RNPs

Influenza virions are roughly spherical particles of approximately 100 nm in diameter [84,86], with naturally occurring isolates showing much greater variability in size and shape than virus grown in culture [84,88]. In clinical isolates, especially, filamentous forms of virus are often observed, with the elongated virions exceeding 300 nm in length [86]. Each influenza A virion is assembled according to the structure shown in Figure 7. The internal RNP structures are surrounded by an envelope of the viral M1 protein, which supports a host-derived lipid bilayer membrane [84,86–88]. This membrane incorporates three viral proteins: the integral M2 protein, which serves as an ion channel, and the two glycoproteins, hemagglutinin (HA) and neuraminidase (NA), which stick out as “spikes” from the viral envelope [84,86–88]. Hemagglutinin is the more prevalent of the two spike proteins and facilitates binding to the host cell through its sialic acid binding site [84,86–88]. Neuraminidase is an enzyme that hydrolytically cleaves sialic acid from glycoproteins and glycolipids and therefore serves to release newly formed virions from the host cell [84,86–88]. Both the HA and NA proteins are antigenic, eliciting immune responses in the host that help protect against infection [85].

Subtypes and Strains of Influenza

To avoid neutralization by host antibodies, both HA and NA undergo considerable mutation to achieve antigenic changes, especially in non-essential portions of the proteins [85]. The accumulation of these changes over time has led to the development of divergent subtypes of both the HA and NA proteins of influenza A [85]. Currently, there are 16 established subtypes of HA and 9 established subtypes of NA [85], where each subtype has been identified by its unique antigenicity based on serological assays [89]. Overall, any two subtypes of HA or NA can differ in amino acid sequence by over 30% [84]. Together, the HA (H) and NA (N) subtypes define the overall subtype of a given influenza A virus, e.g. H1N1. Influenza B and C viruses do not have any subtypes [85]. It should be noted that two additional HA-like and NA-like proteins have been discovered in novel influenza-like viruses in bats [90,91]. These proteins have been proposed as the 17th and 18th HA subtypes and 10th and 11th NA subtypes of influenza A [90,91]. However, this classification is still under debate, since the viruses are substantially dissimilar from influenza A, the proteins do not have canonical HA and NA functionality, and the viruses have not been identified in aquatic birds [92,93].

All established HA and NA subtypes of influenza A have been identified in aquatic birds, establishing waterfowl as the primary reservoir of influenza A virus [85]. Additionally, influenza A virus is now antigenically stable in wild aquatic birds, which suggests that influenza has reached evolutionary equilibrium in these hosts and has adapted for survival within this reservoir [85]. These birds can transmit influenza A to several mammalian species, including humans, pigs, dogs, and horses, as well as to other avian species such as poultry [85]. In addition to direct transmission from waterfowl, both pigs and non-aquatic birds (e.g. poultry) can also transmit influenza A to humans [85]. Influenza B and C viruses both infect humans, but not birds, and have infected humans for much longer than the approximately 150 years of influenza A infection [85]. Consequently, influenza B and C viruses are substantially more evolutionarily stable in humans than influenza A, resulting in lower pathogenicity of these species [85].

Finally, for any given influenza subtype (of flu A) or species (flu B or C), additional mutations continue to develop in the HA and NA proteins while the virus is present in its host, a process known as antigenic drift [85]. These gradual changes in the HA and NA proteins result in the development of different strains of influenza, which vary by year and by location. Each strain of influenza is therefore defined by the nomenclature described in Table 2, with the name of the host species being listed only for non-human sources.

Table 2. Description of influenza virus nomenclature.

Description of the nomenclature used to identify influenza viruses from humans (top row) and non-humans (bottom row) [85,87].

	Type / Host (if non-human) / Location / Strain No. / Isolation Year (Subtype)
Human example	A / California / 07 / 2009 (H1N1)
Non-human example	A / Duck / Hong Kong / 205 / 1977 (H5N3)

Antigenic Shift and Influenza Pandemics

In addition to the gradual antigenic drift of the HA and NA proteins in humans, both proteins can also undergo dramatic antigenic shifts in which one or both proteins of the currently circulating influenza A virus changes suddenly and drastically [85]. These shifts are usually the result of genetic reassortment of RNA segments during the production of new virions, a process that is similar to the swapping of chromosomes during meiosis in humans [84,85]. In particular, this reassortment occurs when a non-human—typically avian—influenza A virus is co-present with a human influenza A virus. This allows a progeny virus to be created that contains some human-based virus genes but with new, non-human-based HA or NA proteins to which the human population generally does not have immunity [85]. In modern human history, four antigenic shifts of the circulating influenza A virus have occurred. The first occurred during the emergence of H1N1 influenza in 1918 (known as the “Spanish influenza”), which is presumed to have transferred from an avian source [85]. This pandemic was the most severe influenza pandemic to date, infecting one third of the U.S. population [85] and claiming a total of 20 to 40 million lives globally [84]. In fact, 80% of the deaths incurred by the U.S. Army during World War I were due to influenza [84]. The next two antigenic shifts occurred by reassortment of the circulating virus with other avian viruses, giving rise to H2N2 in 1957 (the “Asian influenza”) and H3N2 in 1968 (the “Hong Kong influenza”) [85]. In both cases, the novel virus subtype replaced its predecessor, leaving only a single circulating subtype [85]. In 1977, the H1N1 virus reemerged in China and Russia, giving rise to the pandemic known as the “Russian influenza” [85]. Since this virus was closely related to strains that circulated in the 1950s and lacked the mutations that would have been expected over a 25-year span, it is now thought that this reemergence of H1N1 was due to the accidental release of the strain from a laboratory [85]. Since that time, both the H1N1 and H3N2 subtypes have remained the primary two influenza A viruses in circulation in humans [85].

2.3.2. Influenza Infection

Influenza virus primarily infects cells in the respiratory tract, resulting in disease that is characterized by coughing, sneezing, sore throat, rhinorrhea, fever, and myalgia [85]. Given the localization of infection in the airway, the main mode of influenza transmission among humans is through aerosols that are projected during coughing and sneezing by the infected and inhaled by the infectee [85]. Conveniently, the size of these aerosol droplets ($< 2 \mu\text{m}$ in diameter) allows them to be deposited advantageously in the lower respiratory tract of the infectee, propagating the cycle of infection [85]. The virus causes the superficial cells of the respiratory tract to cease protein synthesis and undergo apoptosis, resulting in destruction of the epithelium [85]. Influenza virus is also known to alter phagocytic cell function, which, in combination with the destruction of the epithelium, is thought to prime the respiratory tract for secondary bacterial infections [84]. These bacterial infections often cause the most severe complications associated with influenza infection, such as pneumonia [84]. In high-risk patients, primary viral pneumonia can also occur, without secondary infection [85].

Infections with influenza virus occur year-round, but epidemics typically take place in the winter, peaking between January and April in the U.S. [85]. Every year in the U.S., 5-20% of the population is infected with the flu virus, causing over 200,000 hospitalizations and an average of 23,000 deaths annually [2,94]. Globally, seasonal influenza accounts for 3-5 million infections with severe illness and 250,000 to 500,000 deaths each year [95]. While most people recover from the flu, sometimes with and sometimes without help from antiviral medication, the infection is particularly problematic for young children, the elderly, pregnant women, and people with compromised immune systems [85]. In these groups, the risks of complications, secondary infections, and death are usually substantially increased compared to the rest of the population [85]. In particular, the mortality rate associated with influenza infections in people older than age 65 is 100 times higher than that for people under 65 years old [85]. However, the flu can also be a severe respiratory disease for otherwise healthy adults [85]. In fact, during the 2013-2014 flu season, adults (18-64 years old) accounted for the majority of flu-related hospitalizations and deaths [96]. In addition to being a significant health problem, the flu is also an enormous financial burden. A detailed study on the economic burden of flu by Molinari *et al.* found that influenza costs the U.S. economy \$87B annually, with \$10B in direct medical costs, \$16B in lost productivity, and \$61B in lost economic value due to early death [3].

While no influenza pandemics have been as severe as the “Spanish flu” of 1918, and we now have antivirals to treat influenza infection and antibiotics to treat secondary bacterial infection, the threat of pandemics caused by the emergence of new subtypes remains [85]. In particular, the appearance of H5 influenza subtypes has been increasingly observed in recent years, beginning with the “bird flu” outbreak of 1997 [85]. Like all HA subtypes other than H1, H2, and H3, the H5 subtype is typically restricted to avian hosts, hence the name “bird flu” [85]. While this outbreak wreaked much more havoc in poultry than in humans and caused significant financial loss, it illustrated that avian-to-human transmission of influenza is possible, albeit rare and inefficient [85]. This was and still is a major concern, since the H5N1 strain was extremely pathogenic and resulted in a 33% mortality rate (6 of 18 patients), alarmingly high compared to the 0.1% mortality rate observed for a typical influenza season [85]. Fortunately, this virus did not propagate well in humans, minimizing the scale of the outbreak in people [85]. However, given that an avian virus was able to infect humans, the primary concern now is that a highly pathogenic avian influenza A virus could undergo reassortment with a seasonal, human influenza A subtype and result in a highly virulent subtype that does readily infect and transmit among humans [85]. This concern is echoed by the recent H7N9 outbreak in China, as H7N9 influenza is another previously avian-restricted virus that has now shown the ability to infect humans [97,98]. Fortunately, sustained human-to-human transmission of H7N9 influenza has not yet been observed [98]. Additionally, other influenza viruses of the H7 subtype have infected humans in the past, adding to the concern of the unusual zoonotic potential of this highly pathogenic subtype [85]. Influenza virus of the H9N2 subtype has also been transmitted from birds to humans in isolated cases, but has not been observed to undergo human-to-human transmission and is considered to be of low pathogenicity [85]. Overall, influenza A viruses of the H5 and H7 subtypes are currently of the most concern as possible future pandemics.

2.3.3. Current Influenza Diagnostics

Given the ongoing seasonal influenza burden and the threat of future pandemics, the ability to accurately diagnose influenza is extremely important. In particular, if influenza can be diagnosed within the first 48 hours of infection, the duration and severity of illness can be reduced by treatment with antiviral medication such as oseltamivir (Tamiflu®) [85,99]. Due to the utility of influenza diagnosis, several diagnostic tests for influenza virus have been developed.

Gold Standard Influenza Diagnostics

Historically, gold standard tests for influenza diagnosis evolved from simple viral culture and hemagglutination assays to combined culture and immunostaining methods, such as the direct fluorescence antibody (DFA) test [100]. Throughout this evolution, the time needed to run the given assay improved from weeks to days to hours, with current DFA tests requiring only three hours [100]. Despite this improvement in assay time, these traditional methods are laborious and require highly trained laboratory personnel [1,100]. Due to this drawback and the emergence of nucleic acid amplification tests (NAATs) such as real-time reverse transcription polymerase chain reaction (RT-PCR), NAATs are being increasingly used as the primary means of influenza diagnosis [100–102]. These tests detect the presence of influenza RNA in nasal samples (swabs, aspirates, or washes), either using conserved genes for general influenza detection or type- and subtype-specific genes for influenza subtyping [100]. These influenza NAATs are more sensitive and specific than DFA staining (when compared to culture) and can detect even lower viral loads than culture, establishing influenza NAATs as a new gold standard for influenza detection [4,100]. Despite this great performance, NAATs can only be performed in sophisticated laboratories by highly trained technicians, both of which are typically not available in standard clinics, even in the U.S., and are expensive in settings where they are available [102]. Additionally, these tests still take several hours to perform [100], preventing a diagnosis from being made during a typical patient visit [102].

Rapid Influenza Diagnostic Tests

Due to the shortcomings of nucleic acid testing, several rapid diagnostic tests (RDTs) for influenza have been developed, characterized by a sample-to-result in less than 30 minutes [1,4]. These tests take the form of traditional lateral flow tests, using antibodies to detect the presence of influenza nucleoprotein [103]. Most of these tests detect and differentiate between influenza A and B, which is important, since some influenza antivirals (amantadine, rimantadine) are effective against type A virus only, while others inhibit both type A and B virus (oseltamivir, zanamivir) [85,99]. Additionally, all 15 influenza RDTs currently on the market [4] have received CLIA waiver by the U.S. Food and Drug Administration [104], meaning that they are simple to operate and do not need complexity classification under the Clinical Laboratory Improvement Amendments (CLIA) [105]; these CLIA-waived tests can be used outside of the laboratory by non-technicians [106].

Given their ease of use, influenza RDTs have found considerable utility in physicians' clinics [107]. In particular, a study by Bonner *et al.* showed that the use of influenza RDTs significantly reduced

the cost of patient visits, time of hospitalization, and erroneous use of antibiotics versus antivirals for patients in a pediatric emergency room [34]. Influenza RDTs are also recommended by the Centers for Disease Control and Prevention (CDC) for use in determining the cause of respiratory disease outbreaks in public institutions such as nursing homes and schools [4].

Despite their utility, the diagnostic value of influenza RDTs has suffered from their overall low sensitivity compared to gold standard tests [1,4,108]. A study by Hurt *et al.* compared the performance of six common flu RDTs and found that the sensitivities of five of the six tests ranged from 67% to 71% (with specificities of 99% to 100%), as compared to viral culture [1]. The sixth test, however, had a sensitivity of 10%, indicating the variability in performance of these tests [1]. Other studies have found sensitivities for flu RDTs ranging from 27% to 61% when compared to RT-PCR [103]. A recent study by the CDC compared the ability of 11 flu RDTs to detect 23 recently circulating influenza viruses at various concentrations using mock samples spiked with virus [103]. While not based on clinical samples, this study importantly identified both inter-test and intra-test variability of these RDTs, as well as the dependence of their performance on viral concentration and virus subtype and strain [103]. Overall, current influenza RDTs cannot be solely relied upon for flu diagnosis; instead, physicians must use the symptoms of the patient and knowledge of the current epidemiological status of influenza to help interpret the result, limiting the efficacy of flu RDTs [4]. Unfortunately, gauging the epidemiological status of the current flu season is hindered by the inability of flu RDTs to subtype influenza A, owing to the fact that all current tests detect the internal nucleoprotein of the influenza virus [4]. To achieve subtyping, a test would need to detect either the hemagglutinin protein, the neuraminidase protein, or both. In addition to aiding epidemiological surveillance, having the ability to subtype influenza A could also further improve clinical management of disease, as different subtypes can have different pathological features. For example, H3N2 influenza tends to result in more severe disease than current H1N1 influenza, with higher correlation of the development of croup associated with H3N2 infection [85].

2.3.4. Next-Generation Influenza Diagnostic

Given the inadequacy of current influenza RDTs, our laboratory aims to develop a next-generation influenza diagnostic that is still low-cost and easy to use, but able to achieve more reliable, higher-sensitivity diagnosis of flu. Additionally, we aim to incorporate subtyping of influenza A, based on the hemagglutinin protein. We plan to achieve these goals through the use of our laboratory's 2DPN format, utilizing paper-based microfluidics to enable more sophisticated, but still automated, steps for detection. The work proposed herein will specifically focus on the development of the assay for

HA detection and the manipulation of three important components of this paper-based assay: the substrate material, the affinity reagent, and the immobilization method of the affinity reagent. Before we discuss this proposed work in detail, the state-of-the-art of each of these three assay components will be reviewed below.

2.4. Paper-Based Assay Development Considerations

2.4.1. Assay Substrates

Bioassays based on “paper” utilize porous substrates that enable passive wicking by capillary action. Ideal substrates have pore sizes that are small enough to offer a large internal surface area for capture agent immobilization, but large enough to deliver sufficient flow rates for a rapid assay time. Additionally, the porous substrate should be amenable to the immobilization of capture agents, usually through the direct adsorption of proteins. Here, we give a detailed history and description of the most commonly used assay substrate—nitrocellulose [31]—as well as a discussion of relevant alternatives to nitrocellulose. Finally, we describe our approach, which utilized both regular and modified nitrocellulose membranes.

Nitrocellulose

Given the basic substrate requirements described above, the most ubiquitous substrate for paper-based assays has historically been nitrocellulose. Nitrocellulose is a versatile polymer that has been broadly utilized since the 1800s. Also known as cellulose nitrate, nitrocellulose is created commercially by the reaction of cellulose—purified from plants, such as wood pulp and cotton—with nitric acid [111]. In this reaction, the hydroxyl groups of the cellulose (Figure 8A) are replaced by nitrate ester groups (Figure 8B), with the degree of substitution varying between zero and three nitrate groups per monomer, depending on the concentrations of reactants used [111,112].

Nitrocellulose can be manufactured in many different forms and thus has found utility for numerous purposes. First recognized for its high flammability, nitrocellulose was developed as a

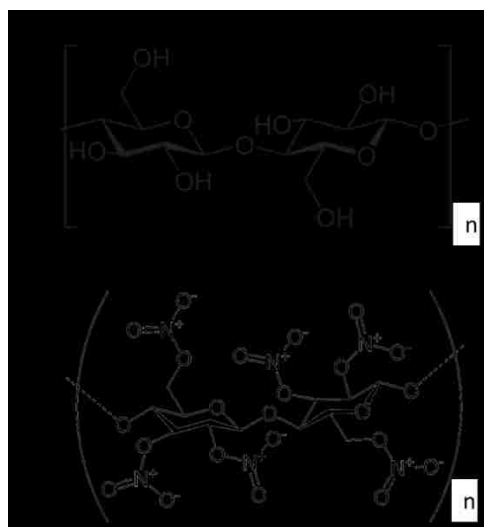


Figure 8. Cellulose and nitrocellulose. Chemical structures of (A) cellulose [109] and (B) nitrocellulose [110].

fibrous solid known as gun cotton in 1846 [113]. In the decades that followed, nitrocellulose was developed as a lacquer for protective coatings [114,115], as well as a base for films such as X-rays and motion pictures [116]. In 1907, Bechhold created the first porous nitrocellulose membrane—for use in ultrafiltration applications—by impregnating filter paper with a solution of nitrocellulose in acetic acid [117–119]. Soon after, Zsigmondy and Bachmann showed that porous nitrocellulose membranes could be created by phase inversion [118–120], which is how such membranes are manufactured today. In this process, nitrocellulose is dissolved in an organic solvent and evaporated in the presence of a non-solvent, leaving a precipitated nitrocellulose membrane with high porosity [111,121], as shown in Figure 9. The porosity and pore size of the membrane can be controlled by the solvents used, the speed of evaporation, temperature, and humidity [111,121]. The result is a material with the unique combination of tunable pore size, high surface-to-volume ratio, and very low cost.

Porous nitrocellulose membranes were first used to immobilize biomolecules in the 1960s [111]. In 1963, Nygaard and Hall demonstrated that RNA-DNA complexes adsorb onto nitrocellulose membranes, while free nucleic acid strands pass through [122]. Others then began immobilizing nucleic acids on nitrocellulose membranes to probe for interactions between a nucleic acid of interest and other biomolecules [123,124]. In 1975, Southern demonstrated the transfer of DNA from polyacrylamide gels to nitrocellulose [125]. This groundbreaking technique, known as the “Southern blot,” allowed specific nucleic acid fragments to be captured for subsequent analysis. The Southern blot inspired the “Northern blot” for RNA transfer [126] and the “Western blot” for protein transfer to nitrocellulose [127,128]. Finally, stemming from the blotting assays, other assays were developed utilizing porous nitrocellulose as a solid support for diagnostic assays incorporating flow. The lateral flow test (see section 2.1.2) is the most ubiquitous example of such an assay and has employed nitrocellulose almost exclusively since its emergence in the 1980s [33,121]. Overall, nitrocellulose has been widely employed in a variety of biological assays, highlighting its unique ability to interact with three of the most important classes of biomolecules: proteins, DNA, and RNA [111].

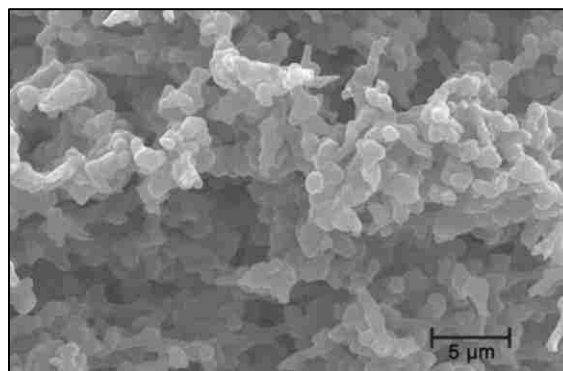


Figure 9. SEM of nitrocellulose membrane. Scanning electron micrograph (SEM) of a porous nitrocellulose membrane (Millipore HFB135), acquired by Gina Fridley [31].

Alternatives to Nitrocellulose

Materials other than nitrocellulose have been explored as assay membranes for LFTs and other paper-based tests. For example, both nylon and polyvinylidene fluoride (PVDF) have been investigated for use in traditional LFTs [33]. These materials have never gained much traction in the LFT industry, however, due to a combination of the superior material properties of nitrocellulose and resistance to change in the industry [33]. Currently, with the emergence of novel paper-based diagnostic platforms (see section 2.2.2), many test developers are also exploring the use of porous substrates other than nitrocellulose. For example, the Whitesides group has effectively demonstrated the use of both cellulose and the cellulose-polyester mixture known as TechniCloth as the assay substrate for their μ PADS [42,57,58,60]. These μ PADS have been used almost exclusively for simple chemical and enzymatic detection systems, however, and have not been vetted as platforms for immunoassays that require immobilization of biological affinity reagents. For such protein-based systems, nitrocellulose proves to be a more effective substrate, as it is known to adsorb proteins more robustly than cellulose [129]. The propensity of nitrocellulose to bind proteins is largely attributed to the dipole of the nitrate ester group (dipole moment = 2.85 D) [53,129,130], which is 70% larger than the dipole of the corresponding hydroxyl group of cellulose (dipole moment = 1.69 D) [129]. The mechanism of protein adsorption to nitrocellulose is discussed further in section 2.4.3.

Our Approach: Regular and Modified Nitrocellulose

Given that nitrocellulose is much more appropriate for the immobilization of biological affinity reagents than other substrates, our approach for the influenza HA assay developed herein was based upon nitrocellulose, with membranes primarily obtained from our collaborators at GE GRC. In addition to regular, commercially available nitrocellulose, we also investigated the use of novel, functionalized nitrocellulose membranes for the covalent attachment of affinity reagents. These membranes are discussed in detail in section 4.4.

2.4.2. Affinity Reagents

Affinity reagents form the basis for analyte detection in any bioassay. Here, we review the three most commonly used types of affinity reagents—antibodies, antibody-derived proteins, and aptamers—and discuss our approach: small, synthetic protein binders.

Antibodies

By far, the most common affinity reagent is the antibody immunoglobulin G (IgG), due to its natural role as an affinity reagent for a given specific target analyte [131]. In humans and other animals, naturally occurring IgG antibodies represent an important component of the adaptive immune system, which develops IgG antibodies that are specific to pathogens that are detected in the body [131]. IgG antibodies consist of two heavy chains and two light chains, which are linked by disulfide bonds to form a Y-like structure of approximately 150 kDa [131], as shown in Figure 10. The specificity of IgG comes from the highly variable

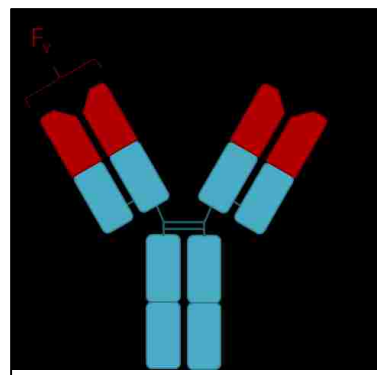


Figure 10. Structure of an IgG antibody.

Adapted from [41,131].

portion (Fv) of the antigen-binding region (Fab) of the antibody, which constitutes the binding *paratope* of the antibody. This antigen-binding region interacts with a specific *epitope* of the target antigen. Each IgG antibody consists of two Fab regions connected by a common stalk known as the Fc region, making IgG antibodies inherently bivalent. Antibodies typically have high affinities for their target antigens, with dissociation constants (K_d) on the order of 10^{-8} to 10^{-12} M (i.e. nanomolar to picomolar affinity) [132].

For use in biotechnology applications, including bioassays, target-specific antibodies are generated in host animals, such as mice, goats, and rabbits [131]. Specifically, the animal is immunized with the target antigen, and the resulting antibodies that are produced by the animal are harvested and purified, typically by affinity chromatography [131]. This type of production generates a *polyclonal* antibody, which is really a distribution of unique antibodies that all have some affinity for the antigen. To generate a *monoclonal* antibody, which consists purely of a single antibody molecule with a given affinity for the antigen, immune cells from the animal are fused to fast-growing myeloma cells to create hybridomas, which are used for the screening and identification of a single, high-affinity clone [131,133]. This monoclonal antibody production is expensive and time-consuming, but yields highly functional antibodies for biorecognition applications [134]. Given their efficacy, IgG antibodies have been used as the affinity reagent for countless bioassays.

Antibody-Derived Proteins

To create affinity reagents at lower cost and with greater customizability, many investigators have developed binding proteins based on the Fab region of the IgG antibody, which is the portion of IgG responsible for antigen binding.

These proteins (Figure 11) include Fab fragments, which contain both variable regions and constant regions; single-chain variable fragments (scFv), which contain only the variable regions (Fv) of the Fab fragment; single-chain bivalent Fc (scBvFv), which contain two scFv connected by a polypeptide linker;

and diabodies, which contain two scFv facing opposite directions [135]. A second class of antibody-derived affinity reagent that has gained popularity is the camelid VHH domain [136]. These proteins are based on antibodies from camelids (e.g. camels and dromedaries), which contain only heavy chains [136]. The VHH domain therefore consists of two variable heavy chain regions, which was discovered to be a highly stable and soluble structure [136]. All of these antibody-derived proteins are smaller than IgG and can be expressed recombinantly, making their production relatively cheap and simple, once a given binder has been developed [135,136].

The development of these antibody-based protein binders usually includes the generation and screening of a large library of candidate proteins. The library is generated through random genetic mutations to the binding region, and the resulting genes are expressed in a yeast- or phage-display system. The displayed proteins are then screened for binding to the target of interest, using a high-throughput system such as flow cytometry, and the process can be iterated to achieve affinity maturation of the binder [137].

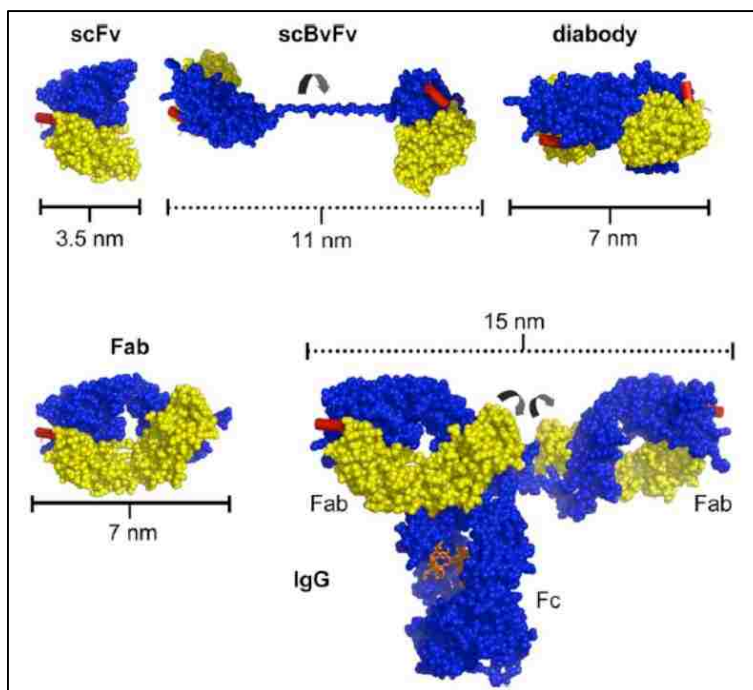


Figure 11. Antibody-derived proteins.

Various antibody-derived proteins that have been used as affinity reagents. From Klein *et al.* [135].

Aptamers

A third class of affinity reagent that has garnered much attention for diagnostic applications is the aptamer [138]. Aptamers are synthetic, single-stranded nucleic acids that fold into three-dimensional structures, which confer binding specificity to the given molecule (Figure 12) [138]. The primary advantage offered by aptamers over protein-based affinity reagents is the ease of their production and selection, which can be done entirely *in vitro*, without the need for a living organism [13,138]. Aptamers have exhibited some success as binding reagents, yielding sub-nanomolar affinities in isolated cases [138]. However, the ability to develop high-affinity aptamers consistently has not been demonstrated. With continued development, aptamers may represent an ideal choice for a bioassay affinity reagent, but currently lack sufficient functionality.

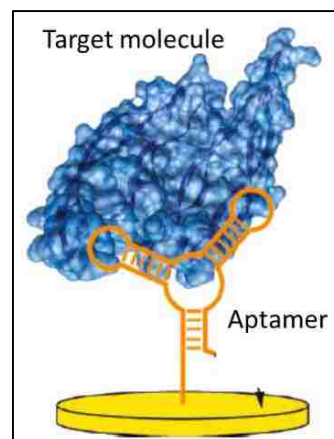


Figure 12. Aptamer structure. Aptamer binding a target molecule. Adapted from [138].

Our Approach: Recombinant Protein Binders

Our approach for the flu HA assay is to use small, recombinant protein binders based on non-immunological scaffolds, which represent a fourth major class of affinity reagent. These binders offer similar benefits to small, antibody-derived proteins, but with increased flexibility in the size, the shape, and ultimately the binding interaction of the protein. Many recombinant, scaffold-based binders have been described in the literature, with the base scaffolds ranging from fibronectin to protein A [134,136]. These protein binders are typically developed using evolutionary design (i.e. random mutagenesis and high-throughput screening), rational design, or some combination thereof [134]. Recombinant protein binders often exhibit nanomolar affinities or better [136], thereby offering similar affinity to monoclonal antibodies, but at a much lower cost of production [139]. To our knowledge, no commercial diagnostic tests have been developed with such binders, however. This lack of use likely owes to the legacy of IgG antibodies as affinity reagents, and to the high degree of protein engineering, including that target epitope crystal structure, that is required to develop recombinant protein binders.

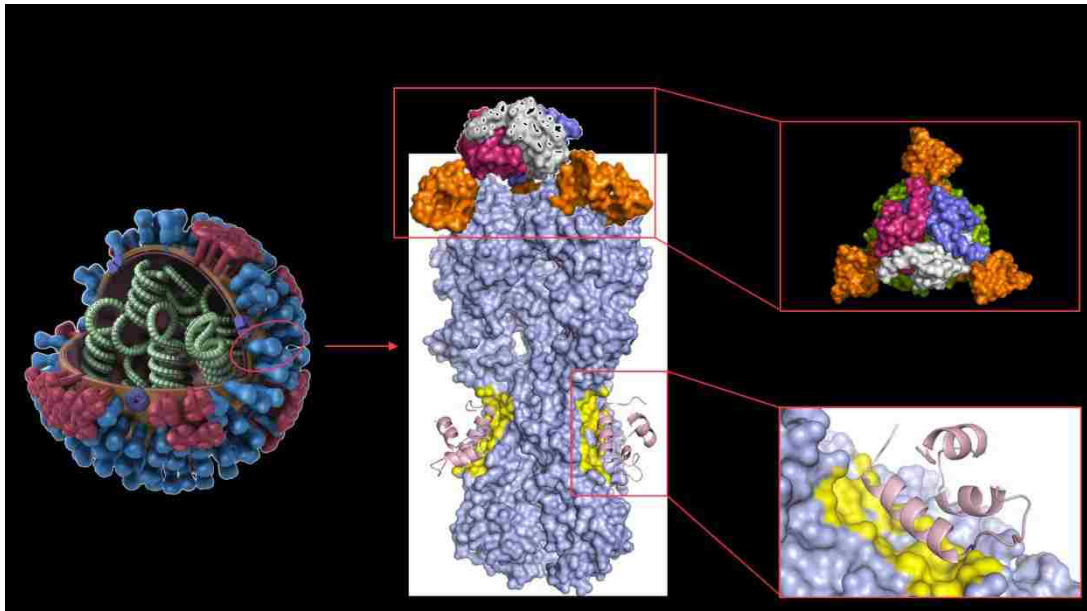


Figure 13. Illustration of the hemagglutinin (HA)-binding “flu binders.”

The flu binders are engineered in the laboratory of Dr. David Baker and are depicted here in complex with the influenza HA trimer, which is one of two influenza surface proteins. Virus image freely available from the CDC [140]. Head region binder images provided by Dr. Eva-Maria Strauch, and stem region binder images provided by Dr. Aaron Chevalier.

For our flu HA assay development, we utilized recombinant protein binders developed by our collaborators in the Baker laboratory, who are expert protein engineers. Specifically, they developed two sets of recombinant proteins that bind to the hemagglutinin protein of influenza with high affinity: a set that binds to the stem region of HA and a set that binds to the head region of HA (Figure 13). These sets of proteins are collectively referred to as *flu binders*. While parts of the HA protein undergo a high degree of antigenic drift in order to evade the host immune system (section 2.3.1), both the stem region and the sialic acid binding site of the head region offer highly conserved areas of the protein [85,141]. The computational design of recombinant affinity proteins therefore gives us the power to target these conserved epitopes with exquisite sensitivity and specificity.

The stem region flu binders were the first type of influenza binders developed by the Baker lab. As their name suggests, these proteins were designed to bind to HA in its stem region, which is highly conserved among different strains and subtypes of HA [142]. Two classes of stem region binders were developed, HB36 and HB80, named as numbered candidates of the *hemagglutinin-binding* proteins designed by the Baker lab. HB80 is based on a 3-helix scaffold from a transcription factor of the snapdragon flower (*Antirrhinum majus*) (Protein Data Bank (PDB) identifier 2CJJ) [143]. It has shown strong binding to HA, but there has been concern about it being unstable, with a low

melting temperature (T_m) of 30 °C and demonstrated sensitivity to trypsin digestion. In contrast, HB36 is based on a 4-helix thermophilic scaffold from the thermophilic bacterium *Bacillus sterothermophilus* (PDB 1U84). As such, it is extremely thermostable, with a melting temperature, T_m , of 66 °C. HB36 is also slightly larger than HB80 (73 vs. 51 amino acids, nominally) and has a larger surface area of interaction with HA.

HB36 and HB80 were originally developed through computational design based on the crystal structure of the HA protein from A/South Carolina/1/1918 (H1N1) (“SC1918”) influenza, followed by the screening of candidate binders through yeast display [142]. In total, 88 designs were screened, 73 designs displayed successfully on the yeast surface, and HB36 and HB80 were the only two designs that showed binding activity toward the HA stem region [142]. Random and site-specific mutagenesis was then used to perform affinity maturation for these two binders, resulting in the first two key flu binder variants: HB36.4 and HB80.3, with binding affinities (K_d) for SC1918 HA of 22 nM and 38 nM, respectively, by surface plasmon resonance (SPR) [142]. HB36.4 was the first flu binder that we received for testing the Yager lab. The Baker lab then applied site-saturation mutagenesis and deep sequencing to bypass bottlenecks in the traditional affinity maturation process and achieve novel flu binder variants with optimized affinity and specificity [144]. This led to the development of flu binders HB36.5 and HB80.4., with SPR binding affinities for SC1918 HA of 900 pM and 600 pM, respectively. These flu binders were the variants used for the majority of the flu HA assay development herein. Most recently, a further optimized variant, HB36.6, was also developed and has been used for some of the most recent testing. The development of flu binder variants for testing in our flu HA assay was led by PhD graduate Dr. Aaron Chevalier, and has since been continued by PhD student Jorgen Nelson.

In addition to these stem region binders, the Baker lab has also developed head region binders, an effort led by post-doctoral fellow Dr. Eva-Maria Strauch. While the head region of HA is the most exposed to the immune system and therefore mutates frequently, the sialic acid binding pocket within the head region must remain highly conserved in order to maintain sialic acid binding and thereby entry into host cells [85,141]. The head region binder is therefore designed to mimic sialic acid and fit into this conserved binding pocket. Unfortunately, the monomeric version of the head region binder exhibited only low affinity for HA. Dr. Strauch therefore designed a trimeric head region binder in order to match the inherent structure of the HA trimer and create increased binding strength through avidity. The trimeric head region binders (Trimer 9 and Trimer 11) are expressed as monomers that include an additional trimerization domain, which causes the proteins

to trimerize in solution. These trimeric head region binder variants showed very strong binding to HA, with unquantifiable binding affinities by SPR due to such slow off-rates. Trimer 11 (“T11”) was the primary variant used for testing in the flu HA assay development herein. Most recently, a new variant with improved stability, Trimer 11.2, has been developed and will begin to replace Trimer 11 for further assay development.

Finally, it should be noted that the flu binders are also expressed with additional small polypeptide tags. Both the stem and head region binders contain a hexa-His tag (HHHHHH; 823 Da), which is used for purification of the protein through nickel-NTA affinity columns. Additionally, all stem region binders contain a FLAG tag, which is a commonly used affinity tag consisting of the

following 8-amino-acid peptide sequence: DYKDDDDK (1013 Da) [145]. This tag is included to increase the solubility of the protein, but is useful in the context of this work for flu binder-specific visualization, using fluorescently labeled anti-FLAG tag antibody. These tags can be expressed on either terminus of the flu binder, both of which are located on the “back” side of the flu binders, relative to their binding paratopes. Unless otherwise specified, though, the hexa-His tag is located on the C-terminus of the protein, and, for the stem region binders, the FLAG tag is located on the N-terminus. A summary of the flu binders used herein is provided in Table 3.

Together, the stem and head region binders have provided us with the opportunity to explore many novel approaches to influenza HA detection. Specifically, we exploited the highly customizable nature of the recombinant flu binders to develop and characterize novel immobilization techniques, as described in chapter 4, using the stem region binder. We then explored novel assay stacks using both the stem and head region binders, described in chapter 5. It is important to note that, since these binders were developed concurrently with the flu HA assay development herein, the work in this thesis does not always contain head-to-head comparisons of different flu binder variants, but instead was performed using the best variants available at the given time. Ultimately, these flu binders have been instrumental in the development of the next-generation paper-based influenza assay developed herein.

Table 3. List of flu binders used in the flu HA assay development herein.

The flu binders used during this thesis work are listed, along with their classification as stem or head region binders, and their molecular weights (MW).

Flu Binder	HA Epitope	MW (kDa)
HB36.4	Stem	11.5
HB36.5	Stem	13.0
HB36.6	Stem	13.3
HB80.4	Stem	8.7
Trimer 9	Head	64.7
Trimer 11	Head	66.9

2.4.3. Immobilization Techniques

Finally, for a given assay substrate and affinity reagent, the success of a bioassay depends critically on the immobilization of that affinity reagent to that substrate. The most common immobilization method is direct, physical adsorption of the affinity reagent, and is discussed in detail below. Other methods include anchor-based immobilization and covalent attachment, which are also reviewed. Our approach, discussed at the end of this section, involved components of all three strategies.

Direct Adsorption

The direct adsorption of capture agents to assay substrates remains the most common immobilization technique for paper-based assays. Protein adsorption to surfaces is a long-studied and widely used phenomenon [146–148]. For nitrocellulose substrates in particular, protein adsorption has been utilized for many years, especially in the creation of antibody-adsorbed test lines in lateral flow tests [13,33,121]. Despite its common use, the process of protein adsorption to nitrocellulose is not well understood [111]. However, several theoretical and empirical concepts have been developed, as discussed below.

First, proteins generally adsorb well to nitrocellulose, at least as compared to their adsorption to other membranes, such as cellulose and cellulose acetate [129,130,149]. For example, it is well established that nitrocellulose-based LF assays are prone to nonspecific protein adsorption and are often pre-treated with a protein-containing blocking solution to fill unused binding sites [121]. This blocking step prevents the sample analyte from nonspecifically adsorbing to the membrane before it can reach the capture line. Overall, protein adsorption to nitrocellulose is a thermodynamically favorable process, with Gibbs free energies reported on the order of -1 mJ/m^2 for both IgG and human serum albumin [149]. While it is well-accepted that protein adsorption to nitrocellulose is governed by non-covalent interactions between the two entities, the exact nature of those interactions has remained elusive [147,149]. Some argue that protein adsorption is based upon hydrophobic interaction between the carbon-containing nitrocellulose and the hydrophobic portion of the protein [121]. Others describe the interaction as primarily electrostatic, based on the attraction between dipoles of the nitrocellulose nitrate ester groups and dipoles within the protein [53].

Perhaps the most plausible model, proposed by Přistoupil *et al.* in 1969, incorporates the possibility of both types of interactions, with the weight of each depending on the particular system [129].

Specifically, these investigators postulated that protein adsorption to nitrocellulose could be attributed to three primary factors: 1) electrostatic interactions, 2) hydrogen bonding, and 3) the hydrophobic effect, i.e. the release of ordered water molecules from the hydrophobic interface, resulting in a favorable gain in entropy. Importantly, this model emphasizes the pH-dependence of adsorption, based on the pH-dependent ionization of both nitrocellulose and proteins. While it is well known that each protein has an isoelectric point (pI) at which its charge switches from positive to negative, nitrocellulose membranes also each have an observable acid dissociation point (pK_a), at which a change in charge also occurs. Although the nitrate groups of nitrocellulose carry no formal charge, the negative charge can result from residual hydroxyl groups (4-22%) that were not substituted during nitration, or from carboxyl groups generated as oxidative byproducts of the membrane preparation process [129], both of which are ionizable and contribute to the pK_a for nitrocellulose (estimated to be pH 6.5 for the particular membrane in their study). Overall, the Přistoupil model states that operating in a regime at which the nitrocellulose is maximally negatively charged and the protein is maximally positive charged results in the best adsorption, as electrostatic attraction helps initiate the adsorption, followed by any favorable hydrophobic interactions in the system [129]. The three potential charge state scenarios are illustrated in Figure 14. First, for pH values above the pI of the protein and above the acid pK_a the nitrocellulose, both entities are negatively charged and therefore encounter electrostatic repulsion, which weakens adsorption (Figure 14A). Second, for low pH values below the pI of the protein, the protein is positively charged, while the nitrocellulose approaches neutrality, resulting in the dominance of hydrophobic interactions for adsorption (Figure 14B). Finally, for pH values that are above the pK_a of the nitrocellulose but below the pI of the protein, the nitrocellulose will be negatively charged and the protein positively charged (Figure 14C). In this case, both electrostatic attraction and ensuing hydrophobic interactions contribute to the adsorption of the protein. While this model is theoretically robust and was developed to explain empirical observations, it has not been vetted experimentally and has not gained much traction in the literature. Instead, the lateral flow literature suggests that spotting proteins at pH values near their pI results in the most robust adsorption, allegedly due to the decrease in their solubility at this point [53]. Work done in this thesis has corroborated the Přistoupil model (see chapter 3), establishing it as the working model for protein adsorption to nitrocellulose for this work.

Second, the kinetics of protein adsorption and desorption to the membrane must be considered during assay development, especially for the immobilization of capture molecules at the test line. Classical adsorption literature describes surface adsorption as an irreversible process [147]. However, this notion is based on simplified, homogeneous test systems at equilibrium [147], which are not representative of actual protein adsorption systems in porous nitrocellulose. In particular, the complex systems of lateral flow assays render protein adsorption at least “somewhat irreversible” [129], if not entirely reversible. Specifically, the fluid flow velocity [43], presence of potential stripping agents such as salts and detergents [150], and reagent drying time [147,149] are all factors that can influence protein adsorption and desorption from nitrocellulose and are therefore important considerations for assays that depend on protein immobilization.

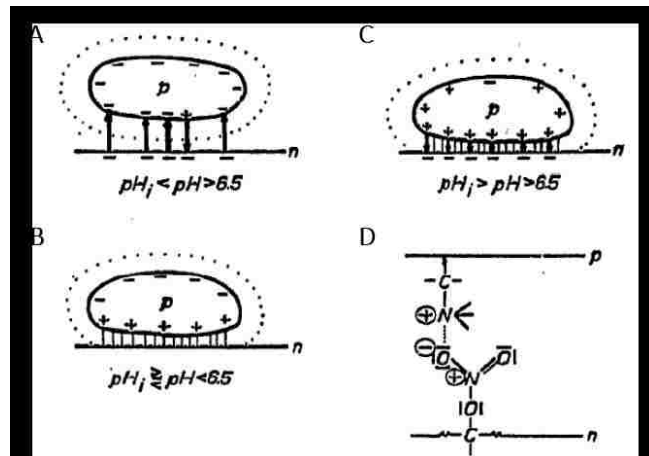


Figure 14. Theoretical model of protein adsorption to nitrocellulose.

This model of protein adsorption was proposed by Přistoupil *et al.* [129]. (A) For high pH, both the protein and nitrocellulose are negatively charged and experience electrostatic repulsion. (B) For intermediate pH, the nitrocellulose is negatively charged and the protein positively charged, resulting in electrostatic attraction, in addition to hydrophobic interactions. (C) For low pH, nitrocellulose charge is reduced, and interactions are primarily non-ionic. (D) Illustration of a dipole-dipole interaction between a lysine residue and a nitrate group.

Despite the lack of understanding of the mechanism of protein adsorption to nitrocellulose, direct adsorption remains the most commonly used method for the immobilization of affinity reagents at the test regions of an assay. The immobilization of IgG antibodies is the most widely used application of this method, although lateral flow tests that detect host-derived antibodies utilize the direct adsorption of protein antigen for the formation of test lines [33]. While simple and effective in many cases, immobilization by direct adsorption can only be optimized by *ad hoc* screening of buffer conditions and does not provide the ability to control the orientation or functionality of the adsorbed protein [151].

Anchor-Based Immobilization

Another common immobilization strategy is the use of an anchor protein that both holds the affinity reagent in place and provides preferential orientation of the affinity reagent to ensure that its binding paratope is accessible. The caveat to this strategy is that it inherently depends on the

direct adsorption of the anchor protein to the assay substrate, which is subject to the same problems and considerations discussed in the previous section. Nevertheless, several anchor-based methods have been successfully demonstrated.

One widely used anchoring system is the coupling of biotinylated affinity reagent to a streptavidin anchor [13]. This method utilizes the extremely high-affinity interaction between streptavidin and biotin ($K_d \approx 10^{-15}$ M), which is the strongest naturally occurring non-covalent bond that has been observed to date [13,152]. This robust interaction therefore allows for extremely efficient immobilization of a biotinylated reagent [13]. Moreover, since streptavidin is a tetramer, some of its binding sites can be perturbed by adsorption to the assay substrate without eliminating its ability to bind biotin. The specific use of this system on nitrocellulose has not been reported in the literature, however, leaving its efficacy on this substrate unknown prior to the work in this thesis.

An interesting example of a different, yet also effective, anchoring method is the use of an anchor protein that specifically binds the assay substrate. In particular, several investigators have used the cellulose binding domain (CBD) as a method of preferential binding to cellulose substrates [151]. The CBD is not an engineered protein, but instead has been isolated from naturally occurring cellulases, which are enzymes that occur in fungi and bacteria for the hydrolysis of cellulose [153,154]. This CBD has been demonstrated as an anchoring protein for affinity reagents in several different cellulose-based assays [151,153,154]. One interesting approach by Hussack *et al.* [153] utilized pentameric structures of CBD-fused antibody fragments to achieve anchoring to cellulose, as well as increased binding strength for both cellulose and the target analyte through the increased avidity on both ends (Figure 15). While no naturally occurring nitrocellulose-binding proteins exist (to our knowledge), one was developed as part of our immobilization approach discussed below.

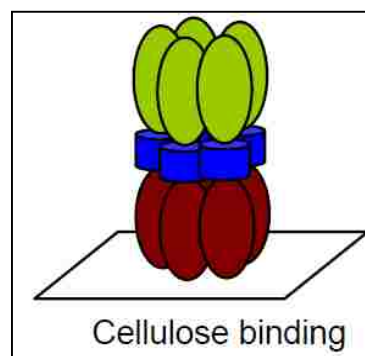


Figure 15. Anchoring through the cellulose binding domain. Demonstration of a cellulose-binding domain for the anchoring of recombinant affinity reagents [153].

Covalent Attachment

The third commonly used immobilization strategy is the covalent attachment of the affinity reagent to the substrate using complementary chemistries on the two entities. Given the limited number of reactive amino acid side chain residues, however, the options for covalent attachment are few, but effective [13]. These options include the following four functional groups: 1) amine groups of lysine,

glutamine, and arginine residues (and the N-terminus of the protein, if accessible); 2) carboxyl groups of aspartic acid and glutamic acid residues (and the C-terminus of the protein, if accessible); 3) hydroxyl groups of serine and threonine; and 4) thiol groups of cysteine residues [13,155]. However, the first three groups are widely prevalent in proteins, making them generally not specific enough to yield orientation-specific immobilization [13]. Therefore, thiol-based immobilization is the most attractive option, if the given affinity reagent contains at least (and ideally) one cysteine residue. Many bioassay systems have employed covalent attachment for protein immobilization [13,155–157], but this method has largely remained unexplored for paper-based assays.

Our Approach: Empirical Testing of Best Immobilization Strategy for Flu Binder

To determine the optimal method for immobilization of the flu binder on nitrocellulose, our approach included the investigation of all three immobilization strategies discussed above. In addition to exploring direct adsorption of the flu binder, we also studied protein adsorption to nitrocellulose for the screening and identification of a nitrocellulose-binding protein unit, analogous to the cellulose-binding protein discussed above. We then tested the anchor-based immobilization of flu binder using this nitrocellulose-binding protein, in addition to a streptavidin-based anchoring system. Finally, we utilized our collaboration with GE GRC to investigate covalent attachment of flu binder to novel, functionalized nitrocellulose membranes. This approach utilized thiolated (i.e. cysteine-containing) versions of the flu binder for attachment to nitrocellulose membranes modified with thiol-reactive chemistries. Using this approach, we developed and characterized three novel immobilization strategies for recombinant affinity proteins, highlighting the strengths and weaknesses of each. Ultimately, the best choice depends on the specific needs of the given assay, as discussed in chapter 4.

3. Protein Adsorption

3.1. Motivation

The functionality of paper-based devices depends critically on the immobilization of affinity reagents at the test region [121]. Direct adsorption is the mainstay of immobilization in paper-based devices to date, but the mechanism of direct adsorption to nitrocellulose is poorly understood [111], as discussed above. This lack of understanding is problematic when one is designing a new test, particularly with a new type of capture agent, since there is no fundamental theory upon which the design can be based. In our case, we wished to develop a flu diagnostic using the flu binders from the Baker lab, described in section 2.4.2. Through our initial work described herein, we quickly found that these flu binders did not immobilize well to nitrocellulose under direct adsorption. This specific case of the flu binder therefore motivated our investigation of protein adsorption to nitrocellulose more generally, with the goal of gaining some fundamental understanding of the factors that enhance and hinder this process. To reduce this large area of study to practice, we have focused our investigation on the development of a nitrocellulose-binding protein. The purpose of such a protein is that it could be fused to an affinity reagent of interest, such as the flu binder, and impart efficient, strong, and orientation-specific immobilization to the affinity reagent.

We first investigated the nitrocellulose adsorption of proteins commonly used in bioassays in order to gain a fundamental, even if basic, understanding of physical properties that promote protein adsorption, as described in section 3.3. We then performed a series of solution depletion experiments to try to gain a more quantitative understanding of the adsorption process. As discussed in section 3.4, this solution depletion approach was ultimately unsuccessful, but taught us valuable lessons. In section 3.5, we returned to the lateral flow challenge and protein spot analysis method, applying the method in a thorough way for the first time to obtain semi-quantitative results and robust insights about IgG adsorption to nitrocellulose. We then honed in on the pH dependence of adsorption, as described in section 3.6, and used several proteins to better understand this pH dependence and the ideal electrostatic regime for strong adsorbers. Finally, we applied the adsorption knowledge gained from this work to screen potential nitrocellulose-binding proteins, as described in section 3.7. Common methods used throughout this work are given in section 3.2, and specific methods are given within each section. Ultimately, this work led to the

identification of two nitrocellulose-binding proteins as candidates for anchor-based affinity reagent immobilization, tested explicitly for the stem region flu binder in chapter 4.

3.2. Common Methods

The lateral flow challenge and protein spot analysis methods were used repeatedly throughout the work in this section (and in this thesis). I developed the initial lateral flow challenge method as tool to screen the robustness of adsorption of a given protein by determining how easily it was stripped away by a challenge solution (section 3.2.1). I then worked with PhD graduate Dr. Gina Fridley to formalize this method into a more rigorous and holistic protein spot analysis method (section 3.2.2).

3.2.1. Lateral Flow Challenge Method

To screen the robustness of adsorption of various proteins, we used a lateral flow challenge system to evaluate how strongly a protein was immobilized to the membrane and to what extent it was subject to stripping by a challenge solution. In this method, nitrocellulose membranes were cut into test strips or multi-legged devices using a CO₂ laser cutter (M360 or VLS360, Universal Laser Systems, Scottsdale, AZ). In most cases, each test strip was 3 mm wide by 24 mm tall, and generally sets of 4 strips were cut together and connected by a 6-mm tall section at the top of the device in order to promote batch processing. The distance between strips was 6 mm, designed to allow each set of strips to fit into the wells of a 96-well plate.

The given protein of interest was spotted onto a strip of nitrocellulose, either by hand using a pipette or in an automated fashion using a piezoelectric spotter (sciFLEXARRAYER S3, Scienion AG, Berlin, Germany). For hand spotting, spots were typically generated using 0.5-1.0 μ L of protein solution, creating a roughly circular spot. For piezoelectric spotting, all protein solutions were filtered through a centrifugal filter device with 0.2- μ m nylon membrane (VWR, Radnor, PA) at 6000 g for 5 minutes prior to spotting to avoid clogging the printer plumbing with particulate from the samples. For this initial lateral flow challenge method, when the piezoelectric spotter was used, the protein solution was typically patterned in the shape of a test line. Test lines were created by 12 spots spaced 250 μ m apart, with 30 droplets per spot, and two passes were printed for each test line to saturate the membrane region. Each droplet was 450-500 pL, resulting in test lines comprising \sim 300 nL of protein solution in total. Droplets were printed at 500 Hz in an enclosed

chamber at ~50% relative humidity and ~68 °F ambient temperature. After spotting, the patterned membranes were dried before use, typically stored under desiccation at least overnight.

For the lateral flow challenge, strips were placed into a well (96-well plate for 3-mm-wide strips) filled with the given challenge solution (50 μ L per well). A cellulose absorbent pad (Millipore #CFSP223000, Billerica, MA) cut to the width of the device and 70 mm tall was secured to the top of the nitrocellulose device to aid wicking, either with tape or with a custom-made plastic housing. Unless otherwise noted, the challenge solution was allowed to wick through the strips for 15 minutes, at which point the strips were removed from the solution. In this work, challenge solutions included deionized H₂O, phosphate-buffered saline (PBS, pH 7.4, Sigma-Aldrich, St. Louis, MO), PBS + 0.1% v/v Tween-20 (Fisher BioReagents #BP337, Thermo Fisher Scientific, Waltham, MA) (PBST), and PBS + 0.02% or 0.1% w/v sodium dodecyl sulfate (SDS, Sigma-Aldrich #L3771) (PBSS). These LF challenge cases were compared with no-LF controls in order to determine the relative amount of desorption in each case.

The amount of protein remaining on the membrane was visualized with one of two nonspecific protein stains: Coomassie Brilliant Blue (Thermo Scientific #20278, Life Technologies, Carlsbad, CA) or Ponceau S (Thermo Scientific #24580). For Coomassie staining, each membrane was incubated for 10 minutes with stain solution, followed by 10 minutes with destain solution, both with shaking. This protocol, adapted from Metkar *et al.* [158], uses a destain solution of 50% H₂O, 40% methanol, and 10% glacial acetic acid, and a stain solution of 0.0025% w/v Coomassie Brilliant Blue in destain solution. For Ponceau S staining, each membrane was typically incubated with shaking for 5 minutes with stain solution (0.1% w/v Ponceau S in 5% acetic acid), followed by 2 minutes with H₂O for destaining, as based on the manufacturer's protocol and optimized in-house. It should be noted that the Ponceau S stain can also be diluted with 40% v/v methanol in order to improve the penetration of dye into the protein spot, for particularly dense protein spots. When this approach is used, the stain and destain times should be increased to approximately 10 minutes and 5 minutes, respectively, which was done for some protein analysis throughout this work. In all cases, the stained devices were taped to a standard piece of printer paper and imaged at 48-bit HDR color, 600 dpi, $\gamma = 1$ using a desktop scanner (Perfection V700 Photo Scanner, Epson, Long Beach, CA).

The signal intensity of the protein remaining in the test spot after LF challenge was quantified using a custom script in MATLAB (MathWorks, Natick, MA) called *quantifyColorimetricSignal.m* (see Appendix B for code and description). Using this program, a region of interest (ROI) is drawn semi-

manually around the test spot of interest, and the average pixel intensity inside this test ROI, I_{test} , is computed. This value is then background-subtracted using the average pixel intensity inside a local background region, I_{bgd} , and normalized on a scale from 0 to 1 to generate the normalized pixel intensity of the spot, I_{norm} , using Eqn 19.

$$I_{norm} = \frac{I_{test} - I_{bgd}}{0 - I_{bgd}} \quad \text{Eqn 19}$$

For each experiment, the channel of the RGB image that was most sensitive to the particular color of signal was chosen for analysis. For the Ponceau S-stained membranes (pink color), the green channel was used. For the Coomassie-stained membranes (blue color), the red channel was used. In both cases, the normalized pixel intensities represent a range from no signal (0) to maximum possible signal (1).

3.2.2. Full Protein Spot Analysis Method

While the lateral flow challenge method described above generates some semi-quantitative information about the relative amount of desorption under each challenge condition, we wanted to learn more about the adsorption process of the protein. I therefore collaborated with PhD graduate Dr. Gina Fridley to develop a more rigorous and holistic method based on the analysis of protein spots. This method depends on precisely patterned protein spots and therefore requires the use of the piezoelectric printer.

In this method, wider nitrocellulose strips cut to 0.8 cm wide by 5 cm tall were used. The piezoelectric printer was then used to deposit a precise volume of the protein solution of interest onto a nitrocellulose strip, forming a single spot. All protein spots were deposited using the same volume, consisting of 1000 droplets at 450-500 pL per droplet, printed at 500 Hz in an enclosed chamber at ~50% relative humidity and ~68 °F ambient temperature. A control spot of the same volume was also deposited using red food coloring diluted 1:10 in H₂O. This red food coloring spot was assumed to have minimal interaction with the membrane and therefore represent the full area that was wetted by the given volume, referred to herein as the full *wet-out area*. After drying under desiccation at least overnight, the spotted membranes were subjected to protein staining using a nonspecific protein stain in order to visualize the protein spots, as described above.

The size of each protein spot was quantified using a custom MATLAB script called *analyzeProteinSpots.m* (see Appendix C for code and description). Using this program, an approximate ROI is drawn semi-manually around the test spot of interest to indicate the

approximate location of the spot. The program then uses edge-finding to find the exact spot based on the derivative of pixel intensity, and then fits the edges with ellipses using a least-squares fitting algorithm. The area of each resulting ellipse is reported as the area of the given protein spot. The average pixel intensity inside this spot area, I_{spot} , is then background-subtracted using the average pixel intensity of a local background region, I_{bgd} , and normalized on a scale from 0 to 1 to generate the normalized pixel intensity of the spot, I_{norm} , using Eqn 19, just as described above.

The size of a given protein spot, relative to the full wet-out area, represents the relative speed of adsorption to the membrane, as illustrated in Figure 16 (top).

For example, a quickly adsorbing protein will generate a spot that is much smaller than the full wet-out area, since the protein adsorbs to the

membrane at a rate faster than that at which the protein

solution is wicked outward through the membrane. For

these rapidly adsorbing

proteins, increasing the protein concentration increases the size of the protein spot. Conversely, a slowly adsorbing protein will adsorb more slowly than the wicking rate, resulting in a spot size equal to the full wet-out area. If the adsorption is very slow, then evaporation at the edge of the spot will cause protein to concentrate at the edge of the spot, resulting in a coffee ring effect [159]. In this manner, the raw protein spots can be used to evaluate the relative rates of adsorption for different proteins or different membranes. Additionally, Dr. Fridley also developed a computational model in COMSOL Multiphysics (COMSOL, Inc., Burlington, MA) to further analyze this type of protein spot data to determine an effective on-rate of adsorption. She applied that model as a proof-of-concept to sets of protein adsorption data described in her thesis [160]. We have combined this work into a manuscript about protein adsorption analysis [161], but since that modeling was her work, it is not described here.

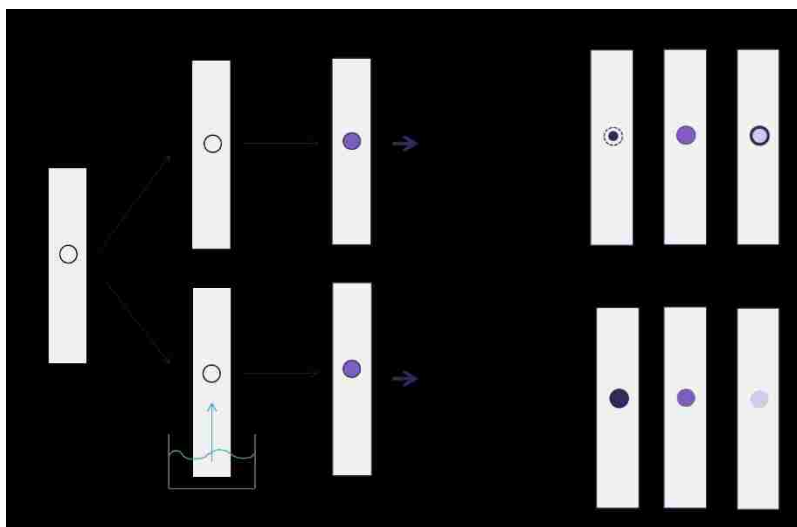


Figure 16. Illustration of the protein spot analysis method for evaluating protein adsorption.

The size of the protein spot (top) indicates the relative rate of adsorption. Additionally, protein spots can be subjected to a lateral flow (LF) challenge (bottom) to determine how resistant a protein is to stripping by a challenge solution, thereby indicating its relative strength of adsorption.

To evaluate the relative robustness of adsorption, protein spots were further investigated via lateral flow challenge analysis and nonspecific protein staining, as described above (section 3.2.1). In this case, sets of strips were placed into a multi-channel pipette reservoir containing 5 mL of the given challenge solution. Unless otherwise noted, the challenge solution was allowed to wick through the strips for 15 minutes, at which point the strips were removed from the solution. As usual, the protein remaining on the membrane was compared to the no-flow control. In this case, the more precisely controlled protein spots allowed for more precise signal quantification and therefore a more rigorous analysis. The spot intensity after staining relative to the no-flow control signifies the robustness of protein adsorption, as illustrated in Figure 16 (bottom). Specifically, if the signal intensities are similar with and without lateral flow challenge, then that protein is considered to be resistant to stripping in those conditions. Conversely, a protein spot that shows weaker intensity after lateral flow challenge is considered to adsorb less robustly and be subject to stripping in those conditions.

3.3. Initial Exploration of Protein Adsorption

In order to gain a fundamental understanding of the physical properties that affect protein adsorption to nitrocellulose, we studied the adsorption of a variety of proteins to nitrocellulose. We began by investigating a set of proteins that varied in size in order to determine if adsorption was correlated with size. We then focused on a well-known nitrocellulose-adsorbing protein, IgG, and compared its adsorption to other commonly used proteins in bioassays, particularly bovine serum albumin (BSA) and streptavidin (SA).

3.3.1. Methods

Lateral Flow Challenge and Protein Spot Analysis

For this work, primarily the initial lateral flow challenge method was used (section 3.2.1). In most cases, proteins were hand spotted. For the IgG vs. BSA comparison, the full protein spot analysis method was used (section 3.2.2).

3.3.2. Results and Discussion

Investigation of Protein Adsorption vs. Size

Early testing of the stem region flu binder revealed that it may not adsorb well to nitrocellulose. We therefore wished to further investigate the robustness of flu binder adsorption to nitrocellulose in more detail. In particular, since the stem region flu binders are small (10-15 kDa, compared to 150 kDa for IgG), we were concerned that their size may limit their ability to adsorb well, given that they have significantly less surface area available for interaction. Based on this reasoning, it has been reported in the literature that the strength of protein adsorption is correlated with the size of the protein [121]. We therefore used the lateral flow challenge to compare the nitrocellulose adsorption of eight proteins, including stem region binder HB36.4, ranging in size from 11.5 kDa to 150 kDa.

For this experiment, eight-leg comb devices with 3-mm-wide strips were cut from Millipore HFB135 nitrocellulose (Millipore, Billerica, MA) using a CO₂ laser cutter. Solutions of the following eight proteins were prepared at 400 µg/mL in PBS:

- Flu binder HB36.4, MW = 11.5 kDa
- Dengue type-3 Domain III antigen, MW = 12 kDa
- Dengue type-3 N-terminal antigen fragment, MW = 23 kDa
- Dengue type-3 N-terminal antigen fragment, MW = 32 kDa
- Human chorionic gonadotropin (HCG), MW = 36.7 kDa
- Dengue type-3 N-terminal antigen fragment, MW = 43 kDa
- Bovine serum albumin (BSA), MW = 66 kDa
- Anti-HA.11 mouse IgG, MW = 150 kDa

All eight protein solutions were hand-spotted onto the nitrocellulose device, using 0.5-µL spots with one protein per leg. The devices were then allowed to dry for 7 hours at room temperature under desiccation. After drying, the devices were subjected to lateral flow challenge with either PBS or PBST using 50 µL per leg with a wicking time of 10 minutes (not enough to wick the full volume to completion). The remaining protein was then visualized via Coomassie staining, and the devices were imaged on a flatbed scanner.

Although the hand-spotting was not uniform for this experiment, the resulting devices (Figure 17) clearly indicate different degrees of adsorption for the eight different proteins, based on the comparison of the lateral flow with PBS and PBST conditions. In particular, some of the smaller proteins (23, 32 and 43 kDa) show partial resistance to lateral flow with PBST, while others (11.5,

12, and 36 kDa) result in nearly complete desorption. Similarly, of the two largest proteins, BSA (66 kDa) is highly prone to stripping under PBST, while IgG (150 kDa) adsorbs robustly and resists desorption, even with PBST. The overall robustness of adsorption therefore does not appear to be a strong function of size. Instead, certain proteins adsorb well and others do not, presumably due to other physical properties of the proteins. These properties were explored in subsequent experiments. Importantly, this experiment also verified the lack of robust adsorption for the stem region flu binder HB36.4, which further motivated our desire to better understand protein adsorption (this chapter) and develop improved methods for protein immobilization (chapter 4).

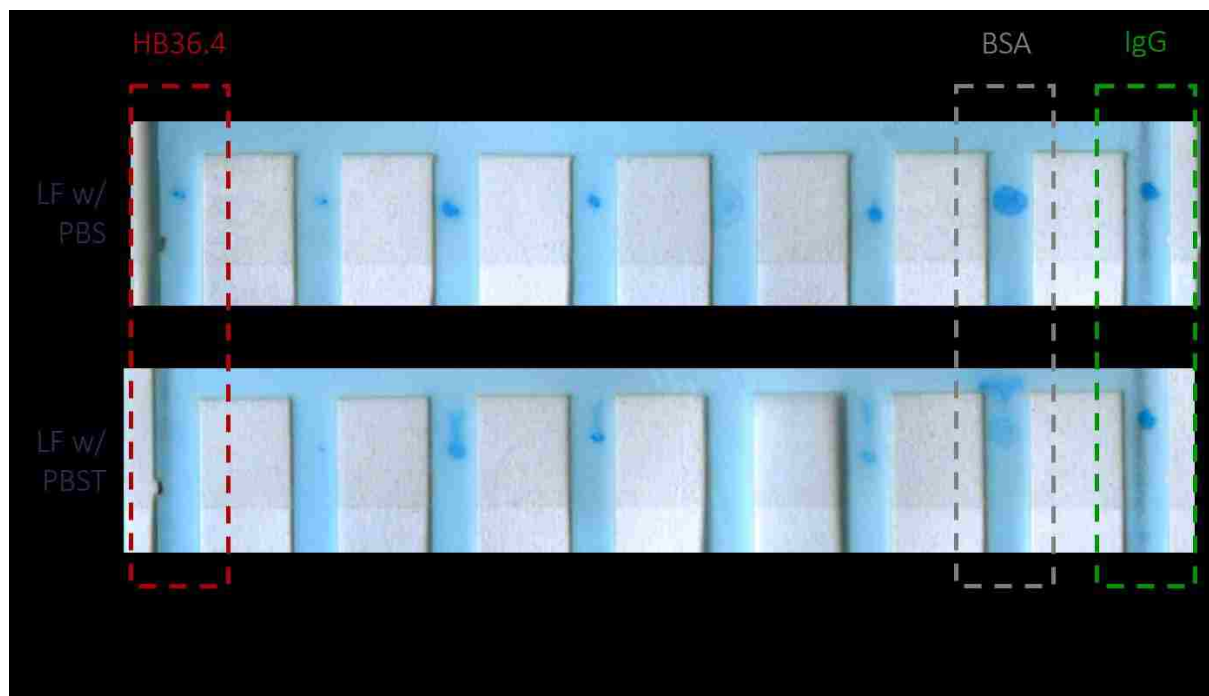


Figure 17. Protein adsorption for proteins ranging in size.

Proteins range in MW from 11.5 kDa to 150 kDa. The comparison of proteins spotted on nitrocellulose and subjected to lateral flow (LF) challenge with either PBS or PBST shows that the robustness of adsorption is not highly correlated with size. In particular, some smaller proteins resist stripping by PBST, while BSA is highly prone to stripping. IgG adsorbs strongly, as expected.

Comparison of IgG and BSA Adsorption

The large differences in adsorptive capacity of the proteins tested in the previous experiment was surprising, since protein binding is so often described as a feature of nitrocellulose [129,130,149]. In particular, the lack of adsorption of BSA was unexpected, since it is a well-characterized “soft” protein known to interact with surfaces [162]. Additionally, BSA is commonly used in blocking buffers to prevent sample fouling of membranes, a mechanism that depends on the adsorption of

BSA to the membrane [121]. We therefore performed a more extensive experiment to compare the adsorption of BSA to that of IgG, in order to learn more about these important proteins.

For this experiment, performed in collaboration with Dr. Gina Fridley, we used full protein spot analysis method. We used the piezoelectric spotter to pattern spots of precise volumes of the protein solutions onto nitrocellulose strips (GE FF80HP, 5 cm x 0.8 cm). We aimed to spot the proteins at three different concentrations, one above, one below, and one at the approximate monolayer concentration. To determine what concentration constitutes a monolayer, we used the size of IgG (~10 nm) to estimate how many IgG molecules would fit on a given area of flat surface, assuming spherical molecules and square packing. We then assumed a surface area ratio of 100 (internal surface area to frontal surface area), based on the information Millipore has provided for HFB135 membranes, which has similar pore size to the GE FF80HP membranes used here. Based on these calculations, we determined that a monolayer of IgG should be achieved at a concentration of 2.5 mg/mL. We also assumed this same monolayer concentration for BSA, since the size difference between BSA and IgG is likely within the error of our calculations and assumptions anyway. We therefore prepared concentrations of IgG (mouse polyclonal IgG, Jackson ImmunoResearch #015-000-003) and BSA (Sigma-Aldrich #A7030) at 5.6 mg/mL (~2x monolayer; highest achievable concentration based on IgG stock concentration), 2.5 mg/mL (1x monolayer), and 0.5 mg/mL (0.2x monolayer), all in PBS.

We used the piezoelectric spotter to deposit these protein solutions onto the nitrocellulose strips, with one protein spot per strip (in the middle, at 2.5 cm). For each protein at each concentration, we spotted two sets of strips with two different total spot volumes, 50 nL (100 drops x 500 pL/drop) and 500 nL (1000 drops x 500 pL/drop). All spotted strips were dried at room temperature under desiccation overnight before use.

To compare the robustness of adsorption of the various protein spots, we performed the lateral flow challenge using solutions of PBS, PBST, and PBS + 0.02% w/v SDS (PBSS), as well as a set of no-flow controls. These lateral flow conditions range from low to high stringency, with the PBSS condition ideally being a fully stripping condition (although turned out not to be in this case). Each challenge solution was allowed to wick for 20 minutes, after which the remaining protein was visualized via Coomassie staining.

The resulting devices (Figure 18) show that, as expected, IgG adsorbs to nitrocellulose more rapidly and robustly than BSA. In particular, the spot area of BSA was 20% larger than that of IgG for the

500-nL volume and 2.5-mg/mL concentration of both proteins (no-flow condition), indicating that BSA interacts with nitrocellulose more slowly than IgG. Additionally, the spot intensity of BSA decreased by 48% after lateral flow with PBST, compared to a 27% decrease for IgG, indicating the BSA is more prone to desorption than IgG. Finally, the BSA was also partially desorbed under the PBS lateral flow condition, while IgG only began to be desorbed for PBSS, the harshest condition tested.

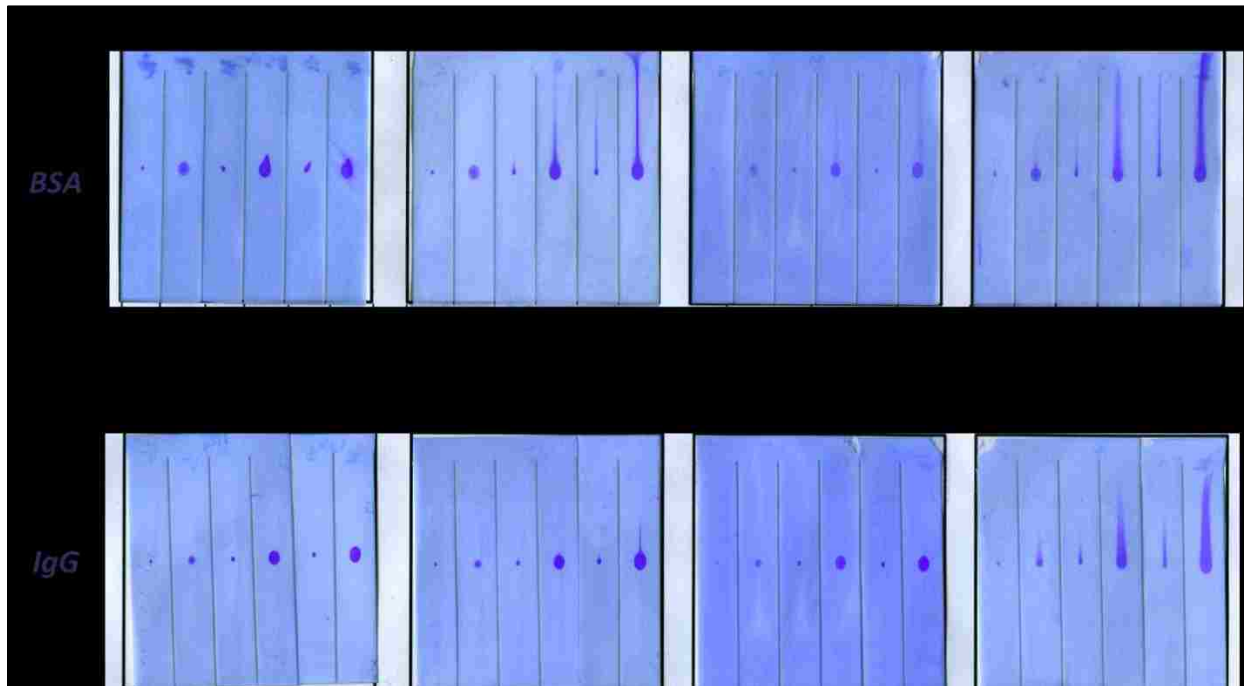


Figure 18. Comparison of IgG and BSA adsorption.

Nitrocellulose strips (FF80HP) spotted with BSA (top) or IgG (bottom) at the indicated concentrations and volumes, challenged with the indicated lateral flow conditions, and stained with Coomassie Brilliant Blue.

The comparison of the different concentrations and spot volumes yields interesting insights into the adsorption of the proteins tested. In particular, the IgG spot size increases for increasing concentration, with the highest concentration yielding a spot size that is approximately equal the area wetted by the buffer upon spotting. This suggests that all three concentrations are sub-monolayer (perhaps with the highest concentration close to monolayer), since the IgG continues to be able to spread to unused binding sites. For BSA, on the other hand, the spot size seems to plateau, and the highest concentration appears to be above monolayer, since some protein comes off even for the no-flow condition. It is hard to be certain based on this observation alone, however, since the spot size is also affected by the rate of adsorption, which we know is slow for BSA.

Overall, we have again confirmed the robust adsorption of IgG to nitrocellulose, which is not surprising, given the success of IgG as a capture agent in lateral flow tests. We have also validated the feeble adsorption of BSA to nitrocellulose, prompting further study of this commonly used blocking protein (see sections 3.4 and 3.6).

Comparison of IgG and SA Adsorption

Given the previous results that not all proteins adsorb well to nitrocellulose, we wanted to continue to explore the adsorption of proteins commonly used in bioassays. We therefore investigated the adsorption of streptavidin, which is commonly used as an anchor protein for the immobilization of biotinylated ligands (see section 2.4.3). Since we know that IgG adsorbs robustly to nitrocellulose, we also included IgG in these experiments to serve as a point of comparison.

To test the robustness of streptavidin adsorption to nitrocellulose, we performed two lateral flow challenge experiments, one using regular proteins visualized with Coomassie staining and one using fluorescently labeled proteins visualized by fluorescence imaging. In both cases, eight-leg comb

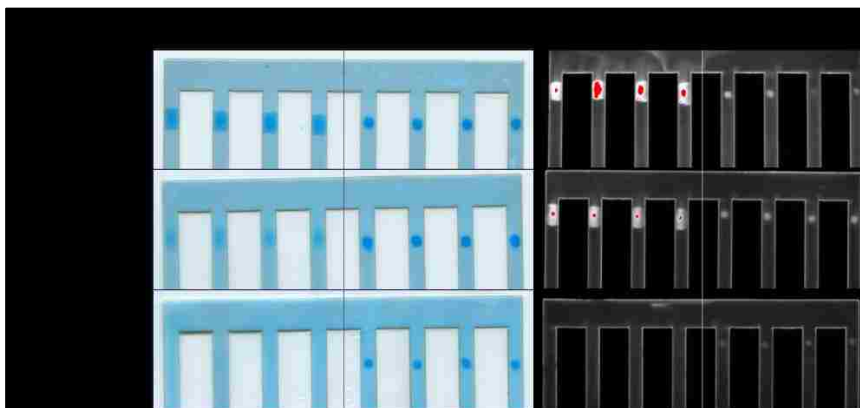


Figure 19. Comparison of streptavidin vs. IgG adsorption.

Streptavidin (SA) vs. IgG adsorption to nitrocellulose, as challenged by lateral flow with water, PBS, and PBST. Both non-labeled (left) and fluorescently labeled (right) versions of the proteins were tested. Streptavidin is completely stripped by PBST, while IgG is resistant to desorption.

devices were cut from Millipore HFB135 nitrocellulose using a CO₂ laser cutter. Solutions of each protein (Streptavidin, Sigma-Aldrich #85878; AlexaFluor488-streptavidin, Invitrogen #S-11223; IgG (goat-anti-human), Sigma #15260; FITC-IgG (human), Sigma #F9636) were prepared at 0.5 mg/mL in PBS. All device were spotted with 1- μ L hand spots, using one spot per leg. For the non-labeled protein set, the devices were stored in the desiccator for six weeks before use, while the devices for the fluorescently labeled protein set were dried under desiccation for one day before use. The devices were split into sets of three and subjected to lateral flow challenge with H₂O, PBS, or PBST. For each strip, 50 μ L of challenge solution was used, which was allowed to wick to completion, taking approximately 30 minutes. The non-labeled protein set was visualized by general protein staining with Coomassie Brilliant Blue. The fluorescently labeled protein set was

visualized by fluorescence imaging using a UV gel imager (Gel Doc EZ System, Bio-Rad, Hercules, CA) with the membrane backed-side-up (to minimize background fluorescence) and a 0.5-second exposure time.

The resulting devices are shown in Figure 19. Based on these results, two key observations can be made: 1) the streptavidin spots are much larger than the IgG spots, indicating that streptavidin adsorbs more slowly to nitrocellulose than does IgG; and 2) the streptavidin spots are partially stripped by lateral flow with PBS and completely stripped by PBST, indicating that streptavidin adsorption to nitrocellulose is easily disrupted by detergent, as well as salt. As observed previously, IgG adsorbs robustly and is only slightly stripped by PBST.

The poor adsorption of streptavidin to nitrocellulose was surprising, since it is so commonly used as an anchor protein, at least on other substrates [13]. These experimental results were therefore valuable lessons in the poorly understood nature of protein adsorption to nitrocellulose and helped guide our development of a streptavidin-biotin immobilization strategy for our flu binder on nitrocellulose (see section 4.5). In order to understand and improve streptavidin adsorption to nitrocellulose, we therefore investigated the pH-dependence of the process, described in section 3.6.

3.4. Solution Depletion

While the lateral flow challenge provides useful semi-quantitative data about protein adsorption, we wanted a more quantitative method for describing the adsorption between a given protein and a given nitrocellulose membrane. To this end, we developed and tested a protocol for solution depletion experiments that was intended to be used to assess the thermodynamics, and possibly kinetics, of protein adsorption. The goal of these experiments was to use the depletion data to create adsorption isotherms that could be fit with well-known adsorption models to derive an adsorption constant for each protein of interest. Ultimately, this method was not successful, but it is included here because it generated some useful insights, and it can be used to help guide future graduate students about what to do (and what not to do).

3.4.1. Methods

Solution Depletion

Following the advice of Professor Jonathan Posner (University of Washington, Mechanical Engineering), we developed a solution depletion protocol in which small pieces of nitrocellulose membrane were incubated with solutions of a given protein at different concentrations, and the solution phase of each tube was probed for protein content over time. Specifically, circles of 5-mm diameter were cut from unbacked nitrocellulose membrane using a CO₂ laser cutter. Unless otherwise noted, we used GE/Whatman AE98 fast, unbacked nitrocellulose, which was provided by our collaborators at GE GRC. These circles were then placed in individual microcentrifuge tubes, using tubes of amber color if the experiment involved a fluorescently labeled protein. To each tube, 0.5-1 mL of protein solution was added at a given concentration. Corresponding control tubes were prepared with protein solution but without nitrocellulose. Typically, three replicates of each test and control condition were performed. The tubes were then placed on the tube rotator and allowed to incubate at room temperature for a given amount of time. For a time-course experiment, n sets of tubes were prepared for n time points, and each set was allowed to incubate until its designated ending time. At each ending time, the nitrocellulose membranes were removed from their tubes to stop the adsorption process.

To determine the amount of protein that was adsorbed to a given piece of nitrocellulose, the protein solution was probed for its protein content to quantify the amount of protein that was depleted relative to the corresponding control tube. For fluorescently labeled proteins, this was done via fluorescence measurement in a multimodal plate reader (Tecan Infinite M200 Pro). In this case, aliquots from each protein solution were plated in a black 96-well plate (Greiner Bio-One #655076) using 100 μ L of solution per well. Samples were typically plated in duplicate or triplicate when enough sample volume was available. A dilution series of the given protein was also prepared and plated (in duplicate or triplicate) for the generation of a standard curve. Blanks (buffer only) were also plated to generate readings for background subtraction. For proteins labeled with fluorescein isothiocyanate (FITC), we used an excitation wavelength of 490 nm (bandwidth < 9 nm) and an emission wavelength of 520 nm (bandwidth < 20 nm). Fluorescence readings were acquired using a 200- μ s integration time with 100 flashes and an automated gain using the “Extended Dynamic Range” feature.

We also tested a variation of this protocol in which non-labeled proteins were used, and protein concentration was measured by general protein staining using the Bradford assay [163]. Specifically, we mixed each supernatant sample or standard solution with Coomassie Plus (Bradford) Assay Reagent (Thermo Scientific #23238) at one of three ratios of sample/stain: 10/290 (for high concentration quantification), 50/250 (for intermediate concentration quantification), and 150/150 (for low concentration quantification). Following the manufacturer's protocol, each 300- μ L mixture was plated (again, typically in duplicated or triplicate) in a transparent 96-well plate (Thermo Scientific, Nunc, #269787) using 300 μ L per well and incubated at room temperature with shaking for 10 minutes. The absorbance of each well was then measured using a multimodal plate reader (Tecan Infinite M200 Pro) at a wavelength of 595 nm.

For either measurement method, the blank readings were used to background-subtract the readings for all standards and samples. The fluorescence or absorbance readings for the standard concentrations were then used to create a standard curve, based on a least-squares curve fit to the experimental readings. For fluorescence measurements, this standard curve followed a simple linear equation, given by Eqn 20, where F is the fluorescence intensity, $C_{protein}$ is the concentration of the fluorescently labeled protein, F_0 represents the fluorescence for the buffer alone, and k is the slope that is fit to define the dependence of fluorescence on protein concentration.

$$F = k \cdot C_{protein} + F_0 \quad \text{Eqn 20}$$

For absorbance measurements, the standard curve followed a four-parameter logistic (4PL) curve, given by Eqn 21, where A is the absorbance, $C_{protein}$ is the concentration of the protein, and parameters a , b , c , and d are fit to define the shape of the sigmoidal curve.

$$A = \frac{a - d}{1 + \left(\frac{C_{protein}}{c}\right)^b} + d \quad \text{Eqn 21}$$

For either method, the resulting standard curve was used to calculate the amount of protein remaining in the supernatant for each test (protein solution + nitrocellulose) and control (protein solution only) sample. The amount of protein depleted and therefore adsorbed to the nitrocellulose was calculated according to Eqn 22.

$$Protein_{depleted} = Protein_{control} - Protein_{test} \quad \text{Eqn 22}$$

Since both the test and control protein amounts have errors associated with those measurements, the standard deviation of the amount of protein depleted is additive and was propagated through the calculation according to Eqn 23.

$$SD_{depletion} = \sqrt{SD_{control}^2 + SD_{test}^2} \quad \text{Eqn 23}$$

Finally, the depletion data was used to fit both Langmuir and Freundlich adsorption curves, which are two common models of surface adsorption of proteins [164,165] and have been used successfully by the Posner group for other applications [166,167]. The Langmuir model is given by Eqn 24, where $Protein_{depleted}$ is the amount of protein depleted by adsorption to the membrane, C_{liquid} is the given input protein concentration, V_{max} represents the maximum level of adsorption, and K_{ads} is the Langmuir adsorption constant.

$$Protein_{depleted} = \frac{V_{max} \cdot K_{ads} \cdot C_{liquid}}{1 + K_{ads} \cdot C_{liquid}} \quad \text{Eqn 24}$$

The Langmuir model can be linearized to Eqn 25.

$$\frac{1}{Protein_{depleted}} = \frac{1}{V_{max} \cdot K_{ads}} \cdot \frac{1}{C_{liquid}} + \frac{1}{V_{max}} \quad \text{Eqn 25}$$

The Freundlich model is given by Eqn 26, where K_F is the Freundlich adsorption constant, and n represents the linearity of the dependence of adsorption on concentration.

$$Protein_{depleted} = K_F \cdot C_{liquid}^n \quad \text{Eqn 26}$$

The Freundlich model can be linearized to Eqn 27.

$$\ln(Protein_{depleted}) = \ln(K_F) + n \cdot \ln(C_{liquid}) \quad \text{Eqn 27}$$

The solution depletion data can therefore be fitted, in a least-squares sense, with either linearized adsorption model, and the resulting slope and intercept can be used to determine the given adsorption constant. This constant represents a single, quantitative measure of the robustness of adsorption for the given protein and nitrocellulose membrane tested. It is important to note that both adsorption models make several assumptions about the system that are not fully satisfied in reality; despite this discrepancy, these adsorption models are commonly applied to solution depletion studies and yield reasonable quantification of the adsorption [164–168]. Additionally, the Freundlich model is theoretically better suited than the Langmuir model to describe protein adsorption to nitrocellulose, as the Langmuir model assumes a planar, homogeneous surface, while the Freundlich model accounts for a rough, heterogeneous surface like porous nitrocellulose [168].

3.4.2. Results and Discussion

Solution Depletion with FITC-BSA

To further characterize the adsorption of BSA, we performed a solution depletion experiment in which the solutions of the protein were incubated with pieces of nitrocellulose in order to determine an adsorption coefficient for the protein. In this experiment, we forwent short time points and the potential kinetic information they might afford in favor of focusing on a single intermediate time point that was presumably close to equilibrium, in order to provide the biggest potential depletion of protein from the solutions. For this experiment, we used BSA that is labeled with both FITC and biotin (NANOCS #BS2-BNFC-1), as it was the only fluorescently labeled protein that we had in a large enough quantity for use in the experiment. We therefore operated under the assumption that biotin, which is a small molecule, would not significantly affect the adsorption of the fluorescently labeled BSA.

To perform the experiment, dilutions of the biotin-BSA-FITC were made in PBS at the following concentrations: 100, 50, 10, 5, 1, 0.5, and 0.1 $\mu\text{g}/\text{mL}$. Each 1.5-mL microcentrifuge tube (amber colored) was filled with 1 mL of the given protein dilution, resulting in total protein amounts of 100, 50, 10, 5, 1, 0.5, and 0.1 μg . These protein amounts therefore spanned the amount of protein estimated to saturate a 5-mm-diameter circle of nitrocellulose ($\sim 5 \mu\text{g}$). As usual, unbacked AE98 nitrocellulose membranes were used for the test conditions, while tubes without any nitrocellulose added were used for the control conditions. Three replicates of each condition were performed. All tubes were placed on a tube rotator and allowed to incubate at room temperature for approximately two hours. At this time, the nitrocellulose membranes were removed from their tubes to stop the adsorption process. In addition to the supernatant measurements described above, we also imaged the nitrocellulose membranes themselves using both an in-house fluorescence light box (6 V) and the UV gel imager (Bio-Rad Gel Doc EZ System, 0.5-sec exposure).

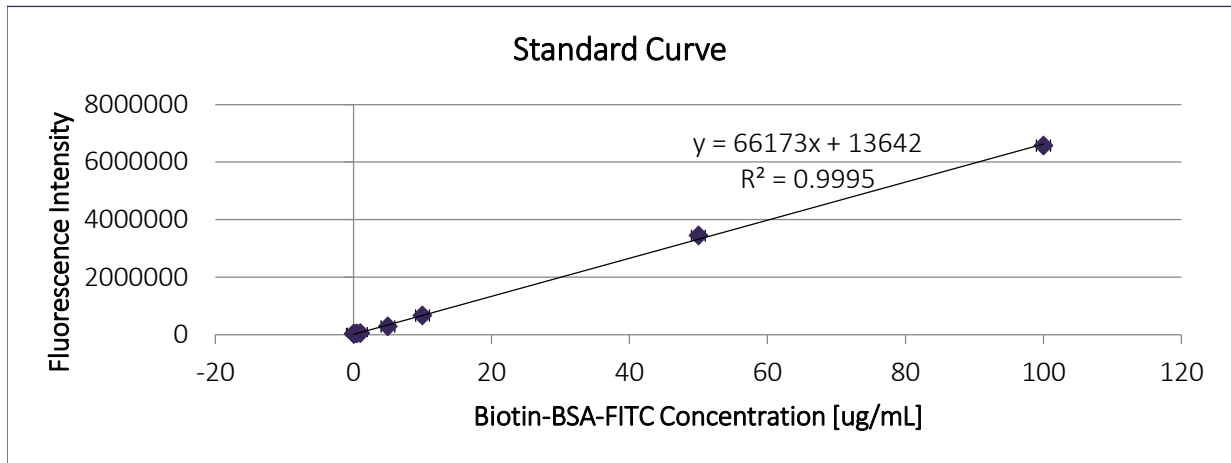


Figure 20. Standard curve for biotin-BSA-FITC quantification in solution depletion experiments. Standard curve based on fluorescence readings. Each point represents the mean +/- SD for n=3 replicates.

The standard curve based on the dilution series of biotin-BSA-FITC is shown in Figure 20, where each point represents the mean of n=3 replicates. Error bars represent +/- one standard deviation. Using this standard curve, the amount of protein depleted from each solution was calculated. These results are shown in Figure 21 (log scale) and Figure 22 (linear scale) as the mean +/- one standard deviation for n=3 replicates of each concentration.

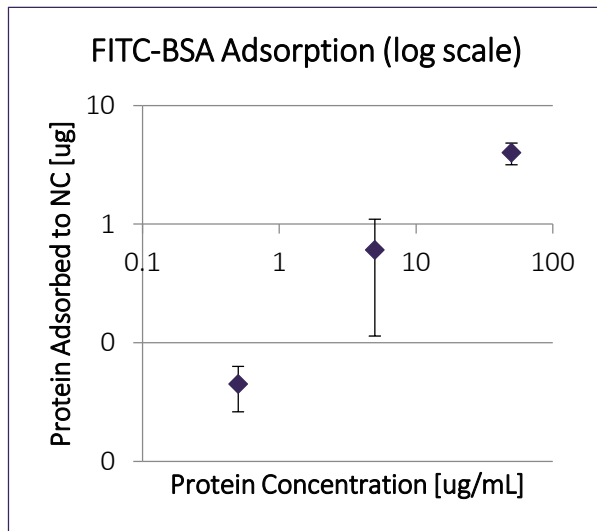


Figure 21. FITC-BSA solution depletion, log scale. Amount of biotin-BSA-FITC adsorbed to nitrocellulose after 2 hrs, plotted on a log scale. Each point represents the mean +/- SD for n=3 replicates.

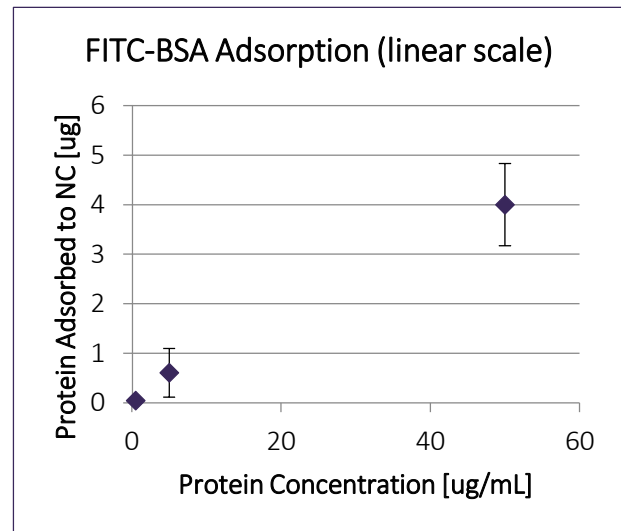


Figure 22. FITC-BSA solution depletion, linear scale. Amount of biotin-BSA-FITC adsorbed to nitrocellulose after 2 hrs, plotted on a linear scale. Each point represents the mean +/- SD for n=3 replicates.

These results indicate that, as expected, an increasing amount of protein is adsorbed to the nitrocellulose for increasing concentrations of protein in the solution. We cannot observe a good saturation curve with only these three data points, but we expect that higher concentrations of

protein solution would result in only modest gains in the amount of protein adsorbed, and that this curve would approach saturation.

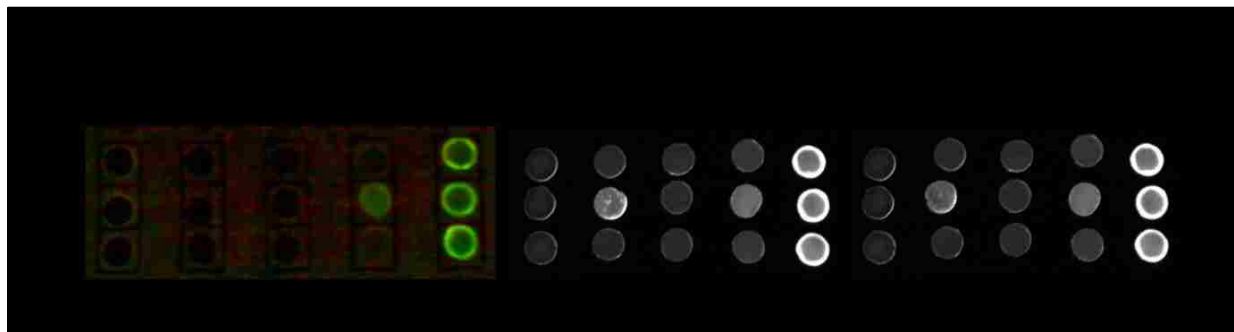


Figure 23. Nitrocellulose membranes after FITC-BSA solution depletion.

Fluorescence images of the nitrocellulose (NC) circles that were incubated with biotin-BSA-FITC.

The corresponding nitrocellulose membrane circles that were incubated in the test solutions were imaged for fluorescence by both the fluorescence light box and the UV gel imager, as shown in Figure 23. One of the circles (row 2, column 2) gave high fluorescence in the gel imager, so I flipped it over and re-imaged it to see if it was an edge effect of that side of the membrane; the flipped circle also gave higher fluorescence than expected. Overall, these membranes show consistent fluorescence for only the highest concentration of biotin-BSA-FITC tested ($50 \mu\text{g/mL}$).

Finally, the depletion data was used to fit both Langmuir and Freundlich adsorption curves using equations Eqn 25 and Eqn 27, respectively. The resulting linearized models and adsorption constants for each model are shown in Figure 24. It appears either that the Langmuir model is not a valid model for this adsorption or that something went wrong with this experiment, as the Langmuir model resulted in a negative maximum adsorption and a negative adsorption constant, which are both nonsensical. The Freundlich model, however, did yield valid numbers, with an adsorption constant of 0.099 and a linearity of adsorption of 0.976 (nearly linear). This result is consistent with the literature in that the Freundlich model is expected to fit adsorption data for porous materials better than the Langmuir model, since the Freundlich model takes into account the heterogeneity of the porous surface [164,168].

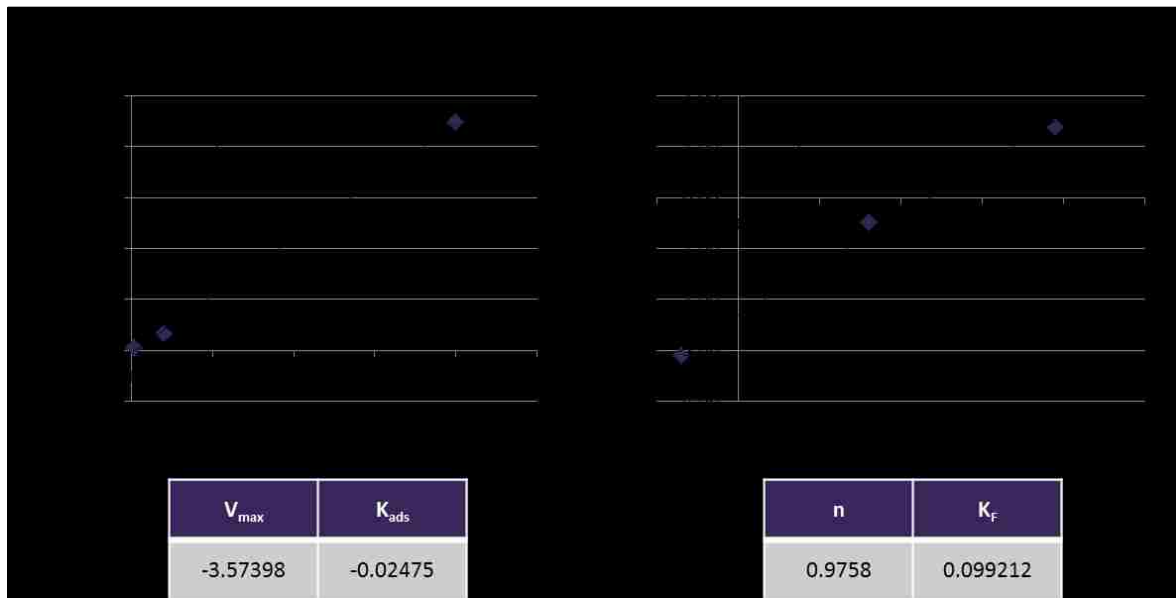


Figure 24. Adsorption models for FITC-BSA solution depletion.

Langmuir and Freundlich adsorption models applied to the solution depletion data for biotin-BSA-FITC.

Overall, these results suggest that solution depletion is a valid method for quantifying protein adsorption to nitrocellulose, at least for fluorescently labeled proteins, and at least when using the Freundlich model. Through this solution depletion experiment, we established a preliminary adsorption constant that describes the adsorption of biotin-BSA-FITC to nitrocellulose (AE 98, unbacked). Without another protein to which to compare this adsorption constant, however, this result is not very meaningful on its own. We therefore aimed to use this same method to determine adsorption constants for other proteins, which could then be compared to each other as a measure of the robustness of adsorption for each protein. We attempted to achieve these comparisons using solution depletion experiments with other, non-fluorescently labeled, proteins; however, as described in the next section, the Bradford protein quantification method was not accurate enough to determine any adsorption constants.

Solution Depletion with Non-Labeled IgG and BSA

In order to investigate protein adsorption more quantitatively we are continued to develop solution depletion experiments to assess the thermodynamics, and possibly kinetics, of protein adsorption through the creation of isotherms and application of adsorption models. We previously demonstrated a working solution depletion assay for the adsorption of biotin-BSA-FITC to unbacked nitrocellulose membrane. However, that experiment was limited in the number of data points used and only worked for a single fluorescently labeled protein. We therefore sought to

extend solution depletion testing to non-labeled proteins using Bradford (Coomassie-based) protein quantification. Here, we describe a full solution depletion experiment that was performed to compare the adsorption of IgG and BSA on unbacked nitrocellulose (AE98 fast). Since we learned from previous solution depletion testing (data not shown) that a single ratio of sample-to-stain for the Bradford assay does not yield accurate enough quantification, we measured all protein solutions here with two sample-to-stain ratios, based on the premise that one should quantify low concentrations well (10/290 sample/stain) and the other should quantify high concentrations well (150/150 sample/stain).

For this experiment, dilutions of IgG (mouse polyclonal IgG, Jackson ImmunoResearch #015-000-003) and BSA (Sigma-Aldrich #A7030) were made in PBS at the following concentrations: 1500, 1250, 1000, 750, 500, 250, 100, 75, 50, 25, 10, 7.5, 5, 2.5, and 1 $\mu\text{g}/\text{mL}$. The 500, 100, 50, and 10 $\mu\text{g}/\text{mL}$ concentrations were used as the test concentrations for the depletion experiment, while the other dilutions were used for the standard curve. Laser-cut circles of unbacked nitrocellulose (GE/Whatman AE98 fast) were placed in individual 0.6-mL microcentrifuge tubes. To each tube, 500 μL of a given protein solution was added at a given concentration. Corresponding control tubes were prepared with protein solution only without nitrocellulose. Three replicates of each condition were performed. The tubes were then placed on the tube rotator and allowed to incubate at room temperature for three different time points (with three replicates per time point): 1.5 hours, 6 hours, and 96 hours (presumed equilibrium). At each time point, the nitrocellulose membranes were removed from their wells to stop the adsorption process, and the supernatants were probed for protein content by two different methods of Bradford staining: 1) the standard Bradford assay, which uses 10 μL protein sample and 290 μL stain per well; and 2) the micro Bradford assay, which uses 150 μL protein sample and 150 μL stain per well. The standard concentrations were measured only with the first time point. As usual for the Bradford assay, the absorbance of each sample and standard was measured at a wavelength of 595 nm.

The standard curves for each protein for each quantification method (i.e. ratio of sample to Bradford reagent) are provided in Figure 25, where each point represents the mean of $n=3$ replicates (for 10/290 set) or $n=2$ replicates (for 150/150 set), error bars represent ± 1 standard deviation, and the red lines represent the four-parameter logistic (4PL) curve fits used to correlate absorbance values to protein concentration. These curves show that the 10/290 sample/stain ratio seems to give more accurate quantification, perhaps with the exception of the very lowest concentrations.

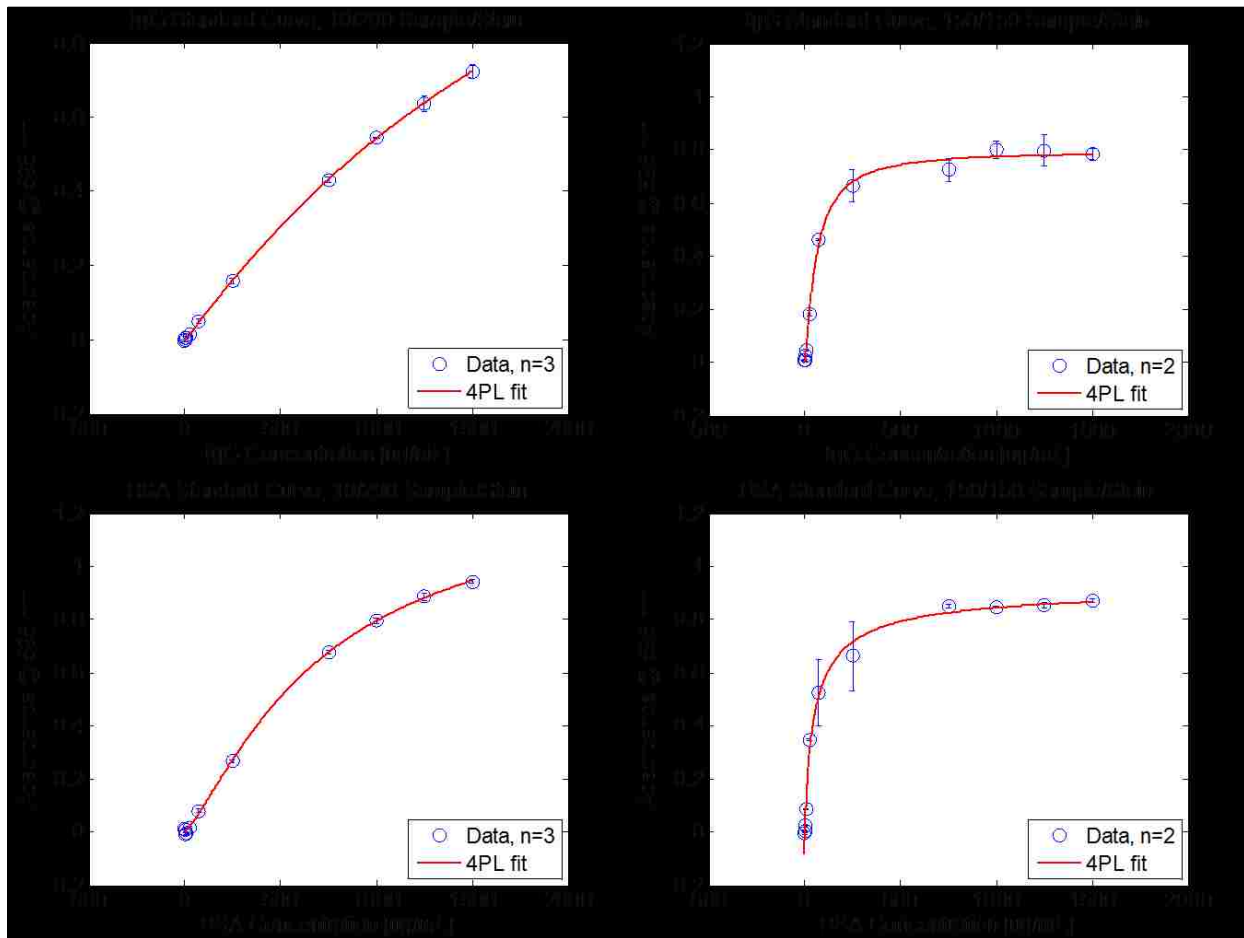


Figure 25. Standard curves for non-labeled protein solution depletion.

Standard curves relate absorbance readings from Bradford assay to protein concentration via a 4PL curve fit.

Using these standard curves, the protein content of each test and control solution was calculated, as shown in Figure 26, Figure 27, and Figure 28 for the 1.5-, 6-, and 96-hour time points, respectively. For both proteins, the absorbance values of some of the concentrations were out of range of the standard curve and could not be quantified. This inability to quantify low concentrations is unfortunate and is due to the overall inaccuracy of the Bradford staining method for protein quantification. For the cases in which both test and control protein concentrations were available, the amount of protein depleted from each solution was calculated according to Eqn 22, with the standard deviation propagated additively according to Eqn 23. These results are also shown in the figures below, plotted as the mean +/- one standard deviation for n=3 replicates of each concentration. Since the standard deviations of the individual test and control measurements were already high, the resulting compounded standard deviations for the amount of protein depleted were prohibitively large, preventing any useful trends in adsorption from being identified above the noise.

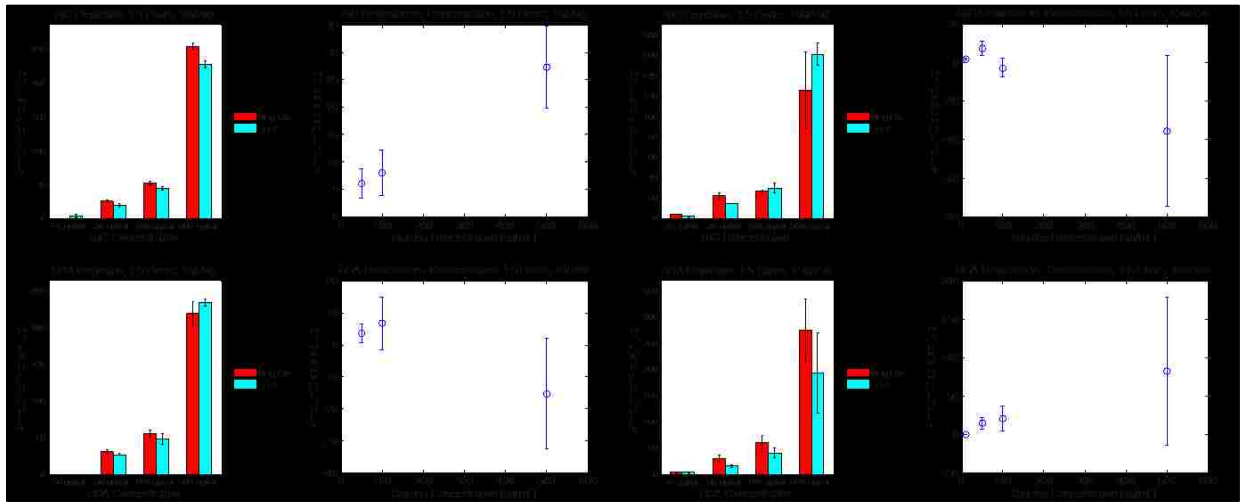


Figure 26. IgG and BSA solution depletion, 1.5 hours.

Solution depletion results for the 1.5-hour time point. Top: IgG. Bottom: BSA. Left side: results from 10/290 Bradford quantification. Right side: results from 150/150 Bradford quantification.

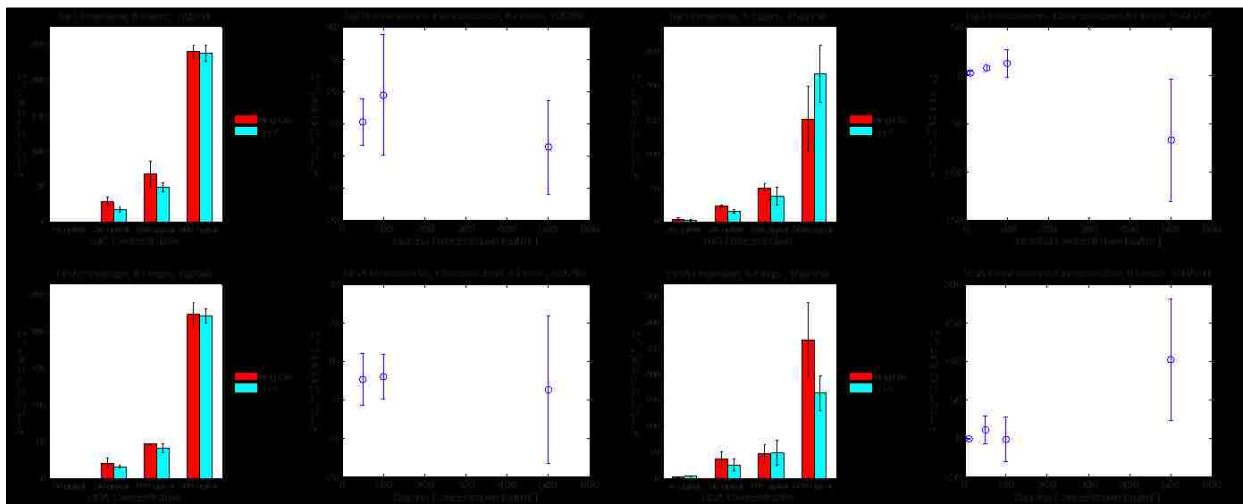


Figure 27. IgG and BSA solution depletion, 6 hours.

Solution depletion results for the 6-hour time point. Top: IgG. Bottom: BSA. Left side: results from 10/290 Bradford quantification. Right side: results from 150/150 Bradford quantification.

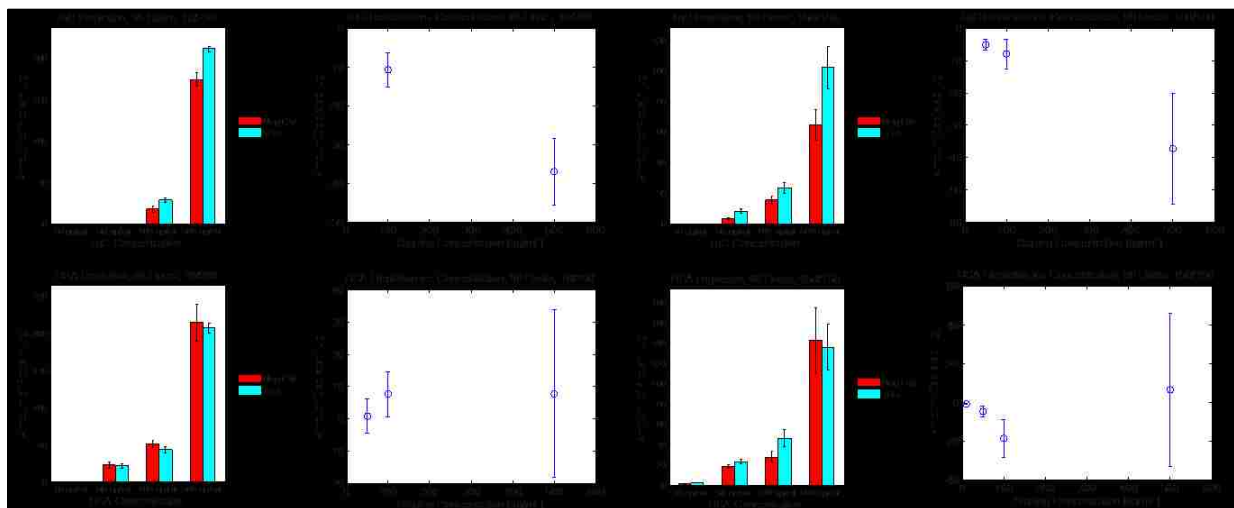


Figure 28. IgG and BSA solution depletion, 96 hours.

Solution depletion results for the 96-hour time point (presumed equilibrium). Top: IgG. Bottom: BSA. Left side: results from 10/290 Bradford quantification. Right side: results from 150/150 Bradford quantification.

Overall, these results are hindered by large error, and no meaningful conclusions can be drawn about the adsorption of IgG as compared to BSA. In some cases, the perceived depletion actually *decreased* with time (although within the large range of the standard error), which is nonsensical. Since the error bars of the depletion results were so large, no attempt was made to fit adsorption models to the data. A part of the error is presumed to be due to the high error of the Bradford assay quantification method. However, other researchers in the lab, including Dr. Gina Fridley, also attempted similar solution depletion experiments with additional fluorescently labeled proteins and also did not have success [160]. We now hypothesize that the majority of the error is due to the lack of transport within the membranes. Specifically, once the membrane pieces are immersed in the protein solution, they quickly become fully saturated, eliminating capillary flow as means by which to generate solute transport through the pores. While the intrapore diameter is small and conducive to fast diffusion times, transport throughout the pore network is much slower and inefficient for mixing the depleted solution within in the pores with the non-depleted bulk solution outside of the pores. In addition, these experiments were also extremely time- and reagent-intensive, given the large number of replicates needed to amass enough data across time points and concentration ranges in order to even attempt to generate adsorption isotherms. Finally, these experiments could only be performed with unbacked nitrocellulose, which does not necessarily reflect the material and adsorption properties of backed nitrocellulose. Therefore, while we began to uncover some interesting adsorption data for FITC-BSA, the most valuable lesson we learned is that the solution depletion method is not well-suited for studying protein adsorption to porous

nitrocellulose membranes. We therefore returned to using the lateral flow challenge method, and the more rigorous protein spot analysis method, in order to gather the most quantitative protein adsorption data possible.

3.5. IgG Adsorption to Nitrocellulose

Since the solution depletion method failed to generate a quantitative understanding of IgG adsorption to nitrocellulose, we returned to the use of the lateral flow challenge and protein spot analysis methods. In this case, we applied the full protein analysis method in a deeper and more rigorous manner than had been done previously in order to generate a semi-quantitative characterization of IgG adsorption to nitrocellulose.

Given that IgG adsorbs so robustly to nitrocellulose and has been used so successfully as an affinity reagent for lateral flow tests, we aimed to understand why IgG sticks so well. In particular, we explored whether or not there was a particular component of IgG that was responsible for its adsorption, from which we could learn and use as input for the design of our anchor

protein. When assay developers use IgG as a capture species, the hope is that all of the IgG molecules on the surface are oriented “right-side up”, with both antigen-binding domains facing outward, though it is generally acknowledged that a more reasonable assumption is of randomly oriented IgG molecules (Figure 29A). We therefore sought to understand if there is a difference in adsorption rates of different regions of the IgG molecule, leading to non-random orientation of IgG molecules on the membrane surface.

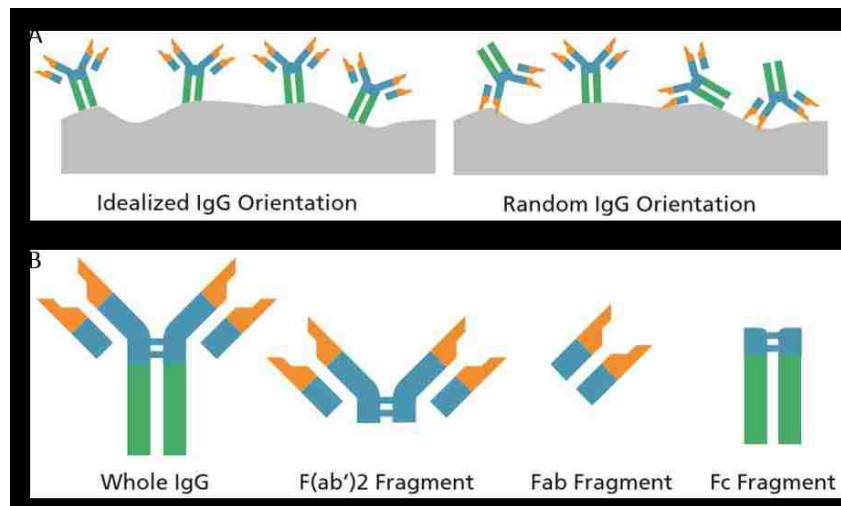


Figure 29. IgG orientation and its fragments.

(A) Comparison of idealized IgG adsorption to a membrane, with all antibody-binding domains facing up, to a more realistic random orientation, which is typically assumed. (B) Schematic representation of the IgG fragments analyzed herein. Figure adapted from Dr. Gina Fridley [160].

3.5.1. Methods

Full Protein Analysis Method

To investigate IgG adsorption, we compared the nitrocellulose adsorption of whole IgG to three different fragments of IgG: Fc fragment, Fab fragment, and F(ab')₂ fragment (Figure 29B). All four proteins were purchased from Jackson ImmunoResearch and originate from polyclonal mouse IgG. Proteins were spotted at 0.5 mg/mL, 2.3 mg/mL, and the stock concentration of the given protein, all in PBS at pH 7.4. These concentrations represent approximately 0.2x, 1x, and ~5x monolayer concentrations, respectively, based on the amount of IgG estimated to fit within the available surface area. The stock concentration of the Fc fragment was 2.3 mg/mL, so it was only studied at two concentrations. Red food coloring diluted 1:10 in H₂O was also spotted to visualize the full wet-out area. All spots consisted of 1000 droplets at 450-500 pL per droplet. After spotting, all strips were stored under desiccation overnight before use. The lateral flow challenge was performed using challenge solutions of PBS, PBST (PBS + 0.1% v/v Tween-20), and PBSS (PBS + 0.1% w/v SDS), as well as a set of no-flow controls. Sets of six strips were run together in a trough (multi-channel pipette reservoir) containing 5 mL challenge solution and allowed to wick for 15 minutes before Ponceau S staining.

3.5.2. Results and Discussion

Adsorption of IgG and Fragments

The full set of results, including a single representative test spot image for each condition tested, is provided in Figure 30. These results indicate that, as expected, IgG adsorbs the most robustly, with the smallest spots and most resistance to stripping by PBS, PBST, and PBSS.

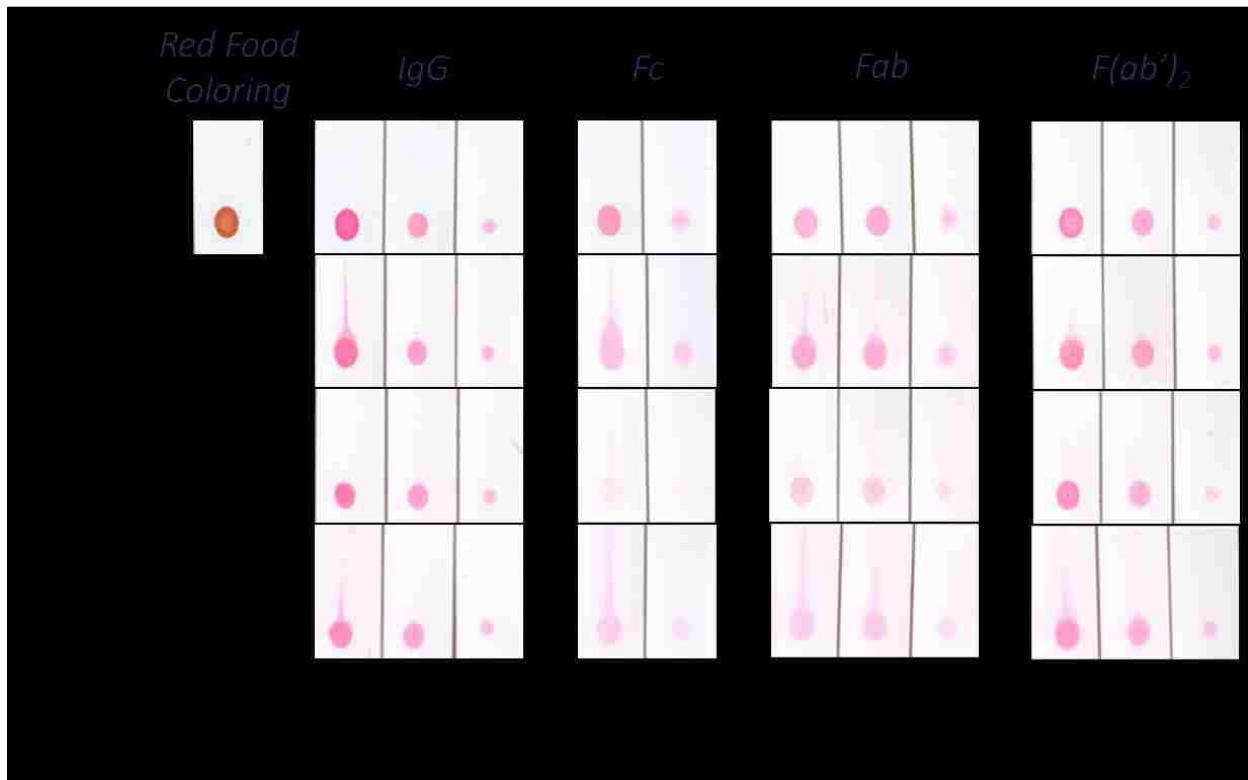


Figure 30. Adsorption of IgG and its fragments, full results.

Comparison of the adsorption of IgG and three of its fragments (Fc, Fab, and $F(ab')_2$). Protein spots were challenged via lateral flow with PBS, PBS + 0.1% Tween-20 (PBST), or PBS + 0.1% SDS (PBSS) and stained with Ponceau S. A set of no-flow controls were also performed, as well as a spot of red food coloring to visualize the full wet-out area.

To delve into the results further, we first focused on the protein spot analysis for the no lateral flow condition. We used the protein spot size analysis to understand the relative rates of adsorption of each fragment. A representative spot for each protein for the no lateral flow condition, as well as the full wet-out area indicated by the red food coloring, is provided in Figure 31A. The average spot area for $n=3$ replicates of each protein, relative to the average full wet-out area, is plotted in Figure 31B. Because the piezoelectric spotting system delivers many small droplets during the printing process (1000 drops at 500 pL per drop), liquid enters the membrane and flows outward radially, creating near-circular spots (which are not perfectly circular due to anisotropy of the membrane).

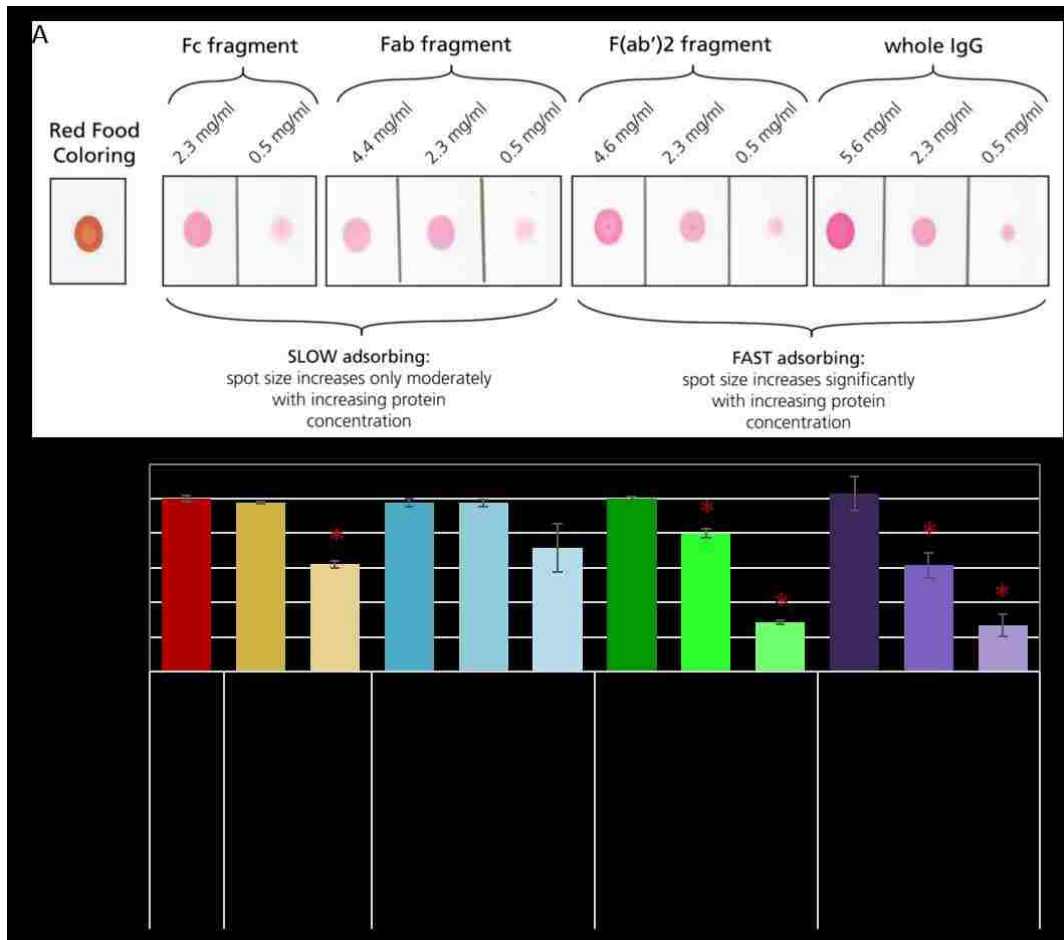


Figure 31. Comparison of protein adsorption speed for IgG and fragments.

Adsorption speed evaluated via protein spot size analysis. (A) Images of IgG fragments that were printed onto nitrocellulose, dried overnight, and stained with Ponceau S to visualize the protein spot. All spots were printed with the same volume of protein solution (500 nL), with varying concentrations. The red food coloring (RFC) spot (left) illustrates the full wet-out area for that volume. Image adapted from Fridley [160]. (B) Spot areas relative to the full wet-out area, plotted as the mean \pm SD for $n=3$ replicates. Asterisk indicates a significantly smaller spot size relative to the next-highest concentration ($p < 0.025$ by one-tailed Student's t -test assuming unequal variance).

As these results show, we observe the fastest binding (smallest protein spot size) for whole IgG, followed closely by the F(ab')₂ fragment. Specifically the average spot sizes of IgG and the F(ab')₂ fragment relative to the wet-out area were 27% and 28% for the 0.5 mg/mL concentration and 61% and 80% for the 2.3 mg/mL concentration, respectively. At the highest concentration, both protein spots approached the size of the full wet-out area (103% for IgG and 100% for the F(ab')₂ fragment), indicating that the total amount of protein deposited was greater than or equal to the amount of protein required to saturate the full wet-out area. The Fab and Fc fragments exhibited the slowest binding, with spot sizes of 72% and 62% of the wet-out area for the 0.5 mg/mL concentration, and 97% and 98% for the 2.3 mg/mL concentration, respectively. Overall, only whole IgG and the F(ab')₂ fragment exhibited spots smaller than the wet-out area for both the 0.5

mg/mL and 2.3 mg/mL concentrations ($p < 0.025$ by Student's one-tailed t -test assuming unequal variance). We therefore characterize whole IgG and the F(ab')₂ fragment as fast-adsorbing proteins to nitrocellulose, while the Fab and Fc fragment are slow adsorbers.

Next, we focused on the protein spots after lateral flow challenge with PBST to evaluate the strength of adsorption of each protein. A representative spot for each protein is provided in Figure 32A and compared side-by-side with the no lateral flow condition for the 2.3 mg/mL concentration of each protein. The average spot intensity for $n=3$ replicates of each protein for each condition is plotted in Figure 32B. Based on these results, whole IgG and the F(ab')₂ fragment showed strong adsorption to nitrocellulose under lateral flow challenge with PBST, with 86% and 85% of signal intensity remaining relative to the no-flow condition, respectively. Interestingly, the loss in signal for the F(ab')₂ fragment was significant ($p < 0.025$ by Student's one-tailed t -test assuming unequal variance), while that for whole IgG was not. In both cases, however, the loss in signal is relatively small and indicates high resistance to stripping even with a mild detergent. The Fab fragment exhibited moderate adsorption, with 51% signal intensity remaining after lateral flow challenge with PBST, a significant loss relative to the no-flow condition ($p < 0.025$). The Fc fragment showed the weakest adsorption and was significantly stripped away from the membrane under this challenge condition, with only 13% of intensity remaining ($p < 0.025$). While Ponceau S staining is only semi-quantitative and cannot be mapped to absolute protein quantification [169], these results reveal the relative robustness of adsorption of each protein and indicate that the Fc and Fab fragments show significant stripping under challenge by PBST relative IgG ($p < 0.025$ by Student's one-tailed t -test assuming unequal variance), while only the F(ab')₂ fragment did not show a significant difference in stripping relative to whole IgG.

Taken together, these results suggest that IgG adsorption to nitrocellulose is largely mediated by antigen-binding domain, since the F(ab')₂ fragment demonstrates IgG-like adsorption. The Fab fragment shows moderate adsorption, which we hypothesize is due to the fact that it contains only a single antigen-binding domain, compared to the two antigen-binding domains present in the F(ab')₂ fragment and in whole IgG. Fc is clearly the weakest adsorber, suggesting that IgG does not adsorb preferentially through this fragment. These results were unexpected, since the success of IgG as a capture agent in lateral flow tests depends on the accessibility of the Fab regions for binding to target antigen. In particular, these results suggest that not only is IgG unlikely to approach the idealized orientation depicted in Figure 29A, but it may actually assume an orientation with preferential binding through the Fab regions, with the Fc fragment facing outward.

Interestingly, there is also a dark dot in the middle of the protein spots for the Fab-containing fragments (whole IgG, Fab, and F(ab')₂), which may represent a certain monoclonal fraction within the polyclonal distribution that has binding sites with particularly high affinity for nitrocellulose.

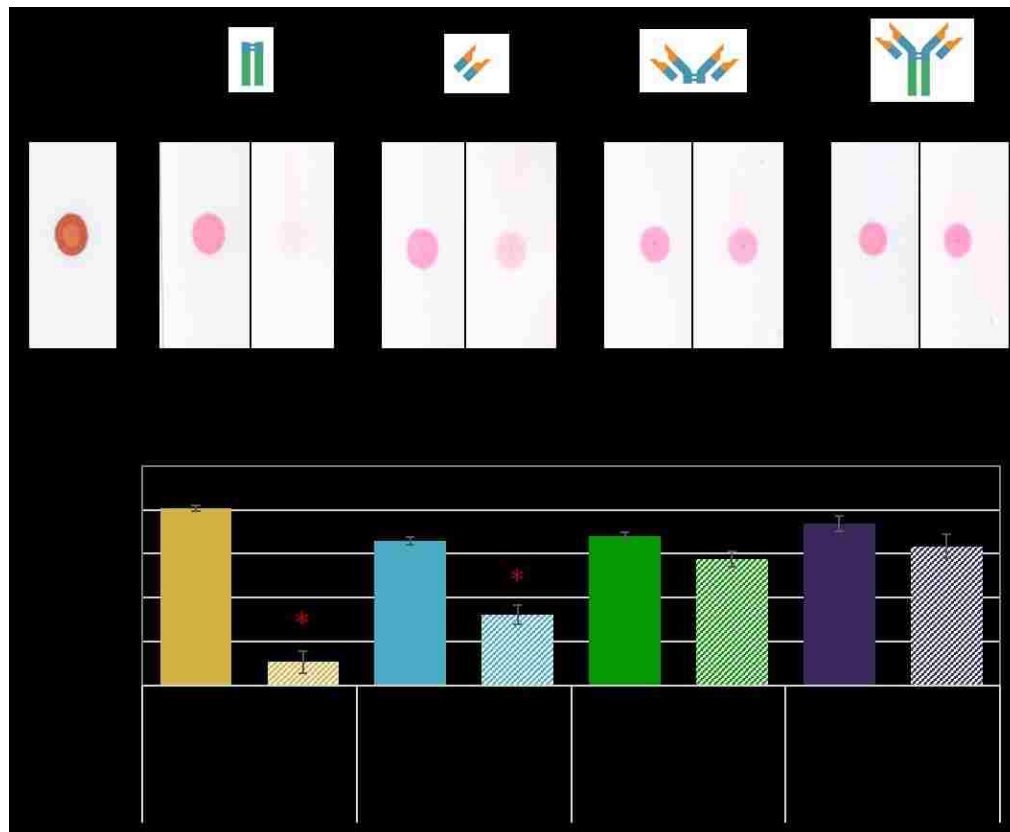


Figure 32. Comparison of protein adsorption strength for IgG and fragments.

Protein adsorption strength for IgG and fragments was evaluated via lateral flow challenge analysis. (A) Images of IgG fragments that were printed onto nitrocellulose, dried overnight, challenged by lateral flow (LF) with PBST (or left unchallenged as no LF control), and stained with Ponceau S to visualize the protein spot. All proteins were spotted at 2.3 mg/mL, with 500 nL per spot. (B) Spot intensities (normalized green-channel pixel intensity), plotted as the mean \pm SD for $n=3$ replicates. Asterisk indicates a significantly greater loss of signal intensity relative to the no LF condition for the given protein, as compared to the loss incurred for IgG ($p < 0.025$ by one-tailed Student's t -test assuming unequal variance).

While these results are only preliminary, they highlight the rich screening capability of this protein spot analysis method. Further studies are needed to fully elucidate and confirm the orientation of IgG adsorbed to nitrocellulose. Nevertheless, these results suggest that paper-based assay performance could be improved by better commanding the immobilization and orientation of IgG on the membrane surface. These results therefore further support the need for a nitrocellulose anchoring protein that can be used to mediate robust, orientation-specific immobilization of any capture agent.

3.6. pH Dependence of Protein Adsorption

In order to focus on particular protein property of interested for identifying a potential nitrocellulose-binding anchor protein (section 3.7), we applied the lateral flow challenge and protein spot analysis methods to a series of proteins across a range of pH values. In this way, we aimed to generate an in-depth understanding of the interplay between pH, pI, and protein charge with regard to adsorption. Specifically, we hoped to either support or refute the model proposed by Přistoupil *et al.* [129] (section 2.4.3, Figure 14).

3.6.1. Methods

Lateral Flow Challenge and Protein Spot Analysis

For this work, primarily the initial lateral flow challenge method was used (section 3.2.1). In most cases, proteins were hand spotted. For the final streptavidin test, the full protein spot analysis method was used (section 3.2.2).

Isoelectric Focusing (IEF) Gel

The isoelectric focusing (IEF) gel was run using our advanced IEF system (SCIE-PLAS #IEF-SYS, Cambridge, United Kingdom) that includes a cooling plate with chiller system (PolyScience #LM61GX1A110C, Niles, IL) and a high-voltage power supply (Consort #EV232, Turnhout, Belgium). The SERVA IEF PRECOTES starter kit (SERVA #39060.01, Heidelberg, Germany) was used, which contained all required reagents and materials for running the gel.

The following eight proteins were run on the gel. For each protein, a 20- μ L sample was prepared at 0.5 mg/mL in H₂O.

- Regular recombinant streptavidin (SA), Thermo Scientific #21125, stock @ 10 mg/mL
- Natural SA from *Streptomyces avidinii*, Sigma-Aldrich #S4762, stock @ 10 mg/mL
- Avidin, Thermo Scientific #21121, stock @ 10 mg/mL
- NeutrAvidin, Thermo Scientific #31000, stock @ 10 mg/mL
- Mutant SA, AbCam #ab51404, stock @ 3.04 mg/mL
- Mutant SA, iPOC #RP-9000, stock @ 3.76 mg/mL
- AlexaFluor488-SA, Life Technologies #S-11223, stock @ 2 mg/mL
- FITC-IgG, Sigma-Aldrich #F0257, stock @ 0.5 mg/mL (no dilution made)

The IEF system was set up according to the protocol provided by the manufacturer, as illustrated in Figure 33. The test lanes of the SERVA gel were each loaded with 15 μ L of the given protein, in the

order listed above. The outside two lanes and the center lane were each loaded with 5 μL of the IEF standard.

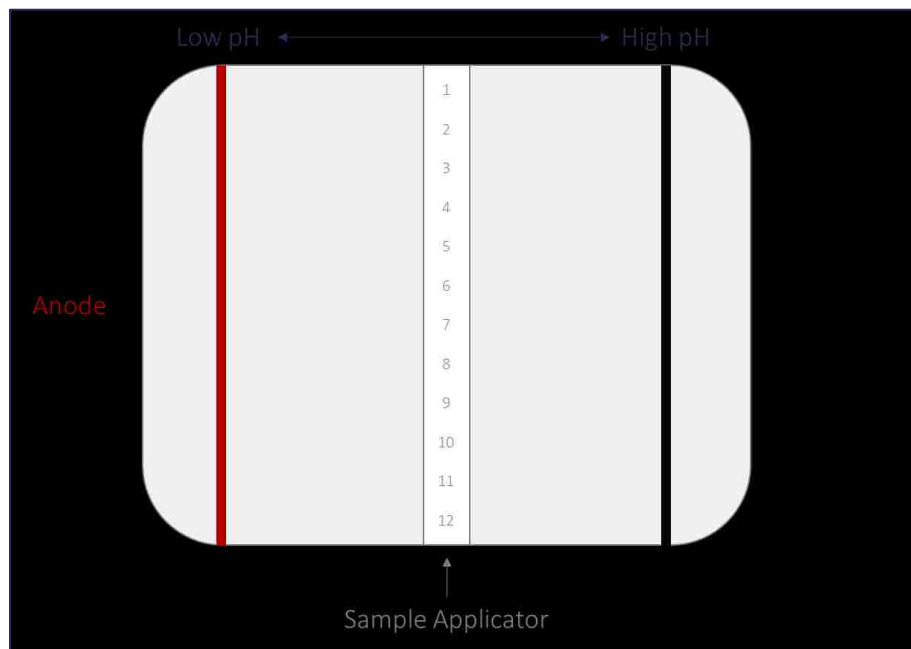


Figure 33. Schematic of the IEF system.

Schematic illustration of the IEF system used to verify isoelectric points of the streptavidin/avidin proteins.

The gel was then run according to the protocol provided by the manufacturer, provided in Table 4.

Table 4. Power supply protocol used to perform the isoelectric focusing.

The power supply protocol for running an IEF gel was provided by the manufacturer.

Step	Voltage (V)	Current (mA)	Power (W)	Time (min.)	Total (V·h)
1	300	53	16	20	100
2	600	27	16	20	300
3	1000	16	16	30	800
4	1200	13	16	30	1400
5	1500	11	16	30	2150
6	2000	8	16	60	4150

The gel was then fixed in 12.5% trichloroacetic acid (TCA) overnight. Note that the protocol recommends 20% TCA for 20 minutes, but this protocol was altered due to the stock of TCA we had on hand and the need to wait until morning to stain the gel. The next day, the gel was stained with Coomassie Brilliant Blue (CBB) using the following protocol:

- Stain
 - 0.1% (w/v) CBB R-250 in {40% methanol, 10% glacial acetic acid, 50% H₂O}
 - 1 x 30 min.

- Destain
 - 40% methanol, 10% glacial acetic acid, 50% H₂O
 - 2 x 30 min. (with Kim wipes)

The gel was then imaged using the Bio-Rad Gel Doc EZ imager using the white sample tray and a 0.7-second exposure time.

3.6.2. Results and Discussion

pH Dependence of BSA Adsorption

Since we had only spotted BSA at pH 7.4 in the previous experiments (section 3.3), the goal of this experiment was to test BSA adsorption to nitrocellulose for spotting buffers with a range of pH values. We were especially interested in testing lower pH values, since the pI of BSA is around 5 [170,171], and there are reports in the literature that protein adsorption is optimized when spotting is performed at a pH that is near the pI [172,173].

To perform this experiment, we prepared solutions of BSA (Sigma-Aldrich #A7030) at 5 mg/mL in six different McIlvaine's buffers (mixtures of citric acid and sodium phosphate) [174] at pH 3, 4, 5, 6, 7, and 8. We also aimed to compare protein adsorption to two different types of nitrocellulose membrane, Millipore HFB135 and GE FF60 (commercial-grade), in order to determine how similarly they behave. We therefore cut six-leg comb devices from each membrane using a CO₂ laser cutter and spotted the nitrocellulose devices with the six different BSA solutions, using 1- μ L hand spots per leg. The spotted devices were allowed to dry overnight at room temperature under desiccation before testing. The robustness of adsorption was probed via the lateral flow challenge assay, using challenge solutions of H₂O, PBS, and PBST, as well as the no-flow control. After lateral flow challenge, all devices were stained for protein content with Coomassie Brilliant Blue. The resulting devices (one set of two replicates) are shown in Figure 34, and the corresponding normalized, local background-corrected, red-channel pixel intensities are plotted in Figure 35 as the mean +/- standard deviation of the n=2 replicates for each condition.

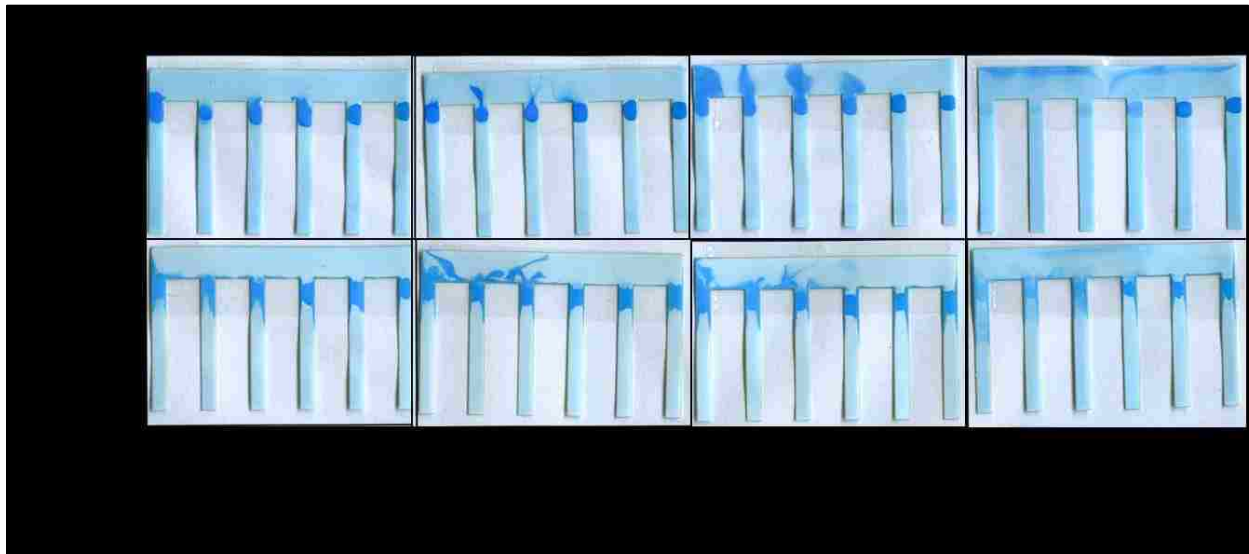


Figure 34. BSA adsorption to nitrocellulose as a function of the pH of the spotting buffer.

Spotted proteins were challenged with three different lateral flow conditions, which are compared to a no-LF control. Only one replicate set (of two) is shown for each membrane type tested (Millipore HFB135 and GE FF60).

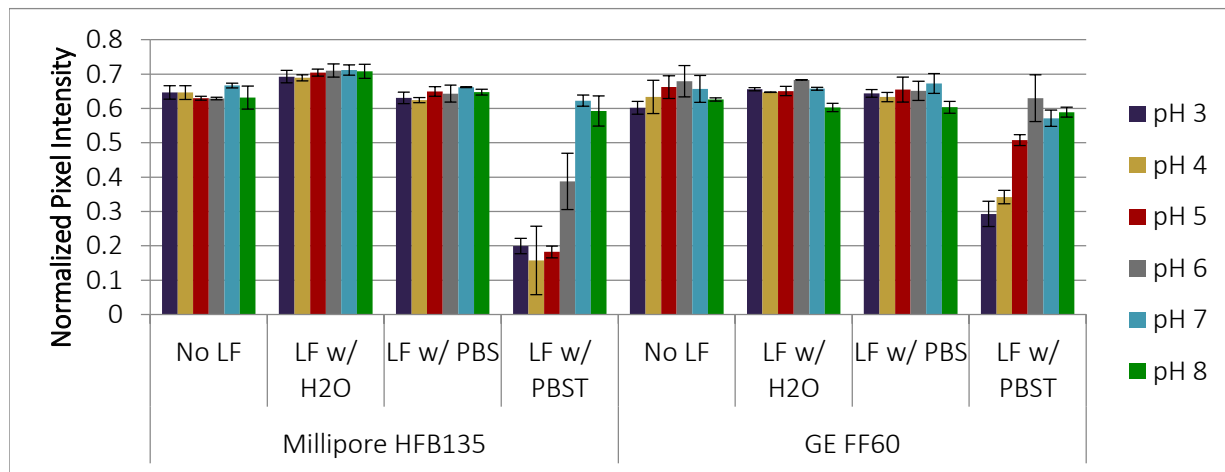


Figure 35. Quantification of signal intensity for BSA adsorption vs. pH.

Normalized red-channel pixel intensities corresponding to the protein spots in Figure 34, used to test the effect of spotting buffer pH on BSA adsorption to two types of nitrocellulose membranes (Millipore HFB135 and GE FF60). Data are plotted as the mean +/- SD of n=2 replicates.

From these results, we initially observe less desorption and streaking of BSA than in the previous experiment performed using BSA at pH 7.4 on GE FF80HP (mostly equivalent to GE FF60) nitrocellulose. We presume that the reason for these differences is the discrepancy in spotting methods used for these experiments. In the previous experiment, the piezoelectric spotter was used to pattern precise spots that were smaller than the width of the nitrocellulose strip, which allowed flow to proceed around the spots. In this case, the protein was spotted by hand using 1- μ L spots

that covered the full width of the strip, due to the slow adsorption rate of the BSA. Also, the concentration of BSA used for this experiment (5 mg/mL) was higher than that in the previous experiment (2.5 mg/mL). These spots therefore are likely to have impeded flow, especially for the GE FF60 membranes, which have inferior wettability to Millipore HFB135, as evidenced by the irregular shapes of protein spots on this membrane. Additionally, the fluid front did not even reach the top of the legs in several cases for this membrane. Overall, these flow problems resulted in less dramatic desorption of BSA than observed in previous experiments.

BSA was still sensitive to desorption, though, especially under lateral flow with PBST. Under this condition, the pH-dependence of the spotting buffer is most visible; in particular, BSA is much more resistant to stripping when spotted at the higher pH buffers tested (pH 7 and 8) than the more acidic buffers, which is consistent for both membranes tested. This result therefore contradicts adsorption literature that states optimal adsorption occurs at pH values near the pI of the protein [172,173]. Instead, it appears that the adsorption of BSA becomes much stronger as the pH is increased above the pI of the protein. At first consideration, this pH-dependence seems to be a charge effect, and suggests that spotting at a pH that is on the correct side of the pI and allows the protein to be charged complementary to the membrane provides the most robust adsorption. However, the observed trend is the opposite of that anticipated, since negatively charged BSA (at pH 7 and 8) is not expected to adsorb robustly to nitrocellulose, which is also described as negatively charged, at least at neutral pH [129,130]. The robust adsorption of BSA at these pH values may therefore be more reasonably attributed to pH-induced conformational change in the protein, which is known to occur at pH 8 to 9 for BSA [170]. To help further elucidate the effect of pH on protein adsorption, we therefore explored additional proteins, as described in the following sections.

pH Dependence of Streptavidin – Initial Test

In the previous experiment that revealed poor streptavidin adsorption to nitrocellulose, the protein was spotted in PBS at pH 7.4. This may not have been the optimal pH for spotting streptavidin, whose pI is between 5 and 6 [175]. We therefore tested streptavidin adsorption for spotting buffers with a range of pH values, as was done previously for BSA. In addition to understanding and optimizing streptavidin adsorption, this experiment allowed us to compare the pH-dependence of adsorption for two proteins (streptavidin, tested here, and BSA, tested previously) with different isoelectric points in order to further ascertain how protein pI, spotting buffer pH, and adsorption are related.

For this experiment, six-leg comb devices were cut from nitrocellulose using a CO₂ laser cutter. As before, we tested both Millipore HFB135 and GE FF60 (commercial-grade) nitrocellulose, to further explore differences in the membranes from the two different manufacturers. We prepared solutions of streptavidin (Sigma-Aldrich #85878) at 5 mg/mL in six different McIlvaine's buffers (mixtures of citric acid and sodium phosphate) [174] at pH 3, 4, 5, 6, 7, and 8. Devices were spotted with 1- μ L hand spots of each solution and dried overnight at room temperature under desiccation before testing. As usual, the robustness of adsorption was probed via the lateral flow challenge assay followed by Coomassie staining. Three lateral flow challenges were tested (H₂O, PBS, and PBST) using 50 μ L per leg, along with a no-flow control. The resulting devices (one of two replicate sets) are shown in Figure 36, and the corresponding normalized, local background-corrected, red channel pixel intensities are plotted in Figure 37 as the average \pm standard deviation of the n=2 replicates for each condition.

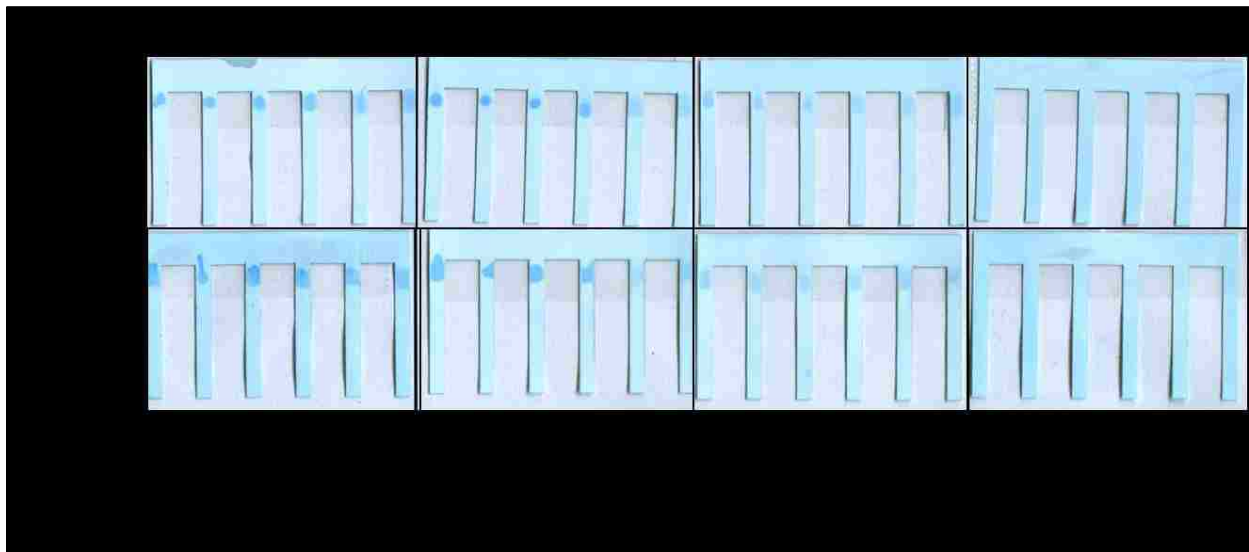


Figure 36. Initial testing of streptavidin adsorption vs. pH.

Streptavidin adsorption to nitrocellulose as a function of the pH of the spotting buffer. Spotted proteins were challenged with three different lateral flow conditions, which are compared to a no-LF control. Only one replicate set (of two) is shown for each membrane type tested (Millipore HFB135 and GE FF60).

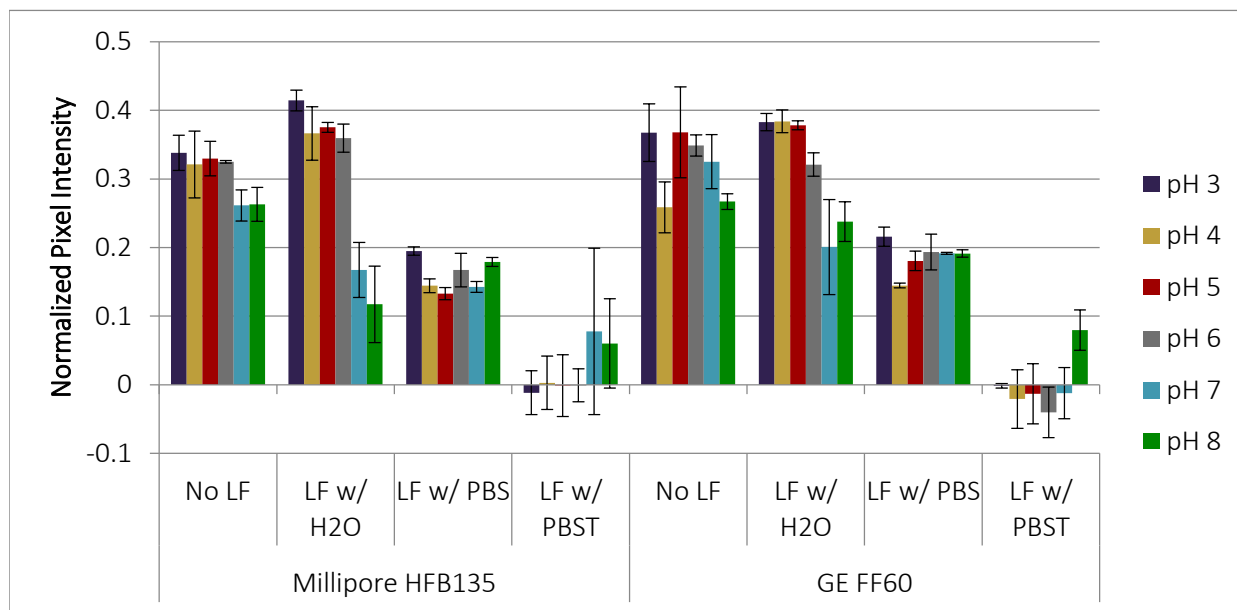


Figure 37. Initial testing of streptavidin adsorption vs. pH, signal intensities.

Normalized red-channel pixel intensities corresponding to the protein spots in Figure 36, used to test the effect of spotting buffer pH on streptavidin adsorption to two types of nitrocellulose membranes (Millipore HFB135 and GE FF60). Data are plotted as the mean \pm SD of n=2 replicates.

From these results, we observe a slight effect of the pH of the spotting buffer on the robustness of adsorption, at least for the range tested. In particular, streptavidin adsorption appears more robust when spotting in more acidic pH buffers and less robust (more prone to stripping) when spotted in the higher-pH buffers tested (up to pH 8). These results were consistent for both membranes tested, suggesting that the two nitrocellulose membranes are similar enough physically to provide the same pH-dependence of adsorption for a given protein.

Comparing these pH-dependence results for streptavidin to those obtained previously for BSA, we observe that streptavidin yields overall weaker adsorption to nitrocellulose for the concentration (5 mg/mL) and pH values (3-8) tested. Interestingly, streptavidin also features a transition point in pH at which adsorption changes from weak to adequate. This transition point occurs around pH 6-7, which is above, but close to, the known pI of streptavidin (5-6). Therefore, for both BSA and streptavidin, the pI of the protein appears to be related to the transition point of adsorption. Unlike BSA, however, streptavidin adsorption shifts from better adsorption below the transition point to worse adsorption above the transition point. This pattern of decreasing streptavidin adsorption for increasing pH is more intuitive than the opposite pattern observed for BSA, since we would expect positively charged proteins to adsorb more efficiently to nitrocellulose, which is net negatively charged at neutral pH. For streptavidin, it appears that a transition occurs around the pI of the

protein, below which adsorption becomes stronger, which is consistent with the theoretical model proposed by Přistoupil *et al.* [129] (see section 2.4.3). This transition therefore corroborates the hypothesis that the charge of the protein is important for adsorption, and that spotting at a pH that is on the correct side of the pI and allows the protein to be charged complementary to the membrane provides more robust adsorption than spotting at a pH that is near the pI. As for the discrepancy in results for BSA and streptavidin, there could be other physical properties that account for the different patterns of pH-dependence on adsorption, since they are two very different proteins. In particular, the proteins could exhibit varying exposure of their hydrophobic regions, which would be consistent with the pH-induced conformational change in BSA [170], discussed above. To focus more specifically on the property of charge, we therefore tested a panel of proteins that are physically similar in other ways, but vary in pI, as discussed next.

pH Dependence of Streptavidin Protein Series

To build upon the previous experiments in which the adsorption of BSA and streptavidin were tested as functions of pH, we performed a more focused set of experiments to test the pH-dependence of a series of related proteins. In particular, we evaluated the nitrocellulose adsorption of four different streptavidin (SA)-related proteins.

Table 5. Proteins evaluated as part of the streptavidin/avidin protein series.

Key properties of the four proteins of the avidin series that was used to test the pH-dependence of protein adsorption to nitrocellulose. Adapted from [175].

Protein	MW	pI	Notes
Streptavidin (natural)	60 kDa (tetramer)	~5	Isolated from <i>Streptomyces avidinii</i> ; low non-specific binding; higher affinity for conjugated biotin than avidin
Streptavidin (recombinant)	53 kDa (tetramer)	6.8-7.5	Recombinant form is slightly smaller than natural form and at near-neutral pI
Avidin	67 kDa (tetramer)	~10	Purified from chicken egg whites; inexpensive; 30% sequence identity with streptavidin, but almost identical folded structure; glycosylated, positively charged; higher non-specific binding; higher affinity for free biotin than streptavidin
NeutrAvidin	60 kDa (tetramer)	6.3	De-glycosylated avidin; more comparable to size, pI, and non-specific binding of streptavidin

The four proteins of this streptavidin/avidin proteins series included the following: avidin (Thermo Scientific #21121), NeutrAvidin (Thermo Scientific #31000), natural streptavidin (Sigma-Aldrich #S4762), and recombinant streptavidin (Thermo Scientific #21125). These proteins all have similar

biotin-binding functionality, but differ substantially in their isoelectric points (Table 11), allowing us to investigate this property more deeply.

As before, we prepared solutions of each protein in buffers with a range of pH values. Since the highest pI (10, avidin) exceeded the highest pH achievable with McIlvaine's buffers (pH ~9), we instead used a more disparate set of buffers that allowed us to achieve a range of pH values spanning the isoelectric points of all four proteins. These buffers are listed in Table 6. The total ionic strength of each buffer was held constant at 50 mM by adding the appropriate amount of excess NaCl, as determined by a computational buffer calculator [176]. Each protein solution was prepared at 1 mg/mL and hand-spotted with 1- μ L spots onto six-legged comb devices cut from nitrocellulose using a CO₂ laser cutter. We again tested both Millipore HFB135 and GE FF60 (commercial-grade) nitrocellulose membranes. Devices were dried overnight at room temperature under desiccation before use.

Table 6. Buffer set used to achieve an extended pH range.

List of the six buffers used to test protein adsorption across an extended pH range (2 – 12).

Buffer	pH	Concentration	Buffer pKa	Acid/Base Name	Total Ionic Strength
Phosphate (low pH)	2.0	10 mM	2.15	Phosphoric acid	50 mM
Acetate	4.0	10 mM	4.76	Acetic acid	50 mM
MES	6.0	10 mM	6.21	MES free acid	50 mM
Tris	8.0	10 mM	8.06	Tris base	50 mM
CAPS	10.0	10 mM	10.51	CAPS free acid	50 mM
Phosphate (high pH)	12.0	10 mM	12.33	Na ₂ HPO ₄ ·7H ₂ O	50 mM

As usual, the robustness of protein adsorption was assessed using the lateral flow challenge. Three challenge solutions were tested (H₂O, PBS, and PBST), using 50- μ L of challenge solution per strip, in addition to a no-flow control set. In all cases, the remaining protein was visualized with Coomassie staining. The resulting devices (one of three replicate sets) are shown in Figure 38 for both the HFB135 and FF60 membranes. Unfortunately, due to corruption of the files, the Millipore HFB135 devices could not be quantified. The FF60 devices were successfully quantified, however, and the corresponding normalized, local background-corrected, red channel pixel intensities are plotted in Figure 39 as the average +/- standard deviation of the n=3 replicates for each condition.

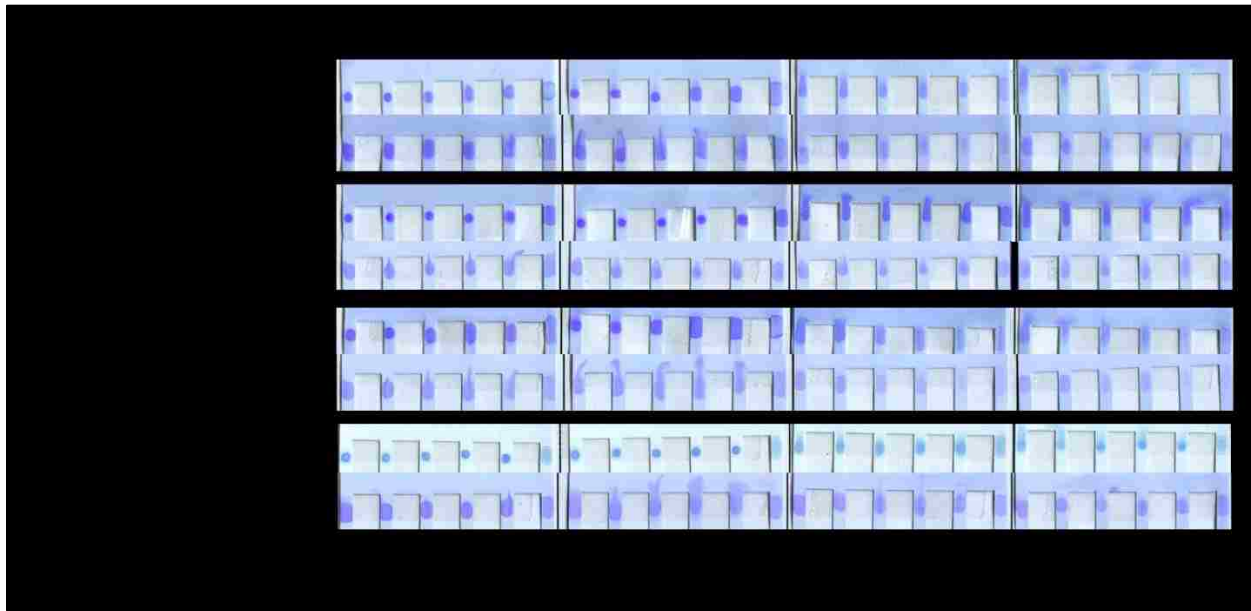


Figure 38. Protein adsorption for the streptavidin/avidin protein series.

Adsorption of four avidin-based proteins as a function of the pH of the spotting buffer, assessed via lateral flow challenge. Adsorption was tested for both Millipore HFB135 and GE FF60 nitrocellulose membranes. One set of three replicate sets is shown here. *The HF135 set of membranes for the avidin protein were scanned three days after the experiment, due to a problem with the initial file, which is why their coloration is slightly different than the other membranes.

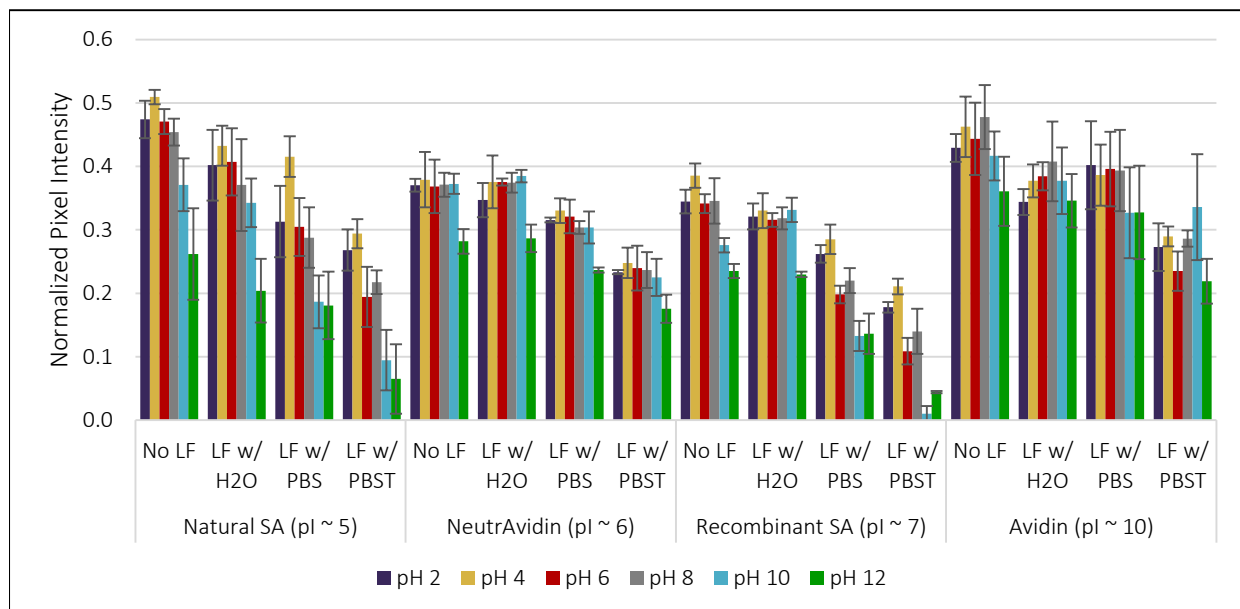


Figure 39. Protein adsorption for the streptavidin/avidin protein series, signal intensities.

Normalized red-channel pixel intensities corresponding to the protein spots in Figure 38, used to test the effect of spotting buffer pH on adsorption of four avidin-based proteins to GE FF60 nitrocellulose (Millipore HFB135 data could not be quantified). Data are plotted as the mean +/- SD of n=3 replicates.

These results corroborate previous findings that the robustness of protein adsorption appears to transition from weak to strong (or at least adequate) at pH values near the pI of the given protein. This transition is fairly gradual, however, making it difficult to verify its exact pI-dependence. Natural streptavidin (pI ~ 5), NeutrAvidin (pI ~ 6), and recombinant streptavidin (pI ~ 7) all have pIs that are relatively close, resulting in relatively similar transition curves of adsorption across the range of pH values tested. Avidin (pI ~ 10) provides a useful point of comparison, though, as its high pI is at or above the pH of five of the six buffers tested. In this case, adsorption is fairly stable for all five lower-pH buffers (2-10), with the most desorption observed for the pH 12 buffer. Presumably, if even higher-pH buffers could be tested, more desorption would occur and the full transition curve would be evident. For all four streptavidin-related proteins, adsorption is more robust when the protein is spotted in more acidic buffer, transitioning to weaker adsorption for increasing pH of the spotting buffer. This trend is again consistent with our expectation that positively charged proteins should interact more favorably with nitrocellulose, which is net negatively charged (at least at neutral pH). However, this trend leaves the opposite results observed for BSA unresolved based on this electrostatic interpretation. Currently, we hypothesize that the incongruity of the BSA result is due to a pH-dependent conformational change in BSA [170], which allows increased hydrophobic interaction with the nitrocellulose that dominates over the electrostatic forces. Overall, this streptavidin/avidin protein series strongly supports the adsorption model proposed by Přistoupil *et al.* [129] (section 2.4.3).

Isoelectric Point Confirmation by IEF

To verify the theoretical isoelectric points of the streptavidin/avidin protein series, the isoelectric points were assessed experimentally via isoelectric focusing (IEF). In addition to the four streptavidin/avidin proteins, two versions of nitrocellulose-binding mutant streptavidin (SA), a fluorescently labeled streptavidin, and a fluorescently labeled IgG protein were also evaluated. The ten proteins assessed are listed below:

- Regular recombinant streptavidin
- Natural streptavidin
- Avidin
- NeutrAvidin
- Mutant streptavidin, AbCam
- Mutant streptavidin, iPOC
- AlexaFluor488-streptavidin
- FITC-IgG

The resulting gel, shown in both grayscale and false color, is shown in Figure 40 and Figure 41, respectively. Note that we observed a strange streak spanning almost all lanes of the gel, which we cannot fully explain. We believe this could be excess Bayol F, which was accidentally applied to the wrong side of the gel before the mistake was corrected, and which therefore may have gotten in the gel and subsequently focused.

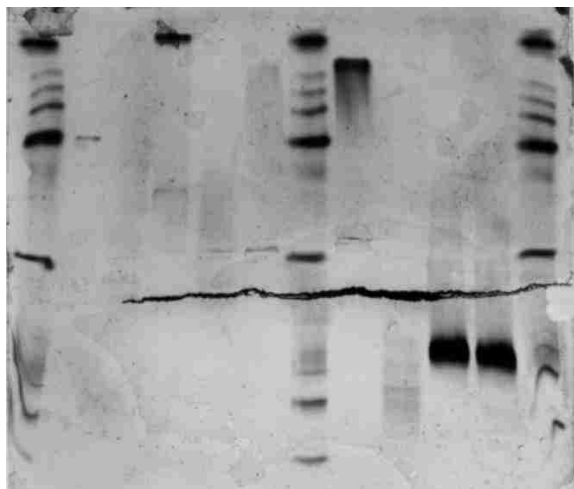


Figure 40. IEF gel, in grayscale.
Resulting IEF gel for the isoelectric point analysis of the streptavidin/avidin proteins, among others. The grayscale image provides the best visualization of high-density bands.

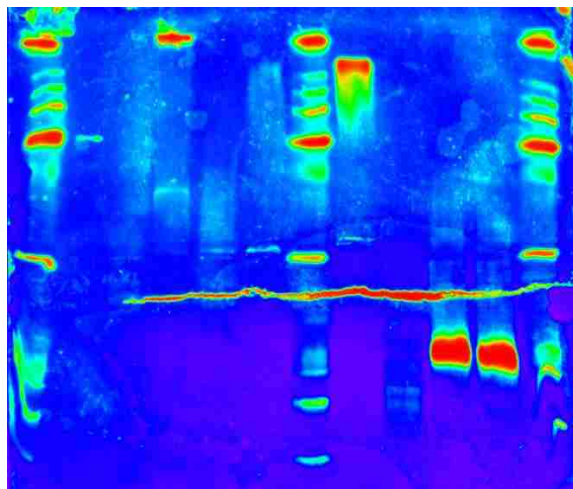


Figure 41. IEF gel, in false color.
Resulting IEF gel for the isoelectric point analysis of the streptavidin/avidin proteins, among others. The false color image provides the best visualization of low-density bands.

In order to determine the isoelectric points of the proteins, we first needed to map our IEF marker lane (used center one only, since lanes 1 and 12 were distorted) with the pI information provided by the manufacturer. This mapping is shown in Figure 42. This mapping was then applied to our full IEF gel, as shown in Figure 43.

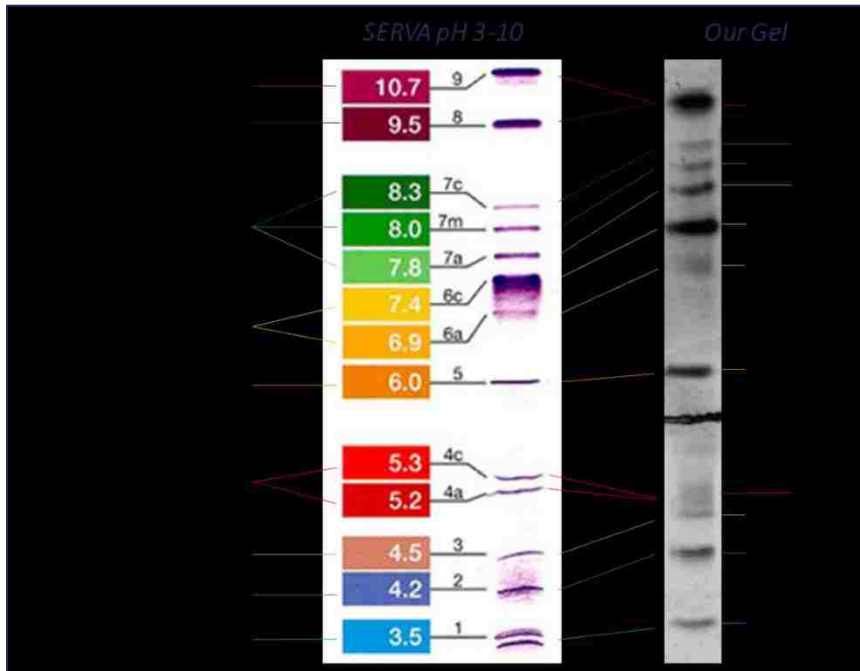


Figure 42. Mapping of IEF gel standard markers.
 Mapping of the manufacturer-provided locations of the IEF markers with the actual locations on our gel.

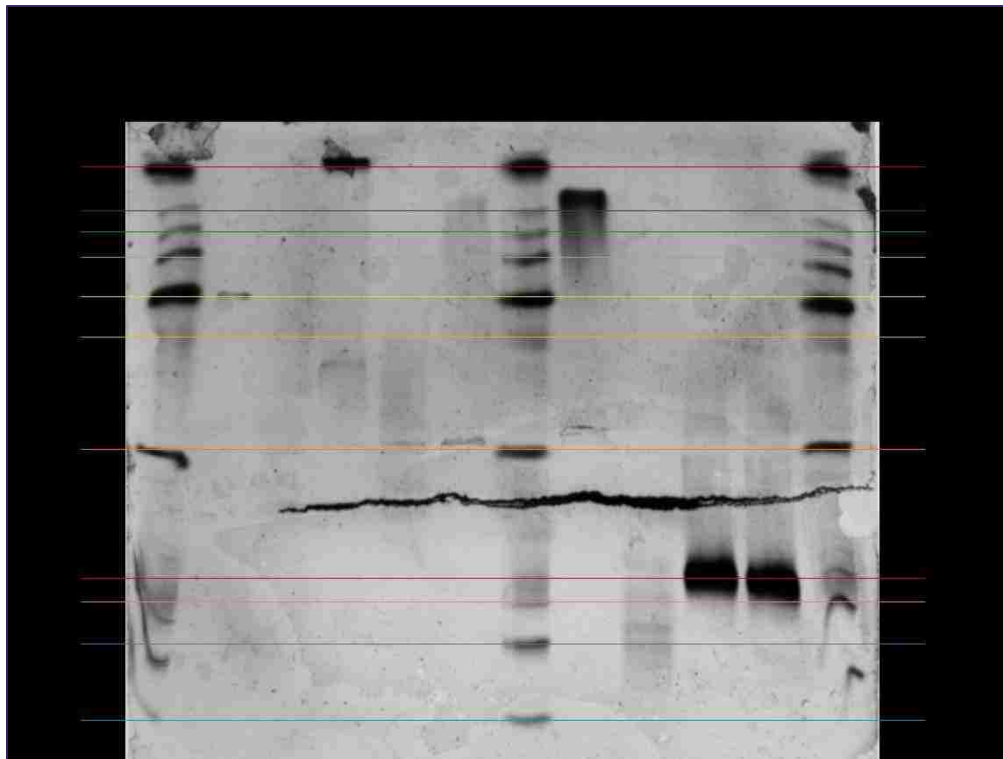


Figure 43. IEF gel for the analysis of streptavidin/avidin protein pIs.
 The resulting IEF gel, with pI values of the standard protein markers indicated.

Based on this gel, we were able to determine approximate isoelectric points for all proteins except natural streptavidin, which either did not focus well enough or was at a lower concentration than expected. The pI values extracted from this gel are listed in Table 7. These results mostly match the expected pI results, when literature- or manufacturer-reported values were known. The one very surprising result is that the AbCam mutant SA, which has been functionally superior to iPOC mutant SA in terms of the flu hemagglutinin assay, either focused poorly or was too dilute. The iPOC mutant SA gave a much darker, better-focused protein band, which was unexpected.

Table 7. Comparison of reported and experimental isoelectric points.

List of the isoelectric points determined experimentally by IEF and comparison with reported values.

Protein	Rec. SA	Nat. SA	Avidin	Neutr-Avidin	AbCam Mut. SA	iPOC Mut. SA	488-SA	FITC-IgG
Reported pI	6.8-7.5	~5	~10	6.3	n/a	9.18	n/a	n/a
pI by IEF	7.4	?	10	6-7?	~8?	8-9	4-5	5

Overall, this IEF gel allowed us to experimentally verify the reported pI values of the streptavidin/avidin series of proteins, in addition to the iPOC mutant streptavidin protein. Given the cumbersome nature of this experiment and the only mediocre focusing of the gel, we did not pursue further IEF testing for additional proteins.

Improved pH Dependence Testing for Recombinant Streptavidin

Finally, we applied the fully protein spot analysis method to acquire comprehensive protein adsorption data about a single streptavidin protein: regular, recombinant streptavidin. (Time constraints prevented this degree of follow-up study on all four proteins.) Given the useful lateral flow challenge data already gathered above, we wanted to determine if further insights could be gathered from the full protein spot analysis method, using piezoelectric spotting instead of hand spotting. Therefore, in collaboration with undergraduate student Karen Keniston, we studied the adsorption of recombinant streptavidin (Thermo Scientific #21125) to nitrocellulose (GE FF80HP, 0.8 cm x 5 cm strips).

Recombinant SA was spotted at 0.5 mg/mL in the extended range buffers (Table 6) at pH 2, 4, 6, 8, 10, or 12. Spots were generated using 1000 drops per spot, at 500 pL/drop, for a total of 500 nL/spot. Red food coloring diluted 1:10 in H₂O was also spotted to visualize the full wet-out area (six replicates). Lateral flow challenge was performed with PBS and PBST, in addition to the no LF control, with 3 replicates per condition. Protein was visualized by Ponceau S staining. A

representative test spot for each condition is provided in Figure 44A. The spot sizes (relative to the mean size of the full wet-out area) are plotted in Figure 44B, and the normalized green-channel pixel intensities are plotted in Figure 44C, each as the mean \pm SD of n=3 replicates per condition.

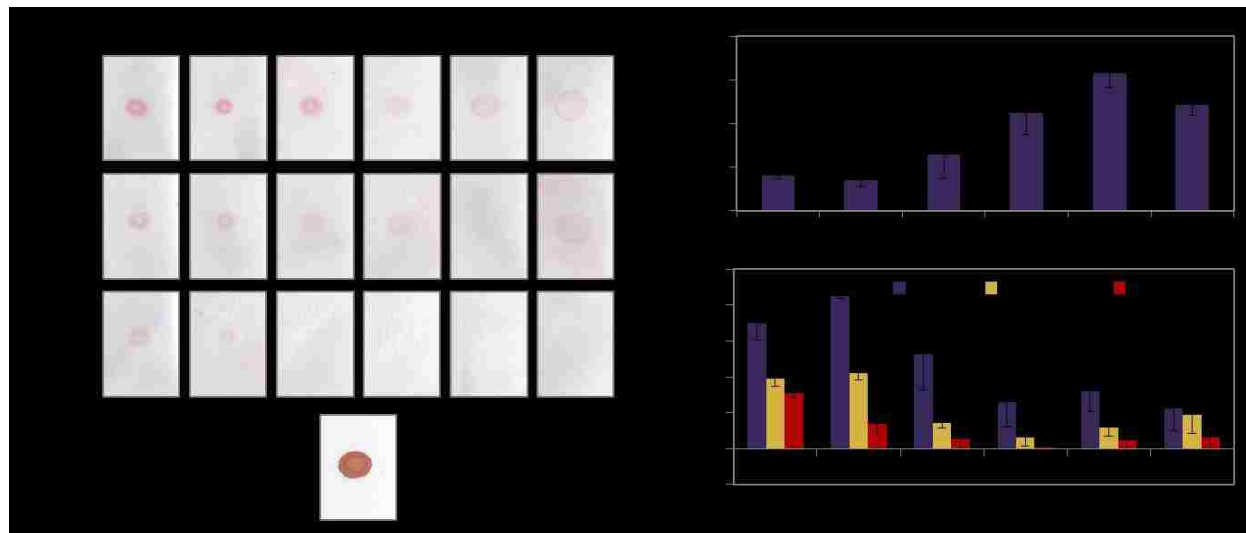


Figure 44. Full protein spot analysis for streptavidin adsorption vs. pH.

In contrast to the previous streptavidin analyses, this test was done using the piezoelectric spotter for precise volume control to enable to full protein spot analysis method. (A) Representative test spot for each spotting pH (2-12) and lateral flow (LF) challenge condition. The red food coloring (RFC) represents the full wet-out area for the volume spotted (500 nL). (B) Spot areas for each condition relative to the wet-out area defined by the RFC, plotted as the mean \pm SD of n=3 replicates. (C) Normalized green-channel pixel intensity for each test spot, plotted as the mean \pm SD of n=3 replicates.

The Ponceau S staining for this experiment was not ideal (longer staining time needed to darken spots, and methanol likely needed to improve penetration of the stain into the protein spots), but these results confirm the previously observed pH-dependence of recombinant streptavidin adsorption. In particular, with this full protein spot analysis method, we can clearly see the spot sizes transition from small sizes at low pH to larger sizes equivalent to the wet-out area at high pH. This transition point occurs roughly between pH 6 and pH 8, which is exactly where the pI for this protein is located. Therefore, these results provided the clearest support for the pH-dependent model of protein adsorption proposed by Přistoupil *et al.* [129] (section 2.4.3). We therefore validated this model as our working model of protein adsorption. Next, we applied this model and the insights gained from these protein adsorption studies for the identification of nitrocellulose-binding anchor proteins.

3.7. Identification of Nitrocellulose-Binding Proteins

Motivated by the case of our stem region flu binder, which does not adsorb well to nitrocellulose, as well as the highly variable adsorption of proteins in general, we aimed to identify an anchor protein that does bind robustly to nitrocellulose. This anchor protein could then be fused to our flu binder—or coupled to any recombinant affinity reagent of interest—to promote immobilization. To do so, we screened a series of recombinant proteins designed by the Baker lab for other purposes, but that harbored some of the key properties for which we were searching. These proteins included a set of five globular proteins (Designs I-V) engineered to have ideal energy landscapes and therefore high stability [177]. Additionally, we screened a 3-helix bundle protein designed to be ultra-stable [178] and have an ideal coating of positive charge, due to its high lysine content (25% lysine by amino acid). While we did not know if these proteins would necessarily be strong adsorbers, their stability was an attractive starting feature, especially for the long-term, ambient storage of paper-based devices that might utilize these anchor proteins. The mid-to-high isoelectric points of these proteins (see Table 8 and Table 9) also matched the Přistoupil model criteria for theoretically good adsorbers (section 2.4.3). We had planned to do further protein engineering, if needed, to optimize the nitrocellulose-binding capability of these proteins, but our screening identified two strong anchor protein candidates, as described below.

3.7.1. Methods

Lateral Flow Challenge and Protein Spot Analysis

For this screening, the full protein spot analysis method (section 3.2.2) was used in almost all cases. However, the initial 3-helix protein screening involved some hand spotting and therefore a focus on the initial lateral flow challenge protocol only (section 3.2.1). Much of this work was done in collaboration with undergraduate student Karen Keniston.



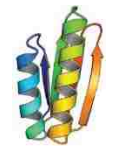

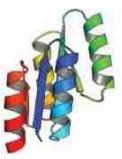
3.7.2. Results and Discussion

Initial Screening of Design I-V Globular Proteins

To begin the search for a nitrocellulose-binding anchor protein, we first screened five recombinant proteins from the Baker lab. These five proteins, listed in Table 8, were computationally designed to have ideal energy landscapes and be highly stable, with all five proteins exhibiting melting temperatures T_m above 95 °C [177]. These designed (D) proteins are denoted as DI-DV.

Table 8. Five globular proteins (DI-V) screened for nitrocellulose binding.

List of the five stable proteins designed by the Baker lab [177], with key properties of each. These proteins were screened as candidates for nitrocellulose-binding anchor proteins.

Designed Protein (Full Name)	PDB ID	Length (AA)	MW (kDa)	pI	T _m (°C)	Protein Structure
Design I (DI_I_5)	2KL8	86	10.1	6.32	>>95	
Design II (DI_II_10)	2LV8	109	12.9	6.10	>>95	
Design III (DI_III_14)	2LN3	82	9.6	5.63	>>95	
Design IV (DI_IV_5)	2LVB	111	12.5	6.72	≈95	
Design V (DI_V_7)	2LTA	109	12.9	6.34	>95	

To test the nitrocellulose adsorption of these five globular proteins, we used the protein spot analysis method. Using the piezoelectric spotter, each protein was spotted onto 0.8-by-5-cm strips of GE FF80HP nitrocellulose. IgG (AbCam mouse anti-HA #ab8262) was also spotted for comparison. All proteins were spotted at 1 mg/mL in PBS, and red food coloring (RFC) diluted 1:10 in H₂O was spotted to visualize the full wet-out area (n=6 replicates). All spots were 500 nL (1000 drops x 500 pL/drop). Devices were dried under desiccation overnight before use. Lateral flow challenge solutions of PBS and PBST were used, in addition to no-flow controls. After the LF challenge, the protein spots were visualized by Ponceau S staining. In total, 3 replicates of each protein for each LF challenge condition were tested.

A representative test spot for each condition is provided in Figure 45. These results clearly indicate that the Design I (DI) protein adsorbs to nitrocellulose most robustly out of the five globular proteins, with the smallest spot size and no visible stripping under challenge by PBS or PBST. It even appears to adsorb better than IgG, in terms of both adsorption speed (spot size) and resistance to stripping under the challenge conditions. Three of the other four proteins (DII, DIII, and DV) showed decent adsorption with roughly IgG-like spot sizes in most cases and only partial stripping under LF challenge. The DIV protein showed the worst adsorption, with significant stripping under LF challenge, despite a fairly small initial spot size. For this initial screen, the spot sizes and intensities were not quantified. Instead, the most promising candidate based on this qualitative data, DI, moved onto to further testing and comparison against another anchor protein candidate, the 3-helix bundle protein.

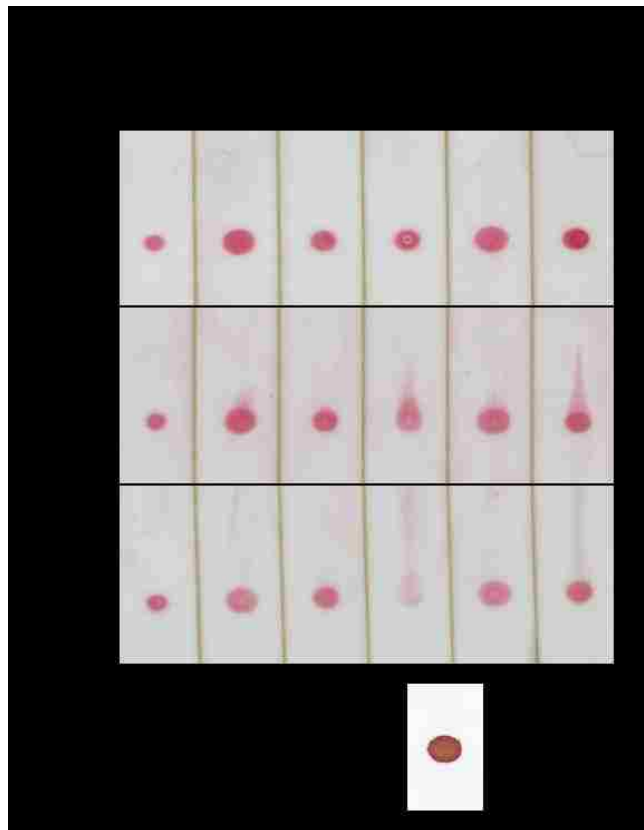


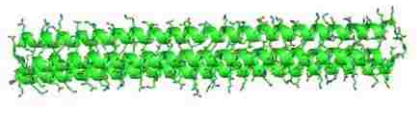
Figure 45. Adsorption screening of DI-V globular proteins. A representative image of each protein spot after LF challenge with PBS, PBST, or no challenge is provided. DI shows the most robust nitrocellulose adsorption of the five proteins.

Initial Screening of 3-Helix Bundle Protein

Next, we screened another promising recombinant protein from the Baker lab, the 3-helix_2 bundle protein (“3-helix”). The 3-helix bundle protein was designed to be ultra-stable, boasting an extrapolated Gibbs free energy of folding of >60 kcal/mol [178]. This high stability partly owes to the idealized coil structure in which charged amino acids are highly localized to the outside of the structure. In particular, the 3-helix protein is 25% lysine by amino acid count, creating a surface coated in positive charge that is theoretically ideal for binding to negatively charged nitrocellulose. The structure of the 3-helix protein and key protein properties are listed in Table 9. In particular, its isoelectric point of 9.4, owing to its high lysine content, made it a very attractive candidate for nitrocellulose binding.

Table 9. 3-helix protein screened for nitrocellulose binding.

Key properties for the 3-helix bundle protein designed by the Baker lab [178]. This protein was screened as a candidate for a nitrocellulose-binding anchor protein.

Designed Protein (Full Name)	PDB ID	Length (AA)	MW (kDa)	pI	T _m (°C)	Protein Structure
3-Helix (3H5L_2)	4TQL	246	29.6	9.40	>>95	

To screen the nitrocellulose binding of the 3-helix protein, we used the protein spot analysis method. The 3-helix protein was spotted at 3, 1, and 0.3 mg/mL in PBS, with 500 nL (100 drops x 500 pL/drop) per spot using the piezoelectric printer. Proteins were deposited onto 0.8-by-5-cm strips of GE FF80HP nitrocellulose. We also compared to IgG (mouse polyclonal IgG, Jackson ImmunoResearch) as an example of a known strong adsorber. Unfortunately, we had difficulty spotting the IgG protein, so it had to be spotted by hand, making its comparison to the 3-helix protein non-ideal. IgG was hand-spotted at 3, 1, and 0.3 mg/mL in PBS using 0.5 μ L per spot, making the volumes for the two proteins equivalent (albeit with different spotting mechanisms). Red food coloring (RFC) diluted 1:10 in H₂O was spotted using the piezoelectric printer to visualize the full wet-out area (n=6 replicates) for the 500-nL volume. Devices were dried under desiccation overnight before use. Lateral flow challenge solutions of PBS and PBST were used, in addition to no-flow controls. After the LF challenge, the protein spots were visualized by Ponceau S staining. In total, 3 replicates of each protein for each LF challenge condition were tested.

One replicate of each protein spot for each condition is shown in Figure 46, along with all six replicates of the red food coloring control. Again, because IgG had to be spotted by hand, 3-helix and IgG cannot be compared directly. However, in comparison to previous spotting experiments, the 3-helix protein spots are very small, indicating that it adsorbs very quickly. It also appears to be quite resistant to stripping by lateral flow challenge. Finally, the increase in protein spot size with increasing concentration of protein further indicates that 3-helix adsorbs rapidly to nitrocellulose. Given the non-ideal comparison of different spotting methods for the two proteins, the results were not quantified. Instead, 3-helix was verified as a very promising anchor protein candidate and subjected to further adsorption, described next.

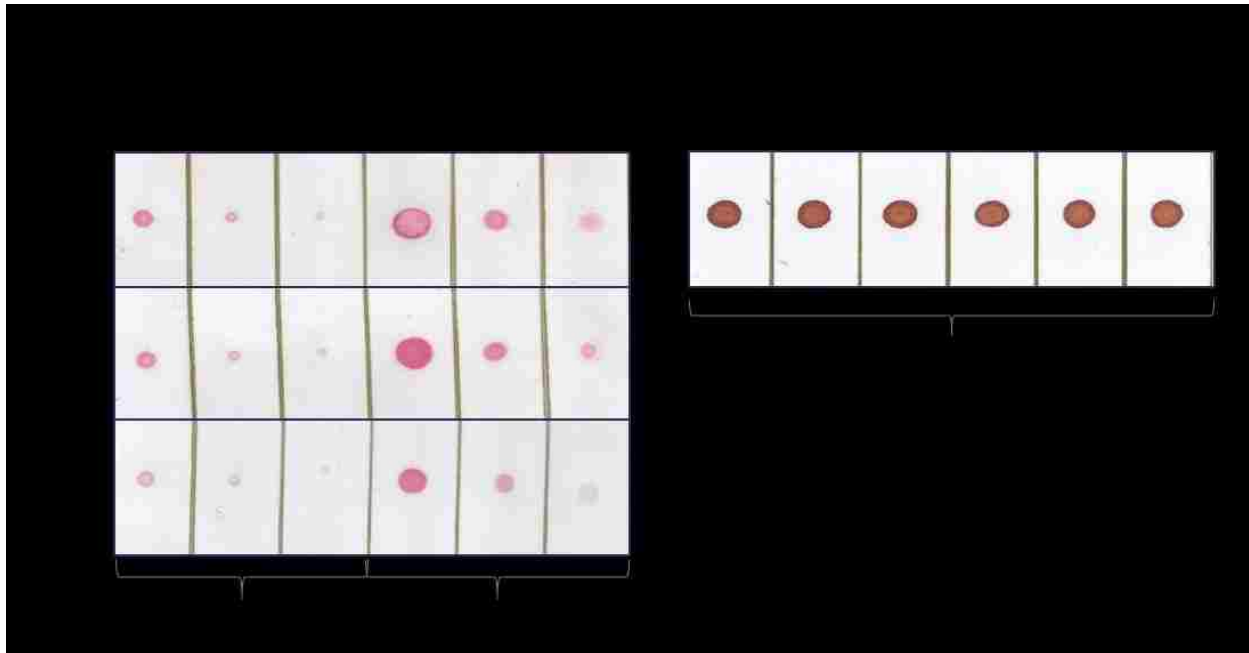


Figure 46. Adsorption screening of 3-helix protein.

Nitrocellulose adsorption of the 3-helix protein is compared to IgG. A representative image of each protein spot after LF challenge with PBS, PBST, or no challenge is provided. All six replicates of the red food coloring are shown.

pH Dependence of 3-Helix Protein Adsorption

Since the 3-helix protein showed such promising adsorption results in the previous two experiments, we further investigated its adsorption by evaluating its ability to adsorb across a range of pH values. We aimed to understand the pH-dependence of 3-helix adsorption in order to both understand the limits of its adsorption and confirm that its strong electrostatic interaction with the membrane is a primary factor in its adsorption.

3-helix protein was spotted at 0.5 mg/mL in the extended range buffers (Table 6) at pH 2, 4, 6, 8, 10, or 12. Spots were generated using 1000 drops per spot, at 500 pL/drop, for a total of 500 nL/spot. Red food coloring diluted 1:10 in H₂O was also spotted to visualize the full wet-out area (six replicates). Lateral flow challenge was performed with PBS and PBST, in addition to the no LF control, with 3 replicates per condition. Protein was visualized by Ponceau S staining. A representative test spot for each condition is provided in Figure 47A. The spot sizes (relative to the mean size of the full wet-out area) are plotted in Figure 47B, and the normalized green-channel pixel intensities are plotted in Figure 47C, each as the mean +/- SD of n=3 replicates per condition.

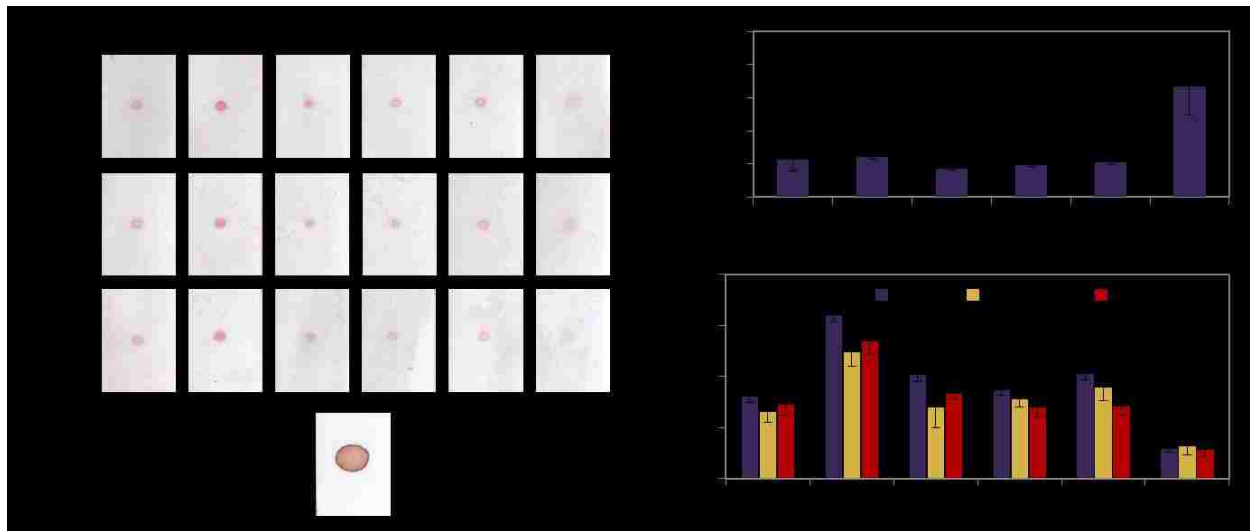


Figure 47. Full protein spot analysis for 3-helix adsorption vs. pH.

The pH-dependence of 3-helix adsorption to nitrocellulose was evaluated. (A) Representative test spot for each spotting pH (2-12) and lateral flow (LF) challenge condition. The red food coloring (RFC) represents the full wet-out area for the volume spotted (500 nL). (B) Spot areas for each condition relative to the wet-out area defined by the RFC, plotted as the mean \pm SD of $n=3$ replicates. (C) Normalized green-channel pixel intensity for each test spot, plotted as the mean \pm SD of $n=3$ replicates.

These results indicate that the adsorption of the 3-helix bundle protein is pH-dependent, as expected. The most dramatic pH dependence is the transition in spot size that occurs after pH 10, with the protein spotted at pH 12 showing significantly larger spot size than the protein spotted at pH 2-10. This transition matches our expectation, since the estimated isoelectric point (pI) of the 3-helix protein is 9.4, which is close to the observed transition at pH 10. We hypothesize that, as described by Přistoupil *et al.* [129] (section 2.4.3), the protein adsorbs quickly to nitrocellulose when it is positively charged (below pH 10), since nitrocellulose is negatively charged (and increasingly so for increasing pH). Conversely, when the pH is raised above the pI of the protein, the protein is negatively charged, which incurs electrostatic repulsion against the negatively charged nitrocellulose, resulting in worse (here, slower and less efficient) adsorption. This is evident from the large spot size at pH 12 and the diminished spot intensity at pH 12. Interestingly, the protein that does adsorb at pH does stay adsorbed and is resistant to stripping under lateral flow challenge.

The spot intensity data indicates that the 3-helix protein adsorbs to nitrocellulose rather robustly, with minimal loss of protein upon lateral flow challenge. Interestingly, the protein spotted at pH 4 generated much more intense spots than protein spotted at all other pH values. Further testing is needed to determine if this result is an artifact due to a dilution error, or if it is indeed a real result that reflects the optimal balance of protein pI, nitrocellulose charge, and spotting buffer pH.

Comparison of Design I and 3-Helix Proteins

Given the promising nitrocellulose adsorption of both the DI and 3-helix proteins, we performed a final protein spot analysis experiment to fully characterize the adsorption of these proteins and compare to IgG. Using the piezoelectric spotter, each protein was spotted onto 0.8-by-5-cm strips of GE FF80HP nitrocellulose. All proteins were spotted at 1 mg/mL in PBS, and red food coloring (RFC) diluted 1:10 in H₂O was spotted to visualize the full wet-out area (n=6 replicates). All spots were 500 nL (1000 drops x 500 pL/drop). Devices were dried under desiccation overnight before use. Lateral flow challenge solutions of PBS and PBST were used, in addition to no-flow controls. After the LF challenge, the protein spots were visualized by Ponceau S staining. In total, 4 replicates of each protein for each LF challenge condition were tested. A representative test spot for each condition is provided in Figure 48A. The spot sizes (relative to the mean size of the full wet-out area) are plotted in Figure 48B, and the normalized green-channel pixel intensities are plotted in Figure 48C, each as the mean +/- SD of n=4 replicates per condition.

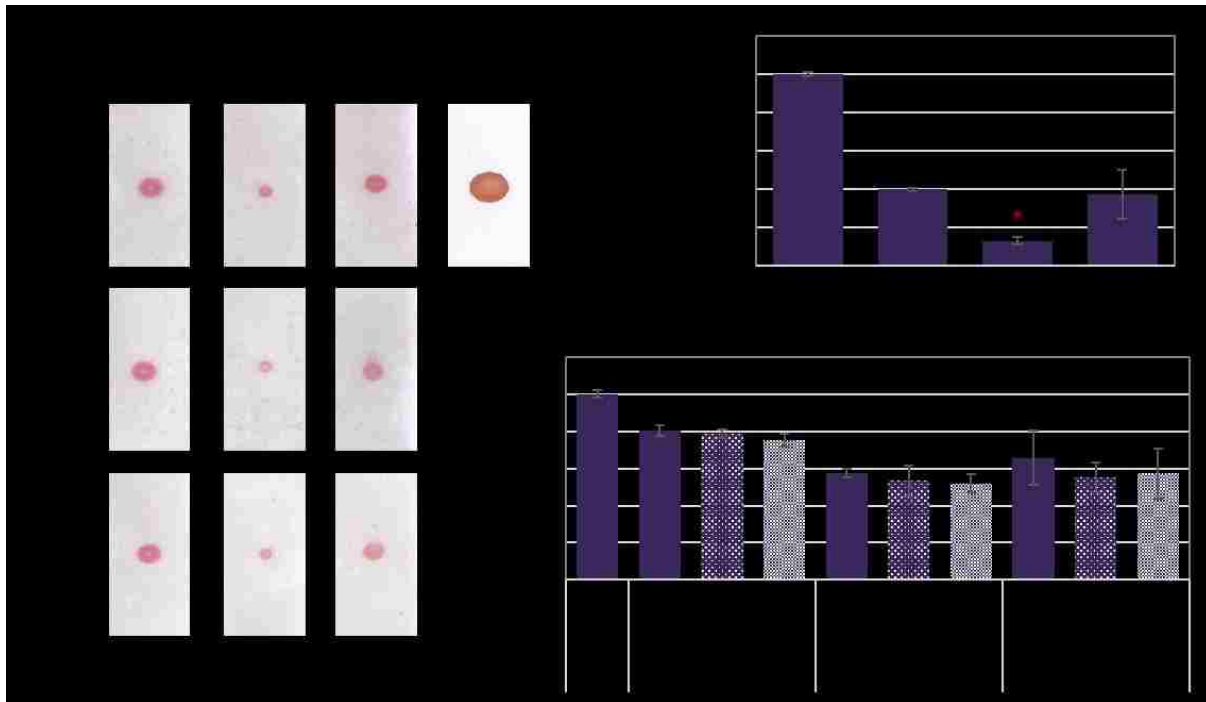


Figure 48. Comparison of DI, 3-helix, and IgG adsorption to nitrocellulose.

Screening of the 3-helix and DI nitrocellulose-binding anchor proteins, with comparison to IgG. (A) Protein spots on nitrocellulose, subjected to lateral flow (LF) challenge with PBS or PBST or no LF control, and stained with Ponceau S. (B) Spot size relative to the full wet-out area indicated by the red food coloring (RFC), plotted as the mean +/- SD for n=4 replicates of each protein and n=6 replicates of the RFC control. Asterisk indicates that the 3-helix protein exhibits the smallest spot size ($p < 0.025$). (C) Normalized pixel intensities of the Ponceau S-stained protein spots after LF challenge, plotted as the mean +/- SD for n=4 replicates.

The small sizes of the protein spots relative to the full wet-out area confirm that all three proteins adsorb to the membrane quickly, which is ideal for anchor protein candidates. In this direct comparison, the 3-helix protein yields the smallest spot size ($p < 0.025$ by one-tailed Student's *t*-test of unequal variance), indicating that it adsorbs to nitrocellulose the most rapidly. The DI protein yields a spot size similar to that of IgG (no significant difference), signifying that it also adsorbs quickly to the membrane. All three proteins are also resistant to stripping under lateral flow challenge with PBS and PBST, with no significant difference in the spot intensity relative to the no LF control for the given protein ($p > 0.025$). Therefore, all three proteins adsorb robustly to the nitrocellulose membrane, with 3-helix showing the best adsorption of the three.

Overall, both the DI and 3-helix proteins are strong candidates for nitrocellulose-binding anchor proteins, as they exhibit adsorption that is equally or more robust than IgG adsorption. This favorable adsorption is consistent with the Přistoupil model [129] (section 2.4.3), which states that the best adsorption occurs under charge states that promote electrostatic interaction, followed by charge states that promote hydrophobic interaction. Given a typical pK_a of $\sim 6-7$ for nitrocellulose [129] and an operating pH of 7.4, the strong adsorption of the 3-helix bundle protein (pI 9.4) exemplifies this adsorption theory, as the positively charged protein binds very tightly to the negatively charged nitrocellulose. While the DI protein (pI 6.3) does not adsorb as rapidly as the 3-helix protein, likely due to the lack of positive charge at pH 7.4, it also does not have an abundance of negative charge to initiate electrostatic repulsion. As described in the model, this scenario therefore yields the protein in a reasonable charge state to allow the hydrostatic interactions to dominate and result in strong adsorption as well. We therefore hypothesize that the robust adsorption of the 3-helix and DI proteins is partially due to the favorable electrostatics of the systems, in addition to favorable hydrophobic properties that are less well-understood.

3.8. Conclusions

Through the in-depth protein adsorption studies described above, we gained valuable insights about specific, commonly used proteins, as well as about protein adsorption in general. We learned that protein adsorption varies widely by protein, and that the robustness of adsorption is not governed by the size of the protein, as previously postulated. We also learned that IgG adsorption appears to be largely Fab-mediated, which is non-ideal for its use as a capture agent. Combined with the fact that our stem region flu binder does not adsorb well to nitrocellulose, these results motivate the need for improved immobilization techniques for affinity reagents of all kinds. Our

work to develop novel immobilization methods for this purpose is described in the next chapter. Most importantly, we used our detailed study of the pH-dependence of protein adsorption both to experimentally corroborate the previously proposed adsorption model by Přistoupil *et al.* [129] (section 2.4.3) and to identify two anchor protein candidates, the DI and 3-helix proteins. The ability of these proteins to serve as anchor proteins through genetic fusion to the stem region flu binder is described in the next chapter.

4. Flu Binder Immobilization

4.1. Motivation

Although direct adsorption is the mainstay of protein immobilization for use in nitrocellulose-based assays, it may not be the most effective method for all affinity reagents, as evidenced by the variability in adsorption among proteins in the previous chapter. In particular, we are interested in immobilizing the flu binders from the Baker lab (see section 2.4.2) for use as capture agents in our paper-

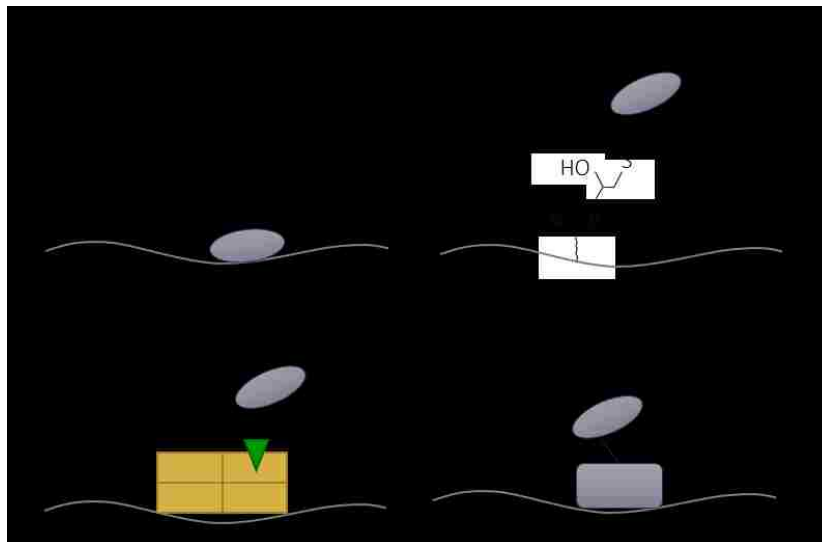


Figure 49. Illustration of the four immobilization strategies developed herein. (A) Direct adsorption of affinity protein to nitrocellulose. (B) Covalent attachment of thiolated affinity protein to GMA-modified nitrocellulose. (C) Anchoring of biotinylated affinity protein to streptavidin (regular and nitrocellulose-binding mutant version). (D) Genetic fusion of affinity protein to custom nitrocellulose-binding anchor protein.

-based influenza diagnostic. We therefore used the flu binders as motivation for which to develop and test different methods of immobilization. Overall, four immobilization strategies were developed, characterized, and demonstrated using the recombinant stem region binder as a representative affinity protein. The four immobilization methods, illustrated in Figure 49, included: (1) direct adsorption, (2) covalent attachment of thiolated affinity protein to epoxide-functionalized nitrocellulose, (3) anchoring of biotinylated affinity protein through streptavidin, and (4) genetic fusion of the affinity protein to a custom nitrocellulose-binding anchor protein. Each method was assessed for its immobilization efficiency via lateral flow challenge and for its resulting functionality in a lateral flow-based flu HA assay, as described in section 4.2. Each method of immobilization is described in detail in the sections thereafter. Finally, the best-performing immobilization method is compared to standard antibody capture by direction adsorption in section 4.7, illustrating the merit of these novel immobilization methods. Much of this work was done in collaboration with undergraduate student Steven Bennett.

4.2. Common Methods

4.2.1. Lateral Flow Challenge

To assess the efficiency of immobilization for each method, the lateral flow challenge system was used. This is the same method described in section 3.2.1, with a few minor changes. In this method, nitrocellulose membranes were cut into multi-legged “comb” devices using a CO₂ laser cutter (M360 or VLS360, Universal Laser Systems, Scottsdale, AZ). Each test strip was 3 mm wide by 24 mm tall, and generally sets of 4 strips were cut together and connected by a 6-mm tall section at the top of the device in order to promote batch processing. The distance between strips was 6 mm, designed to allow each set of strips to fit into the wells of a 96-well plate.

The given protein of interest was typically spotted onto a strip of nitrocellulose in an automated fashion using a piezoelectric spotter (sciFLEXARRAYER S3, Scienion AG, Berlin, Germany). Proteins were prepared at 100 μM, unless otherwise indicated.

The HB80 flu binders were prepared in HEPES-buffered

saline (HBS), and the HB36 flu binders were prepared in phosphate-buffered saline (PBS), which were the preferred buffers for each type of binder (per Baker lab) and the same buffers already contained in the stock solutions. All protein solutions were filtered through a centrifugal filter device with 0.2-μm nylon membrane (VWR, Radnor, PA) at 6000 g for 5 minutes prior to spotting to avoid clogging the printer plumbing with particulate from the samples. Proteins were typically patterned in the shape of test lines, which were created by 12 spots spaced 250 μm apart, with 30 droplets per spot, as shown in Figure 50. Two passes were printed for each test line to saturate the membrane region. Each droplet was 450-500 pL, resulting in test lines comprising ~300 nL of protein solution in total. Droplets were printed at 500 Hz in an enclosed chamber at ~50% relative humidity and ~68 °F ambient temperature. After spotting, the patterned membranes were dried before use, typically stored under desiccation at least overnight.

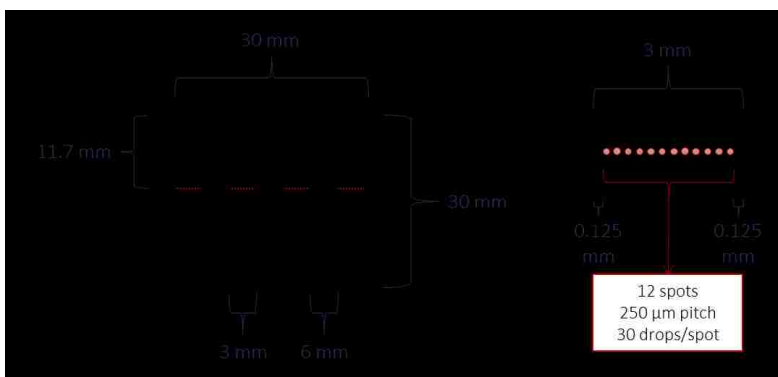


Figure 50. Test line pattern created with the piezoelectric spotter. Spotting pattern used to create test lines on lateral flow comb devices. (A) Layout of test lines on legs of devices. (B) Pattern used for each test line.

For the lateral flow challenge, strips were placed into a well (96-well plate) filled with the given challenge solution (50 μ L). A cellulose absorbent pad (Millipore #CFSP223000) cut to the width of the device and 70 mm tall was secured to the top of the nitrocellulose device to aid wicking, either with tape or with a custom-made plastic housing. Unless otherwise noted, the challenge solution was allowed to wick through the strips for 15 minutes, at which point the strips were removed from the solution. In this work, challenge solutions included deionized H₂O, phosphate-buffered saline (PBS), and PBS + 0.1% v/v Tween-20 (PBST).

The amount of protein remaining on the membrane was visualized in one of three ways, as illustrated in Figure 51A: staining with a specific FITC-labeled anti-FLAG tag antibody, nonspecific protein staining with

Coomassie Brilliant Blue (Thermo Scientific #20278, Life Technologies, Carlsbad,

CA), or nonspecific protein staining with Ponceau S (Thermo Scientific #24580). For Coomassie staining, each membrane was incubated for 10 minutes with stain solution, followed by 10 minutes with destain solution, both with shaking. This protocol, adapted from Metkar *et al.* [158], uses a destain solution of 50% H₂O, 40% methanol, and 10% glacial acetic acid, and a stain solution of 0.0025% w/v Coomassie Brilliant Blue in destain solution. For Ponceau S staining, each membrane was incubated with shaking for 5 minutes with stain solution (0.1% w/v Ponceau S in 5% acetic acid), followed by 2 minutes with H₂O for destaining, as based on the manufacturer's protocol and optimized in-house. In both cases, the stained devices were taped to a standard piece of printer paper and imaged at 48-bit HDR color, 600 dpi, $\gamma = 1$ using a desktop scanner (Perfection V700 Photo Scanner, Epson, Long Beach, CA).

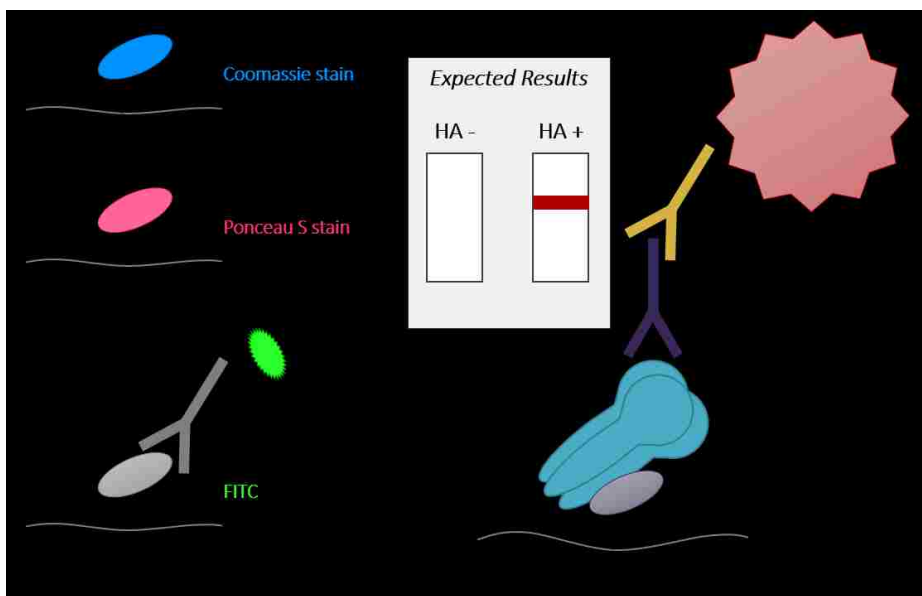


Figure 51. Methods used to assess each immobilization strategy.

(A) Immobilization efficiency was tested via lateral flow challenge and protein staining with Coomassie Brilliant Blue, Ponceau S, or FITC-anti-FLAG tag. (B) Flu binder functionality was tested as a capture agent for a flu HA assay, using an antibody detection system.

In the case of FITC-anti-FLAG tag staining, this fluorescently labeled antibody was used to specifically recognize the FLAG tag present in the recombinant HA binders. In these experiments, FITC-anti-FLAG (Sigma-Aldrich #F4049) was diluted to a working concentration of 100 $\mu\text{g}/\text{mL}$ in fetal bovine serum (FBS, Gibco #16000-077, Life Technologies), which prevents the antibody from adsorbing nonspecifically to the membrane. This FITC-anti-FLAG solution was then applied to the strips via lateral flow, using 20 μL of solution per well of a 96-well plate, followed by a rinse with 40 μL buffer (PBS). The resulting fluorescently stained membranes were visualized by imaging under ultraviolet (UV) excitation using a commercial UV gel imager (Gel Doc EZ System, Bio-Rad, Hercules, CA). This imager utilizes a UV sample tray (Bio-Rad #170-8271) to achieve UV illumination of the membrane from broadband light, with the strength of fluorescence signal being controlled by the time of exposure. Membranes were imaged backing-side-up, as this orientation was determined to give the lowest background fluorescence. The signal intensity of the protein remaining in the test spot after LF challenge was quantified as described in section 4.2.3.

4.2.2. Flu Hemagglutinin Assay

Since protein immobilization efficiency only tells us how well the protein stays on the membrane, we also wanted to determine how functional a protein was for a given immobilization strategy. To test this functionality, each immobilization strategy was tested using the recombinant stem region binder as a capture agent for an influenza hemagglutinin (HA) assay. All assays utilized standard antibody-based detection to complete the assay sandwich, in order to focus solely on improvements gained by the immobilization method.

Nitrocellulose strips were prepared with test lines patterned with flu binder as described above (section 4.2.1). Each flu assay was performed in a dipstick lateral flow format using a 96-well plate pre-loaded with the given assay reagents (Figure 52). The test strips were manually moved between wells to initiate each assay step. A cellulose absorbent pad (Millipore #CFSP223000) cut to the width of the device and 70 mm tall was secured to the top of the nitrocellulose device to aid wicking, either with tape or with a custom-made plastic housing. The generic assay stack is illustrated in Figure 51B. After the assay was complete, the wicking pads were removed, and all devices were taped to a standard piece of printer paper and imaged at 48-bit HDR color, 600 dpi, $\gamma = 1$ using a

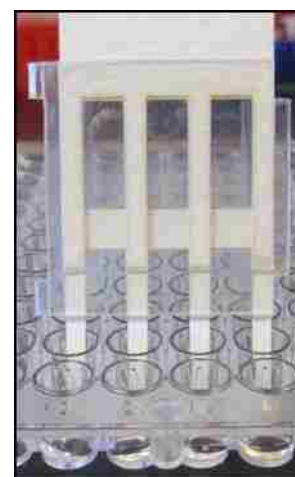


Figure 52. Dipstick format. The dipstick lateral flow format used for all assays.

desktop scanner (Epson Perfection V700 Photo Scanner). The signal intensity of each test line was quantified as described in section 4.2.3.

Unless otherwise noted, each assay consisted of the following steps: 1) 20 μ L recombinant HA or negative control, 2) 20 μ L wash, 3) 20 μ L mouse anti-HA detection antibody, 4) 20 μ L wash, 5) 20 μ L gold-conjugated goat-anti-mouse IgG antibody, and 6) 20 μ L wash. Recombinant HA was from one of three influenza strains, as indicated: A/New Caledonia/20/1999 (Protein Sciences, Meriden, CT), A/California/04/2009 (Influenza Reagent Resource (IRR)), or A/Solomon Islands/03/2006 (IRR), all of which are H1N1 strains. Matching detection antibodies were used accordingly. The gold-conjugated secondary (Au-2°) antibody (Au-goat-anti-mouse IgG, Arista Biologicals, Inc., Allentown, PA) was used at optical density (OD) 2.5. All reagents were diluted in a running buffer of PBS or PBST + 1% w/v bovine serum albumin (BSA, Sigma-Aldrich #A7030). Wash buffer was either PBS or PBST, as indicated.

4.2.3. Signal Quantification

All signal intensities from protein lines and test lines were quantified using the custom MATLAB script, *quantifyColorimetricSignal.m* (see Appendix B for code and description). As described in section 3.2.1, this program is used to compute the average pixel intensity, I_{test} , of an ROI drawn semi-manually around the test line of interest. This value is then background-subtracted using the average pixel intensity inside a local background region, I_{bkgd} , and normalized on a scale from 0 to 1 to generate the normalized pixel intensity of the spot, I_{norm} , using Eqn 19.

For each experiment, the channel of the RGB image that was most sensitive to the particular color of signal was chosen for analysis. For the flu HA assays (red color from gold nanoparticles) and the Ponceau S-stained membranes (pink color), the green channel was used. For the Coomassie-stained membranes, the red channel was used. Finally, for the fluorescence images based on FITC-anti-FLAG signal, inverted grayscale quantification was used (signal = white, background = black). In all cases, the normalized pixel intensities represent a range from no signal (0) to maximum possible signal (1).

4.3. Immobilization by Direct Adsorption

Since direct adsorption is the state-of-the-art for the immobilization of affinity reagents on paper-based diagnostics, we first investigated this basic form of immobilization for the stem region flu binder. Although we had preliminary evidence that direct adsorption was not effective for the flu

binder (see Figure 17), we wanted to fully characterize this method in terms of both immobilization efficiency and flu binder functionality in order to establish a baseline upon which to improve. We also investigated the inherent susceptibility or resistance to protein fouling of the various membranes used in this immobilization work.

4.3.1. Methods

Protein Fouling Challenge

Since protein immobilization is a function of both the protein and the substrate, we used the protein fouling challenge to characterize candidate nitrocellulose membranes for their amenability or resistance to protein fouling. While we desire a membrane that can immobilize our flu binder efficiently and robustly, we ideally want the membrane to be resistant to subsequent protein fouling, either with or without blocking. This protein fouling experiment was therefore performed by challenging different membranes of interest, under different blocking conditions, with a fluorescently labeled IgG solution, and using fluorescence imaging to visualize the amount of protein that stuck to each membrane.

Specifically, multi-legged comb devices were cut from the desired nitrocellulose membranes using the CO₂ laser cutter. Half of the devices of each membrane type were pre-blocked using Invitrogen Membrane Blocking Solution (#00-0105), while the other half were left unblocked. The devices undergoing blocking were allowed to incubate with the blocking solution (in a Petri dish, with shaking) for 1 hour and then oven-dried at 37 °C for 30 minutes, before storing at room temperature under desiccation overnight.

All devices were challenged with a protein solution via lateral flow to determine their resistance (or lack thereof) to fouling. In particular, a cellulose wicking pad was taped to the top of each device, and each device was set into wells of a 96-well plate pre-filled with 50 µL of the challenge solution. The challenge solution consisted of FITC-IgG (Sigma-Aldrich #F9636) at 2 mg/mL in either PBS (Sigma-Aldrich #P3813) or FBS (fetal bovine serum, Gibco #16000-077), the latter serving as a real-time blocking condition. After wicking of the challenge solution was complete, the devices were moved to a new set of wells, each containing 75 µL of PBS to serve as a wash step. After the fouling challenge was complete, the wicking pads were removed, and the devices were imaged fluorescently to detect the amount of FITC-IgG that had fouled the membranes. To do so, the devices were imaged using the UV gel imager using a 0.4-second exposure. The average fluorescence

intensity of each strip was then quantified using my custom MATLAB program, *quantifyColorimetricSignal.m*, using the inverted grayscale option (see section 4.2.3).

Immobilization Testing via Lateral Flow Challenge

The immobilization efficiency of the stem region flu binder HB80.4 on each membrane of interest was tested using the lateral flow challenge system described in section 4.2.1.

Functionality Testing via Flu Hemagglutinin Assay

The functionality of the stem region flu binder HB80.4 was tested as a capture agent for the flu HA assay, as described in section 4.2.2.

4.3.2. Results and Discussion

Protein Fouling Characterization for Different Nitrocellulose Membranes

Before testing flu binder immobilization, we first wanted to characterize all candidate nitrocellulose membranes in terms of their inherent nature to interact with proteins. In particular, while we desire a membrane that can immobilize our flu binder efficiently and robustly, we ideally want the membrane to be resistant to subsequent protein fouling, either with or without the addition of blocking. We therefore tested the ability of each candidate membrane to resist protein adsorption using the protein fouling challenge, described in section 4.3.1. The four candidate membranes tested were the following:

- Millipore HFB135 nitrocellulose; available commercially
- GE FF60 nitrocellulose; available commercially (*Note: this membrane later evolved to FF80HP)
- GE FF60-GMA; confidential membrane developed at GE GRC by grafting glycidyl methacrylate (GMA) onto FF60 nitrocellulose (*Note: this membrane later evolved to FF80HP-GMA)
- GE FF60-PEG; confidential membrane developed at GE GRC by grafting polyethylene glycol (PEG) methacrylate onto FF60 nitrocellulose (*Note: this membrane later evolved to FF80HP-PEG)

For each membrane, two pre-blocking conditions were tested: 1) unblocked; and 2) blocked with Invitrogen Membrane Blocking Solution, air-dried at room temperature for 30 minutes, and stored

under desiccation overnight. For each pre-blocking condition, two different real-time blocking conditions were tested: 1) no real-time blocking, i.e. FITC-IgG diluted in PBS; and 2) real-time blocking using FITC-IgG diluted in FBS. The resulting fluorescence images of the devices are shown in Figure 53A, and the corresponding normalized pixel intensities are plotted in Figure 53B as the mean \pm standard deviation of the n=3 replicate strips for each condition.

These results indicate that both unmodified, commercial nitrocellulose membranes (Millipore HFB135 and GE FF60) are prone to fouling and therefore require blocking of some sort, whether that be pre-blocking with a protein-containing solution or real-time blocking using FBS. Both of the modified nitrocellulose membranes from GE (FF60-GMA and FF60-PEG), on the other hand, are inherently resistant to fouling and may not require blocking for use in an assay. This result was expected for FF60-PEG, since PEG is a commonly used anti-fouling agent and was grafted to these membranes for this purpose. The non-fouling nature of FF60-GMA is a fortuitous property of this membrane, as the primary purpose of the GMA is to provide a reactive epoxide moiety for immobilization of affinity reagents. The resistance to fouling observed here is consistent with internal results from GE GRC that indicate low background signal for assays performed using this membrane.

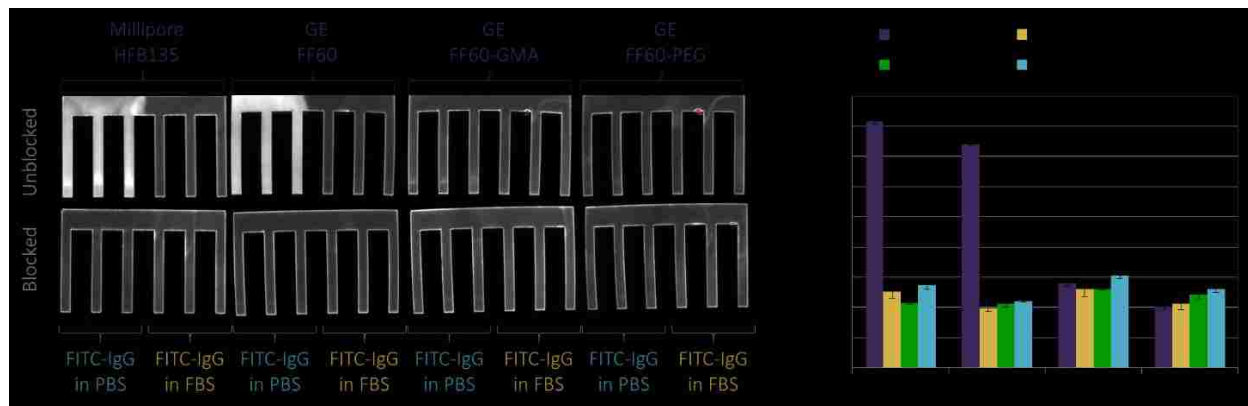


Figure 53. Protein fouling characterization of different nitrocellulose membranes.

Protein fouling of four different nitrocellulose membranes under different blocking conditions. (A) Fluorescence images of unblocked or blocked nitrocellulose membranes challenged with FITC-IgG in PBS (no real-time blocking) or FBS (for real-time blocking). (B) Normalized fluorescence intensities, plotted as the mean \pm SD for the n=3 replicate strips of each condition. FF60-GMA and FF60-PEG are resistant to fouling, while HFB135 and FF60 require blocking.

Immobilization of Flu Binder HB80.4 by Direct Adsorption

The ability of flu binder HB80.4 to be immobilized to nitrocellulose via direct adsorption was assessed using the lateral flow challenge method described above. This flu binder was spotted at 100 μ M in HBS using the piezoelectric spotter, and membranes were dried at room temperature

under desiccation at least overnight before use. The following four nitrocellulose membranes were tested:

- Millipore HFB135 nitrocellulose; available commercially
- GE FF60 nitrocellulose; available commercially
- GE FF60-GMA; confidential membrane developed at GE GRC
- GE FF60-PEG; confidential membrane developed at GE GRC

Lateral flow challenge solutions of H₂O, PBS, and PBST were tested (50 μ L per strip), along with no-flow controls. After lateral flow challenge, flu binder was visualized using both general protein staining with Coomassie Brilliant Blue and flu binder-specific staining using FITC-anti-FLAG (20 μ L at 100 μ g/mL in FBS). Coomassie-stained devices were scanned at 48-bit HDR color, 600 dpi, $\gamma=1$, and FITC-stained devices were imaged in the UV gel imager, backing-side up, using a 0.2-second exposure.

The resulting images of the flu binder test lines are shown in Figure 54. These results indicate that, as for stem region binder HB36.4 (Figure 17), the stem region binder HB80.4 does not adsorb robustly to nitrocellulose.

Interestingly, adsorption is more robust for GE FF60

nitrocellulose than for Millipore HFB135 nitrocellulose, as evidenced by the differential resistance to stripping by PBST for these two membranes. Direct adsorption of flu binder HB80.4 to the two modified membranes, FF60-GMA and FF60-PEG, results in inefficient immobilization, but for both, the protein that does become immobilized is fairly resistant to desorption under lateral flow challenge. Overall, we observed that flu binder HB80.4 could be immobilized to nitrocellulose by direct adsorption, but not very robustly, depending on the membrane chosen. The next step was to

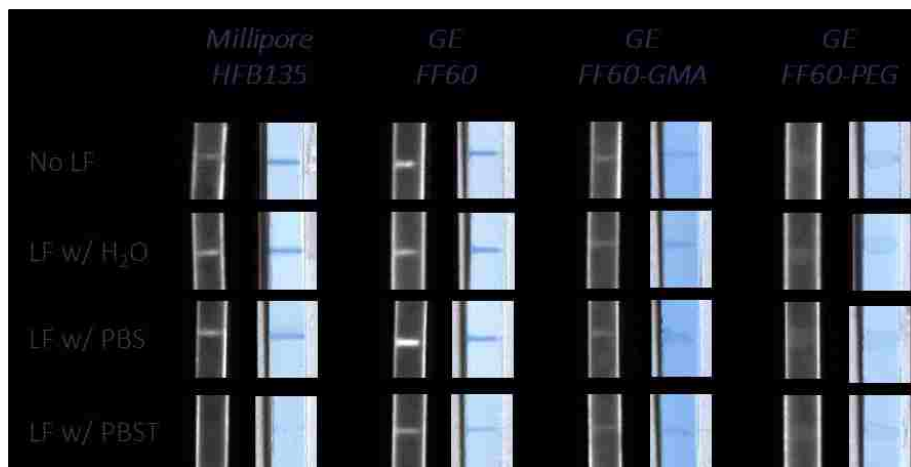


Figure 54. Flu binder immobilization by direct adsorption.

Immobilization of flu binder HB80.4 to four different nitrocellulose membranes by direct adsorption. The amount of flu binder remaining after lateral flow (LF) challenge is visualized with both fluorescence imaging (left columns) and Coomassie protein staining (right columns).

determine whether or not the flu binder was functional when immobilized by direct adsorption, described next.

Functionality of Flu Binder HB80.4 by Direct Adsorption

The functionality of flu binder HB80.4 immobilized to nitrocellulose by direct adsorption was assessed using the bench-top flu HA assay described above. All reagents were diluted in PBS + 1% BSA as the running buffer for the assay. Two different nitrocellulose membranes were tested: GE FF60 and GE FF60-GMA. The average pixel intensity of each test line was quantified with my MATLAB program *quantifyColorimetricSignal.m*, using the green channel option. The resulting assays yielded no visible signal for FF60 and only slightly visible signal for FF60-GMA, as shown in Figure 55A. The quantified signal (Figure 55B) for test samples (100 nM HA in PBS + 1% BSA) was not, however, statistically greater than the signal for negative controls (PBS + 1% BSA) for either membrane ($p > 0.025$ by unpaired, right-tailed Student's *t*-test of unequal variance). From these results, we can conclude that flu binder HB80.4 is non-functional when immobilized to nitrocellulose by direct adsorption.

4.4. Immobilization by Covalent Attachment

Since direct adsorption is not an effective means of flu binder immobilization, we leveraged the strengths of our collaborators to explore novel, covalent attachments of flu binder to nitrocellulose. Specifically, we have utilized the customizability of the recombinant flu binder from the Baker lab to create thiolated versions of the binder through the mutation of a single (non-critical) amino acid to a cysteine. For the stem region binder HB80.4, this resulted in the variation HB80.4_K315C, also known as “cys-HB80.4” or “cys-HB80.” Since HB80.4 does not normally contain any cysteine residues, the mutation to cys-HB80.4 provides a single, site-specific thiol residue that can be exploited for attachment to thiol-reactive moieties. Later, thiolated versions of the HB36.5 variant were also developed. Our collaborators at GE GRC have developed nitrocellulose (NC) membranes

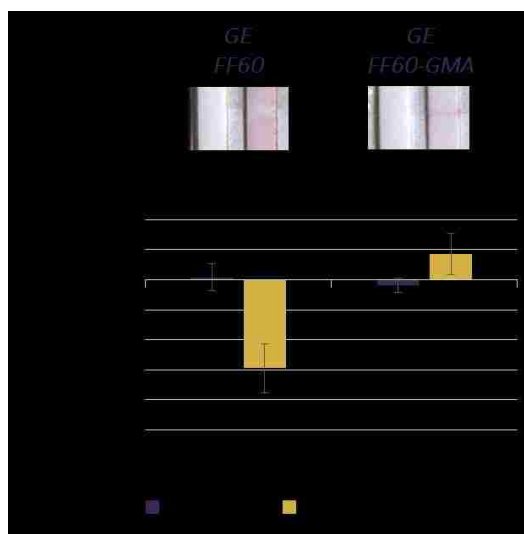


Figure 55. Flu binder functionality when immobilized by direct adsorption.

Flu binder HB80.4 is non-functional when immobilized to nitrocellulose by direct adsorption. (A) No significant signal is observed at the test lines (arrows) for the flu HA assay. (B) Normalized green-channel pixel intensities of the test lines, plotted at the mean \pm SD for $n=2$ replicates for each condition.

that are modified to contain thiol-reactive moieties. The primary membrane of interest has been NC-GMA, which is created by grafting glycidyl methacrylate (GMA) onto regular nitrocellulose (initially FF60, transitioned to FF80HP), as shown in Figure 56A [179]. This grafting results in a porous nitrocellulose membrane that is functionalized with epoxide rings, which are highly reactive with thiols. We have therefore studied the immobilization of thiolated flu binder to NC-GMA extensively, as described below. The investigators at GE GRC also developed a maleimide-functionalized nitrocellulose membrane (NC-maleimide), which was also tested (Figure 56B) briefly, as described below. Finally, a nitrocellulose membrane functionalized with *N*-hydroxysuccinimide (NHS) ester was also developed and tested briefly; however, because this NC-NHS-ester does not offer site-specific immobilization, it did not yield remarkable results, so it is not included here.

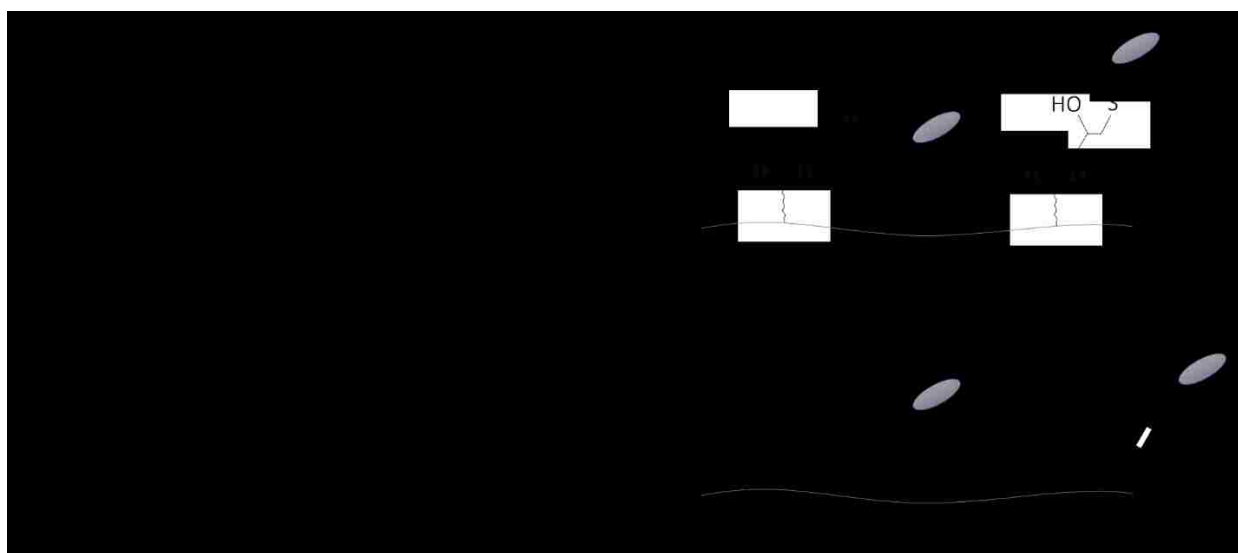


Figure 56. Covalent attachment of thiolated flu binders to functionalized nitrocellulose.

Chemistries of (A) NC-GMA and (B) NC-maleimide modified nitrocellulose membranes. The left half of each reaction scheme shows the chemistry used to modify the base nitrocellulose membrane. The right half of each reaction scheme illustrates how thiolated flu binder (purple oval) reacts with each modified membrane. Chemical structures provided by GE GRC.

4.4.1. Methods

Immobilization Testing via Lateral Flow Challenge

The immobilization efficiency of the thiolated stem region flu binder cys-HB80.4 was tested using the lateral flow challenge system described in section 4.2.1 and compared to the non-thiolated binder HB80.4. Regular and GMA-modified nitrocellulose membranes were compared.

Functionality Testing via Flu Hemagglutinin Assay

The functionality of the thiolated stem region flu binder cys-HB80.4 was tested as a capture agent for the flu HA assay, as described in section 4.2.2, and compared to the non-thiolated binder HB80.4. Regular and GMA-modified nitrocellulose membranes were compared.

Flu Binder HA-Binding Comparison by SPR

To obtain an independent measure of flu binder functionality, we analyzed flu binder interactions with hemagglutinin (HA) using surface plasmon resonance (SPR). To do so, we used the Biacore T100 in the Analytical Biopharmacy Core facility, and we utilized the

Biacore Biotin CAPture chip (#28920234), which is designed for

immobilization of biotinylated ligands. This worked well for our system, since the Baker lab had access to biotinylated HA, which we could immobilize and test for binding to our flu binders of interest (Figure 57). The Biotin CAPture chip comes with proprietary oligonucleotides covalently attached to the gold surface, which constitutes the regenerated state. The chip contains four flow cells, but we typically only used two at a time. To begin an experiment, we flowed the streptavidin capture solution across the chip, which consisted of streptavidin molecules conjugated to oligonucleotides that are complementary to those on the surface of the chip. The complementary oligonucleotides hybridized, creating a surface of streptavidin molecules to which biotinylated ligands could be immobilized. In our case, we flowed biotinylated HA across one flow cell, while flowing buffer through a parallel flow cell in order to serve as the reference channel. We then flowed our flu binder of interest through both flow cells to determine the specific binding of the flu binder to HA. Based on our protocol, we expected approximately 400 response units (RU) of signal upon binding of biotin-HA and approximately 40 RU upon binding of a flu binder, since it is about

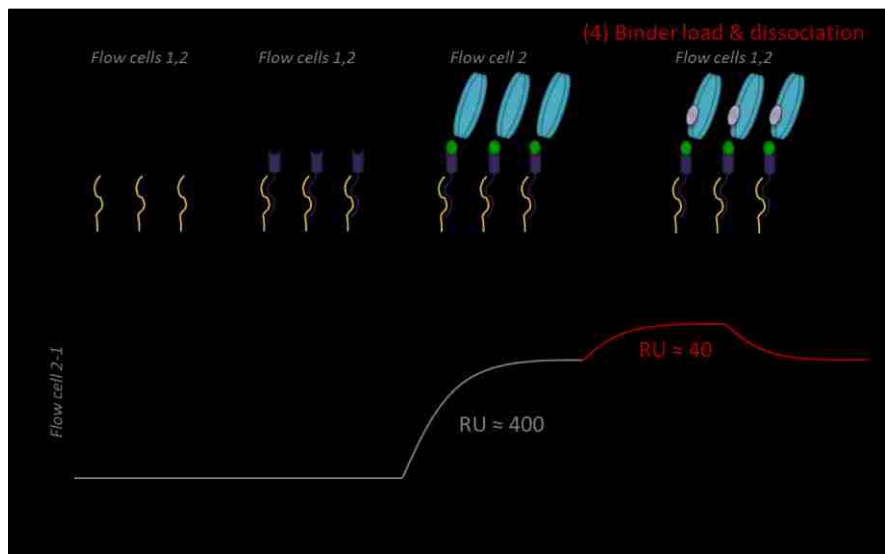


Figure 57. Flu binder HA-binding analysis by SPR.

Illustration of the SPR system used to analyze interaction between flu binders and HA. Top: Binding events included in the process. The flu binder loading and dissociation (highlighted in red) is the primary step of interest. Bottom: Ideal response curve for the difference between flow cells 2 and 1.

ten times smaller than HA. This ultimately provided binding signal that was sufficiently large to distinguish above noise (~5 RU).

To perform SPR analysis of flu binders of interest, the Biotin CAPture chip reagents were prepared according to the manufacturer's instructions. The biotinylated HA was diluted to approximately 300 nM. This concentration had been previously optimized by Dr. Aaron Chevalier of the Baker lab. Dilutions of each flu binder were prepared at various concentrations near the expected dissociation constant of the binder and were used for scouting to determine the final concentrations for testing. All dilutions were made in the running buffer of the experiment to avoid mismatches in the index of refraction. This running buffer was HBS-EP (Biacore #BR100188; 10 mM HEPES, 150 mM NaCl, 3 mM EDTA, 0.05% (v/v) Tween-20, pH 7.4), which provides better protection against nonspecific binding than pure HBS. For each sample cycle, the reagents were injected into the flow cell(s) according to the protocol listed in Table 10, which was also developed by Dr. Chevalier.

Table 10. SPR run procedure for each sample cycle.

Each step of the SPR procedure is listed with the associated flow cell(s), time, and flow rate.

Step #	Step Name	Flow Cells	Time (s)	Flow Rate ($\mu\text{L}/\text{min}$)
1	Inject streptavidin	1, 2	300	2
2	Inject biotin-HA	2	60	2
3	Inject flu binder	1, 2	120	50
4	Wait for dissociation	n/a	varies	n/a
5	Regenerate	1, 2	120	20

Fluorothiol Assay

To assess the thiol content of the thiolated flu binder under different reducing conditions, we used a commercial thiol detection kit (Fluorescent Thiol Detection Kit, Cell Technology Inc. #5057, Mountain View, CA). This kit contains a dye that, upon binding to a reduced thiol, results in a fluorescent analog with excitation at 488 nm and emission at 515-530 nm. Following the manufacturer's instructions, the fluorescent dye was reconstituted in 100 μL acetonitrile, then mixed with lysis buffer at a ratio of 40 μL dye to 2000 μL lysis buffer. Standard dilutions of glutathione (GSH) were prepared in 2x dilutions from 50 μM to 0.781 μM in lysis buffer. Samples of thiolated flu binder cys-HB36.5 were prepared with TCEP-HCl (Thermo Scientific #20490) at 0, 10, 100, or 1000 μM . Subsequently, 50 μL of each GSH standard concentration and each cys-HB36.5 + TCEP dilution was added to a flat black 96 well plate in triplicate. Then, 50 μL of fluorescent dye was added to each well. Note: the concentrations of GSH and cys-HB36.5 get halved due to the addition of the dye. For example, the 25 μM GSH standard originally had 50 μM added, but was

diluted in half with the dye reagent. Once all reagents were plated, the plate was covered with a sheet of aluminum foil and incubated for 15 minutes. After incubation the plate was loaded into the multimodal plate reader (Tecan Infinite M200 Pro), and the fluorescence measurement was conducted with the following conditions: excitation at 488 nm, emission at 520nm, Z height optimized to well A1, and automatic gain.

4.4.2. Results and Discussion

Optimization of Covalent Attachment of Thiolated Flu Binder Cys-HB80.4 to GMA-Modified Nitrocellulose

In order to test the immobilization of thiolated flu binder to NC-GMA, we first needed to optimize the covalent attachment between the thiol and epoxide groups in terms of the reducing agent required. In particular, we knew that including a reducing agent in the protein solution would be necessary to prevent the flu binder from forming disulfide bonds and thereby dimerizing. Through iterative preparations of cys-HB80.4, we tested the immobilization of this thiolated flu binder to FF60-GMA nitrocellulose with 1) no reducing agent present, 2) dithiothreitol (DTT) present at 1 mM, and 3) *tris*(2-carboxyethyl)phosphine (TCEP) present at 1 mM. The structures of these reducing agents are provided in Figure 58. We also included regular FF60 nitrocellulose as a control. As usual, the robustness of immobilization of each flu binder solution was evaluated via lateral flow challenge. Here, each flu binder solution was spotted at approximately 100 μ M and dried at least overnight at room temperature under desiccation before testing. Lateral flow challenge solutions of PBS and PBST were tested, in addition to no-flow controls. The remaining flu binder was visualized with FITC-anti-FLAG staining and imaging with the UV gel imager. The average pixel intensity of each test line was quantified with my MATLAB program *quantifyColorimetricSignal.m*, using the inverted grayscale option.

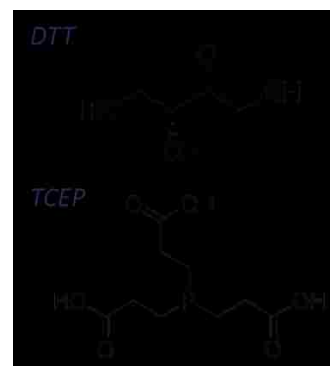


Figure 58. Reducing agents for thiolated flu binder. Chemical structures of the reducing agents DTT [180] and TCEP [181].

The resulting test lines are shown in Figure 59A, and the corresponding normalized grayscale pixel intensities are plotted in Figure 59B as the mean \pm standard deviation of $n=3$ replicates for the cys-HB80.4 and cys-HB80.4 + DTT conditions, and of $n=4$ replicates for the cys-HB80.4 + TCEP condition. These data indicate that DTT results in worse immobilization as compared to cys-HB80.4 without any reducing agent. We hypothesize that this reduction in immobilization is due to the fact that DTT itself contains two thiol groups, which can react with the epoxide groups of the NC-GMA

and thereby quench the available binding sites for cys-HB80.4. The addition of TCEP, on the other hand, improves immobilization of cys-HB80.4 to NC-GMA. We presume this improved immobilization is due to the fact that TCEP retains cys-HB80.4 in reduced form, allowing its thiols to react with NC-GMA, without the TCEP itself reacting with the membrane.

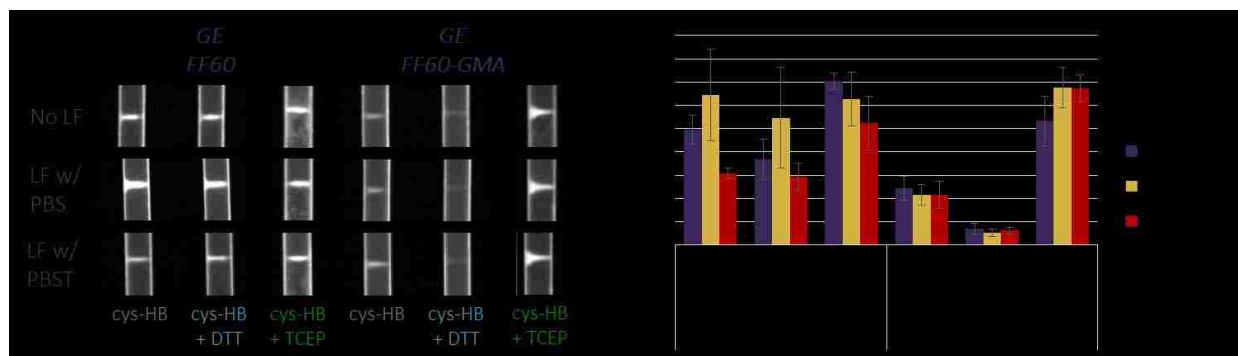


Figure 59. Optimization of reducing agent for cys-HB80.4 immobilization to FF60-GMA.

(A) Images of test lines spotted with thiolated flu binder cys-HB80.4 without reducing agent, with DTT, or with TCEP on FF60 or FF60-GMA and subjected to lateral flow (LF) challenge. (B) Corresponding normalized, background-subtracted, inverted grayscale pixel intensities of the test lines, plotted as the mean \pm SD of $n=3$ replicates (cys-HB and cys-HB + DTT) or $n=4$ replicates (cys-HB + TCEP).

In addition to optimizing the reducing agent needed for the covalent attachment of cys-HB80.4 to NC-GMA, we have also demonstrated the robust immobilization of flu binder achieved with this strategy. In particular, for cys-HB80.4 + TCEP immobilized on FF60-GMA, the flu binder is not stripped away by lateral flow with either PBS or PBST. Based on these results, we moved forward with 1 mM TCEP as the standard reducing agent for all preparations of thiolated flu binder. In the next section, we perform further characterization of this immobilization strategy by comparing it to direct adsorption of regular flu binder. Then, we describe the functionality of the flu binder using this immobilization strategy.

Finally, while this optimization of reducing agent was successful on the time scale of these particular experiments (weeks-months), we eventually encountered problems with high variability in this method over the several years in which this thesis work was performed. We therefore revisited the issue of TCEP optimization later in the project, described in the end of this section.

Immobilization of Thiolated Flu Binder Cys-HB80.4 to GMA-Modified Nitrocellulose by Covalent Attachment

The ability of thiolated flu binder cys-HB80.4 to be immobilized to GMA-modified nitrocellulose (FF60-GMA) by covalent attachment was assessed using the lateral flow challenge method

described above. In order to compare directly to immobilization by direct adsorption (i.e. non-covalent attachment), the immobilization of cys-HB80.4 on FF60, HB80.4 on FF60, and HB80.4 on FF60-GMA were also tested. All flu binders were spotted at 100 μM in HBS using the piezoelectric spotter, and membranes were dried at room temperature under desiccation for two days before use.

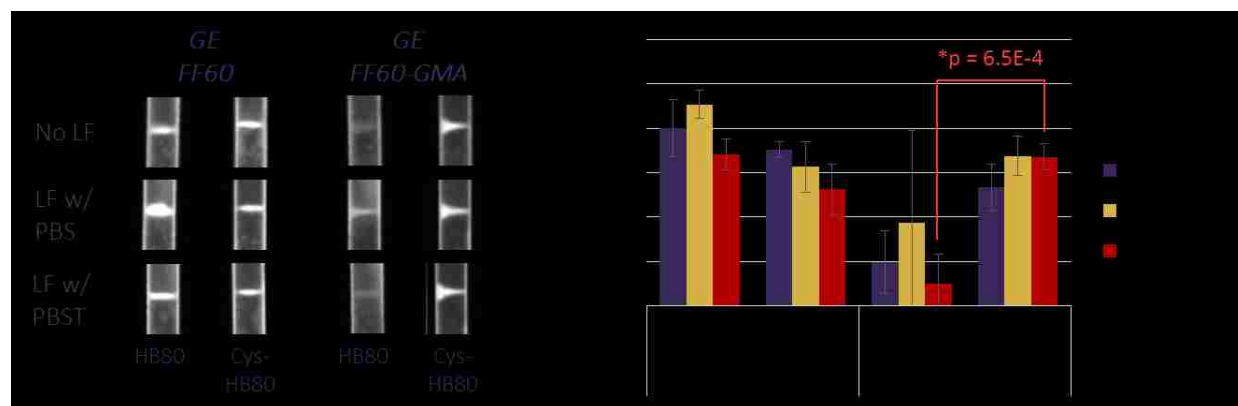


Figure 60. Immobilization of thiolated flu binder to NC-GMA.

Immobilization of thiolated flu binder cys-HB80.4 to FF60-GMA by covalent attachment, as compared to direct adsorption to FF60 and to adsorption of HB80.4. (A) The amount of flu binder remaining after lateral flow (LF) challenge is visualized with both fluorescence imaging. (B) The corresponding normalized, background-subtracted, inverted grayscale pixel intensities of the test lines plotted as the mean \pm SD of $n=4$ replicates.

Lateral flow challenge solutions of PBS and PBST were tested (50 μL per strip), along with no-flow controls. After lateral flow challenge, flu binder was visualized using FITC-anti-FLAG staining (20 μL at 100 $\mu\text{g}/\text{mL}$ in FBS). The FITC-stained devices were imaged in the UV gel imager, backing-side up, using a 0.35-second exposure, and the average pixel intensity of each test line was quantified with my MATLAB program *quantifyColorimetricSignal.m*, using the inverted grayscale option. The resulting images of the flu binder test lines are shown in Figure 60A, and the corresponding normalized, background-subtracted, inverted grayscale pixel intensities of the test lines are plotted in Figure 60B as the mean \pm standard deviation of $n=4$ replicates for each condition.

These results indicate that cys-HB80.4 immobilizes much better to FF60-GMA than does HB80.4, as the amount of binder initially immobilized (no LF control) is higher, and the binder that is immobilized is more resistant to stripping by PBS and PBST. As indicated in Figure 60B, the amount of flu binder that remained immobilized to FF60-GMA after LF challenge with PBST was significantly higher for cys-HB80.4 than for HB80.4 ($p = 6.5 \times 10^{-4}$ by right-tailed, unpaired Student's *t*-test of unequal variance). This result therefore implies that the cysteine-epoxide linkage between cys-HB80.4 and FF60-GMA provides significant improvement in immobilization efficiency over direct adsorption to this membrane. The amount of HB80.4 immobilized to regular FF60 by

direct adsorption was also high (albeit slightly stripped by Tween-20), so the next step was to compare the functionality of these flu binders under these immobilization conditions, described next.

Functionality of Thiolated Flu Binder Cys-HB80.4 Immobilized to GMA-Modified Nitrocellulose by Covalent Attachment

The functionality of thiolated flu binder cys-HB80.4 immobilized to GMA-modified nitrocellulose (FF60-GMA) by covalent attachment was assessed using the bench-top flu HA assay described above. In order to compare directly to the functionality of flu binders immobilized by direct adsorption (i.e. non-covalent attachment), the functionality of cys-HB80.4 on FF60, HB80.4 on FF60, and HB80.4 on FF60-GMA were also tested. All flu binders were spotted at 100 μ M in HBS using the piezoelectric spotter, and membranes were dried at room temperature under desiccation overnight before use.

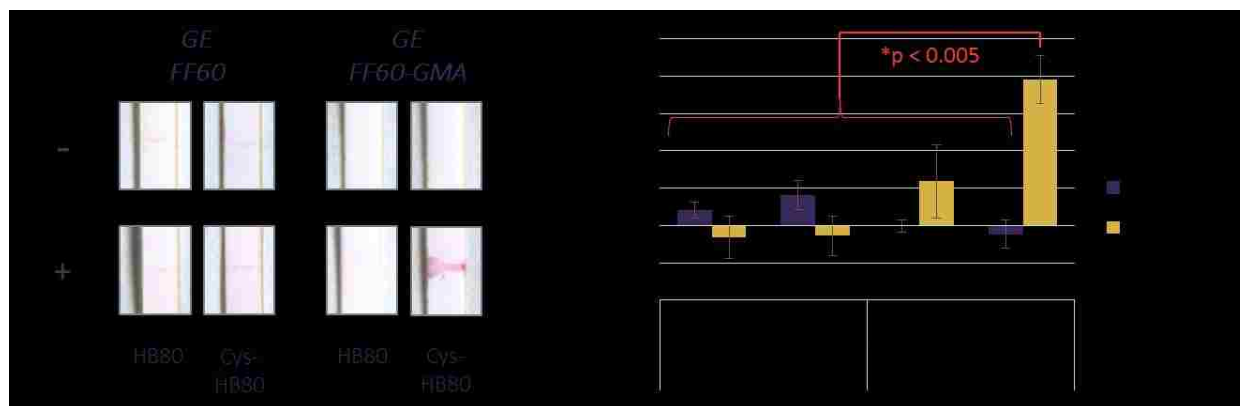


Figure 61. Functionality of thiolated flu binder immobilized to NC-GMA.

Functionality of thiolated flu binder cys-HB80.4 as a capture agent in the flu HA assay when immobilized to FF60-GMA by covalent attachment. For comparison, the functionality of HB80.4 on FF60-GMA and of both cys-HB80.4 and HB80.4 on FF60 were also tested. (A) Signal generated in the flu HA assay. (B) The corresponding normalized, background-subtracted, green-channel pixel intensities of the test lines plotted as the mean \pm SD of $n=4$ replicates.

For the flu assay, we used recombinant HA from A/New Caledonia/20/1999 influenza (Protein Sciences #rHA) at 100 nM and accompanying mouse-anti-HA antibody (AbCam #ab66189) at 100 nM. All reagents were diluted in a running buffer of PBS+BSA, and PBS was used for all washes in this experiment. Four replicates were run for each condition, in addition to four replicates of the negative control. After the assay was complete and the devices scanned, the average pixel intensity of each test line was quantified with my MATLAB program *quantifyColorimetricSignal.m*, using the green channel option. A representative test line for each condition is shown in Figure 61A, and the

corresponding normalized, background-subtracted, green-channel pixel intensities are plotted in Figure 61B as the mean +/- standard deviation of n=4 replicates for each condition.

These results clearly indicate, both qualitatively and quantitatively, that the only combination of membrane and flu binder that yields a functioning flu HA assay is NC-GMA with cys-HB80.4. For all other combinations, which rely on direct adsorption, no detectable signal was observed for the test concentration (100 nM HA) over negative controls. Statistically, the signal for cys-HB80.4 on FF60-GMA is greater than all other signals, including both test and negative controls ($p < 0.005$ for all comparisons by right-tailed, unpaired Student's *t*-test of unequal variance). Overall, we have established that the covalent attachment of thiolated flu binder to NC-GMA not only immobilizes the flu binder efficiently, but also immobilizes it in a functional form, allowing it to capture HA in this paper-based system. In the following sections, we explore additional improvements to the thiolated flu binder.

Improved Thiolated Flu Binder Functionality Using Polypeptide Linker

Since the covalent attachment of thiolated flu binder to NC-GMA proved to be successful, we investigated modifications to the thiolated flu binder to improve its functionality further. In particular, we were still concerned about the small size of the stem region flu

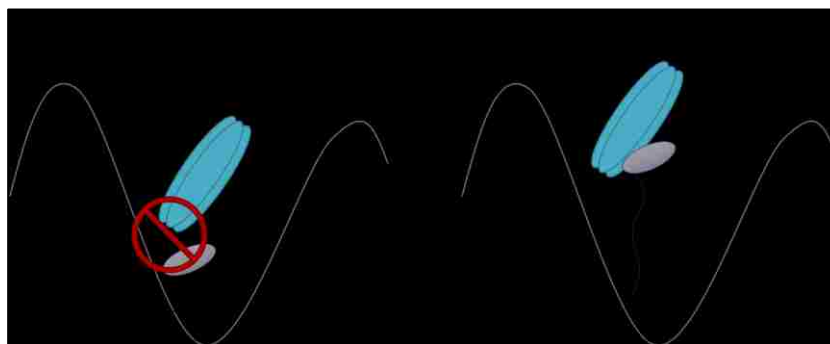


Figure 62. Illustration of flu binder immobilization with and without linker. Hypothesized benefit of adding a linker to the flu binder. Without a linker (left), the small flu binder (purple) may be inaccessible to HA (blue). Adding a linker (right) may improve HA capture by increasing the accessibility of the flu binder.

binder and that it may be partially inaccessible to passing HA due to local undulations of the nitrocellulose membrane. We hypothesized that adding a stalk of some sort would increase its accessibility and thereby improve its functionality, as depicted schematically in Figure 62. To this end, the Baker lab designed versions of the thiolated flu binder with polypeptide linkers between the binder and cysteine residue, employing repeats of the commonly used {Gly₄Ser} unit to form the linkers. Four different versions of these “binders with linkers” were generated, two with 20-amino acid (AA) linkers (4 {Gly₄Ser} repeats) and two with 35-amino acid linkers (7 {Gly₄Ser} repeats). For each set of two binders with linkers, one was generated with the linker on the amino (N)-terminus of the protein and the other on the carboxy I-terminus of the protein. Since all flu binders

are expressed with the FLAG tag (normally on the N-terminus), the FLAG tag was included in each of these binders on the opposite terminus of the linker. These four binders with thiolated linker are illustrated schematically in Figure 63 and abbreviated herein as follows:

- C-20 linker: FLAG-HB80.4- $\{\text{Gly}_4\text{Ser}\}_4\text{-Cys}$
- N-20 linker: Cys- $\{\text{Gly}_4\text{Ser}\}_4\text{-HB80.4-FLAG}$
- C-35 linker: FLAG-HB80.4- $\{\text{Gly}_4\text{Ser}\}_7\text{-Cys}$
- N-35 linker: Cys- $\{\text{Gly}_4\text{Ser}\}_7\text{-HB80.4-FLAG}$

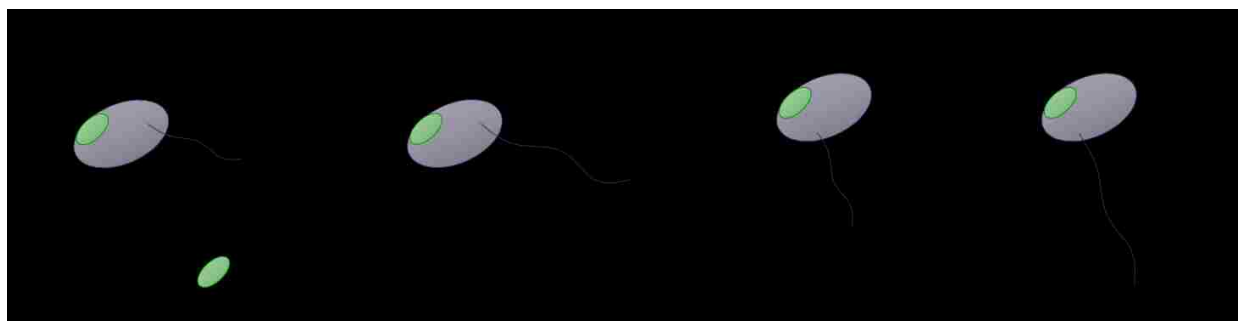


Figure 63. Stem region flu binders with polypeptide linkers.

Illustration of the four versions of the HB80.4 flu binder with thiolated linkers produced by the Baker lab.

The purity and initial HA-binding capacity of each linker construct was assessed by PhD graduate Dr. Aaron Chevalier of the Baker lab via gel and SPR, respectively. The N-20 linker construct did not purify well and therefore did not show HA binding by SPR, while the other three constructs passed these initial screening measures. The N-20 construct was therefore not tested in our paper assay, while the other three were moved forward for testing.

To test the functionality of each binder-with-linker construct on paper, we used the bench-top flu HA assay, as described above. In order to elucidate the benefit of the linker, these binders were compared to the non-linker thiolated flu binder, cys-HB80.4. Since all flu binders investigated in this experiment were thiolated, we tested only NC-GMA (FF80HP-GMA) as the substrate, which is the only type of membrane that yields a functional assay for thiolated flu binders. All flu binders were spotted at 100 μM in HBS, and the spotted membranes were dried at room temperature under desiccation overnight before use.

For the flu assay, we used recombinant HA from A/New Caledonia/20/1999 influenza (Protein Sciences #rHA) at 100 nM and accompanying mouse-anti-HA antibody (AbCam #ab66189) at 100 nM. All reagents were diluted in a running buffer of PBS+BSA, and PBS was used for all washes in this experiment. Three replicates were run for each condition, in addition to three replicates of the

negative control. After the assay was complete and the devices scanned, the average pixel intensity of each test line was quantified with my MATLAB program *quantifyColorimetricSignal.m*, using the green channel option. A representative test line for each condition is shown in Figure 64A, and the corresponding normalized, background-subtracted, green-channel pixel intensities are plotted in Figure 64B as the mean \pm standard deviation of $n=3$ replicates for each condition.

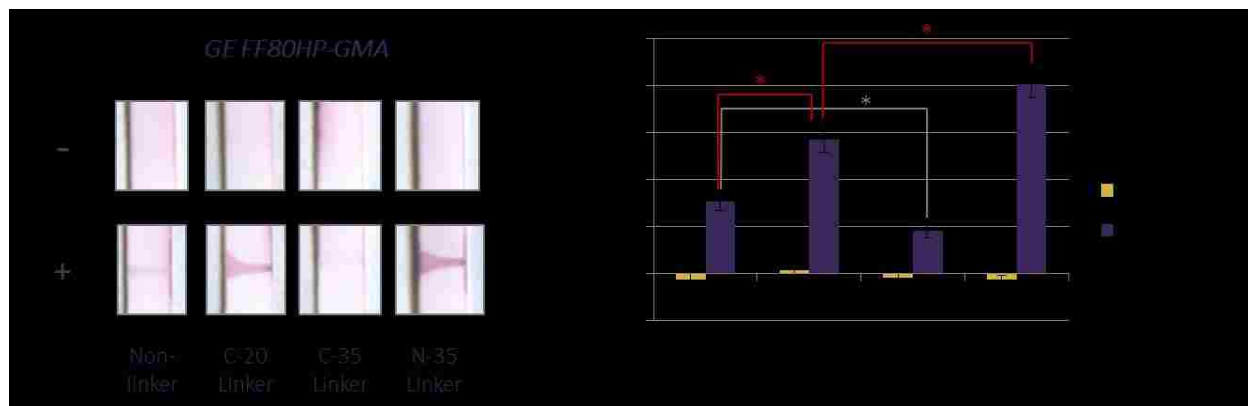


Figure 64. Functionality of flu binders with thiolated linkers immobilized to NC-GMA.

Functionality of flu binders with thiolated linkers as capture agents in the flu HA assay when immobilized to FF80HP-GMA by covalent attachment. For comparison, the functionality of non-linker cys-HB80.4 was also tested. (A) Signal generated in the flu HA assay for each flu binder. (B) The corresponding normalized, background-subtracted, green-channel pixel intensities of the test lines plotted as the mean \pm SD of $n=3$ replicates. Asterisk (*) denotes significant difference ($p < 0.01$) by right-tailed, unpaired Student's t -test of unequal variance.

These results indicate that, in general, adding the linker to flu binder improves its functionality, as hypothesized. Specifically, both the C-20 and N-35 linker constructs yield signal that is significantly higher than that produced by non-linker cys-HB80.4 ($p < 0.005$ by right-tailed, unpaired Student's t -test of unequal variance). Of these two linker constructs, the N-35 linker produces even greater signal than C-20 ($p = 0.0034$), indicating that this N-35 linker is best of the four linker constructs. The non-linker cys-HB80.4 outperformed only the C-35 linker construct ($p = 0.0059$). We do not know why this C-35 construct performed so poorly, since it shares its length with the N-35 construct and its linker location with the C-20 construct, both of which were highly functional. Nevertheless, we have established that linkers generally do improve flu binder functionality and the N-35 linker construct provides a viable option for a capture agent in the flu HA assay.

Finally, the overall signal levels observed for this assay were lower than expected. Specifically, the signal for non-linker cys-HB80.4 here was much less intense than observed previously for the same assay (Figure 61). The only known difference was the exact membrane used, with GE FF80HP-GMA used here, and GE FF60-GMA used previously. However, additional testing revealed only minor differences, if any, due to different membrane versions and lots. Therefore, this discrepancy was the

first hint of the high variability in signal experienced for this covalent attachment method. This issue was further investigated, as described at the end of this section.

Functional Comparison of HB80.4 and HB36.5 Flu Binders by SPR

In addition to the linker constructs described above, we also explored flu binders based on an alternate protein scaffold to HB80. As described in section 2.4.2, the Baker lab also created another set of stem region flu binders, HB36, based on an alternate scaffold protein that is slightly larger and has much higher stability. The goal of this SPR session was to test the HA-binding capacity of the newly developed HB36.5 flu binder variants for hemagglutinin (HA). As a point of reference, we also tested HB80.4 and cys-HB80.4, both of which were known to bind HA well, based on previous experiments from the Baker lab. For this experiment, we used the Biacore T100 and the Biacore Biotin CAPture chip, as described in section 4.4.1. For the biotinylated HA, we used biotinylated H1 HA from A/Solomon Islands/3/2006 (H1N1) influenza, which was provided to us from the Baker lab via an external collaborator who makes the HA recombinantly. While this is an H1 HA and is therefore an HA that both HB80.4 and HB36.5 should bind, it was not a strain that had been tested before for the flu binder.

The biotinylated HA was used at 300 nM, and flu binders were tested at 10 nM, the concentration for which was determined by scouting. We used HBS-EP as the running buffer, and made all sample dilutions in this buffer. In total, our SPR experiment included seven cycles testing the following flu binders:

- HB80.4 @ 10 nM
- HB80.4_K315C (“cys-HB80.4”) @ 10 nM
- HB36.5 @ 10 nM
- HB36.5_H312A @ 10 nM
- HB36.5_Q265C @ 10 nM
- HB36.5_A276C @ 10 nM
- HB36.5_A341C @ 10 nM

Each sample cycle consisted of the steps listed in Table 10, run via the manual acquisition method.

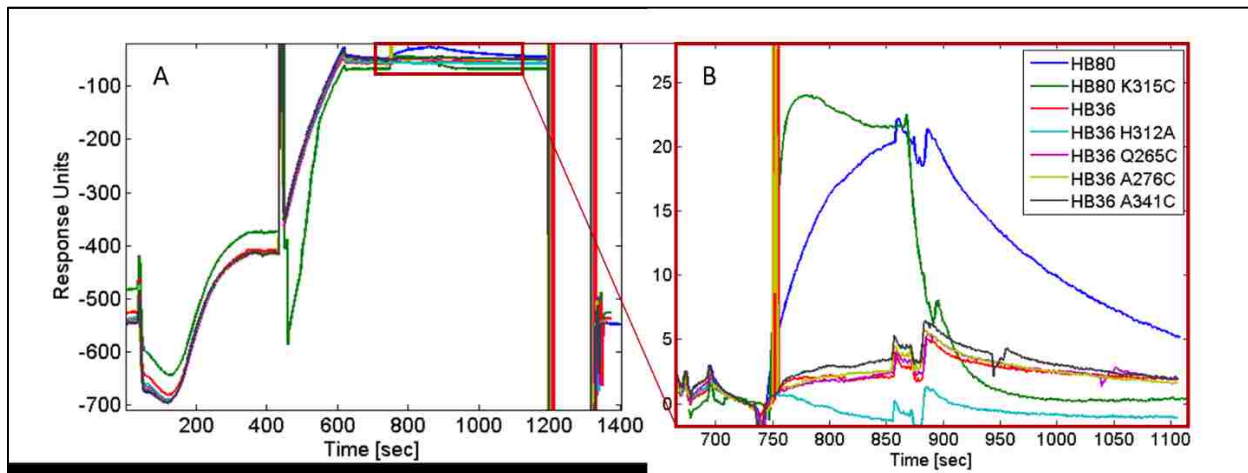


Figure 65. SPR results comparing HA-binding of HB80.4 and HB36.5 flu binder variants.

(A) Full SPR curves for all sample cycles, including all steps of the experimental cycle. (B) Inset from red box in (A) shows the SPR curves for the step of interest for each cycle: the interaction between each flu binder and the HA immobilized on the SPR chip.

The resulting full SPR curves are shown in Figure 65A. The step of interest, namely the interaction between each flu binder and the HA immobilized on the SPR chip, is outlined in the red box and expanded in Figure 65B. Unfortunately, since I was only able to run one concentration per binder, I was unable to fit the data with binding curves to obtain any quantitative kinetic or thermodynamic constants for these binding interactions. The qualitative results are useful, though, and show that, as expected, HB80.4 binds this strain of HA well. Interestingly, HB80.4_K315C (cys-HB80.4) seems to have both a higher on-rate and off-rate, binding HA quickly and then falling off quickly, as compared to regular HB80.4. All of the HB36.5 variants bind this strain of HA much worse than the HB80.4 variants, which was unexpected. It is possible, however, that the low affinity of the HB36 variants observed here (relative to HB80) is due to the specific strain of HA tested (A/Solomon Islands/3/A2006), and that we would observe better signal for the strain we were testing in our paper assay (A/New Caledonia/20/1999). We therefore moved on to testing these binders in our paper flu assay, which is described in the next section.

Improved Thiolated Flu Binder Functionality Using Alternate Scaffold HB36.5

Since the thiolated flu binder cys-HB80.4 (HB80.4_K315C) proved to be an effective capture agent when immobilized to NC-GMA via covalent attachment, we aimed to test the functionality of the analogous cys-HB36.5 flu binder variants, based on the more stable HB36 scaffold. To do so, we used the bench-top flu HA assay, as described above. Since the Baker lab developed three different cys-HB36.5 variants, each based on the mutant of a different amino acid to a cysteine, we compared

the functionality of each of these variants to that of cys-HB80.4. Since all flu binders investigated in this experiment were thiolated, we tested only NC-GMA (FF80HP-GMA) as the substrate, which is the only type of membrane that yields a functional assay for thiolated flu binders. Since the concentrations of the HB36 variants were low, we were not able to spot each flu binder at the usual concentration of 100 μ M. Instead, each HB36 variant was spotted at its stock concentration (HB36.5_Q265C at 42 μ M, HB36.5_A276C at 23 μ M, and HB36.5_A341C at 60 μ M), and cys-HB80.4 was spotted at the highest matching concentration (60 μ M). All spotted membranes were dried at room temperature under desiccation for two days before use.

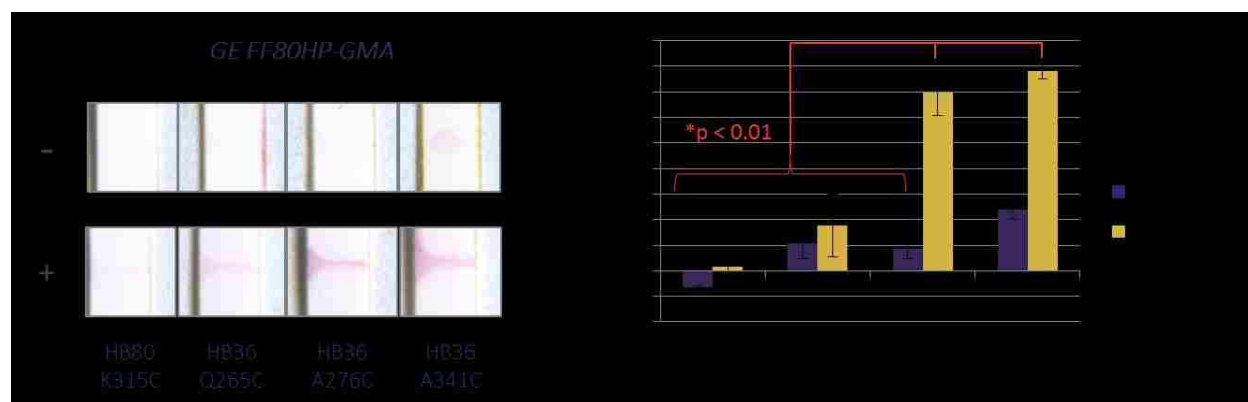


Figure 66. Functionality of cys-HB36.5 flu binder variants immobilized to NC-GMA.

Functionality of cys-HB36.5 flu binder variants as compared to cys-HB80.4 (HB80.4_K315C). All four thiolated flu binders were immobilized to FF80HP-GMA by covalent attachment. (A) Signal generated in the flu HA assay for each flu binder. (B) The corresponding normalized, background-subtracted, green-channel pixel intensities of the test lines plotted as the mean \pm SD of $n=3$ replicates.

For the flu assay, we used recombinant HA from A/New Caledonia/20/1999 influenza (Protein Sciences #rHA) at 100 nM and accompanying mouse-anti-HA antibody (AbCam #ab66189) at 100 nM. All reagents were diluted in a running buffer of PBS+BSA, except for the HA sample, which was diluted in PBST + 1% BSA to prevent nonspecific binding of this particular lot of HA. PBS was used for all washes in this experiment. Three replicates were run for each condition, in addition to three replicates of the negative control. After the assay was complete and the devices scanned, the average pixel intensity of each test line was quantified with my MATLAB program *quantifyColorimetricSignal.m*, using the green channel option. A representative test line for each condition is shown in Figure 66A, and the corresponding normalized, background-subtracted, green-channel pixel intensities are plotted in Figure 66B as the mean \pm standard deviation of $n=3$ replicates for each condition.

These results indicate that two of the cys-HB36.5 variants (HB36.5_A276C and HB36.5_A341C) yield significantly higher signal than cys-HB80.4 ($p < 0.01$ by right-tailed, unpaired Student's *t*-test of unequal variance). Of these two variants, HB36.5_A276 yields the highest signal-to-noise ratio, based on the comparison of signal for the test concentration (100 nM HA) and negative control, making this the top-performing variant of all thiolated flu binder variants tested. Fortunately, this binder was spotted at the lowest concentration of the four, ensuring that it did not yield higher signal because of its concentration, but instead in spite of its concentration. Interestingly, the superiority of HB36.5 over HB80.4 in this paper-based assay contradicts the opposite results observed by SPR. This discrepancy is due either to the difference in the strain of HA used in these experiments, to the difference in immobilization of flu binder in this experiment, or some combination thereof. Overall, we have further improved the flu HA assay with the use of HB36.5_A276C, and we continued on with further development using this cys-HB36.5 variant.

Finally, in this experiment, we again observed extremely low signal for cys-HB80.4 on NC-GMA compared to the strong signal observed previously for this binder (Figure 61). We therefore investigated this variability in signal for the covalent attachment of thiolated flu binders to GMA-modified nitrocellulose, described in the following two sections.

Variability Issues for Thiolated Flu Binder Assay and Testing of Immobilization to Maleimide-Functionalized Nitrocellulose

Given the initial observations of the variability in signal for cys-HB80.4 as a capture agent for the flu HA assay when immobilized covalently to GMA-modified nitrocellulose, we continued evaluating this assay system. Concurrently, we also investigated the use of another novel membrane from GE GRC, maleimide-functionalized nitrocellulose, as an alternate means for covalent attachment of thiolated flu binders.

The use of NC-maleimide was compared to NC-GMA for the covalent attachment of thiolated flu binder cys-HB80.4. This flu binder was spotted at 100 μ M. As usual, the immobilization efficiency was tested via lateral flow challenge, using challenge solutions of PBS and PBST, and protein visualization with Ponceau S staining. After the staining was complete and the devices scanned, the average pixel intensity of each test line was quantified using my MATLAB program *quantifyColorimetricSignal.m*, using the green channel option. A representative test line for each LF condition is shown in Figure 67A, along with the corresponding normalized pixel intensities, plotted as the mean \pm standard deviation of $n=3$ replicates for each condition.

The functionality of the flu binder as a capture agent for the flu HA assay was also evaluated. For the flu assay, we used recombinant HA from A/New Caledonia/20/1999 influenza (Protein Sciences #rHA) at 100 nM and accompanying mouse-anti-HA antibody (AbCam #ab66189) at 100 nM. All reagents were diluted in a running buffer of PBS+BSA, except for the HA sample, which was diluted in PBST + 1% BSA to prevent nonspecific binding of this particular lot of HA. PBS was used for all washes in this experiment. Four replicates were run for each condition, in addition to four replicates of the negative control. After the assay was complete and the devices scanned, the average pixel intensity of each test line was quantified using my MATLAB program *quantifyColorimetricSignal.m*, using the green channel option. A representative test line for each condition is shown in Figure 67B, along with the corresponding normalized pixel intensities, plotted as the mean +/- standard deviation of n=4 replicates for each condition.

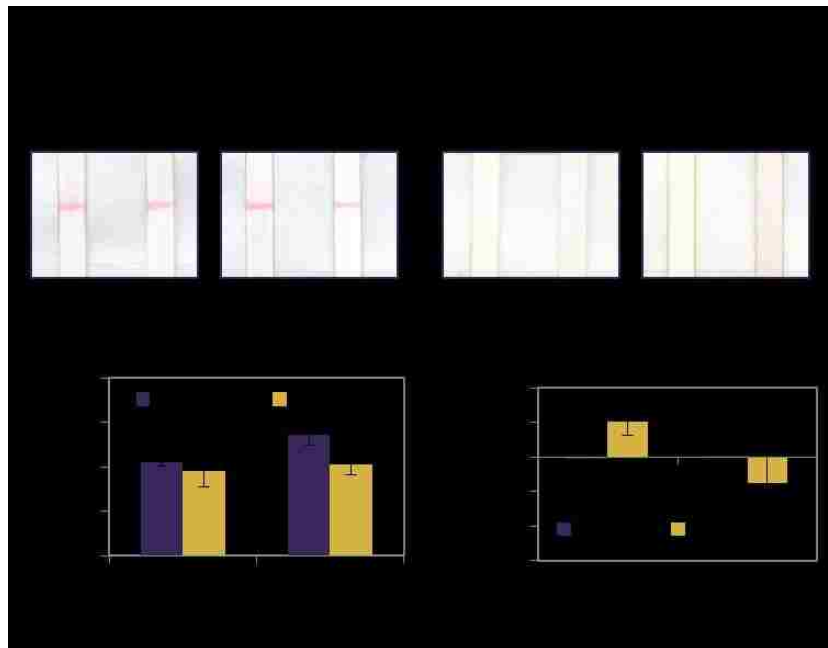


Figure 67. Comparison of NC-GMA and NC-maleimide.

The covalent attachment of thiolated flu binder cys-HB80.4 is compared for FF80HP-GMA and FF80HP-maleimide membranes. (A) Immobilization efficiency via lateral flow challenge and Ponceau S staining. (B) Flu binder functionality as a capture agent for the flu HA assay. The FF80HP-GMA membrane yields very low signal (much lower than previously observed for this assay), while the FF80HP-maleimide membrane yields no assay signal.

The LF challenge data shows that FF80HP-maleimide is able to immobilize cys-HB80.4 fairly well, although it yields some stripping under challenge by PBST, which is not observed for FF80HP-GMA. The flu HA assay yielded no signal for FF80HP-maleimide. However, the assay also yielded very little signal for FF80HP-GMA, which had shown good signal in the past and was our positive control. These results therefore further exposed the variability issue for these functionalized membranes.

At this point, we were battling this variability in covalent immobilization of flu binder, on top of several quality control problems with reagents. A summary of the declining signal observed for this flu HA assay system is provided in Figure 68A. We therefore performed a side-by-side comparison

of the flu HA assay on two different lots of FF80HP-GMA, as well as the new FF80HP-maleimide membrane. We also compared cys-HB80.4 and cys-HB36.5 (HB36.5_A276C). For this assay, the two flu binders were spotted at 40 μ M, instead of the usual 100 μ M, since 40 μ M was the highest common concentration achievable. We used recombinant HA from A/New Caledonia/20/1999 influenza (Protein Sciences #rHA) at 100 nM and accompanying mouse-anti-HA antibody (AbCam #ab66189) at 100 nM. All reagents were diluted in a running buffer of PBST + BSA. (We switched to adding Tween-20 to all reagents to mitigate nonspecific binding problems.) PBS was used for all washes in this experiment. Four replicates were run for each condition, in addition to four replicates of the negative control. A representative test line for each condition is shown in Figure 68B.

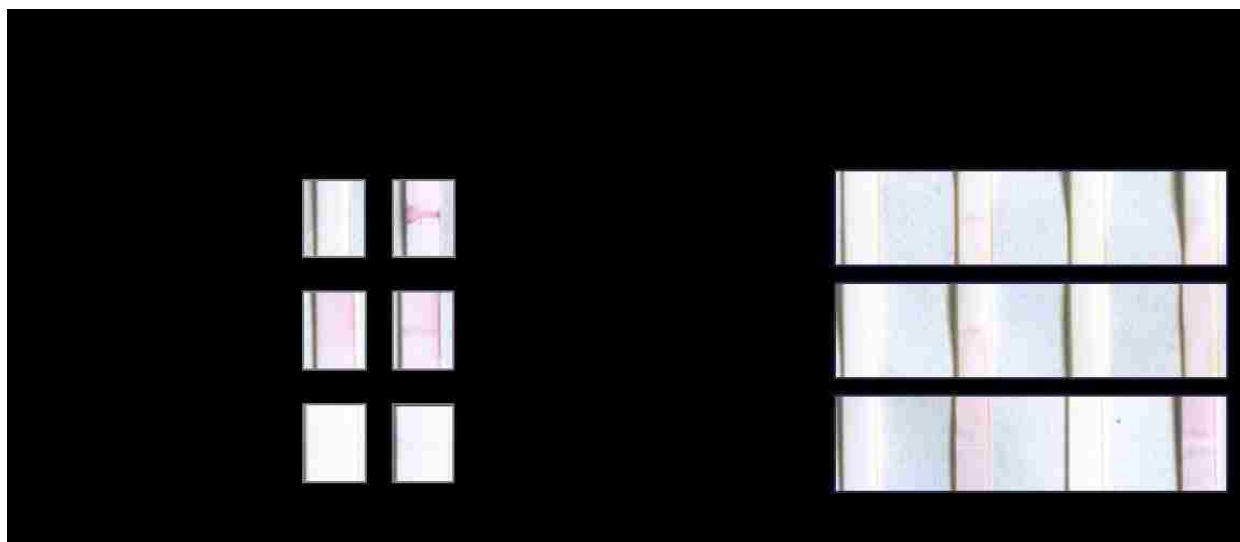


Figure 68. Comparison of assay signal on NC-GMA and NC-maleimide membranes.

The variability of flu HA assay signal for thiolated flu binder on NC-GMA membranes was investigated. The use of NC-maleimide was also tested. (A) Summary of the declining flu HA assay signal observed across previous experiments for cys-HB80.4 on NC-GMA. The batch date of each NC-GMA membrane is provided, in addition to the date on which the assay was performed. (B) Side-by-side comparison of cys-HB80.4 and cys-HB36.5 on two different NC-GMA membranes, in addition to the NC-maleimide membrane.

These results helped us understand several aspects of the signal variability problem we were facing. First, the comparison of different experiments in Figure 68A shows that we had observed a distinct decline in assay signal over time. Second, the side-by-side comparison of two different batches of NC-GMA in Figure 68B shows that, when tested at the same time, with the same exact reagents, the two membranes perform similarly. Therefore, these results revealed that our variability problem was not due to the age of the membrane, but instead to some other aspect of the assay. Finally, despite the low assay signal on NC-GMA observed here, the comparison to NC-

maleimide confirmed that NC-maleimide does not immobilize thiolated flu binder in a functional manner. Therefore, we deemed this membrane to be non-functional for our assay purposes.

Effect of TCEP on Thiolated Flu Binder Functionality

Since we had ruled out the membrane age as being a primary factor in the variability in assay signal observed for the NC-GMA membrane, we turned our attention to the chemistry of the thiolated flu binder. Using a new set of assay reagents (recombinant HA and detection antibody) from the Influenza Reagent Resource (IRR), we revisited the use of thiolated flu binder on NC-GMA. Specifically, our collaborators at GE GRC had hypothesized that the TCEP added to the thiolated flu binder solutions upon preparation may get oxidized over time, thereby reducing its ability to serve as a reducing agent. We therefore hypothesized that adding fresh TCEP to the thiolated flu binder solution prior to spotting on NC-GMA would result in improved performance.

To test this hypothesis, we prepared solutions of thiolated flu binder cys-HB36.5 (HB36.5_A276C) with 0, 10, 100, or 1000 μM additional TCEP (TCEP-HCl, Thermo Scientific #20490). Note that this TCEP is in addition to the 1 mM TCEP that had been included in the original flu binder preparation by the Baker lab seven months earlier, which we presumed was now oxidized. These flu binder solutions were spotted at 20 μM , the highest concentration achievable.

As usual, the immobilization efficiency was tested via lateral flow challenge, using challenge solutions of PBS and PBST, in addition to no-flow controls. Protein was visualized with Ponceau S staining. After the staining was complete and the devices scanned, the average pixel intensity of each test line was quantified using my MATLAB program *quantifyColorimetricSignal.m*, using the green channel option. A representative test line for each LF condition is shown in Figure 69A, along with the corresponding normalized pixel intensities, plotted as the mean \pm standard deviation of $n=3$ replicates for each condition.

The functionality of the flu binder as a capture agent for the flu HA assay was also evaluated. For the flu assay, we used recombinant HA from A/California/04/2009 (H1N1) ("CA2009") influenza (IRR #FR-180, lot #59007343, 91% trimer) at 100 nM and accompanying mouse-anti-HA antibody (IRR #FR-505, "CA09/Ab2") at 100 nM. All reagents were diluted in a running buffer of PBST+BSA, and PBST was used for all washes in this experiment. Three replicates were run for each condition, in addition to three replicates of the negative control. After the assay was complete and the devices scanned, the average pixel intensity of each test line was quantified using my MATLAB program

quantifyColorimetricSignal.m, using the green channel option. A representative test line for each condition is shown in Figure 69B, along with the corresponding normalized pixel intensities, plotted as the mean \pm standard deviation of $n=3$ replicates for each condition.

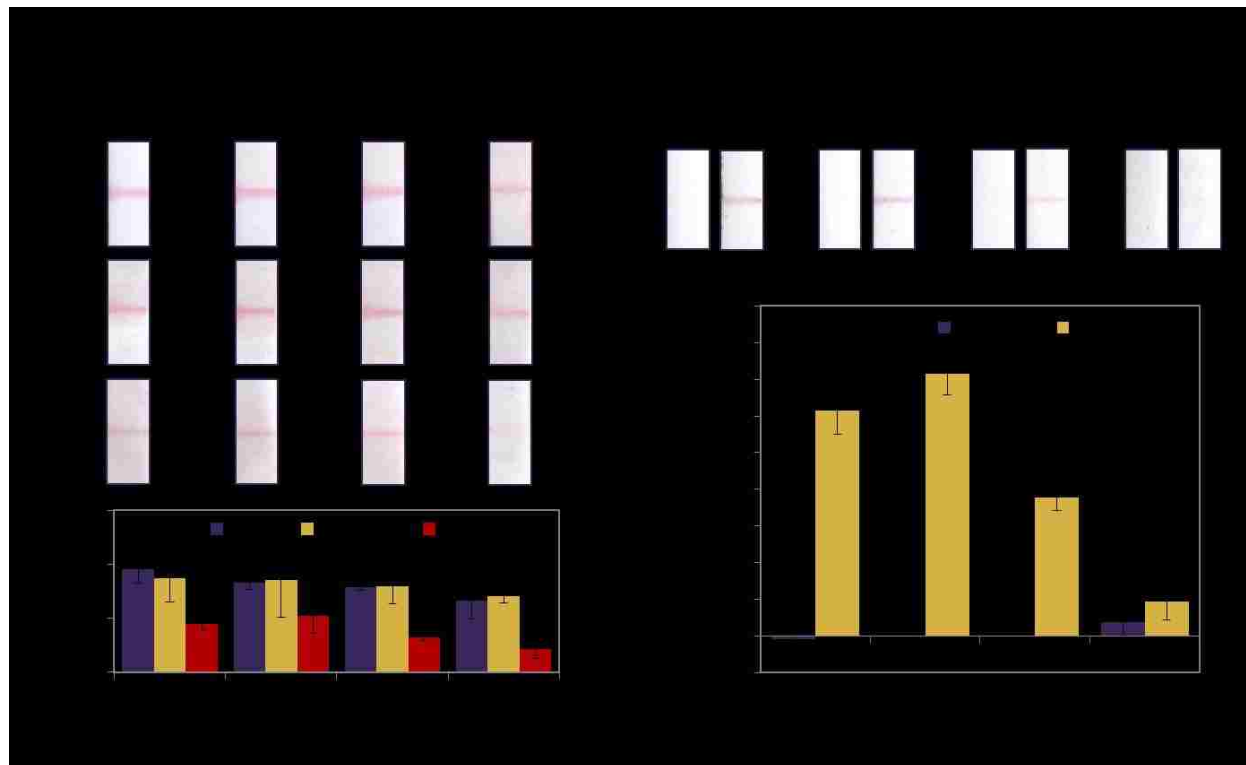


Figure 69. Effect of added TCEP on cys-HB36.5 performance.

The covalent attachment of thiolated flu binder cys-HB36.5 was evaluated as a function of the amount of TCEP added. (A) Immobilization efficiency via lateral flow challenge and Ponceau S staining. (B) Flu binder functionality as a capture agent for the flu HA assay.

These results show that the addition of extra TCEP to the cys-HB36.5 flu binder preparation prior to spotting does not greatly affect its immobilization efficiency. The flu binders with 0, 10, and 100 μ M added TCEP all yield similar levels of stripping under challenge by PBST, while the addition of 1 mM TCEP begins to yield more considerable desorption. However, the flu HA assay results show a clear trend of decreasing signal for increasing concentration of added TCEP. This result was surprising, since it contradicts our previous optimization work that showed the addition of 1 mM TCEP yielded improved performance of no TCEP (Figure 59) and our successful use of TCEP in the thiolated flu binder preparations thereafter. In this case, though, the TCEP added was in addition to the original 1 mM TCEP already present. Taken together, these results indicate that this added TCEP disrupts flu binder performance not by reducing the efficacy of its attachment to NC-GMA (at least not primarily), but instead by diminishing its functionality in some way. One possible

contributing factor is the acidity introduced by the large amounts of TCEP, which was added in the form of TCEP-HCl.

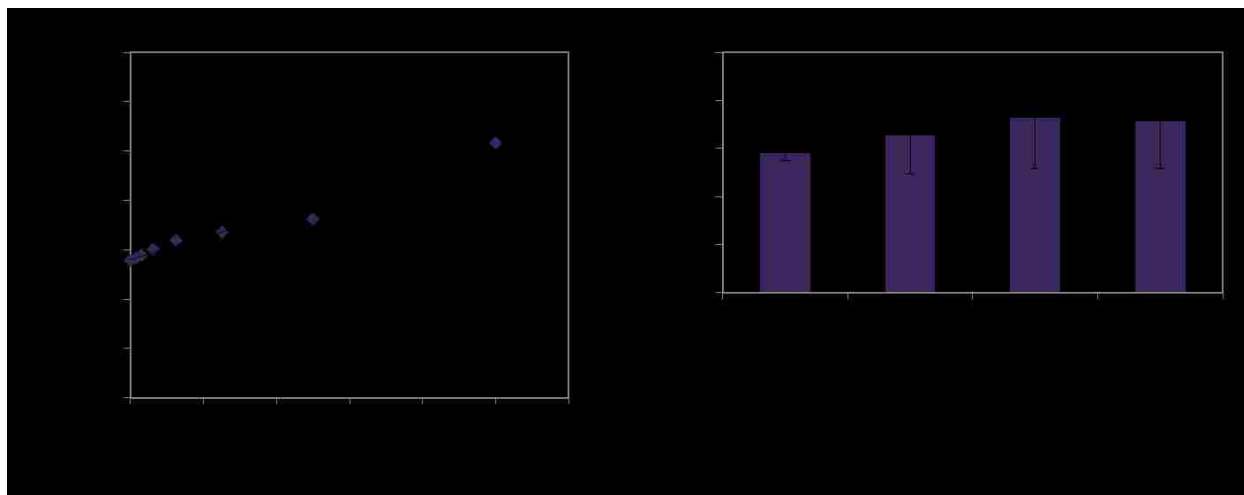


Figure 70. Fluorothiol assay for quantification of reduced thiol content in flu binder samples.

Use of the commercial fluorothiol assay kit for quantification of the reduced thiol content in cys-HB36.5 prepared with 10, 100, or 1000 μM additional TCEP, a reducing agent. (A) Standard curve generated with GSH. (B) Resulting thiol quantification of the flu binder samples, which were all out of range of the standard curve, and of the maximum theoretically possible amount of reduced thiol (20 μM).

Adding to the complexity of these results, we also evaluated the cys-HB36.5 + TCEP preparations for their thiol content to determine if the added TCEP did indeed result in an increased concentration of reduced thiols. Using the fluorothiol assay described above, we obtained the GSH standard curve shown in Figure 70A, and the resulting thiol concentrations plotted in Figure 70B as the mean \pm SD for three replicate readings. While quantification of the standard curve worked successfully, the resulting thiol concentrations of the flu binder solutions were nonsensical. Specifically, all four preparations yielded thiol concentrations above 1000 μM , which is not possible, since the thiolated flu binder contains a single cysteine per molecule and was only present at 20 μM . This erroneous result may have been compounded by the fact that the calculated thiol concentrations were outside of the range of the concentration curve (which covered the range of theoretically possible thiol concentrations for the flu binders). We therefore do not know what caused these high thiol readings, but these results highlight the need to focus carefully on the thiol chemistry at hand for thiolated flu binder attachment to NC-GMA.

Overall, while this method of covalent attachment echoes previous thiol-based immobilization strategies for other assay substrates [13,155–157], it is the first demonstration of the covalent immobilization of a protein affinity reagent on functionalized nitrocellulose membrane, to our knowledge. However, the above studies of thiolated flu binder on NC-GMA suggest that this

immobilization system is highly dependent upon the specific chemical properties of the flu binder solution, as they affect both its covalent attachment to the membrane and its functional performance of a capture agent. Therefore, while we have demonstrated a promising, novel immobilization strategy for the covalent attachment of thiolated affinity proteins to modified nitrocellulose, this system requires further optimization for performance and reliability, with specific attention to the protein chemistry, especially for long-term storage. We also recognize that this method is less feasible for researchers without access to this high level of membrane manipulation, so we sought to develop more broadly applicable techniques as well. These methods are described next.

4.5. Immobilization by Streptavidin-Biotin Anchoring

Since streptavidin-biotin systems have commonly been employed for surface immobilization of affinity reagents [13], and since we have the ability to customize our recombinant flu binders, we investigated the immobilization of biotinylated flu binder to nitrocellulose via a streptavidin anchor. This strategy, however, depends critically on the robust immobilization of streptavidin to nitrocellulose by direct adsorption, which was not previously characterized in the literature. We therefore investigated the adsorption of streptavidin to nitrocellulose in depth and established that it binds slowly to nitrocellulose and is prone to desorption in the presence of salt (PBS) and especially detergent (PBST) (see section 3.3). Based on these results, we expected that regular, recombinant streptavidin would not make a successful anchor for the immobilization of biotinylated flu binder. We therefore identified an alternative protein that is a mutant version of streptavidin that was engineered to bind to nitrocellulose (AbCam #51404). While the sequence of this commercial product is proprietary, we do know that its molecular weight is 96 kDa, compared to ~60 kDa for regular streptavidin, which implies that a NC-binding moiety has been added to the protein. Additionally, both the manufacturer's data and our own IEF analysis reveal that this mutant streptavidin has a pI of ~9, which is considerably higher than regular recombinant streptavidin, whose pI is ~7 (see section 3.6, Table 7). A main focus of this section was therefore to characterize the utility of this mutant streptavidin, as compared to regular, recombinant streptavidin. As usual, we compared both the immobilization efficiency and functionality of each protein in a flu HA assay. Finally, we further optimized the system by adding a biotin-BSA wash step, as described at the end of this section.

4.5.1. Methods

Immobilization Testing via Lateral Flow Challenge

The immobilization efficiency of regular, recombinant streptavidin was tested using the lateral flow challenge system described in section 4.2.1 and compared to a nitrocellulose-binding mutant version of streptavidin.

Functionality Testing via Flu Hemagglutinin Assay

The functionality of biotinylated stem region flu binder biotin-HB80.4 was tested as a capture agent for the flu HA assay, as described in section 4.2.2, when anchored to the membrane by regular vs. mutant streptavidin. Additionally, the assay with the mutant streptavidin anchor was further tested with and without a biotin-BSA wash, using biotin-HB36.5 as the affinity reagent. The biotinylated flu binders were produced in the Baker lab by recombinantly expressing a version of the flu binder with a C-terminal AVI tag, a patented peptide sequence (GLNDIFEAQKIEWHE) for site-specific biotinylation [182,183]. The purified protein was then biotinylated enzymatically using the biotin ligase *BirA*, which specifically recognizes the AVI tag and adds a biotin moiety at that location. This process results in a flu binder that has a single, site-specific biotin moiety on each flu binder protein, with the site of biotin attachment (C-terminus) being located on the opposite side of the binding paratope. Biotinylation was confirmed by the Baker lab using mass spectrometry.

4.5.2. Results and Discussion

Immobilization of Regular vs. Mutant Streptavidin to Nitrocellulose

The ability of NC-binding mutant streptavidin (AbCam #51404) to be immobilized to nitrocellulose by direct adsorption was assessed using the lateral flow challenge method. In order to make a side-by-side comparison, the adsorption of regular, recombinant streptavidin (Thermo Scientific #21125) was also tested. Since we did not know *a priori* which nitrocellulose membrane would provide the best immobilization, we tested the following four membranes:

- Millipore HFB135
- GE FF80HP
- GE FF80HP-GMA
- GE FF80HP-PEG

Both streptavidin proteins were spotted at 1 mg/mL in

PBS using the piezoelectric spotter, and membranes were dried at room temperature under desiccation for two days before use.

Lateral flow challenge solutions of PBS and PBST were tested (50 μ L per strip), along with no-flow controls. After lateral flow challenge, protein was visualized using Ponceau S staining. The stained devices were imaged on a desktop scanner, and the average pixel intensity of each test line was

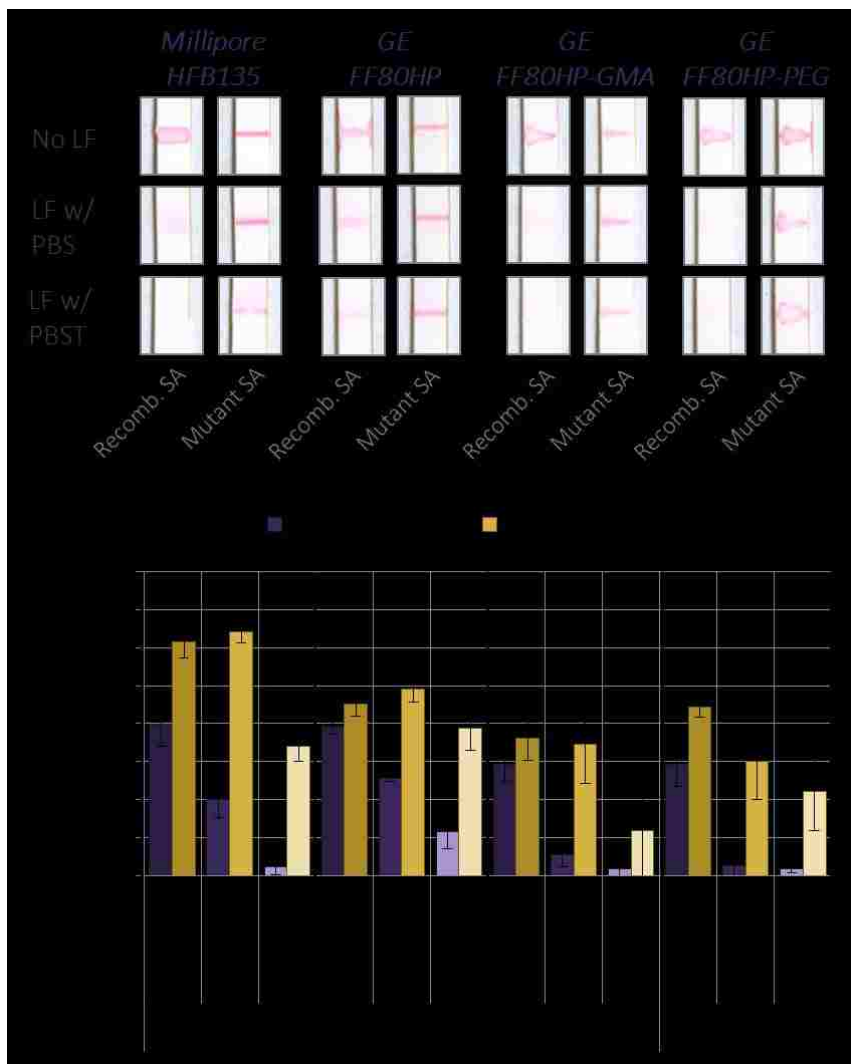


Figure 71. Immobilization of regular vs. NC-binding mutant streptavidin. Adsorption of regular, recombinant streptavidin (SA) vs. NC-binding mutant streptavidin SA. (A) Protein remaining after lateral flow (LF) challenge. (B) Corresponding normalized pixel intensities of the protein lines plotted as the mean \pm SD of n=6 replicates of each condition.

quantified with my MATLAB program *quantifyColorimetricSignal.m*, using the green channel option. Representative images of the streptavidin test lines are shown in Figure 71A, and the corresponding normalized green-channel pixel intensities of the test lines are plotted in Figure 71B as the mean +/- standard deviation of n=6 replicates for each condition.

These results clearly show that the NC-binding mutant streptavidin adsorbs to nitrocellulose much more robustly than regular recombinant streptavidin. In particular, recombinant streptavidin is prone to substantial stripping by PBS and nearly complete stripping by PBST on all four membranes. Mutant streptavidin, on the other hand, is not significantly stripped by PBS and is only mildly stripped by PBST, with results varying by membrane. As for the four different membranes tested, GE FF80HP yields the least desorption overall, which is consistent with previous adsorption studies. Millipore HFB135 yields intermediate desorption, while both FF80HP-GMA and FF80HP-PEGMA are most susceptible to stripping. Now that we have established the adsorption of each streptavidin protein, the ability of each protein to serve as an anchor for biotinylated flu binder is described in the next section.

Functionality of Biotinylated Flu Binder HB80.4 Anchored by Regular vs. Mutant Streptavidin

The functionality of biotinylated flu binder b-HB80.4 immobilized to nitrocellulose via streptavidin anchoring was assessed using the bench-top flu HA assay above. The use of NC-binding mutant streptavidin (AbCam #51404) as the anchor was compared directly to the use of regular, recombinant streptavidin (Thermo Scientific #21125). Since we did not know *a priori* which nitrocellulose membrane would provide the best results, we tested the following four membranes, each of which was tested for immobilization in the section above:

- Millipore HFB135
- GE FF80HP
- GE FF80HP-GMA
- GE FF80HP-PEG

Both streptavidin proteins were spotted at 1 mg/mL in PBS using the piezoelectric spotter, and membranes were dried at 37 °C for one hour, then stored at room temperature under desiccation overnight before use. Note that this is a slightly different drying protocol than the one used for the immobilization study (desiccation only); due to a mix-up in the experimental design, exactly matching protocols were not used.

For the flu assay, we used recombinant HA from A/New Caledonia/20/1999 influenza (Protein Sciences #rHA) at 100 nM and accompanying mouse-anti-HA antibody (AbCam #ab66189) at 100 nM. All reagents were diluted in a running buffer of PBS+BSA, except for the HA sample, which was diluted in PBST + 1% BSA to prevent nonspecific binding of this particular lot of HA. PBS was used for all washes in this experiment. After the assay was complete and the devices scanned, the average pixel intensity of each test line was quantified with my MATLAB program *quantifyColorimetricSignal.m*, using the green channel option. A representative test line for each condition is shown in Figure 72A, and the corresponding normalized green-channel pixel intensities are plotted in Figure 72B as the mean +/- standard deviation of n=4 replicates for each condition.

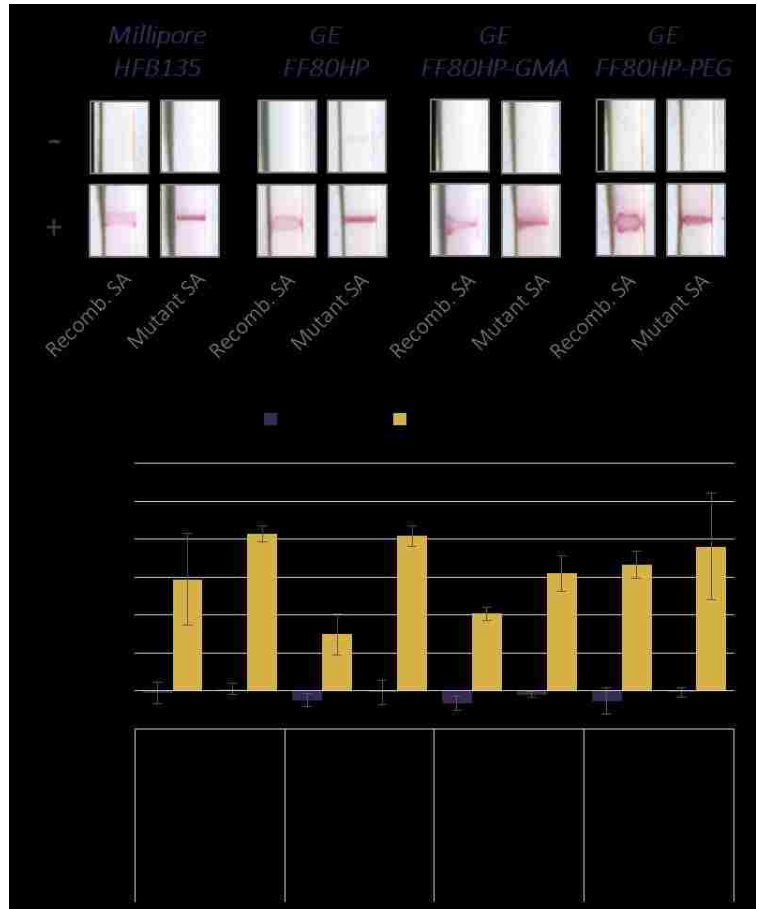


Figure 72. Regular vs. mutant streptavidin anchoring of b-HB80.4. Utility of regular recombinant streptavidin (SA) and NC-binding mutant SA as anchors for biotinylated flu binder b-HB80.4. (A) Signal generated in the flu HA assay for anchor. (B) The corresponding normalized, green-channel pixel intensities of the test lines plotted as the mean +/- SD of n=4 replicates.

These results indicate that the NC-binding mutant streptavidin yields overall stronger assay signal than regular recombinant streptavidin for all four membranes tested. The regular streptavidin still yields a reasonable signal, however, considering its susceptibility to desorption under lateral flow challenge. However, in future versions of the assay, we added Tween to all reagents of the system, providing further opportunity for stripping of the anchor. We therefore moved forward with the NC-binding mutant streptavidin as the anchor of choice.

Finally, to reduce the low level of false-positive signal observed for the negative controls for the mutant streptavidin anchor system (see Figure 72), we added biotinylated bovine serum albumin (BSA) to the first wash step to block any unused streptavidin and prevent the nonspecific binding of other assay reagents to the test line, particularly the gold-conjugated secondary antibody. We also optimized the reagent delivery strategy, ultimately choosing to premix the HA antigen with the biotinylated flu binder and the primary detection antibody prior to flow down the test strip. This experiment was performed using Millipore HFB135 nitrocellulose only. Mutant SA was spotted at 1 mg/mL, and devices were stored under desiccation for two days before use. The assay was run using biotin-HB36.5 at 100 nM, recombinant HA from A/California/04/2009 (IRR #FR-180), and accompanying mouse-anti-HA antibody (IRR #FR-505) at 100 nM. We compared the use of biotin-BSA (BioVision #7097-25, Milpitas, CA) at 1 mg/mL in PBST versus regular PBST as the first wash step after delivery of the biotinylated flu binder-antigen-antibody mixture. The first wash was followed by the delivery of the gold-conjugated secondary antibody, and then a PBST wash, as done previously. Reagents were diluted in a running buffer of PBST+BSA. Here, a dilution series of HA concentrations was tested, with HA at 3125, 625, 125, 25, 5, and 1 pM, in addition to no-HA negative controls.

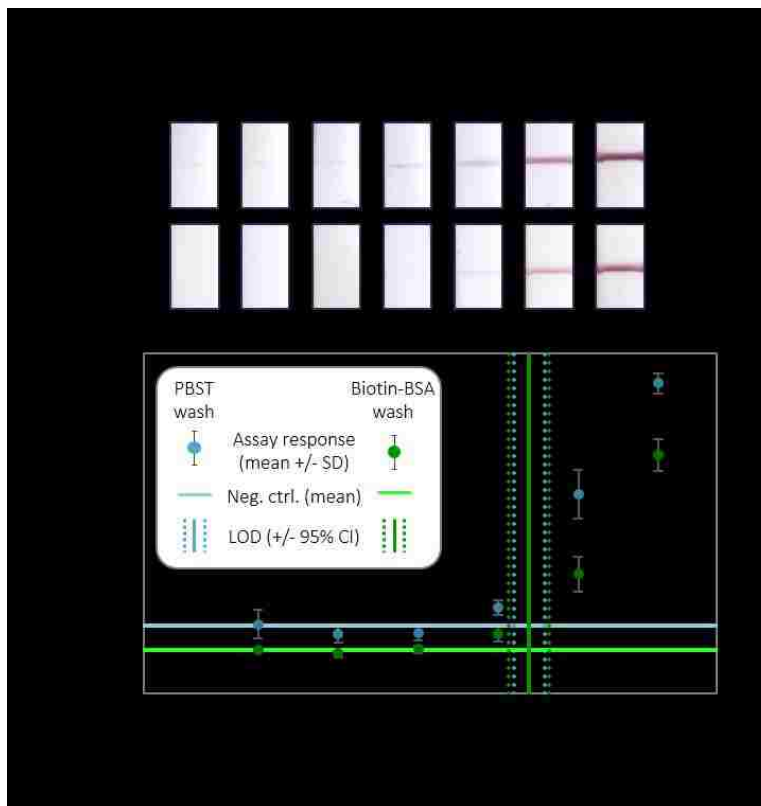


Figure 73. Effect of biotin-BSA wash on mutant SA anchor system.

(A) Flu HA assay signal using biotin-HB36.5 anchored by mutant SA on NC using a PBST wash versus a PBST + biotin-BSA wash to reduce non-specific signal. (B) Normalized pixel intensities of the assay test lines, plotted as the mean +/- SD for n=4 replicates. The mean of the negative control is plotted as a horizontal line in each case, and the LODs +/- 95% confidence interval are plotted in vertical lines.

A representative test line for each condition is shown in Figure 73A. The normalized pixel intensities are plotted in Figure 73B as the mean +/- SD for n=4 replicates. Visually, these results

show that the PBST wash results in higher signal intensities, including higher false-positive signal for the negative control, while adding biotin-BSA to the wash knocks down all signal levels. The biotin-BSA wash therefore results in a better assay in terms of reduced false-positive signal, which is important for assays that will be interpreted by the end user by eye. However, when the limit of detection (LOD) of each assay is calculated statistically (see chapter 6), both assays yield similar LODs. Specifically, the assay with PBST wash has an LOD of 233 pM (95% confidence interval: [171 pM, 316 pM]), and the assay with biotin-BSA wash has an LOD of 232 pM (95% confidence interval: [155 pM, 348 pM]), which are not statistically different ($p > 0.05$ by Welch's *t*-test). Therefore, the performance of the assay is not improved by the addition of the biotin-BSA wash, if the assay were to be interpreted by a reader and computational algorithm. In our case, we were optimizing for a read-by-eye result, so we chose to implement the biotin-BSA wash for all mutant streptavidin anchor systems for the flu HA assay, in order to bring the false-positive signal down to a nonvisible level.

The mutant streptavidin anchor system for biotinylated affinity proteins performs extremely well for nitrocellulose-based lateral flow assays, providing stronger signal than the covalent epoxide-thiol attachment tested previously. This anchor system is relatively costly, however, requiring the additional expenses of the commercial mutant streptavidin protein, in addition to the enzymatic biotinylation reagents, which offset the advantage of the low cost of the recombinant affinity protein. We therefore explored a fully recombinant alternative to the nitrocellulose-specific streptavidin-biotin system, as described next.

4.6. Immobilization by Nitrocellulose-Binding Anchor Protein

In order to develop a lower-cost alternative to the mutant streptavidin-biotin anchoring system, we sought to develop a fusion of the recombinant flu binder protein to a custom nitrocellulose-binding anchor protein. As described in chapter 3, we leveraged our knowledge of protein adsorption to identify anchor protein candidates. Of the proteins initially screened, both the Design I (DI) globular protein and the 3-helix bundle protein showed promising adsorption to nitrocellulose, besting that of even immunoassay mainstay IgG.

Given the successful adsorption of the 3-helix and DI proteins, PhD graduate Dr. Aaron Chevalier of the Baker lab prepared genetic fusions of the stem region flu binder (HB36.6) to each of these nitrocellulose anchor proteins. Unfortunately, the 3-helix-binder fusion protein did not express well in the recombinant expression system and requires further optimization. The DI-binder fusion

protein (DI-HB36.6) did express successfully, and three different versions were prepared: fusion with a 12-AA linker ($\{\text{Gly}_3\text{Ser}\}_3$) and standard nickel (Ni) purification (“DI-12-HB36.6-Ni”), fusion with a 4-AA linker ($\{\text{Gly}_3\text{Ser}\}_1$) and standard Ni purification (“DI-4-HB36.6-Ni”), and fusion with a 12-AA linker ($\{\text{Gly}_3\text{Ser}\}_3$) and a higher-purity cobalt (Co) purification (“DI-12-HB36.6-Co”). Each fusion variant was tested for immobilization efficiency and functionality as a capture agent for the flu HA assay.

4.6.1. Methods

Immobilization Testing via Lateral Flow Challenge

The immobilization efficiencies of the DI-HB36.6 fusion proteins were tested using the lateral flow challenge system described in section 4.2.1.

Functionality Testing via Flu Hemagglutinin Assay

The functionality of each DI-HB36.6 fusion protein was tested as a capture agent for the flu HA assay, as described in section 4.2.2.

4.6.2. Results and Discussion

Immobilization and Functionality of DI-HB36.6 Fusion Protein to Nitrocellulose

To evaluate the performance of the DI-HB36.6 fusion proteins, both the immobilization efficiency and flu HA functionality were tested. The three fusion variants (DI-12-HB36.6-Ni, DI-4-HB36.6-Ni, and DI-12-HB36.6-Co) were compared to regular stem region flu binder HB36.6. Each flu binder protein was spotted at 70 μM in PBS using the piezoelectric spotting onto GE FF80HP nitrocellulose.

As usual, the immobilization efficiency of the DI-HB36.6 fusion proteins was tested via lateral flow challenge, using challenge solutions of PBS and PBST, in addition to no-flow controls. Protein was visualized with Ponceau S staining. After the staining was complete and the devices scanned, the average pixel intensity of each test line was quantified using my MATLAB program *quantifyColorimetricSignal.m*, using the green channel option. A representative test line for each LF condition is shown in Figure 74A, along with the corresponding normalized pixel intensities, plotted as the mean \pm standard deviation of $n=3$ replicates for each condition.

The functionality of the novel DI-HB36.6 fusion proteins as capture agents for the flu HA assay was also evaluated. For the flu assay, we used recombinant HA from A/California/04/2009 (H1N1) (“CA2009”) influenza (IRR #FR-180, lot #59007343, 91% trimer) at 100 nM and accompanying mouse-anti-HA antibody (IRR #FR-505, “CA09/Ab2”) at 100 nM. All reagents were diluted in a running buffer of PBST+BSA, and PBST was used for all washes in this experiment. Three replicates were run for each condition, in addition to three replicates of the negative control. After the assay was complete and the devices scanned, the average pixel intensity of each test line was quantified using my MATLAB program *quantifyColorimetricSignal.m*, using the green channel option. A representative test line for each condition is shown in Figure 74B, along with the corresponding normalized pixel intensities, plotted as the mean +/- standard deviation of n=3 replicates for each condition.

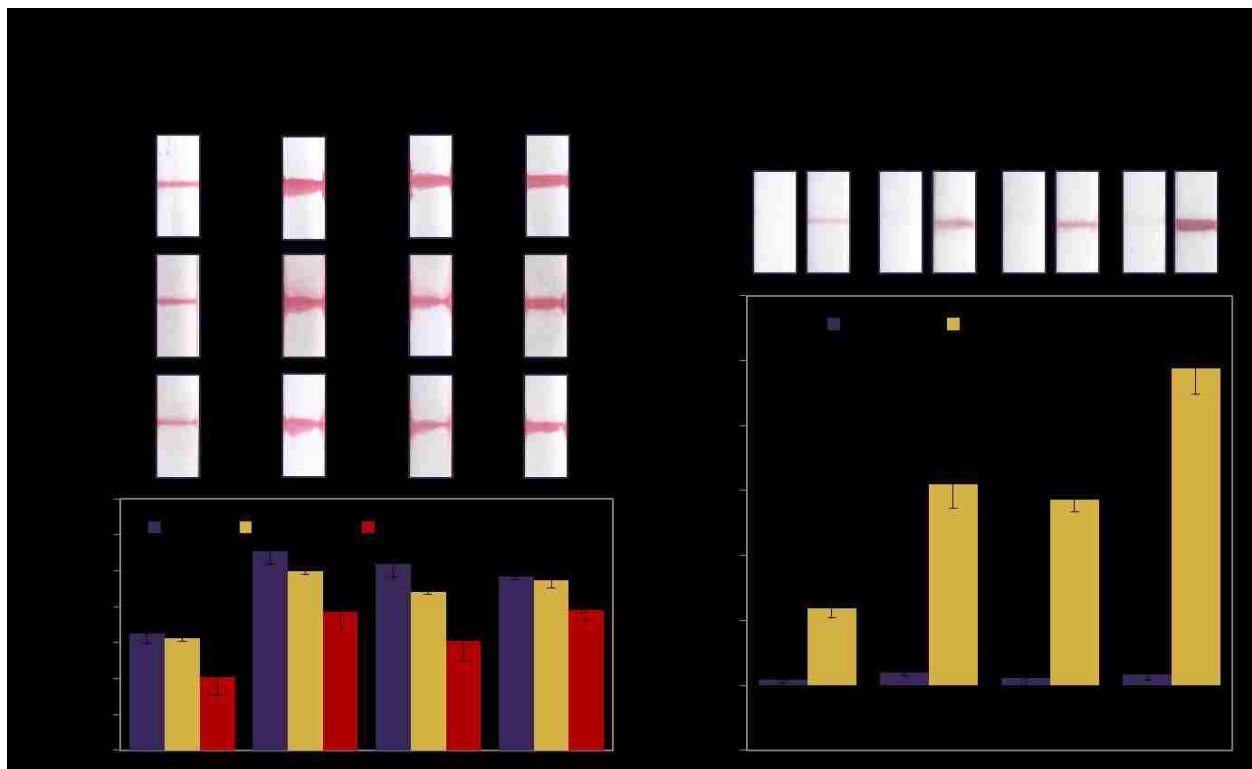


Figure 74. Performance of DI-HB36.6 fusion proteins.

The immobilization of flu binder HB36.6 through genetic fusion to the nitrocellulose-binding anchor protein DI was evaluated. Three different fusion variants were tested and compared to regular HB36.6 (A) Immobilization efficiency via lateral flow challenge and Ponceau S staining. (B) Flu binder functionality as a capture agent for the flu HA assay.

These results show that all three DI-HB36.6 proteins immobilize well to nitrocellulose, as expected, and are more resistant to stripping under challenge by PBST than HB36.6 alone. The assay results indicate that all three fusion proteins outperform regular HB36.6. Taken together, these results confirm that genetic fusion of the flu binder to a nitrocellulose-binding anchor protein not only

provides robust immobilization, but also effective display of the flu binder for improved functionality as a capture agent. The DI-12-HB36.6-Co variant produced the greatest signal over, and was therefore the variant the moved onto further testing for flu HA assay development, discussed in chapter 5.

If we compare the assay signal here for the DI-12-HB36.6-Co fusion protein (referred to as “DI-HB36.6” from this point forward), which was run with 100 nM HA, to the signal obtained for the mutant SA + b-HB36.5 system run with 3 nM HA (Figure 73), we can see that the mutant SA anchoring system still outperforms this custom anchoring by genetic fusion. The lower signal for DI-HB36.6 may be due to the lower degree of control of the orientation of the affinity protein as compared to the streptavidin anchor system. More specifically, since the fusion protein is immobilized by direct adsorption, it is subject to random orientation, which likely results in a portion of the affinity protein that is adsorbed binding-site-down and is therefore unavailable for capture of the incoming antigen. Despite this somewhat lower signal intensity, the recombinant fusion protein system is approximately 1,000 times cheaper than the nitrocellulose-specific streptavidin-biotin system (~\$0.0006/test versus ~\$0.4845/test), thereby offering good performance at a much lower cost. The high cost for the mutant streptavidin system—which is due to the high costs of the commercial mutant streptavidin protein and biotinylation reagents—would likely be partially mitigated by the purchase of bulk reagents for at-scale production, but is expected to remain significantly more expensive. The choice in immobilization system for any given assay will therefore depend on the sensitivity and cost restraints at play.

4.7. Comparison to Standard IgG Immobilization

Given the superior performance of the nitrocellulose-specific streptavidin-biotin anchoring system to the other methods developed herein, we sought to compare this novel immobilization system to the gold standard method of IgG capture by direct adsorption. Since commercial lateral flow tests do not exist for HA detection (all commercial influenza rapid diagnostic tests detect the internal nucleoprotein instead), we developed the standard IgG-based lateral flow strips in-house.

4.7.1. Methods

Functionality Testing via Flu Hemagglutinin Assay

The functionality of biotinylated stem region flu binder biotin-HB36.5 as a capture agent for the flu HA assay (section 4.2.2) when anchored by mutant streptavidin was compared to a traditional IgG antibody immobilized by direct adsorption.

4.7.2. Results and Discussion

Biotinylated Flu Binder HB36.5 Anchored by Mutant Streptavidin Outperforms Traditional IgG Capture by Direct Adsorption

To develop the standard IgG-based lateral flow immunoassay for HA, an antibody binding pair was determined from the IgG antibodies available from the IRR for HA from A/Solomon Islands/3/2006 influenza. The capture antibody (IRR #FR-503) was patterned onto GE FF80HP nitrocellulose at 0.5 mg/mL in PBS (stock concentration) in the form of test lines, as described above. The detection antibody (IRR #FR-502) was conjugated directly to gold nanoparticles using a commercial conjugation kit (InnovaCoat Gold 40 nm Gold Particle Kit, #230-0005, InnovaBiosciences, Cambridge, United Kingdom).

The assay was run through the sequential delivery of the following reagents: 1) 20 μ L HA at 10 nM or negative control, 2) 20 μ L PBST wash, 3) 20 μ L gold-conjugated detection antibody at OD 2.5, and 4) 20 μ L PBST wash. All reagents were

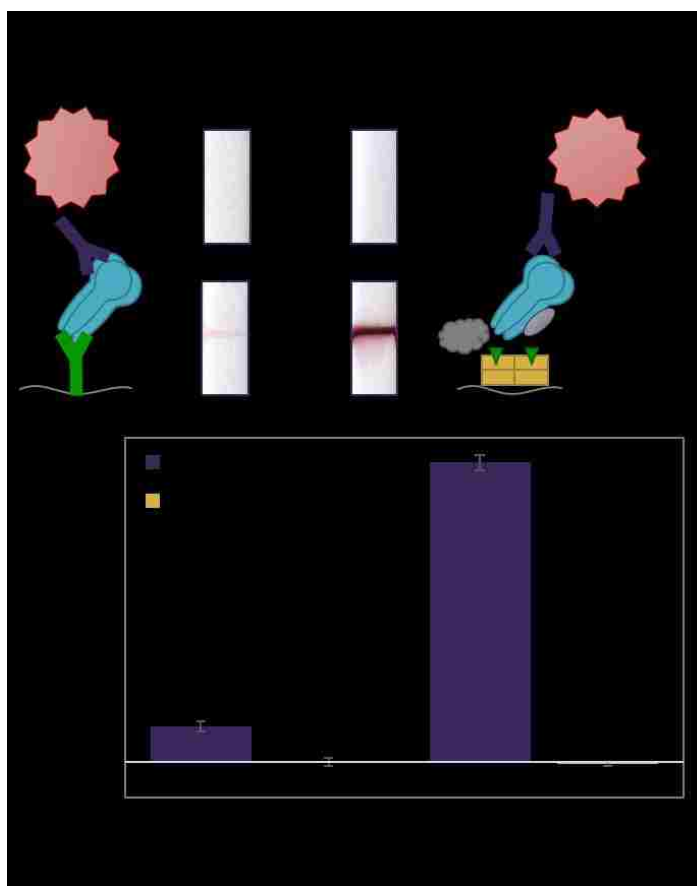


Figure 75. Mut. SA + b-HB36.5 outperforms standard Ab capture. Comparison of the novel mut. SA + b-HB36.5 capture system for the flu HA assay to a traditional Ab capture system. (A) Flu HA assay signal for each system, in addition to an illustration of each assay stack. (B) Normalized pixel intensities of the assay test lines, plotted as the mean \pm SD for n=4 replicates.

diluted in a running buffer of PBST+BSA. This assay was compared side-by-side with the mutant streptavidin-biotin system, performed using biotin-HB36.5 at 100 nM, A/Solomon Islands/3/2006 HA at 10 nM, and the same gold-conjugated detection antibody as above. Here, the biotinylated binder and HA were premixed prior to flow, and a biotin-BSA wash was used for the first wash step. The gold-conjugated detection antibody was then added sequentially, followed by the final PBST wash. In doing so, this test provided a comparison of the novel nitrocellulose-specific streptavidin-biotin immobilization system developed herein to the gold standard of IgG capture by direct adsorption, using the same exact detection system in order to focus solely on the impact of the capture agent and immobilization method.

A representative test line for one test and one negative control replicate for each assay system are shown in Figure 75A. The normalized pixel intensities are plotted in Figure 75B as the mean \pm SD for $n=4$ replicates of each condition. These results show that the combination of the recombinant stem region flu binder with the mutant streptavidin-biotin anchor system provides much stronger assay signal than the use of standard IgG capture by direct adsorption ($p < 0.025$ by right-tailed Student's *t*-test of unequal variance). Overall, this work not only demonstrates the use of novel immobilization methods for capture agents on nitrocellulose, but also illustrates the improvements in assay functionality that can be made by using these methods.

4.8. Conclusions

The work in this chapter represents novel efforts to immobilize affinity reagents to nitrocellulose membranes for use in paper-based assays. While this work was done using the computationally designed stem region flu binder, these methods can be applied to any recombinant affinity protein (e.g. other designed affinity proteins, scFv, or other antibody-derived protein fragments) or modified protein (e.g. IgG antibody that has been biotinylated or reduced/thiolized). Therefore, even the immobilization of IgG itself could be improved through these more sophisticated and controlled immobilization techniques.

Recombinantly expressed or modified proteins provide many options for attachment to the assay substrate. Here, we have focused on nitrocellulose membrane, which is the most commonly used membrane for lateral flow tests, but these methods could be applied to other assay substrates as well. We found that direct adsorption was not successful for our small stem region flu binder, indicating that adsorption is not an effective strategy for all affinity proteins, despite the fact that it is the mainstay of antibody immobilization for traditional lateral flow immunoassays. Covalent

attachment through epoxide-thiol linkage is a novel method that takes advantage of the customizability of the affinity protein and a new modified nitrocellulose membrane. This method showed promising results, but requires further optimization, including careful attention to the chemistry of the buffers used and the storage conditions. Attachment through the tried-and-true streptavidin-biotin linkage is extremely effective and enhanced by the use of a mutant version of streptavidin specifically designed to bind to nitrocellulose. Since this mutant streptavidin is a commercial product, it creates an added expense that counteracts the financial advantage of using recombinant affinity proteins instead of antibodies. Lower-cost work-arounds represent an important area of future work. As an intermediate solution, the nitrocellulose anchor protein that we employed here represents one alternative to the streptavidin-biotin system, although closer mimics could be developed to improve attachment and binding functionality. While each method has its benefits and drawbacks, the nitrocellulose-specific streptavidin-biotin system yielded the overall strongest signal for the influenza HA assay. This system resulted in improved assay performance compared to the traditional method of IgG antibody directly adsorbed to nitrocellulose membrane. Overall, we have demonstrated that these novel immobilization methods for recombinant affinity proteins can be used to improve paper-based assay performance. This work represents an important toolbox for the development of robust capture regions in paper-based diagnostics. In the next chapter, we apply these immobilization strategies for our own development of the influenza HA assay.

5. Flu HA Assay Development

5.1. Motivation

Given the successful demonstration of the flu binder immobilization strategies described in chapter 4, we wanted to apply them, in combination with novel flu binders emerging from the Baker lab, for the development of a paper-based assay for improved influenza detection. We focused on two aspects of development: (1) achieving the most sensitive assay possible and (2) detection of real influenza virus instead of just the recombinant hemagglutinin (HA) protein detected in the previous chapter. This work included countless iterations of the assay, optimizing aspects ranging from wash buffer and running buffer design to reagent delivery strategy. We also tested many combinations of both the stem and head region flu binders for various capture and detection strategies, in addition to traditional IgG antibodies. The highlights of the flu HA assay development are described in this chapter. For the full details of this assay development, I direct interested parties to my electronic lab notebook and assay log. Much of this work was done in collaboration with undergraduate student Steven Bennett and, more recently, graduate student Caitlin Anderson. Ultimately, we arrived at two promising assays, one using stem region binder capture and one using head region binder capture, whose full characterizations are provided at the end of this chapter. These novel assays are compared to a standard antibody-based lateral flow immunoassay in chapter 7 to illustrate the improvements accomplished through this assay development.

5.2. Common Methods

5.2.1. Flu Hemagglutinin Assay

The experiments described in this chapter consisted almost entirely of influenza hemagglutinin (HA) assays, run with either recombinant HA or cultured influenza virus. Since the assay details varied by the particular experiment and assay iteration, those details are provided in each section.

In general, nitrocellulose strips were patterned with test lines (typically a flu binder) using the piezoelectric spotter, as described in section 4.2.1 (see Figure 50). Each flu assay was performed in a dipstick lateral flow format using a 96-well plate pre-loaded with the given assay reagents, as described in section 4.2.2 (see Figure 52). The test strips were manually moved between wells to initiate each assay step. A cellulose absorbent pad (Millipore #CFSP223000) cut to the width of the device and 70 mm tall was secured to the top of the nitrocellulose device to aid wicking, either with

tape or with a custom-made plastic housing. After the assay was complete, the wicking pads were removed, and all devices were taped to a standard piece of printer paper and imaged at 48-bit HDR color, 600 dpi, $\gamma = 1$ using a desktop scanner (Epson Perfection V700 Photo Scanner). The signal intensity of each test line was quantified as described in section 4.2.3.

Unless otherwise noted, each assay consisted of the following steps: 1) 20 μL virus, recombinant HA, or negative control, 2) 20 μL wash, 3) 20 μL detection reagent, 4) 20 μL wash, 5) 20 μL gold-conjugated secondary label, and 6) 20 μL wash. Recombinant HA was from one of two influenza strains from the Influenza Reagent Resource (IRR), as indicated: A/California/04/2009 or A/Solomon Islands/03/2006, both of which are H1N1 strains. Matching detection antibodies were used accordingly, when antibodies were used for detection. Gold-conjugated secondary (Au-2°) labels (Au-goat-anti-mouse IgG or Au-streptavidin, Arista Biologicals, Inc., Allentown, PA) were used at optical density (OD) 2.5. All reagents were diluted in the optimized assay running buffer of PBST+ BSA (PBS + 0.1% v/v Tween-20 + 1% w/v BSA (Sigma-Aldrich #A7030)). Wash buffer was PBST.

5.2.2. Signal Quantification

All signal intensities of the test lines were quantified using the custom MATLAB script, *quantifyColorimetricSignal.m* (see Appendix B for code and description). As described in section 3.2.1, this program is used to compute the average pixel intensity, I_{test} , of an ROI drawn semi-manually around the test line of interest. This value is then background-subtracted using the average pixel intensity inside a local background region, I_{bkgd} , and normalized on a scale from 0 to 1 to generate the normalized pixel intensity of the spot, I_{norm} , using Eqn 19. For assay signal, which in all cases was generated by gold nanoparticle labels, the green channel of the RGB image was used for analysis. This channel is the most sensitive to the red color of the gold nanoparticle-based signal. As usual, the normalized pixel intensities represent a range from no signal (0) to maximum possible signal (1).

5.3. Stem Region Flu Binders Fail to Capture Whole Virus

Since the stem region flu binder was demonstrated as a successful capture agent for the flu HA assay using three different immobilization strategies in chapter 4, we wanted to further apply these assays for the detection of real influenza virus. The recombinant HA used in the previous chapter, while a useful antigen for assay development, does not necessarily reflect the actual HA produced

by and presented on the surface of influenza virus. For example, the recombinant HA lacks the transmembrane region, leaving only the ectodomain of HA, or the portion that sticks out from the virus surface. Additionally, the recombinant HA includes an artificial trimerization domain to further encourage the HA monomers to associate into trimers, resulting in a trimeric structure that is likely more stable than a real HA trimer. While isolating real HA from influenza virus would be ideal for the development of our assay, we learned, after discussions with influenza virus experts in Dr. Kelly Lee's lab, that this process can be difficult and time-consuming. We therefore tested our assay systems with whole influenza virus from culture, in order to evaluate the performance of our systems with real HA on real virus. Note that, since we are not intentionally lysing the virus sample, we presume that this sample contains intact virions, an assumption that is further evaluated in section 5.4.

5.3.1. Methods

Functionality Testing via Flu Hemagglutinin Assay

The functionality of each stem region binder capture system was tested using the flu HA assay, as described in section 5.2.1. In each case, the ability to capture whole influenza virus was tested side-by-side with the ability to capture recombinant HA, in order to serve as a positive control (since recombinant HA detection had already been verified in the previous chapter).

5.3.2. Results and Discussion

Mutant SA + b-HB36.5 vs. DI-HB36.6 for Whole Virus Capture

The ability of the stem region flu binder to capture whole influenza virus was compared side-by-side for the two anchor-based immobilization systems: mutant SA + biotin-HB36.5 and DI-HB36.6 fusion protein. Mutant SA was spotted at 1 mg/mL in PBS, and DI-HB36.6 was spotted at 66 μ M in PBS, both on GE FF80HP nitrocellulose membranes. Membranes were dried in the desiccator overnight before use. For the flu assay, we tested both whole virus and recombinant HA from A/Solomon Islands/03/2006 (H1N1) ("SI2006") influenza. Whole virus (IRR #FR-331) was tested at $\frac{1}{2}$ stock concentration, i.e. 1.25×10^8 CEID₅₀/mL. Recombinant HA (IRR #FR-67) was tested at 10 nM. Matching mouse monoclonal antibody for SI2006 HA (IRR #FR-502, "SI06/Ab3") was used for detection at 100 nM. Au-2° (Au-goat-anti-mouse IgG, Arista Biologicals, Inc.) was used at OD 2.5. All reagents were diluted in a running buffer of PBST+BSA. PBST was used for all washes, except for the first wash of the mutant SA stack, in which biotin-BSA was used at 1 mg/mL in PBS, as

described in section 4.5. All reagents were delivered sequentially. Four replicates were run for each condition, in addition to eight replicates of the negative control. Scanned images of the test lines were quantified according to section 5.2.2. A representative test line for each condition is shown in Figure 76, along with the corresponding normalized pixel intensities, plotted as the mean \pm standard deviation of all replicates ($n=4$ for test samples, $n=8$ for negative control).

These results clearly show that, while both stem region binder assay stacks can capture recombinant HA successfully, they cannot capture whole virus. Since the stem region flu binder have been shown to bind to and neutralize real influenza virus [144], we do not suspect that the lack of binding for virus here is due to an inability to bind real HA. Instead, we hypothesize that binding is prevented by steric hindrance, due to the difficulty of the stem

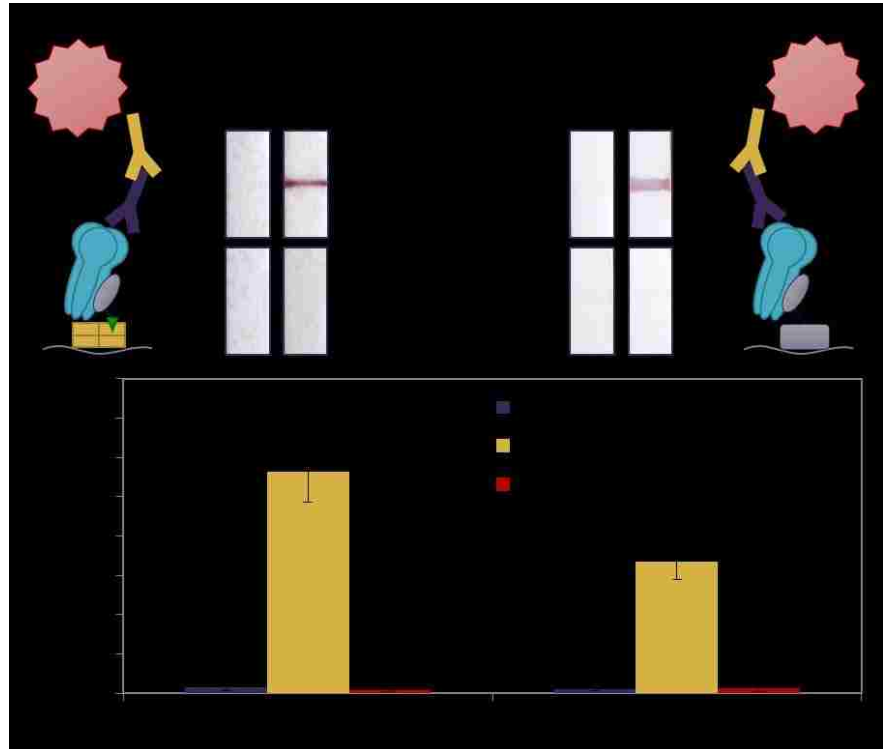


Figure 76. Anchor-based stem region binder systems fail to capture whole virus. Side-by-side comparison of biotin-HB36.5 anchored by mutant SA and the DI-HB36.6 fusion protein as flu assay capture agents. Both systems capture recombinant HA, but not whole virus. (A) Assay illustrations and a representative test line for each condition. (B) Normalized pixel intensities of the test lines, plotted as the mean \pm SD of all replicates.

region binder to access the stem region of HA when HA is bound to viral surface and the binder is immobilized to the assay membrane. Therefore, these stacks may be useful if HA can be isolated from virus through sample pre-processing, but unless the accessibility of the binder can be improved, these assay systems will not find utility for whole virus detection.

Thiolated Flu Binders for Whole Virus Capture

Similarly to the anchor-based systems above, the functionality of thiolated stem region binder covalently attached to NC-GMA was assessed for whole virus capture. The most recent non-linker (cys-HB36.5, or HB36.5_A276C) and linker (cys-linker-HB80.4, or cys-{Gly₄Ser}₇-HB80.4, or “N35”

linker) variants were compared, with the hypothesis that the linker variant would have the most accessibility and therefore the best chance of overcoming the presumed steric hindrance problem of the anchor-based systems. The maximum common concentration achievable was 20 μM , so each flu binder was spotted at 20 μM in PBS onto GE FF80HP-GMA membranes, this time using 7 passes instead of the usual 2, thereby achieving test lines as close to the usual capture density as possible with the amount of reagent available. Membranes were dried in the desiccator overnight before use.

For the flu assay, we tested both whole virus and recombinant HA from A/Solomon Islands/03/2006 (H1N1) (“SI2006”) influenza. Whole virus (IRR #FR-331) was tested at $\frac{1}{2}$ stock concentration, i.e. 1.25×10^8 CEID₅₀/mL. Recombinant HA (IRR #FR-67) was tested at 10 nM. Matching mouse monoclonal antibody for SI2006 HA (IRR #FR-502, “SI06/Ab3”) was used for detection at 100 nM. Au-2° (Au-goat-anti-mouse IgG, Arista Biologicals, Inc.) was

used at OD 2.5. All reagents were diluted in a running buffer of PBST+BSA, and PBST was used for all washes. All reagents were delivered sequentially. Four replicates were run for each condition, in addition to eight replicates of the negative control. Scanned images of the test lines were quantified according to section 5.2.2. A representative test line for each condition is shown in Figure 77, along with the corresponding normalized pixel intensities, plotted as the mean +/- standard deviation of all replicates (n=4 for test samples, n=8 for negative control).

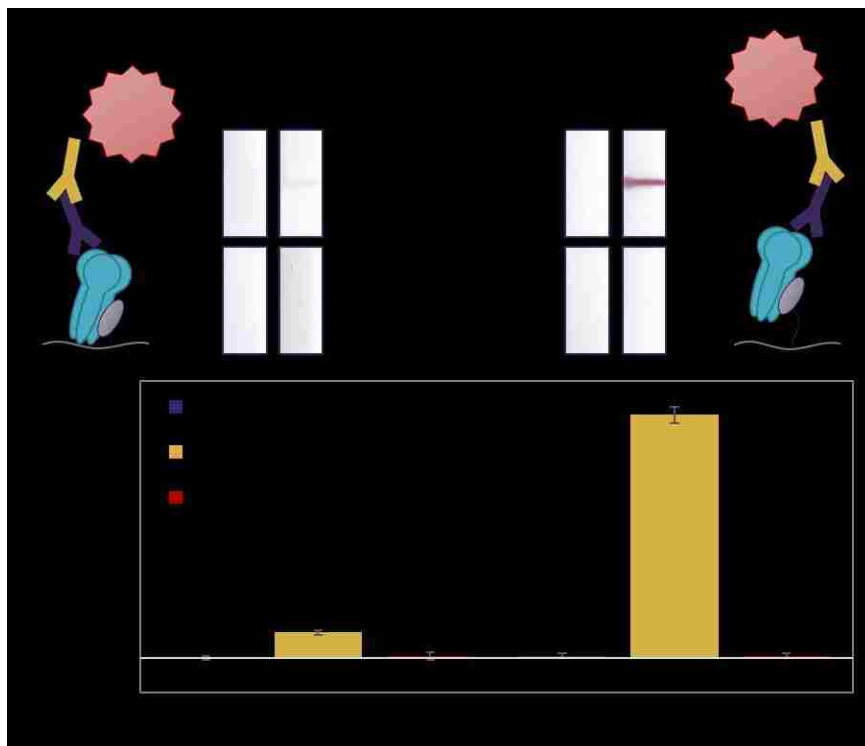


Figure 77. Thiolated stem region binder systems fail to capture whole virus. Side-by-side comparison of cys-HB36.5 and cys-linker-HB80.4, covalently attached to NC-GMA, as flu assay capture agents. Both systems capture recombinant HA (the linker version much better than the non-linker), but not whole virus. (A) Assay illustrations and a representative test line for each condition. (B) Normalized pixel intensities of the test lines, plotted as the mean +/- SD of all replicates.

These results clearly show that both thiolated flu binders are unable to capture whole virus. As observed previously, the linker improves the accessibility of the flu binder, as it yields increased signal relative to the non-linker binder (although some of this difference may also be attributable to different strain preferences of these two variants), but this improved accessibility is still not enough to capture HA attached to virus. We therefore shifted our focus to the head region flu binder in hopes of having improved accessibility and whole virus capture, as described next.

5.4. Head Region Flu Binder for Whole Virus Capture

Around the time of our unsuccessful attempts to capture whole virus with the stem region binder assay systems, the Baker lab developed the first head region flu binders, an effort led by post-doctoral fellow Dr. Eva-Maria Strauch. As described in section 2.4.2, these head region binders showed only modest binding as monomers, so Dr. Strauch engineered trimeric versions to match the inherent trimeric structure of HA and thereby gain binding strength through avidity. These head region binders were tested for use in the flu HA assay, primarily as capture agents, but also as detection agents. As the work below describes, we were able to successfully develop an assay for whole influenza virus capture based on one of these head region binder variants (Trimer 11).

5.4.1. Methods

Immobilization Testing via Lateral Flow Challenge

The immobilization efficiency of the head region binders Trimer 9 and Trimer 11 was tested using the lateral flow challenge system described in section 4.2.1.

Functionality Testing via Flu Hemagglutinin Assay

The functionality of each head region binder capture system was tested using the flu HA assay, as described in section 5.2.1. In the early stages of assay development, only recombinant HA was tested. Then, in later stages of assay development, the ability to capture whole influenza virus was typically tested side-by-side with the ability to capture recombinant HA. In some cases, only whole virus capture was evaluated.

5.4.2. Results and Discussion

Comparison of Head Region Binders Trimer 9 and Trimer 11 for Recombinant HA Capture

In order to screen the performance of the two new head region binder constructs, Trimer 9 and Trimer 11, we first tested their immobilization efficiency by lateral flow challenge. We wanted to determine if these binders could be immobilized by direct adsorption, or if we needed to employ one of the other immobilization strategies developed in chapter 4. To perform the immobilization testing, each head region binder was spotted at 8 μ M in PBS, which was the highest common concentration achievable. We tested both Millipore HFB135 and GE FF80HP nitrocellulose membranes. Devices were stored under desiccation for 11 days before use.

The lateral flow challenge was performed with challenge solutions of PBS and PBST, in addition to no-flow controls, and protein was visualized by Ponceau S staining. A representative test line for each condition is shown in Figure 78, along with the corresponding normalized pixel intensities, plotted in as the mean \pm SD of the n=4 replicates for each condition. Overall, these results indicate that both head region binders, Trimer 9 and Trimer 11,

adsorb robustly to both nitrocellulose membranes, Millipore HFB135 and GE FF80HP. In all cases, the flu binder incurred only minimal stripping when subjected to that harshest lateral flow challenge, PBST. We therefore determined that these head region binders stay adsorbed well to nitrocellulose, suggesting that direct adsorption may be an effective mode of immobilization for them. The next step was to test their functionality as capture agents in the flu HA assay.

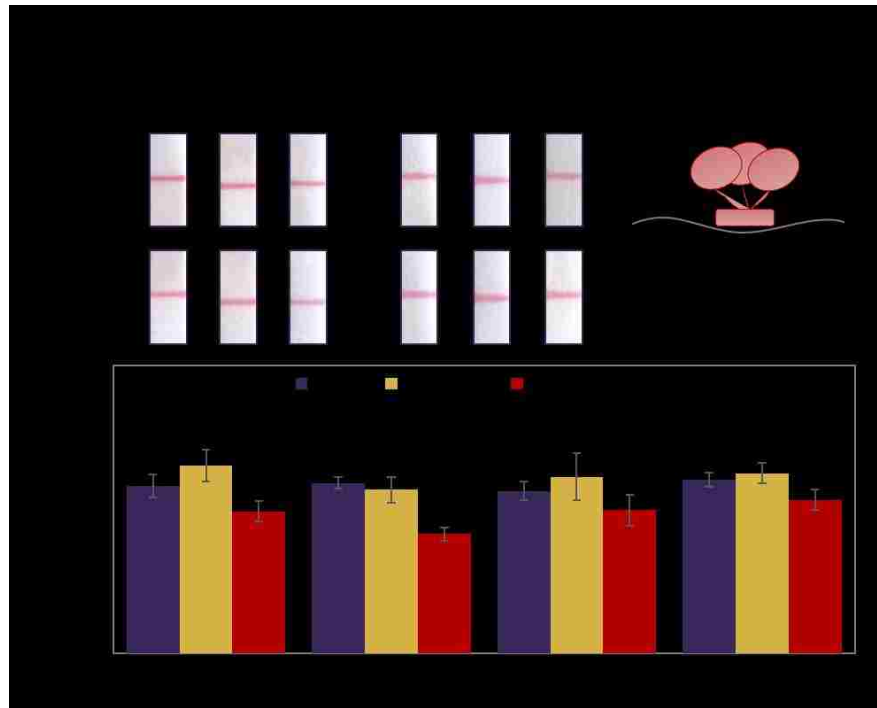


Figure 78. Immobilization of head region binders by direct adsorption.

The immobilization efficiency of head region flu binders Trimer 9 and Trimer 11 was evaluated by lateral flow challenge and Ponceau S staining. Two nitrocellulose membranes were compared: Millipore HFB135 and GE FF80HP. A representative test line image for each condition is provided, along with the corresponding normalized pixel intensities (mean \pm SD of n=4 replicates).

To perform the flu HA assay, we tested recombinant HA from both A/Solomon Islands/03/2006 (H1N1) (“SI2006”) influenza (IRR #FR-67) and A/California/04/2009 (H1N1) (“CA2009”) influenza (IRR #FR1-80), since we did not know which strain the head region binders would recognize best. Both strains of recombinant HA were tested at 100 nM. In this case, biotinylated stem region binder b-HB36.5 was used for detection at 100 nM. (While this is the first demonstration of this detection scheme in this thesis, we had already demonstrated detection with this reagent for other stem region binder capture systems.) Au-2° (Au-streptavidin, Arista Biologicals, Inc.) was used at OD 2.5. All reagents were diluted in a running buffer of PBST+BSA, and PBST was used for all washes. All reagents were delivered sequentially. A representative test line for each condition is shown in Figure 79, along with the corresponding normalized pixel intensities, plotted as the mean +/- SD of all replicates (n=3 for test samples, n=6 for negative controls).

These results indicate that only Trimer 11 is a functional capture agent for the flu HA assay, and only for the SI2006 strain of HA, not the CA2009 strain. We therefore moved forward with further assay developing using Trimer 11 capture, immobilized by direct adsorption, for SI2006 influenza.

Additionally, since both the Millipore

and GE membranes showed similar performance (GE FF80HP yielded slightly higher average intensity, but difference was not significant by Student’s *t*-test of unequal variance), we moved

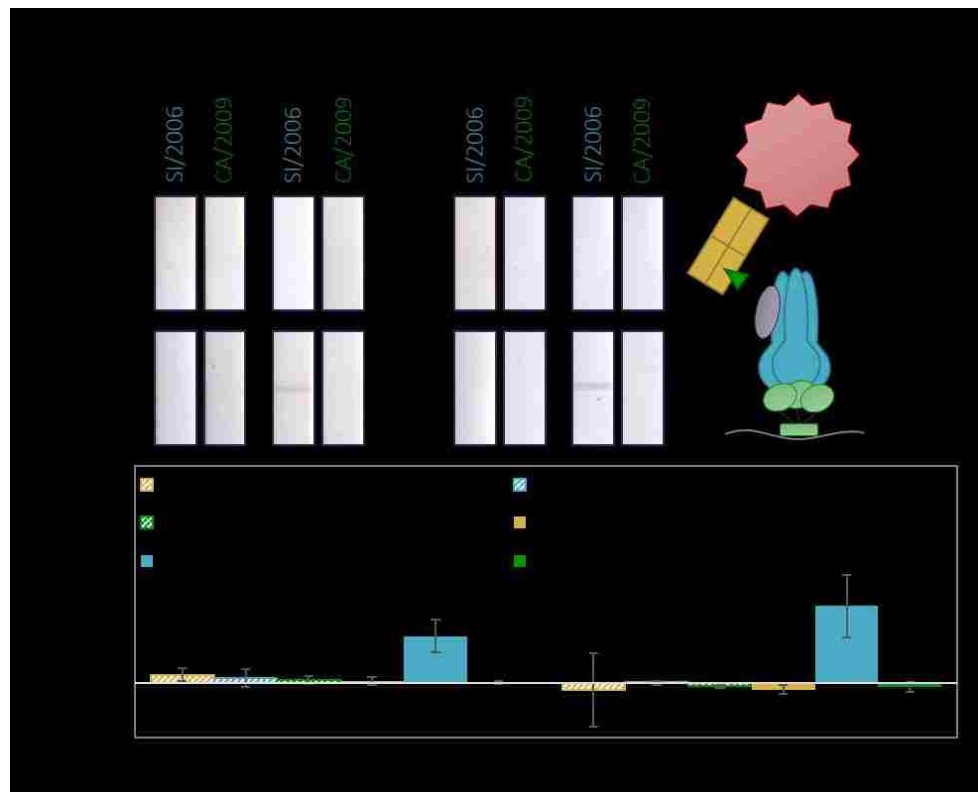


Figure 79. Functionality of head region binders for HA capture by direct adsorption.

The functionality of head region flu binders Trimer 9 and Trimer 11 as capture agents for the flu HA assay was evaluated using the stack with b-HB36.5 detection, as illustrated. Two nitrocellulose membranes (Millipore HFB135 and GE FF80HP) and two strains of HA (SI2006 and CA2009) were compared. A representative test line image for each condition is provided, along with the corresponding normalized pixel intensities (mean +/- SD of n=3 replicates for test samples, n=6 replicates for negative controls).

forward with GE FF80HP as the primary membrane for further assay development, since it was supplied by our collaborators at GE GRC.

Comparison of Detection Reagents for Trimer 11 Capture of Recombinant HA vs. Whole Virus

Given the successful demonstration of Trimer 11 as a capture agent for recombinant HA, we wanted to test its ability to capture whole virus. Unlike the stem region binder, we hypothesized that the head region binder would have easy access to its HA epitope, since it represents the outermost part of the virus. Additionally, since biotin-HB36.5 showed only modest signal as a detection agent, we wanted to test other possibilities, including all four monoclonal antibodies for SI2006 HA available from the Influenza Reagent Resource.

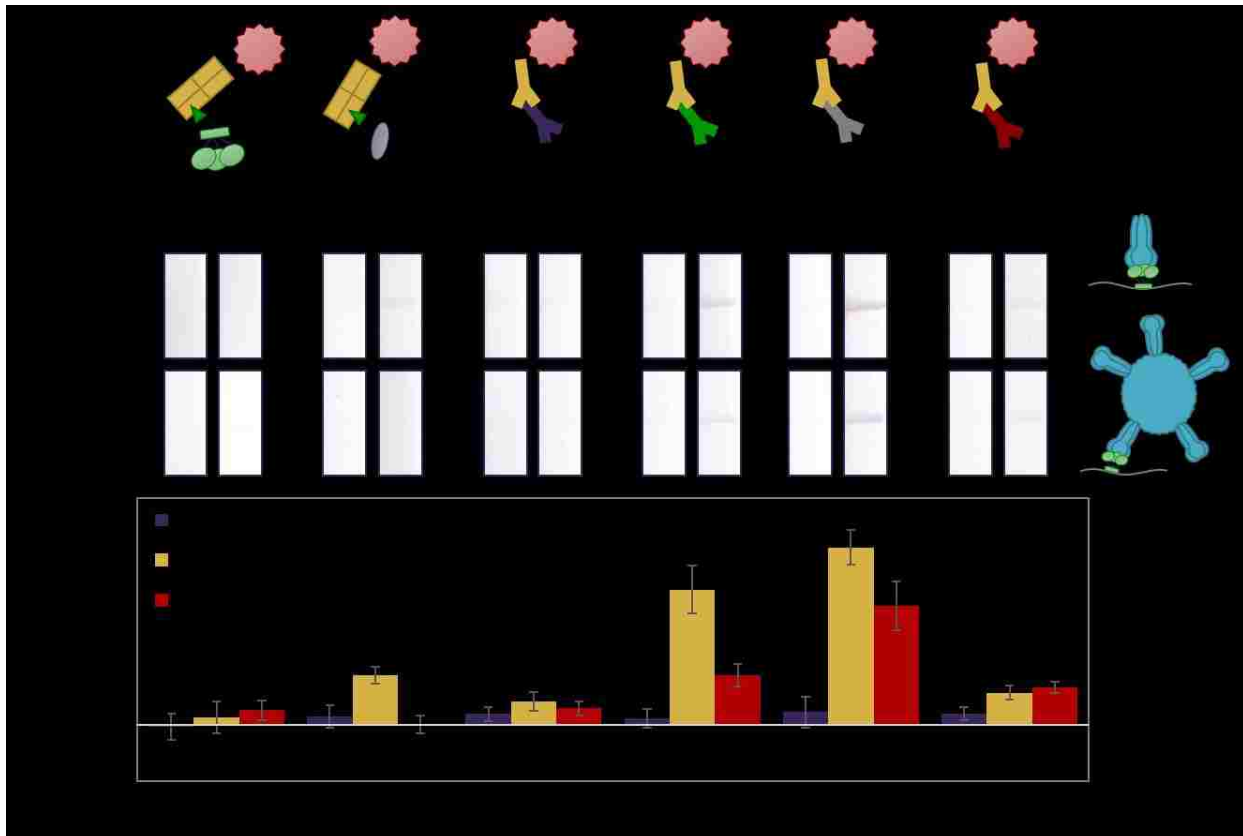


Figure 80. Trimer 11 capture of recombinant HA and whole virus.

The functionality of head region binder Trimer 11 was evaluated as a capture agent for the flu assay with both recombinant HA and whole virus. Six different detection reagents were compared. For the first time, we observed detection of real influenza virus. A representative test line for each condition is provided, along with the corresponding normalized pixel intensities (mean \pm SD of $n=4$ replicates for test samples, $n=8$ replicates for negative controls).

For this experiment, Trimer 11 was pre-concentrated to achieve a higher concentration for spotting. (We later determined unconcentrated binder performed better and moved away from this

concentration step.) Trimer 11 was therefore spotted at 100 μ M (7.76 mg/mL) in PBS onto GE FF80HP nitrocellulose membranes. Devices were stored under desiccation overnight before use.

To perform the flu HA assay, we tested whole virus (IRR #FR-331) side-by-side with recombinant HA (IRR #FR-67), both from A/Solomon Islands/03/2006 (H1N1) ("SI2006") influenza.

Recombinant HA was tested at 10 nM, and virus was tested at $\frac{1}{2}$ stock concentration, i.e. 1.25×10^8 CEID₅₀/mL. Six different detection agents were compared: biotinylated stem region binder b-HB36.5, biotinylated head region binder b-Trimer 11, and four monoclonal antibodies for SI2006 HA from the IRR (SI/Ab1: #FR-499; SI/Ab2: #FR-501; SI/Ab3: #FR-502; and SI/Ab4: #FR-503). Biotin-HB36.5 and all four antibodies were used at 100 nM. Biotin-Trimer 11 was used at its post-biotinylation stock concentration, which was unknown. Au-2° (Au-streptavidin for b-HB36.5 and b-T11 detection, Au-goat-anti-mouse IgG for antibody detection, Arista Biologicals, Inc.) was used at OD 2.5. All reagents were diluted in a running buffer of PBST+BSA, and PBST was used for all washes. All reagents were delivered sequentially. A representative test line for each condition is shown in Figure 80, along with the corresponding normalized pixel intensities, plotted as the mean \pm SD of all replicates (n=4 for test samples, n=8 for negative controls).

These results showed, for the first time, that we could use the head region binder Trimer 11 to capture real influenza virus. Antibodies SI/Ab2, SI/Ab3, and SI/Ab4 all showed signal for the virus samples, with SI/Ab3 yielding the strongest signal overall. Biotinylated stem region binder b-HB36.5 showed detection of recombinant HA, but not whole virus, again echoing the steric hindrance concerns discussed above. Biotinylated head region binder b-T11 did not show any detection capability. Through further experimentation, we later learned that b-T11 has difficulty flowing through the test strip on its own, but can be used as a detection reagent if premixed with the sample (see last experiment of this section).

Overall, we determined that the use of Trimer 11 for capture and SI/Ab3 for detection yields a functional paper-based assay for influenza virus detection. We therefore moved forward with this stack for further assay development.

Lysis Buffer Testing for Trimer 11 Capture of Recombinant HA vs. Whole Virus

The previous Trimer 11-based assay (and all assays developed up to this point) was performed in the absence of any known lysis agents. Here, we tested the compatibility of this assay with different lysis agents. The purpose of this experiment was two-fold. First, we wanted to determine if the

assay was compatible with lysis buffer, since lysis is required for the nucleoprotein (NP) assay being developed by PhD student Koji Abe in our laboratory. In order to integrate the HA assay here with that NP assay, finding a common buffer system would be ideal. We also hypothesized that certain lysis agents may actually release HA into an isolated form that would result in an inherent amplification from the number of virions in a given sample. Second, if the assay were not compatible with lysis agents, it would support our assumption that the assay does indeed detect—and depend on—whole virions.

For this experiment, Trimer 11 was spotted at its stock concentration of 15 μM (1 mg/mL) in PBS onto GE FF80HP nitrocellulose membranes. Devices were stored under desiccation for five days before use. To perform the flu HA assay, we tested whole virus (IRR #FR-331) side-by-side with recombinant HA (IRR #FR-67), both from A/Solomon Islands/03/2006 (H1N1) (“SI2006”) influenza. Recombinant HA was tested at 10 nM, and virus was tested at $\frac{1}{2}$ stock concentration, i.e. 1.25×10^8 CEID₅₀/mL. Here, both recombinant HA and virus were diluted into one of four buffers: (1) standard running buffer PBST+BSA (no lysis), (2) PBST+BSA + 5% v/v Triton X-100, (3) PBST+BSA + 2% w/v octylglucoside (OG), and (4) PBST+BSA + 5% OG. The Triton X-100 buffer represents the lysis buffer used for the flu NP assay and the buffer with which we would ideally like to integrate the HA assay. The OG lysis buffers were also tested because they have been reported in the literature to be compatible with HA retaining HA in trimeric form [184,185].

Monoclonal anti-HA antibody SI/Ab3 (IRR #FR-502) was used for detection at 100 nM. Au-2° (Au-goat-anti-mouse IgG for antibody detection, Arista Biologicals, Inc.) was used at OD 2.5. Both reagents were diluted in a running buffer of PBST+BSA, as usual, and PBST was used for all washes. All reagents were delivered sequentially. A representative test line for each condition is shown in Figure 81, along with the corresponding normalized pixel intensities, plotted as the mean \pm SD of all replicates (n=4). Illustrations of the assay stacks expected for recombinant HA (or isolated HA) and whole virus are also provided.

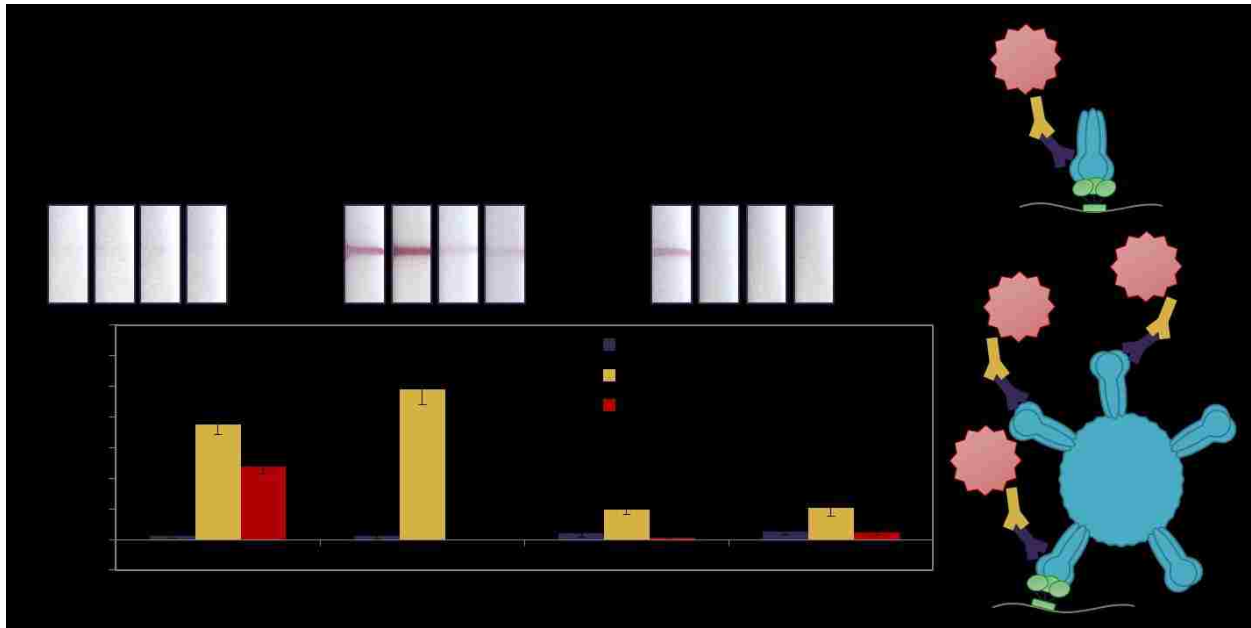


Figure 81. Performance of head region binder-based assay with and without lysis.

The performance of the flu assay employing Trimer 11 capture for recombinant HA and whole virus was evaluated in the presence of lysis agents Triton X-100 and octylglucoside (OG). A representative test line for each condition is provided, along with the corresponding normalized pixel intensities (mean +/- SD of n=4 replicates).

These results clearly show that all three lysis buffers eliminate assay signal for virus, relative to the assay signal observed when no lysis agents are used. These results therefore support our presumption that this assay detects—and depends on—whole influenza virions, as the assay no longer works when the whole virions are disrupted by lysis agents. Interestingly, the addition of Triton X-100 actually improves the detection of recombinant HA. This is likely due to a combination of the recombinant HA trimer being artificially stabilized by its added trimerization domain and of the Triton X-100 slowing fluid flow and increasing interaction time at the test line. The addition of octylglucoside, on the other hand, diminishes assay signal even for recombinant HA. We do not know the mechanism of this reduced signal, but we hypothesize that OG may encourage micelle formation of the HA trimers, thereby reducing the effective antigen concentration. However, both Triton X-100 and OG could also be influencing the biochemistry of the assay in other ways as well.

In any case, these results strongly suggest that the Trimer 11 assay captures whole influenza virions. To verify this result orthogonally, we attempted to evaluate the viral RNA content of the test lines, described next.

While the previous lysis buffer testing indicated that the Trimer 11 assay detects whole influenza virions, we wanted to confirm this result with more direct evidence. In collaboration with post-doctoral fellow Dr. Paula Ladd, we therefore used PCR to evaluate the influenza RNA content in the test line region of the membrane, compared to non-test line regions of the membrane. We hypothesized that, if virus captured on the test line could be lysed and the corresponding RNA content released, PCR analysis would show elevated levels of influenza RNA on the test line relative to other regions of the membrane.

To prepare the membranes, Trimer 11 head region binder was spotted at its stock concentration (after filtering) of 6 μM (0.4 mg/mL) in PBS onto GE FF80HP nitrocellulose membranes. Devices were stored under desiccation for six weeks before use. (Trimer 11 has been tested up to 1-2 months of storage without significant decrease in functionality.)

To perform the experiment, we first subjected all test strips to the first two steps of a standard flu assay: (1) delivery of virus sample (or negative control), followed by (2) a PBST wash. In total, four 4-leg devices (16 test strips) were run, half with virus (SI2006 virus @ 1.25×10^8 CEID₅₀/mL in PBST+BSA) and half with negative control (PBST+BSA). Two of the devices were reserved for PCR analysis, described below. The other two devices moved on to receive the remaining steps of the flu assay in order to ensure virus was successfully captured, serving as a positive control. Using that standard flu assay described above, detection antibody (SI/Ab3, IRR #FR-502) was used 100 nM and Au-2° label at OD 2.5. All reagents were diluted in a running buffer of PBST+BSA, and PBST was used for all washes. All reagents were delivered sequentially. The resulting test lines for all four replicates of the test samples and negative controls are shown in Figure 83A. These results confirmed that the Trimer 11-based capture of virus worked successfully.

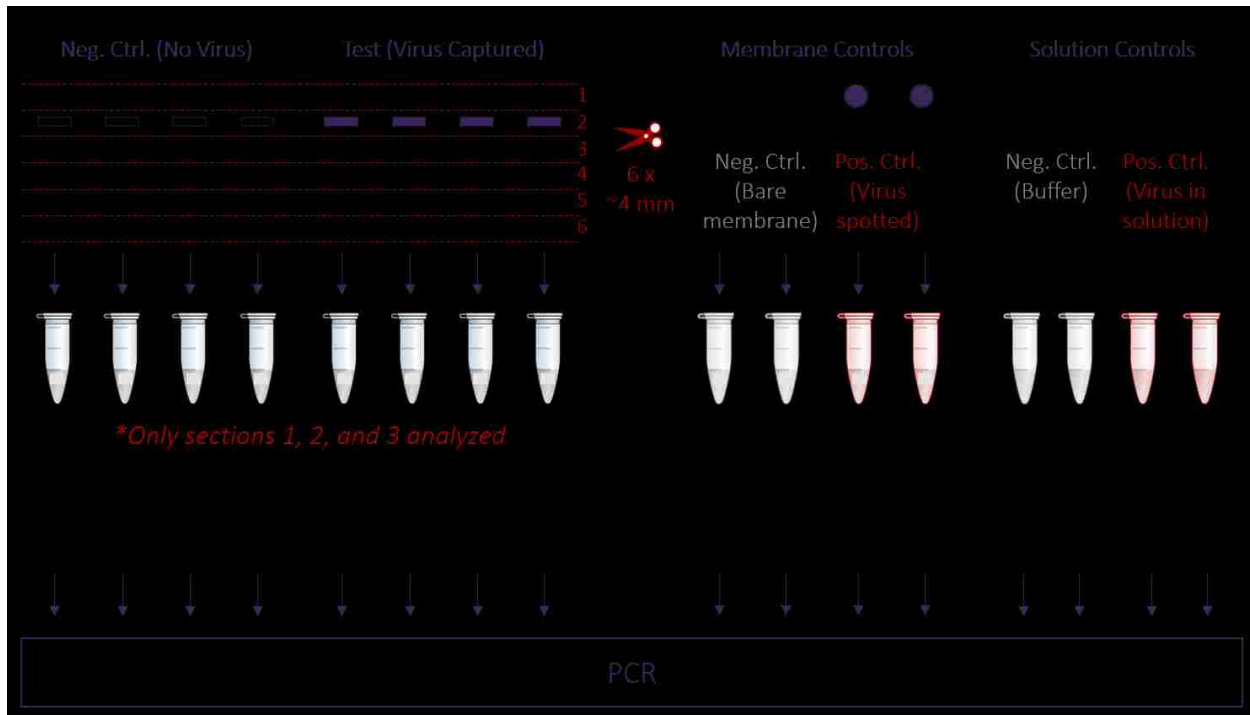


Figure 82. Experimental design for the PCR analysis of flu assay test strips.

Test strips with Trimer 11 test lines were subjected to flow with virus or negative control, then cut into sections, each of which was analyzed for its influenza RNA content by qRT-PCR. Membrane controls and solution controls were also prepared, as illustrated.

To perform the PCR analysis of the influenza content on the test lines, the test strips that remained unlabeled by the full HA assay were prepared for analysis. As shown in Figure 82, each test strip was cut into six ~4-mm-long pieces, numbered 1-6 from the top of the strip to the bottom. The test line region was located in piece #2. Care was taken to minimize contamination as much as possible, handling negative control membranes first, and cleaning the scissors with 70% ethanol in between each cut. Extra bare pieces of membrane (also ~4-mm long) were hand-spotted with 0.5 μL of virus at 1.25×10^8 CEID₅₀/mL, or left bare, to serve as positive and negative membrane controls, respectively. All membrane pieces were incubated with 50 μL H₂O in 1.5-mL tubes. Half of the tubes were heated at 95 °C for 5 minutes to induce lysis (a protocol previously developed by Dr. Ladd), and the other half remained unheated and presumably unlysed. After incubation, each membrane piece was removed from its tube. To recover the small amount of liquid still contained within the membrane piece, each piece was placed in a 0.6-mL tube and centrifuged (14,000 g, 3 min) to spin out the residual liquid. (A 0.6-mL tube was used because its geometry prevented the membrane piece from touching the bottom of the tube, allowing for separation of the liquid from the membrane.) This residual liquid was then added back to its corresponding master 1.5-mL tube with the master liquid sample.

Positive and negative control solutions were also prepared based on the amount of liquid expected in a 4-mm long strip, 3.3 μL (20 μL for 24 mm \rightarrow 3.3 μL for 4 mm). The positive control solution therefore consisted of 3.3 μL of virus at 1.25×10^8 CEID₅₀/mL added to 50 μL H₂O. The negative control solution consisted of 3.3 μL of buffer (PBST+BSA) added to 50 μL H₂O.

Each solution was analyzed for its influenza RNA content using qRT-PCR, performed by Dr. Ladd using a protocol and standards developed by Dr. Jane Kuypers in UW Virology and Dr. Brandon (Troy) Leader at PATH. A standard curve of known influenza RNA content was used to correlate CT values with copy number. All samples were plated in duplicate. The resulting copy numbers of the standards and test samples are plotted in Figure 83B as the mean \pm SD of $n=2$ replicates. Note that these results are plotted on a log scale, which exaggerates the noise at low copy numbers. The standards are plotted in blue, the unheated (unlysed) samples are plotted in yellow, and the heated (lysed) samples are plotted in purple.

These results indicate that both heated and unheated membrane samples release similar levels of amplifiable RNA. We hypothesize that this lack of difference in released RNA content is due to the RNA being retained in the membrane when the protein stack at the test line is heated and denatured, blocking the release of RNA. This hypothesis is corroborated by the comparison of the membrane controls to the solution controls: on-membrane, heating does not change the amount of RNA detection, while in solution, heating leads to a release of 82% of detectable RNA.

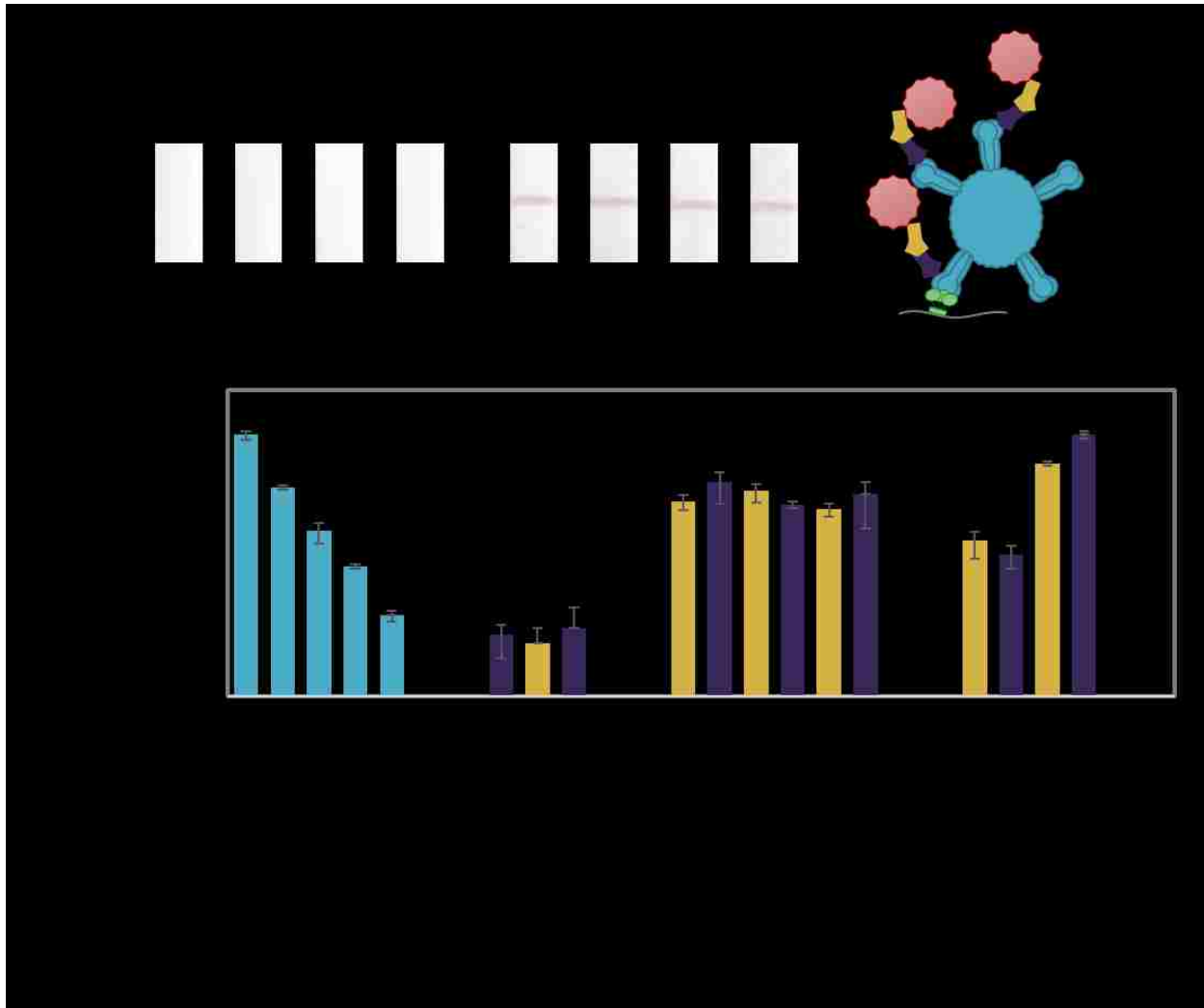


Figure 83. Results from the PCR analysis of flu assay test strips.

(A) One set of strips was run with the full flu assay to ensure influenza virus was successfully captured at the test lines. (B) The other set of strips was run with virus or negative control only (no antibody or label), then cut into sections according to Figure 82. Sections 1-3 were analyzed for influenza RNA content by qRT-PCR. The resulting copy numbers for the standards (blue bars), samples without heating/lysis (yellow bars), and samples with heating/lysis (purple bars) are plotted as the mean \pm SD of $n=2$ replicates.

Therefore, we have determined this method of performing qRT-PCR on eluate from membrane sections does not work well, because virus and/or RNA is not efficiently released from the membrane. Influenza RNA was identified across the test strips, but due to this inability to release RNA content from membrane, especially in the test region, we were unable to definitely prove or disprove that influenza virions are captured by Trimer 11. Therefore, we are left only with the lysis buffer evidence from above, which again strongly suggests that the assay captures influenza virions that are wholly or mostly intact.

In the final developmental step of the head region binder-based flu assay, we sought to develop an all-flu-binder assay. While the assay shown previously with Trimer 11 capture and biotin-HB36.5 detection did yield low signal for recombinant HA, it failed to detect whole influenza virus. Here, we combined the strength of the Trimer 11 head region binder for whole virus capture with the nitrocellulose-specific streptavidin-biotin anchoring system developed in chapter 4. Specifically, we premixed influenza virus with a biotinylated version of Trimer 11 (b-T11), captured the complex on nitrocellulose-binding mutant streptavidin (SA) test lines, and labeled with SA-Au, as shown in Figure 84.

For this experiment, mutant SA was spotted at 1 mg/mL in PBS onto GE FF80HP nitrocellulose membranes. Due to a poor spotting session, the test lines were patterned irregularly, but were sufficient to run the assay herein. Devices were stored under desiccation for four days before use. To perform the flu HA assay, we tested whole virus (IRR #FR-331) from A/Solomon Islands/03/2006 (H1N1) (“SI2006”) influenza. Biotin-Trimer 11 was premixed with virus to achieve final concentrations of 100 nM b-T11 and 1.25×10^8 CEID₅₀/mL virus. These samples were prepared in PBS instead of the usual assay buffer (PBST+BSA) to avoid disrupting the b-T11 structure, which we had preliminary evidence suggesting may be unstable. Au-2° (Au-streptavidin) was used at OD 2.5 in PBST+BSA. PBST was used for all washes. In this case, the assay consisted of the following steps: 1) 20 µL premixed bT11+virus, 2) 20 µL wash, 3) 20 µL SA-Au, and 4) 20 µL wash. Three negative controls were also run: b-T11 premixed with recombinant HA, b-T11 premixed with buffer, and buffer only (buffer premixed with buffer). The recombinant HA sample did contain the usual PBST+BSA buffer, as it was left over from a previous experiment.

A representative test line for each condition is shown in Figure 84, along with the corresponding normalized pixel intensities, plotted as the mean \pm SD of all replicates (n=4). These results show that the test case (bT11+virus) results in a significantly greater signal intensity than all three negative controls ($p < 5 \times 10^{-4}$ in all cases, by Student’s right-tailed *t*-test of unequal variance). An illustration of the assay stack is also provided. Additionally, analyzing the full assay strips, also shown in Figure 84, provides useful observations about this assay. Specifically, the bT11+buffer case shows that the unbound bT11 gets stuck toward the tip of the assay strip, confirming the flow problems we had been hypothesizing for this reagent. In contrast, when bT11 is premixed with recombinant HA or virus, it is able to flow down the strip successfully. We believe the flow problem for bT11 on its own is due to its instability, which has been mentioned by the Baker lab. Dr. Strauch

has therefore recently developed a new, more stable version of Trimer 11, called Trimer 11.2, which will also be biotinylated. Finally, since the recombinant HA sample was the only one of the four samples containing Tween-20, its clear membranes confirms that this running buffer helps reduce background signal in the membrane due to nonspecific binding.

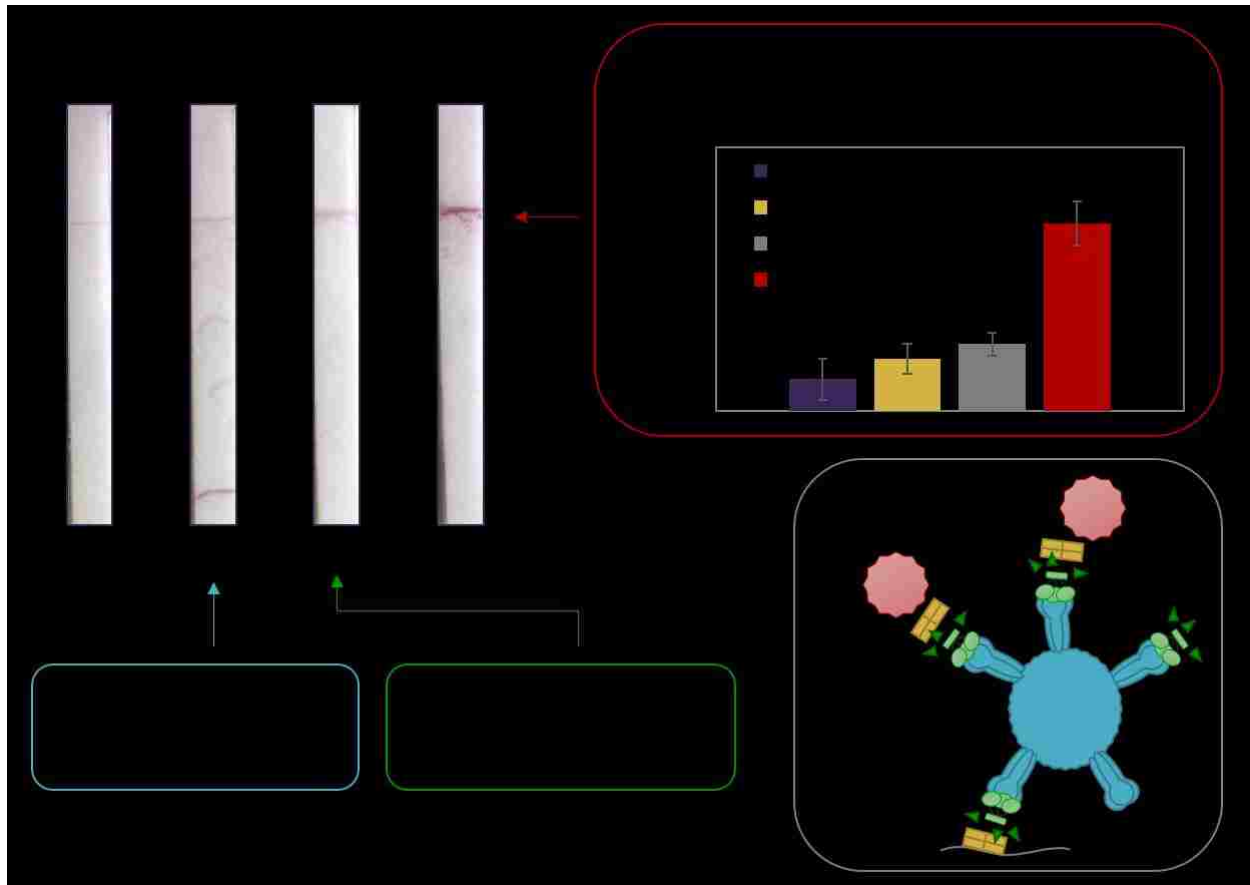


Figure 84. All-flu-binder assay for influenza virus detection.

Influenza virus was premixed with biotin-Trimer 11 (bT11), which served as both the capture and detection agent. This complex was anchored by mutant SA test lines and labeled by SA-Au. A representative image of each test case is provided, along with the normalized pixel intensities of the test lines, plotted as the mean \pm SD of $n=4$ replicates.

Overall, we successfully demonstrated an all-flu-binder assay, albeit with very high false-positive signal for the negative controls. After several follow-up experiments, we believe this false-positive signal is due both to nonspecific interaction of the SA-Au label with the mutant SA test line and to specific interaction of the SA-Au label with the available biotins of b-T11 captured on the mutant SA test line (since b-T11 contains three biotins per trimer). While this false-positive signal could be subtracted out by an automated algorithm, this assay would not work for cases when a visual readout is needed. Currently, the assay with Trimer 11 capture and antibody detection provides the best option for a read-by-eye assay that detects influenza virus, despite the fact that it contains an

antibody. This assay was moved forward for final assay characterization, described in the next section.

5.5. Final Assay Characterization

After all of the flu HA assay development using novel flu binders, novel membranes, and novel immobilization strategies, the two most promising assays were fully characterized based on their analytical sensitivities. The first assay was Trimer 11 head region binder capture and antibody detection, given its strong performance for the detection of whole influenza virus. This limit of detection (LOD) of this assay was determined for both recombinant HA and whole virus. The second assay characterized was the mutant SA anchoring system for biotinylated stem region binder (b-HB36.5) capture and antibody detection. While this assay cannot detect whole virus, it has shown superior performance for recombinant HA detection and may still be a useful assay scheme if HA can be isolated from virus. Finally, the analytical sensitivities for these novel assays are compared to that of a traditional antibody-based lateral flow immunoassay in chapter 7.

5.5.1. Methods

Functionality Testing via Flu Hemagglutinin Assay

The analytical sensitivity of each final assay was characterized using the flu HA assay described in section 5.2.1, with a dilution series of test HA or virus concentrations. In each case, the statistical limit of detection was determined according to the method described in chapter 6, resulting in an LOD estimated with 95% confidence interval.

5.5.2. Results and Discussion

Limits of Detection of Flu HA Assay with Trimer 11 Capture for Recombinant HA and Whole Virus

Two assay series were performed to characterize the analytical sensitivity of the novel flu HA assay using Trimer 11 head region binder capture, one with recombinant HA antigen and one with whole influenza virus. For these experiments, Trimer 11 was spotted at its stock concentration of $\sim 10 \mu\text{M}$ ($\sim 0.7 \text{ mg/mL}$) in PBS. Devices were stored under desiccation overnight before use. To perform the flu HA assay, we tested recombinant HA (IRR #FR-67) and whole virus (IRR #FR-331) from A/Solomon Islands/03/2006 (H1N1) ("SI2006") influenza. Recombinant HA was tested at concentrations of 78 nM, 15 nM, 3 nM, 625 pM, 125 pM, 25 pM, and 5 pM, in addition to no-HA

negative controls. Virus was tested at concentrations of 1.25×10^8 , 2.5×10^7 , 1.25×10^7 , 2.5×10^6 , 1.25×10^6 , 2.5×10^5 , and 1.25×10^5 chicken embryo infectious dose (CEID₅₀/mL), in addition to no-virus negative controls. Note that the first dilution represents $\frac{1}{2}$ stock concentration, which was the highest concentration we could test while still maintaining at least 50% running buffer content. Detection antibody (SI/Ab3, IRR #FR-502) was used at 100 nM. Au-2° (Au-goat-anti-mouse IgG, Arista Biologicals, Inc.) was used at OD 2.5. All reagents were diluted in a running buffer of PBST+BSA, and PBST was used for all wash steps. All reagents were delivered sequentially, which was determined to be the optimal reagent delivery strategy for this system (data not shown). The recombinant HA dilution series is shown in Figure 85A, and the virus dilution series is shown in Figure 85B. In both cases, a representative test line for each concentration is provided, along with the corresponding normalized pixel intensities, plotted as the mean \pm SD of all replicates (n=4).

Based on these results, the Trimer 11 assay with recombinant HA yields a statistical LOD of 451 pM (95% CI: [358 pM, 569 pM]), and the assay with virus yields an LOD of 3.54×10^7 CEID₅₀/mL (95% CI: [1.88×10^7 CEID₅₀/mL, 6.66×10^7 CEID₅₀/mL]). Note that, while the virus signal intensities are low, we were limited to these test concentrations due to the concentration of the virus stock solution (2.5×10^8 CEID₅₀/mL) and the need to dilute in running buffer by at least 50%. Although there is no straightforward relationship between molar concentration of HA, concentration of cultured virus, and concentration of virus in clinical samples, our best estimation indicates that these LODs are within the clinically relevant range of HA concentration during influenza infection, as described in 7.4 (see Table 14).

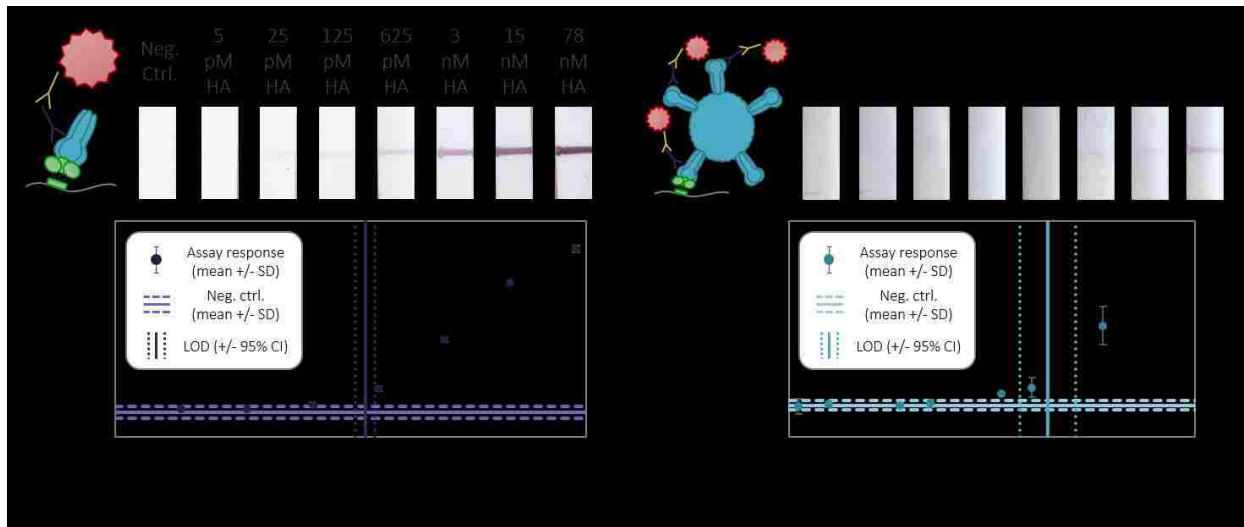


Figure 85. Analytical sensitivity of the novel flu HA assay with Trimer 11 capture.

Representative test lines and the full assay response curves are provided. Each condition was tested with n=4 replicates. (A) Assay run with recombinant HA. (B) Assay run with whole virus.

Limit of Detection of Flu HA Assay with Mutant SA + b-HB36.5 Capture for Recombinant HA

To characterize the analytical sensitivity of the novel flu HA assay using biotinylated stem region binder capture, anchored by nitrocellulose-binding mutant streptavidin, we performed a dilution series using varying concentrations of recombinant HA antigen. For this experiment, nitrocellulose-binding mutant SA (AbCam #ab51404) was spotted at 1 mg/mL in PBS. Devices were stored under desiccation overnight before use. To perform the flu HA assay, biotin-HB36.5 was pre-mixed with recombinant HA samples. Biotin-HB36.5 was used at a final concentration of 100 nM. Recombinant HA (SI2006, IRR #FR-67) was tested at final concentrations of 100 nM, 10 nM, 1 nM, 500 pM, 100 pM, 50 pM, and 10 pM, in addition to no-HA negative controls. Detection antibody (SI/Ab3, IRR #FR-502) was used at 100 nM. Au-2° (Au-goat-anti-mouse IgG, Arista Biologicals, Inc.) was used at OD 2.5. All reagents were diluted in a running buffer of PBST+BSA. PBST was used for all washes, except for the first wash, in which biotin-BSA was used at 1 mg/mL in PBS, as described in section 4.5. The assay stack is illustrated in Figure 86A, and the dilution series is shown in Figure 86B. A representative test line for each concentration is provided, along with the corresponding normalized pixel intensities, plotted as the mean +/- SD of all replicates (n=4).

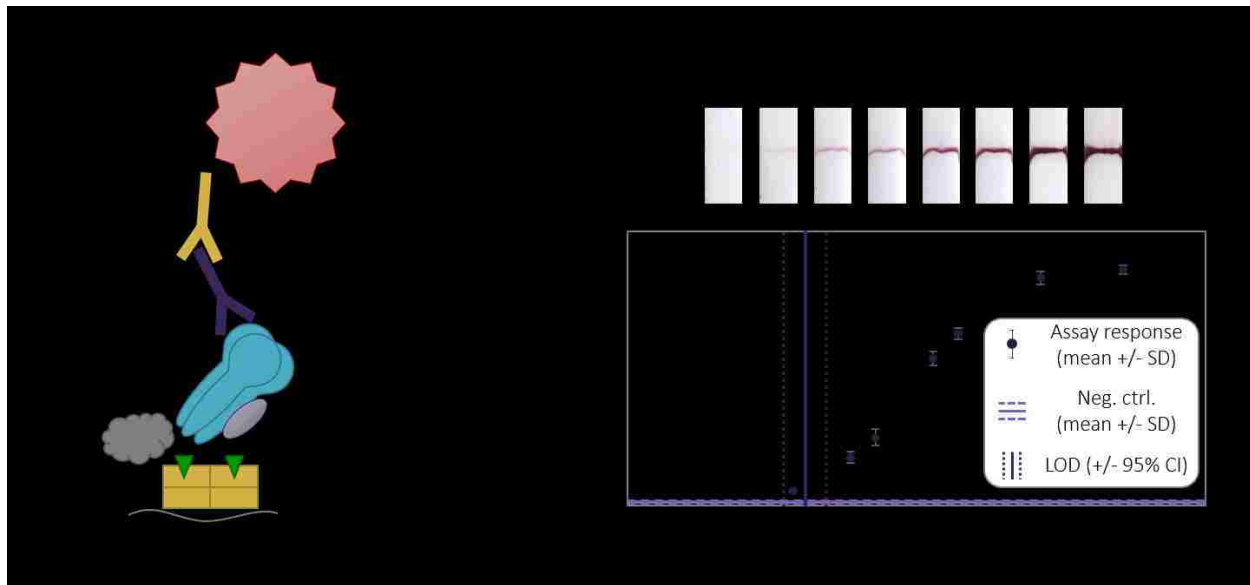


Figure 86. Analytical sensitivity of novel flu HA assay with biotin-HB36.5 anchored by mut. SA.

(A) Illustration of the assay stack. (B) Dilution series results. Representative test lines and the full assay response curves are provided. Each condition was tested with $n=4$ replicates.

Based on these results, the mutant SA + b-HB36.5 assay with recombinant HA yields a statistical LOD of 14 pM (95% CI: [8 pM, 25 pM]). This LOD is significantly lower than that of the Trimer 11 assay described above ($p = 2.4 \times 10^{-14}$ by Welch's t -test), indicating that this stem region binder-based assay is more sensitive than the head region binder-based assay.

5.6. Conclusions

Through the assay development described above, we arrived at two highly functional flu HA assays.

The most sensitive is the use of biotinylated stem region flu binder b-HB36.5 and anchoring by nitrocellulose-binding mutant streptavidin, yielding an LOD of 14 pM for recombinant HA.

However, the stem region binder has not been successfully demonstrated as a capture agent for whole influenza virus, which we hypothesize is due to steric hindrance issues resulting from the difficulty of accessing the stem region epitope when the flu binder is immobilized on paper. The second assay using head region binder Trimer 11 for capture, on the other hand, successfully captures both recombinant HA and whole influenza virus with LODs of 451 pM and 3.54×10^7 CEID₅₀/mL, respectively. Therefore, the head region binder-based assay demonstrated herein represents an important development in influenza detection, especially when whole virus is the target of interest. Detection of intact virus is an attractive option for simple point-of-care tests, when sample pre-processing must be minimized or eliminated. However, when more complex diagnostic devices are acceptable, and HA can be isolated from virus prior to detection, then both

the head and stem region binder can be used to enable maximum customization and sensitivity. Finally, both the Trimer 11 and mutant SA + b-HB36.5 assays are compared to a standard antibody-based lateral flow immunoassay in chapter 7 to fully demonstrate the strides we have made through this assay development work. In the next chapter, the statistical limit of detection method used to compare these assays is described in detail.

6. Limit of Detection Analysis

6.1. Motivation

The development of diagnostic bioassays represents a large focus area of scientific research and product development, with a global in vitro diagnostics market valuation of \$49.2B in 2012 [186] and over 30,000 assay-related publications listed in PubMed in the same year [187]. While clinical sensitivity and specificity serve as the ultimate rulers of any diagnostic assay, analytical sensitivity remains a critical marker for benchmarking an assay and comparing its performance to other systems. Analytical sensitivity is also a primary metric by which assay developers track the performance of an assay during development, prior to the point of clinical testing. It was this need for a way to characterize and compare the different versions of my assays statistically that motivated my development of the novel limit of detection analysis (LOD) method herein.

Despite the need for analytical sensitivity measurements, the diagnostic assay literature lacks the use of robust statistical methods for determining the analytical LOD of an assay. Instead, researchers often use simple and idealized methods that are readily available, which limits the LOD calculations to rough estimates. I believe this use of idealized methods reflects a realistic preference for simple and accessible methods, and a lack of such methods that have reduced the concepts of limit of detection theory to practice for the specific application of bioassays. It is therefore my goal to provide an accessible method for estimating statistically robust LODs for bioassays, when researchers desire a more rigorous estimate. To this end, I collaborated with several statisticians in the Department of Statistics through the University of Washington Statistical Consulting Program, which provides free consulting services to students and researchers on campus. In particular, Master's student Jing Hong performed the initial analysis and guidance, followed by in-depth methods development by PhD student Maryclare Griffin. Both students were supervised by Professor Paul Sampson in the Department of Statistics, who also provided guidance during the process. With the help of these statistics experts, I developed and validated the statistical method for LOD analysis herein.

The method described herein addresses three primary shortcomings of commonly used LOD methods. First, our method considers both the standard deviation of the blank samples (σ_{Blank}) and the standard deviation of test samples (σ_{Test}). This is different from commonly used methods that report the LOD based on $3\sigma_{\text{Blank}}$ and do not consider the variance in the test signals at all. Other researchers, including experts at the Clinical Laboratory Standards Institute (formerly NCCLS),

have opened this dialogue and suggested helpful methods for calculating statistically valid LOD values based on both blank and test samples [188–191]. Faber [191] and Armbruster and Pry [190] address this point in particular, explaining that a robust LOD calculation should consider the variance in both blank samples and test samples in order to account for both Type I error (false positives) and Type II error (false negatives). These authors provide simple and useful equations for obtaining such LOD estimates in the signal domain. However, these methods, like others, stop short of translating the LOD to the more useful concentration domain [189–191], or only suggesting methods for translation to the concentration domain when signal and concentration are linearly related [188]. The second improvement our method makes is therefore using a calibration curve to determine the LOD estimate in the concentration domain.

Third, commonly used methods typically do not provide a level of confidence in the LOD estimate in the concentration domain, preventing two different LOD estimates from being compared statistically to determine if one assay outperforms another. The most robust statistical analysis that we have identified in the literature comes from Lavagnini and Magno [192], who describe methods for LOD determination in the concentration domain with 95% confidence intervals (Cis) for both linear and quadratic calibration curves. While these methods are incredibly robust for their applications of gas chromatography and mass spectrometry, diagnostic bioassays that are based on biomolecular interactions, such as protein binding, are described by more complex calibration curves and can therefore benefit from accompanying methods to estimate analytical sensitivity.

Here, we build on the above methods by describing a statistically robust method for calculating the analytical LOD of an assay with a sigmoidal relationship between assay signal and analyte concentration. This sigmoidal relationship, described by a four-parameter logistic (4PL) curve (or 5PL, in the case of asymmetry), is commonly observed for assays that employ protein-protein binding interactions and reflect the underlying binding kinetics [193–196]. However, our method can also be applied to any other type of calibration curve for which an explicit equation can be determined. Finally, the method described herein includes the determination of the 95% confidence interval for the LOD estimate in the concentration domain, which allows two different LODs from two different assays to be compared for statistical significance. Using this method, assay developers can determine which assay changes result in significant improvements in the assay performance, thereby bringing increased rigor and objectivity to the assay development and characterization process.

The method is described in detail below (section 6.2.1), followed by an illustration of the method (section 6.2.2) using the flu HA assay from section 5.5 (Trimer 11 capture, antibody detection). Additionally, the ability of this method to compare two different assays statistically is illustrated by comparing the Trimer 11 assay to the mutant SA + b-HB36.5 assay with biotin-BSA wash from section 4.5. Finally, a comparison to the commonly used $3\sigma_{\text{Blank}}$ method is also provided (section 6.2.3). The MATLAB code for this novel statistical LOD analysis method is provided in Appendix D, and the code for comparing two assays is provided in Appendix E.

6.2. Novel Method for Statistically Robust Limit of Detection Analysis

6.2.1. Method Description

Step 1: Calculate L_C Value (Limit of Blank)

The method begins by identifying the signal threshold at which there is an α probability of generating a false positive result and a β probability of generating a false negative result. This signal threshold, illustrated in Figure 87, is described in previous methods as the L_D value [188–191], which is the limit of detection of the assay in the signal domain.

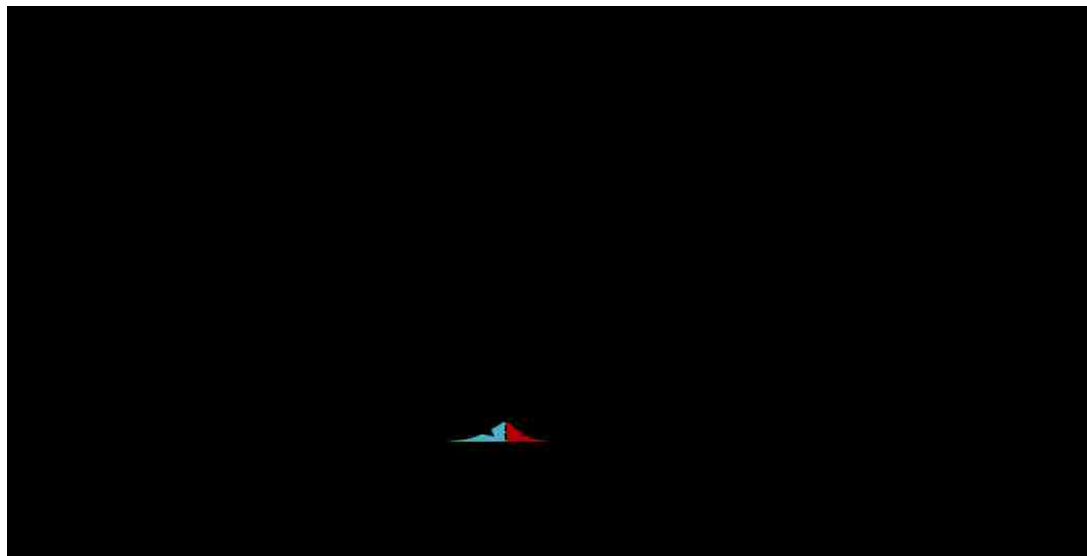


Figure 87. Illustration of the how the L_C and L_D values are determined for LOD analysis.

This method is based on previously described methods [188–191]. Here, we utilize all test concentration data to generate σ_{Test} as a pooled standard deviation, rather than choosing a single, low-concentration sample (see Step 2).

In order to calculate L_D , we start by first determining the critical value, L_C (also known as the limit of blank), exactly as described previously [188–191]. This calculation is given by Eqn 28, where

μ_{Blank} is the mean of the signal intensities for n blank (negative control) replicates, σ_{Blank} is the standard deviation of the blank replicates, and $t(1-\alpha, n-1)$ is the $1-\alpha$ percentile of the t -distribution given $n-1$ degrees of freedom.

$$L_C = \mu_{Blank} + t(1 - \alpha, n - 1) \cdot \sigma_{Blank} \quad \text{Eqn 28}$$

Note that we set $\alpha = \beta = 0.05$, but these significance levels can be chosen by the researcher for the particular dataset at hand.

Step 2: Determine Representative Standard Deviation for Test Concentrations

We then determine L_D in a very similar manner to the methods described above. To do so, we must determine a standard deviation that best represents the test signals at the L_D level. Previously, researchers have chosen a single, representative test concentration from which to draw the standard deviation. With a sufficient number of replicates and a low-concentration test sample to utilize, this approach can produce a reliable representative standard deviation. However, for a small number of replicates, the sample variance of a single concentration level may not accurately represent the population variance, so using a single empirical standard deviation is not recommended when there are fewer than 10 replicates per concentration level [197,198]. In our case, with four replicates per concentration level, choosing a single representative concentration is not recommended. Instead, we opted to calculate a pooled standard deviation for all test samples in the dilution series, as shown in Eqn 29, where σ_i is the standard deviation in signal intensities for n replicates of the i th test concentration, with a total of m different test concentrations. Henceforth, we assume that n_i does not depend on concentration level, i.e. $n_i = n$.

$$\sigma_{Test} = \sqrt{\frac{\sum_{i=1}^m \sigma_i^2}{m}} \quad \text{Eqn 29}$$

This approach better leverages the full dataset than the previously described approach of using a single test concentration and removes the user bias of selecting a representative low-concentration sample. This pooled SD approach is effective for datasets in which there is variability in the variances across test concentrations, allowing that variability to be averaged out and resulting in a representative SD for all test concentrations. However, this approach requires that the variance in signal is not directly correlated with analyte concentration across the range of concentrations tested. If a dataset instead shows a clear trend of increasing variance with increasing analyte concentration, one can either attempt to transform the data to achieve more uniform variances

(such as a log transformation), or can revert to choosing a representative low-concentration sample or set of low-concentration samples from which to derive the representative standard deviation. A variance model can also be applied if the number of replicates per test concentration is high, but, as for the use of empirical variances, applying a variance model is also not recommended when there are fewer than 10 replicates per concentration level [197,198].

Step 3: Calculate L_D Value (Limit of Detection in the Signal Domain)

Once a standard deviation of the test samples is determined, the L_D value can be calculated as usual with Eqn 30, where σ_{Test} is the pooled standard deviation of n test replicates and $t(1-\beta, m(n-1))$ is the $1-\beta$ percentile of the t -distribution given $m(n-1)$ degrees of freedom.

$$L_D = L_C + t(1 - \beta, m(n - 1)) \cdot \sigma_{Test} \quad \text{Eqn 30}$$

Again, we set $\alpha = \beta = 0.05$, but these significance levels can be chosen by the researcher.

Step 4: Perform Curve Fit to Generate Calibration Curve between Signal and Concentration Domains

Expanding on the previously described methods, we then apply a 4PL calibration curve to translate the L_D value in the signal domain to an LOD estimate in the concentration domain. The 4PL curve (or 5PL curve in the case of asymmetry) is commonly used to fit data from bioassays, such as ELISAs, as it captures the sigmoidal relationship between signal and analyte concentration that is observed for these assays [193,194]. While the 4PL and 5PL curves do not have a theoretical basis for bioassays, they effectively describe the shape of binding curves that are derived from protein binding kinetics [194]. Importantly, this sigmoidal shape of the binding curve only exists on a log scale of analyte concentrations, so the first step in our method is to transform the analyte concentration I to a log scale (\log_{10}). Additionally, in order to include the negative controls ($C = 0$) in the fitting process, we add 2 before taking the log, which will be subtracted back out at the end. This ensures that the derivatives of the 4PL curve with respect to the 4PL parameters are well defined at all concentration levels, including $C = 0$, and has little effect on the results once transformed back to the concentration scale. Therefore, our full transformation is from C to $\log(C+2)$, and we use these log-transformed concentrations for the remainder of the analysis. Finally, we have chosen to use the 4PL curve instead of the 5PL curve in order to avoid over-fitting the data from the limited number of replicates that we typically have available during early stage assay development. However, if one has a large enough dataset, then a 5PL curve would be advantageous for taking into account potential asymmetry in the binding curve, which can improve the accuracy of the fit [194].

In the 4PL (Eqn 31) and 5PL (Eqn 32) equations below, S represents the signal intensity at analyte concentration C .

$$S = \frac{a - d}{1 + \left(\frac{\log(C + 2)}{c}\right)^b} + d \quad \text{Eqn 31}$$

$$S = \frac{a - d}{\left[1 + \left(\frac{\log(C + 2)}{c}\right)^b\right]^e} + d \quad \text{Eqn 32}$$

We used MATLAB (MathWorks, Natick, MA) to apply a 4PL curve fit to all replicates of all test concentrations and negative controls. The built-in MATLAB function *fit* uses a non-linear least-squares approach to determining estimates of the parameters (in this case, a , b , c , and d) that create the curve (in this case, 4PL, Eqn 31) that best describes the data. The initial conditions and bounds on the parameters were set to eliminate nonsensical parameter space and increase the speed of the fitting process. In our case, since our signal is pixel intensity that has been normalized on a scale from 0 to 1, we set the bounds on the a and d parameters (bottom and top asymptotes) as $[-10, 10]$ and $[0, 10]$, respectively. Parameter c (inflection midpoint) could be ascribed bounds that are well beyond the range of analyte concentrations tested, but in this case the bounds were simply restricted to positive values with $[0, \text{infinity}]$. Parameter b (slope factor for the curve) is the least well known, except that it must be positive to account for increasing signal with concentration, so it was assigned bounds of $[0, \text{infinity}]$. The starting value for all four parameters was set to 1. While the data points could be weighted by inverse variance in order to take into account variability in variance, this approach is not recommended when there are fewer than 10 replicates per concentration level [197,198], so an unweighted fit was used here. The unweighted fit is also consistent with the assumption of homoscedasticity for the pooled estimate of variance used above. Although the 4PL curve fit is expected to work well for most bioassays that rely on protein binding kinetics, this method can be adapted for any type of assay by substituting the 4PL (or 5PL) model for an equation that describes the shape of that assay system (e.g. logarithmic, exponential, polynomial, etc.), and by choosing the parameter bounds and starting values appropriately. The parameter estimates determined from the curve fitting are denoted as $\hat{\beta}$, defined in Eqn 33.

$$\hat{\beta} = (\hat{a}, \hat{b}, \hat{c}, \hat{d}) \quad \text{Eqn 33}$$

Step 5: Use Calibration Curve to Translate L_D Value into LOD Estimate in Concentration Domain

Once the specific 4PL fit has been determined, it can be used to determine the LOD estimate by rearranging the 4PL equation (Eqn 31) as a function of signal intensity, S . We denote this inverse 4PL equation as $f(S; \hat{a}, \hat{b}, \hat{c}, \hat{d})$, given by Eqn 34 below.

$$f(S; \hat{a}, \hat{b}, \hat{c}, \hat{d}) = \log(C + 2) = \hat{c} \cdot \left[\left(\frac{\hat{a} - \hat{d}}{S - \hat{d}} \right) - 1 \right]^{1/\hat{b}} \quad \text{Eqn 34}$$

We can then plug in the L_D value for assay signal and solve for the corresponding analyte concentration, given by Eqn 35.

$$\log(LOD + 2) = \hat{c} \cdot \left[\left(\frac{\hat{a} - \hat{d}}{L_D - \hat{d}} \right) - 1 \right]^{1/\hat{b}} \quad \text{Eqn 35}$$

This returns the LOD estimate on the $\log(C+2)$ scale. To get the final LOD estimate on the concentration scale, we simply exponentiate the result and subtract 2.

Step 6: Calculate 95% CI of LOD Estimate

To calculate the 95% confidence interval of the LOD estimate, we return to the $\log(C+2)$ scale. On this scale, we can determine the standard error of the LOD estimate, from which the 95% CI can be constructed. To do so, we approximate the asymptotic variance of the LOD estimate using the method described by Davidian and Giltinan [195]. This asymptotic variance estimate, given by Eqn 37, is derived from the estimated asymptotic variance-covariance matrix, $\hat{\Sigma}_\beta$, of the parameters from the curve fit, as well as the estimated residual variance, $\hat{\sigma}^2$, defined in Eqn 36.

$$\hat{\sigma}^2 = \frac{1}{mn - 1} \sum_{i=1}^m \sum_{j=1}^n \left(\frac{\hat{a} - \hat{d}}{1 + \left(\frac{\log(C_{ij} + 2)}{\hat{c}} \right)^{\hat{b}}} + \hat{d} - S_{ij} \right)^2 \quad \text{Eqn 36}$$

The asymptotic variance takes into account both the variability from error in the curve fitting and the variability from error in the signal measurement.

$$Var_{asympt} \approx \sigma^2 \left(\frac{\partial f}{\partial S} \right)^2 / n + \left(\frac{\partial f}{\partial \beta} \right)' \hat{\Sigma}_\beta \frac{\partial f}{\partial \beta} \quad \text{Eqn 37}$$

Note that n represents the number of replicates per concentration level (which in our case was 4). While we calculated the estimated variance-covariance matrix ($\hat{\Sigma}_\beta$) manually (see code in Appendix D), many software packages will return this matrix directly as output from the curve fit.

Calculating the asymptotic variance according to Eqn 37 requires determining the derivatives of the 4PL inverse function with respect to signal, S , and each of the 4PL parameters, which can be obtained by hand or using symbolic differentiation software, such as Mathematica (Wolfram Research, Champaign, IL). These derivatives are given in the provided MATLAB code (Appendix D). The standard error of the LOD estimate is then calculated as the square root of the asymptotic variance, as shown in Eqn 38.

$$\widehat{se} = \sqrt{Var_{asympt}} \quad \text{Eqn 38}$$

Finally, this standard error can be used to construct a confidence interval for the LOD estimate on the $\log(C+2)$ scale. Letting $z_{0.025}$ and $z_{0.975}$ be the lower 2.5th percentile and upper 97.5th percentile of a standard normal distribution, we can obtain the lower and upper bounds of the 95% confidence interval, as shown in Eqn 39.

$$\begin{aligned} \log(LOD_{0.025} + 2) &= \log(LOD + 2) + z_{0.025}\widehat{se} \\ \log(LOD_{0.975} + 2) &= \log(LOD + 2) + z_{0.975}\widehat{se} \end{aligned} \quad \text{Eqn 39}$$

These lower and upper bounds are then transformed back to the concentration scale by exponentiating and subtracting 2, resulting in the 95% confidence interval of the LOD estimate, $[LOD_{0.025}, LOD_{0.975}]$.

Step 7: Compare LOD Estimates of Two Assays using Welch's t-Test

The mean and standard error of the LOD estimate can be used to compare LOD estimates for two different assays, i.e. assay A and assay B, to determine if one assay is statistically more sensitive than the other. It is important to note that we continue to use the $\log(C+2)$ scale for this analysis, which is the scale on which the LOD estimates are approximately normally distributed. We can then use Welch's t -test, which allows for unequal variances, to test for the equality of the two LOD estimates [199]. This is also known as the Student's t -test of unequal variances.

Letting μ_i and $s\hat{e}_i$ denote the mean and standard error of the LOD estimate of assay $i=A,B$, the t -statistic for Welch's t -test is given by Eqn 40.

$$t_{stat} = \frac{\mu_A - \mu_B}{\sqrt{\widehat{se}_A^2 + \widehat{se}_B^2}} \quad \text{Eqn 40}$$

Next, we compute the effective degrees of freedom for the test using the Satterthwaite approximation [200], given in Eqn 41. In this equation, n represents the total number of replicates for a single assay. Note that we use $n-4$ as the initial degrees of freedom term in this equation, which represents the degrees of freedom remaining in the system after estimating the 4PL parameters.

$$df = \frac{(\widehat{se}_A^2 + \widehat{se}_B^2)^2}{(\widehat{se}_A^4 + \widehat{se}_B^4)/(n - 4)} \quad \text{Eqn 41}$$

Finally, we can use the t -statistic and effective degrees of freedom to evaluate the t -distribution and determine the probability, p , of observing this difference in LOD estimates by chance, i.e. under the null hypothesis that the two distributions are equal. This calculation is shown in Eqn 42, where t_{cdf} is the cumulative density function of the t -distribution.

$$p = 1 - t_{cdf}(|t_{stat}|, df) - t_{cdf}(-|t_{stat}|, df) \quad \text{Eqn 42}$$

This process yields a p -value that describes the significance by which the distributions of the two LOD estimates A and B are different from each other. In our case, we call the LOD estimates statistically significantly different when $p < 0.05$, i.e. when the probability of observing t_{stat} under the null hypothesis is less than 0.05. Using this method, researchers can therefore compare different versions of their assay under different conditions to determine whether or not a change to the assay design results in a significant improvement in the analytical sensitivity.

6.2.2. Method Illustration with Example Assay Data

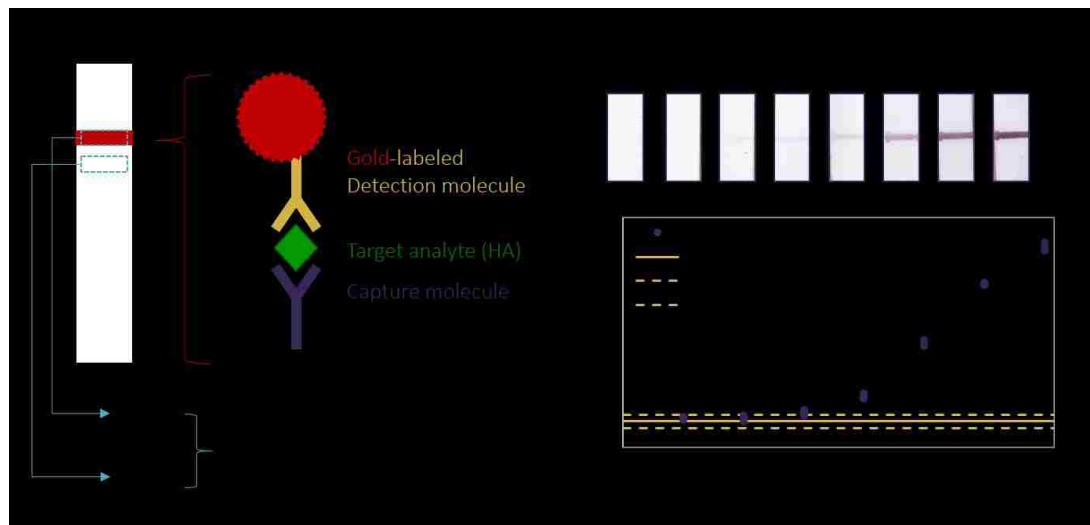


Figure 88. Description of the dataset used to demonstrate the LOD analysis method herein.

Illustration of the test strip on a macroscale and the corresponding nanoscale on which the colorimetric signal is generated in the presence of the target analyte (in this case, influenza HA). The average green-channel pixel intensity of the test line (I_{test}) is background-subtracted using a local background region (I_{bkgd}) and normalized on a scale from 0 to 1 to generate the normalized pixel intensity (I_{norm}) for the test line. (B) Scanned images of a representative test line for each of the 7 test concentrations, as well as a negative control (blank). (C) Plot of the normalized pixel intensities for 4 replicates of each test concentration, as well as the mean \pm SD of 4 replicates of the negative controls.

We applied this method to a dataset generated during the development of our paper-based assay for influenza HA. In particular, we used the data from the assay employing Trimer 11 capture and antibody detection (section 5.5). However, for the purpose of describing this LOD analysis method, the immunoassay-like detection sandwich is illustrated generally in Figure 88A. As usual, the antibody-gold nanoparticle conjugate used for labeling generates a red colorimetric signal at the test line upon completion of the assay (Figure 88B). The assay membranes were scanned at 600 dpi, 48-bit HDR color, $\gamma=1$ (Epson Perfection V700 Photo Scanner). The mean green-channel pixel intensity of each test line was computed, background-subtracted using a local background region near the test line, and normalized on a scale from 0 (white) to 1 (dark), as described in Figure 88A and in detail in section 3.2.1. The normalized pixel intensities for the dataset at hand are plotted in Figure 88C. These normalized pixel intensities were used as the assay signal for the statistical LOD analysis example herein, but this method can be applied to any type of bioassay with any type of signal. Following steps 1-6 outlined above, an LOD estimate with 95% CI was determined for this assay. These results are illustrated in Figure 90, and the numerical values are summarized in Table 11.

Step 1: Calculate L_C Value (Limit of Blank)

The signal intensities of the four negative control (blank) replicates were used to calculate the L_C value using Eqn 28. These four replicates are plotted in Figure 90 (open blue circles) along with the corresponding L_C value (cyan line). Note that these negative controls represent an analyte concentration of 0, but are plotted on the log scale due to the transformation from C to $\log(C+2)$.

Step 2: Determine Representative Standard Deviation for Test Concentrations

In order to determine a representative standard deviation for the test samples, we first analyzed the standard deviations of each data point versus test concentration (Figure 89). These results indicate that there is variability among the standard deviations, but that there is no clear trend between standard deviation and analyte concentration.

Therefore, as described above, a pooled standard deviation represents the best approach for determining a representative SD

to use in determining the L_D value (see Figure 87). In fact, this variability in estimated standard deviations for these data points illustrates the difficulty of estimating or modeling variance with a low number of replicates [197,198], as described above. The pooled test standard deviation was therefore calculated according to Eqn 29.

As described above, other approaches can be used to determine a representative standard deviation, if a particular dataset shows increasing variance with increasing analyte concentration. It should be reiterated, though, that empirical and modeled variances are not recommended when there are fewer than 10 replicates per concentration level [197,198]. In fact, the variability in sample standard deviations for this dataset (see Figure 89) illustrates this difficulty of estimating or modeling variance with a low number of replicates.

Step 3: Calculate L_D Value (Limit of Detection in the Signal Domain)

The representative test standard deviation and the L_C value were used to calculate the L_D value using Eqn 30. The test data (all four replicates for each of the seven test concentrations) are plotted

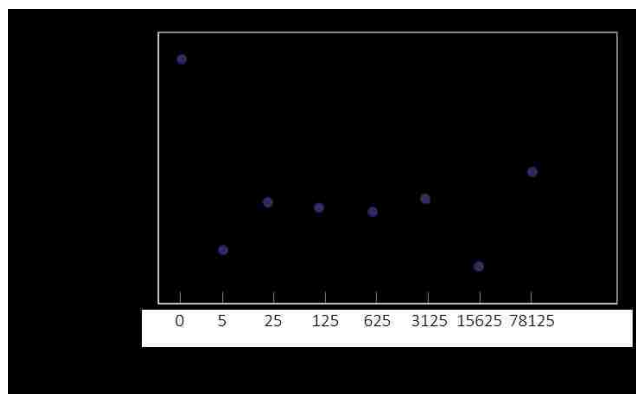


Figure 89. Variance check for example data.

The standard deviation of normalized pixel intensity is plotted vs. test concentration. These results indicate that the variance in signal intensity is variable but not correlated across this concentration range.

in Figure 90 (blue dots), along with the L_D value (green line), which represents the limit of detection in the signal domain.

Step 4: Perform Curve Fit to Generate Calibration Curve between Signal and Concentration Domains

In order to translate the L_D value in the signal domain to an LOD estimate in the concentration domain, all replicates of all concentrations (both test concentrations and negative controls) were fit with a 4PL curve according to Eqn 31. The resulting fit yielded the parameter values listed in Table 11 and an adjusted R^2 value of 0.9975. The 4PL calibration curve is plotted in Figure 90 (solid red line), and the 95% confidence interval of the fit is also provided for reference (dashed red lines). This confidence interval was obtained using the *predint* MATLAB function for the purpose of visualizing the confidence in the curve fit, but was not used for any part of the analysis.

Step 5: Use Calibration Curve to Translate L_D Value into LOD Estimate in Concentration Domain

The 4PL calibration curve and the L_D value were used to calculate the LOD estimate in the concentration domain using Eqn 35. This LOD estimate is plotted in Figure 90 (solid magenta line), representing the intersection of the L_D value with the 4PL calibration curve.

Step 6: Calculate 95% CI of LOD Estimate

The 95% confidence interval of the LOD estimate was obtained through the asymptotic variance-covariance matrix

of the 4PL fit, as described in Eqn 37-Eqn 39. These confidence bounds are plotted with the full results from the LOD analysis in Figure 90 (dashed magenta lines). All numerical results from steps 1-6 are provided in Table 11. Overall, these results illustrate both the ease of use and success of this method for the analysis of a real bioassay dataset.

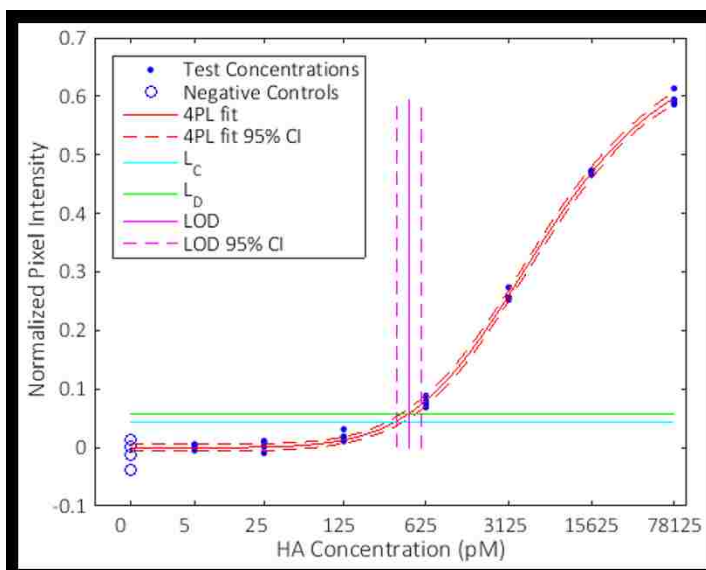


Figure 90. Results from the LOD analysis method.
The method was demonstrated with our influenza HA assay data.

Table 11. LOD analysis method results.

Results for steps 1-6 of the LOD analysis method for the example dataset described in Figure 88 are provided. These results are also visualized in Figure 90.

Step	Value	Result
1	L_C	0.0436 (signal domain)
2	σ_{Test}	0.0085 (signal domain)
3	L_D	0.0583 (signal domain)
4	4PL curve fit	a: -0.0002 (signal domain) b: 6.805 (dimensionless) c: 3.776 (log(concentration + 2) domain) d: 0.6989 (signal domain)
5	LOD	2.6563 (log(concentration + 2) domain) 451.3 pM (concentration domain)
6	LOD 95% CI	[2.5559, 2.7568] (log(concentration + 2) domain) [357.7 pM, 569.2 pM] (concentration domain)

Step 7: Compare LOD Estimates of Two Assays using Welch's t-Test

To illustrate how this method can be used to compare LOD estimates for two different assays, the same process outlined by steps 1-6 above was applied to a second version of our flu HA assay (mutant SA + b-HB36.5 capture, antibody

detection, with biotin-BSA wash, section 4.5). This second version of the assay utilized different capture and detection molecules, and we wanted to be able to answer the question: does assay B yield improved sensitivity, i.e. a lower LOD, than assay A? The means, standard errors, and 95% CIs for the LOD estimates of the two assays are given in Table 12. The two datasets are also overlaid in Figure 91. Using Eqn 40-Eqn 42, the *t*-test comparing these two LOD estimate distributions resulted in a *p*-value of 0.0076, indicating that Assay B has a significantly lower LOD than Assay A. We therefore know that the changes made in Assay B result in a more sensitive assay for influenza HA, solidifying this design choice in the assay development process. In this case, that means that the assay stack with mutant SA + b-HB36.5 capture outperforms the stack with Trimer 11 capture in the case of recombinant HA detection.

Table 12. Comparison of the LODs for two different influenza HA assays.

Two example assays are compared, Assay A and Assay B. All values are reported in the log(concentration + 2) domain, the scale on which the analysis is performed. These two assays are compared visually in Figure 91. The *t*-test resulted in a *p*-value of 0.0076, indicating that Assay B has a significantly lower LOD than Assay A.

Value	Assay A	Assay B
Difference between assays	Trimer 11 capture, Ab detection	Mutant SA + b-HB36.5 capture, Ab detection
LOD μ	2.6563	2.3700
LOD se	0.0513	0.0887
LOD 95% CI	[2.5559, 2.7568]	[2.1962, 2.5439]

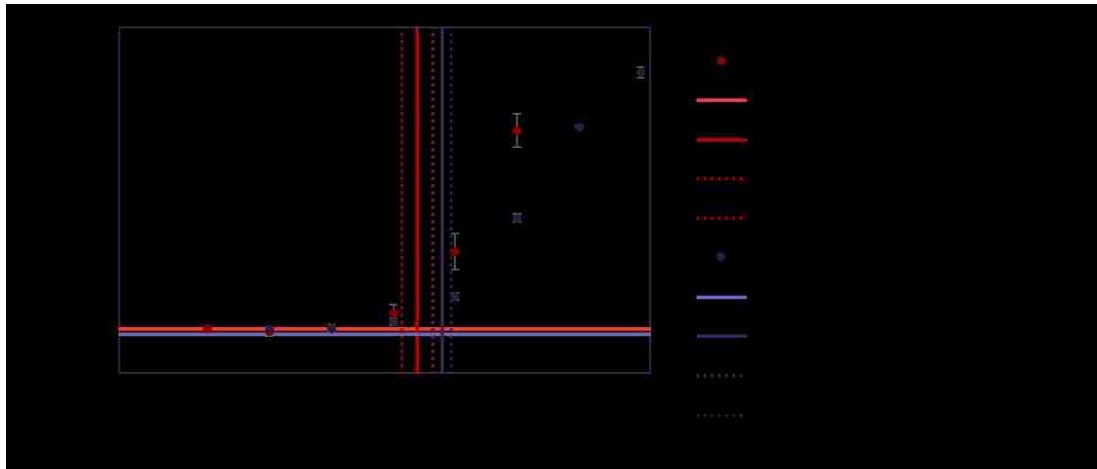


Figure 91. Visual comparison of LOD estimates for two different versions of the flu HA assay.

Trimer 11 capture = Assay A, mutant SA + b-HB36.5 capture = Assay B. The 95% confidence intervals for these two assays visually indicate that the LODs are different, and the *t*-test result confirms that this difference is significant, with $p=0.0076$.

Overall, this example highlights the ease of use of this method and the power that it provides to characterize, understand, and compare different bioassays during development. We recognize that previously described methods may not have fully met the needs of bioassay developers or have been reduced practice, so we hope that this work will provide researchers with an accessible method for calculating statistically robust limits of detection with confidence estimates. Overall, it is our aim to provide researchers with an additional option to employ that is simple to understand and implement, yet still provides statistically robust LOD values, thereby fulfilling a gap that has existed in the literature and in the assay developer's toolkit.

6.2.3. Comparison to Standard Method

The statistical LOD analysis method described above was compared to the commonly used method in the literature based on $3 \cdot \sigma_{\text{Blank}}$, in order to evaluate the differences between the two methods. The $3 \cdot \sigma_{\text{Blank}}$ method is commonly used by researchers in the field, including those in our own laboratory, due to its ease of use for obtaining a rough LOD estimate. Using this method, the L_D value is calculated simply based on this standard deviation of the blank samples, as shown in Eqn 43.

$$L_D = 3 \cdot \sigma_{\text{Blank}} \quad \text{Eqn 43}$$

Note that the L_D estimation in Eqn 43 is similar to our L_D estimation in Eqn 29, where 3 is approximately equal to 2 times the 95th percentile of the normal distribution (1.645), thus taking into account a 5% false-positive and a 5% false-negative rate, under the assumption that σ_{Blank} is

equal to σ_{Test} [192]. However, the mean of negative control signal (μ_{Blank}) is never considered, which means this method of L_D estimation will systematically under-represent the true L_D value.

Additionally, since the multiplier of 3 is based on a normal distribution, this method does not account for uncertainty in the population distribution based on the sample size. In contrast, our L_D calculation in Eqn 30 is based on a t -distribution, which does account for this sampling effect.

Under this standard method, in order to translate the L_D value from Eqn 43 to an LOD estimate in the signal domain, a linearized calibration curve is constructed based on an arbitrary set of data points near the LOD estimate, yielding a characteristic slope, m . The LOD is then estimated according to Eqn 44.

$$LOD = L_D/m = 3 \cdot \sigma_{\text{Blank}}/m \quad \text{Eqn 44}$$

This method is a reasonable approach when the standard deviation of the blank samples is approximately the same as the standard deviation of a test concentration near the LOD estimate, and when the appropriate data points are collected near the LOD estimate such that a linearized calibration curve in that region is a reasonable approximation. However, these assumptions are not always true, and it is difficult to know this correct concentration range across which to collect data *a priori*. Therefore, the method I have developed not only eliminates these assumptions and is therefore more statistically robust, but it is also applicable to a wider range of datasets, making it a more robust tool for assay developers.

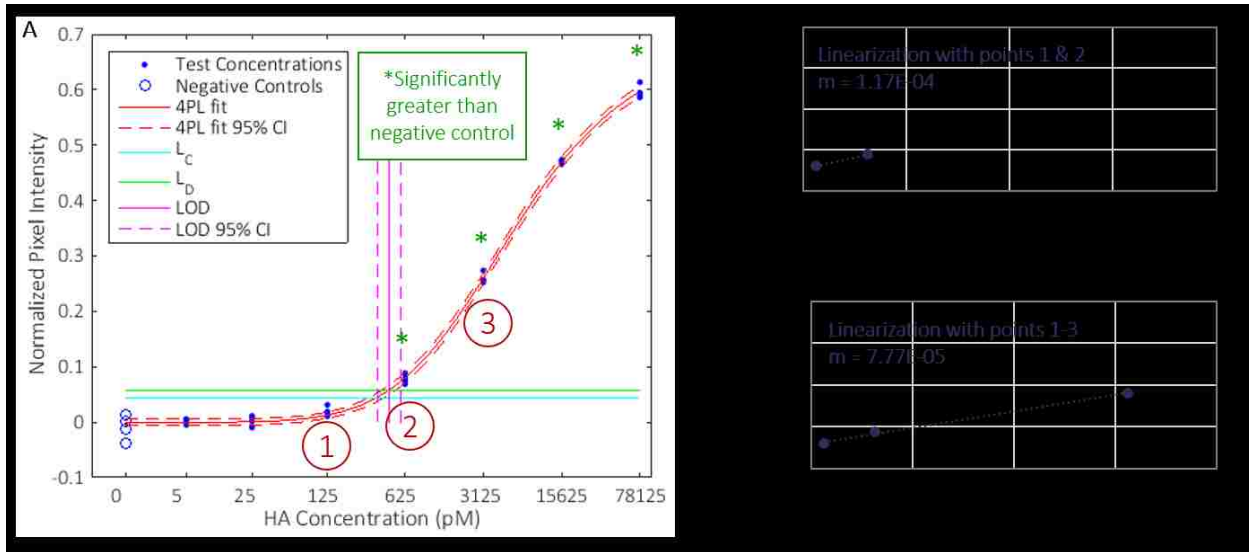


Figure 92. Comparison of 4PL calibration curve to linear calibration curves.

The 4PL calibration curve for the statistical LOD analysis developed herein is compared to two different linear calibration curves used for the standard $3\sigma/m$ LOD analysis. (A) 4PL calibration curve marked with which concentrations have signal significantly greater than the negative control (green asterisks) and labeled with data points 1, 2, and 3, used for the linearizations in parts B and C (red circles). (B) Linear calibration curve for standard method, based on data points 1 and 2. (C) Linear calibration curve for standard method, based on data points 1-3.

As for how the two methods compare, the results for each method as applied to the same flu HA assay dataset (Trimer 11 capture, Ab detection, section 5.5) are listed in Table 13. In order to perform the standard LOD analysis, a region of the curve had to be chosen to form the linearized calibration curve. Two different plausible linearizations were chosen and compared, each based on the lowest detectable concentration, i.e. the test concentration with signal significantly greater than negative control signal ($p < 0.025$, Student's one-tailed t -test of unequal variance). That concentration is labeled as data point 2 in Figure 92A. The first linearization (Figure 92B) was between this concentration (data point 2) and the next-lowest test concentration (data point 1). The second linearization (Figure 92C) spanned data point 2 and included the next-lowest concentration (data point 1) and the next-highest concentration (data point 3). It is important to note that neither of these linearizations represents the most ideal linearization for this method, since this data was not collected for the purpose of analyzing with this method. In other words, a set of concentrations near the anticipated LOD were not tested. However, these two linearizations are intended to represent the fairest comparisons possible for this dataset. The 4PL calibration curve with labeled data points and the two linearizations are provided in Figure 92.

The resulting LOD estimates in Table 13 show that the standard method, under both linearizations, produces LOD estimates outside of the 95% CI of the LOD estimate from my 4PL method. Although I cannot definitively prove which estimate is correct, these results illustrate the variability in the LOD estimate for the standard method based on the choice of linearization. While this standard LOD estimate would likely be improved with more data points near the LOD estimate to use for the linearization, this comparison highlights the benefits of my 4PL method of removing the user bias of choosing a linearization region and eliminating the need to choose the right range of test concentrations *a priori*.

Table 13. Comparison of the 4PL-based LOD method to standard $3\sigma/m$ method.

Comparison of the 4PL-based LOD method developed herein to the standard $3\sigma/m$ method, which is often encountered in the literature. Two different linearizations were used for the $3\sigma/m$ method, as shown in Figure 92.

Method	Lower 95% CI	LOD (pM)	Upper 95% CI
4PL	358	451	569
$3\sigma/m$, points 1&2	n/a	574	n/a
$3\sigma/m$, points 1-3	n/a	868	n/a

6.3. Conclusions

This work represents a novel method, based on the iteration and combination of previously described techniques, to perform statistically robust LOD calculations for bioassays. With this work, we aim to arm researchers with a statistically valid yet accessible method for determining and comparing LOD values during the assay development process. In doing so, we hope to help improve the statistical robustness of the assay development literature and allow researchers to better compare assays internally as well as with other researchers in the field. Importantly, this method allowed for the statistical characterization and comparison of the LODs for all assays described throughout this thesis work.

7. Towards Improved Flu Testing

7.1. Motivation

In this final chapter, we describe the work that has been done to leverage the accomplishments of the previous chapters to demonstrate or build towards improved flu testing. Considering the drawbacks of current influenza testing described in section 2.3.3, we aim to develop a diagnostic that is more sensitive than current influenza RDTs, is easy to use at the point of care, and has the ability to perform virus subtyping. In this chapter, we describe the work done to achieve these goals and evaluate where we stand currently.

7.2. User Assessment

In order to develop a diagnostic that would be suitable for use at the point of care, we paid careful attention to the simplicity of the assay and the user operations that would be needed to run it. In collaboration with PhD graduate Dr. Gina Fridley, PhD student Shefali Oza, undergraduate student Sugandhan Venkatachalam, and Dunia Faulx at PATH, we performed a usability study of our diagnostic platform to ensure that our end product would meet the needs of actual users of the test. In this user assessment study, we compared the usability of our lab's two primary 2DPN platforms: the folding card (see Figure 93A) and the dipping card (see Figure 93B). The folding card meters the volume of reagents delivered to the 2DPN network through the size of sample pads that are included on the card, which need to be filled to saturation by the user prior to folding and activating the card. The dipping card, on the other hand, meters volume based on the length of the input legs, as each leg will stop wicking fluid when the fluid level in the buffer reservoir drops below the leg. In this case, the user must fill the reservoir with buffer prior to inserting the 2DPN device into the reservoir. Since this insertion process was unregulated in early versions of this 2DPN platform, we improved the device by employing a rigid case in which the 2DPN card slides down into the buffer reservoir upon user activation. This platform therefore came to be known as the sliding card format.

7.2.1. Methods

User Assessment of Two Different 2DPN Platforms

In preparation for the user assessment sessions, Shefali Oza, Gina Fridley, Sugandhan Venkatachalam, and I worked together to design and create two usable prototypes based on our

lab's two primary 2DPN platforms: the folding card and the sliding card. Once we developed the working prototypes, we prepared 8 kits for each prototype, each of which contained the device, its supporting materials (tubes of water and droppers), and a laminated instruction card, as shown in Figure 93.

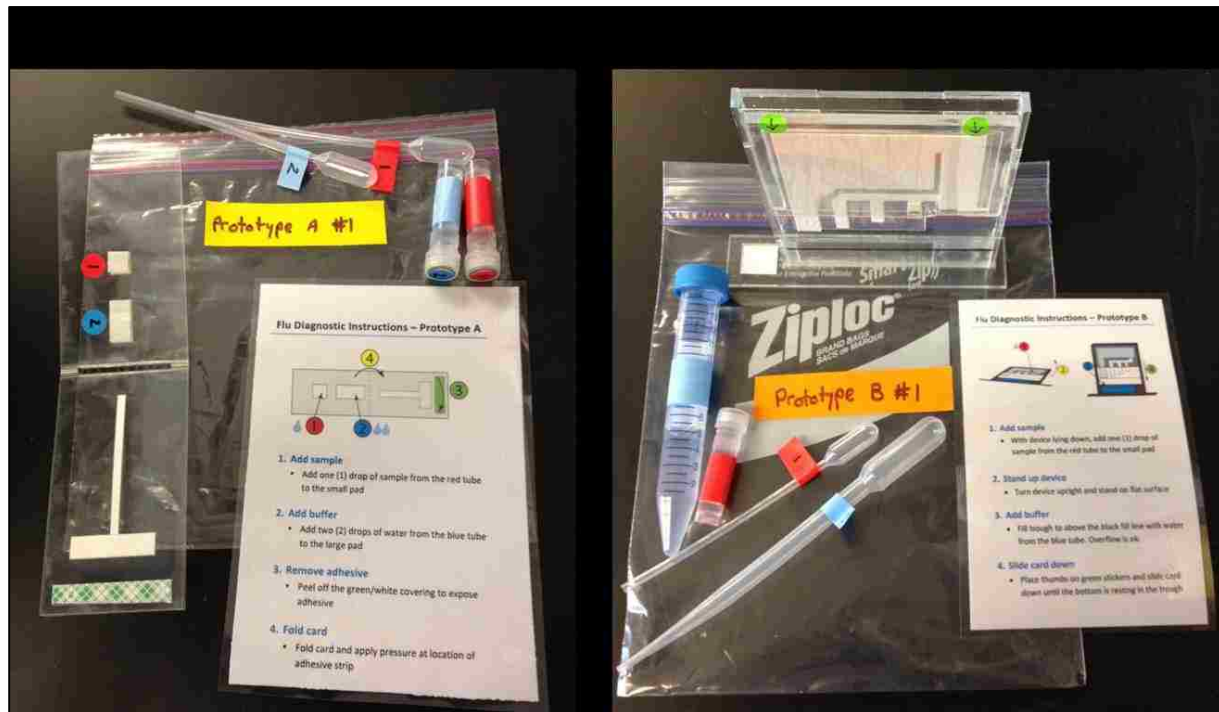


Figure 93. 2DPN prototype kits for user assessment.

Pictures of the kits prepared for the two 2DPN prototypes tested at the flu diagnostic user assessment sessions: Prototype A, the folding card, and Prototype B, the sliding card.

To compare our two different 2DPN platforms in terms of usability, we performed a set of user assessment sessions in which participants interacted with preliminary prototype devices of the two platforms. This set included two separate sessions, each of which took place at Seattle Children's Hospital in Seattle, WA. The type of participants varied slightly between the sessions, but generally included a mix of doctors, nurses, and laboratory staff at Children's Hospital. Session 1 included 7 participants, and session 2 included 6 participants. Both sessions were facilitated by Dunia Faulx, a usability study specialist from PATH. Together with my colleagues Gina Fridley and Shefali Oza, we observed the participants using the devices, listened to and noted their comments and suggestions, and asked them specific questions about the prototypes.

7.2.2. Results and Discussion

User Assessment of Two Different 2DPN Platforms

Overall, the user assessment sessions went well and generated valuable information for the development of our 2DPN devices. For Prototype A, the folding card, the users appreciated its simplicity, ease of use, intuitive flow, and small size, including its potential portability. They did not have much negative feedback about this prototype, but there was some problem with the adhesive in a few cases, and there was some confusion about the proper orientation of the device. The feedback for Prototype B, the sliding card, was overwhelmingly negative, due its large and bulky size and non-intuitive user steps. The users largely found the device to be cumbersome and intimidating, and there was a lot of concern about waste, both for developing-world settings as well their own setting at Children's Hospital. Additionally, the participants worried about the device tipping or being knocked over. The users were somewhat accepting of the sliding action and said that this general action would be suitable, if the rest of the device were vastly improved.

In summary, the users strongly preferred prototype A, the folding card. They also gave several useful suggestions for improving the devices and kits, such as the use of twist-off ampule droppers to store pre-measured amounts of buffer. The users also emphasized the importance of a read-out method that is easy to interpret and an overall fast assay run-time, although these factors were not tested in this user session.

7.3. 2DPN Folding Card Development

Based on the feedback from the usability study, we pursued the initial development of a 2DPN folding card to implement the flu HA assay. Specifically, this card was developed for and demonstrated with the stem region-binder based assay employing mutant streptavidin + b-HB36.5 capture of recombinant HA. This work was done in collaboration with undergraduate student Steven Bennett, who led the folding card design.

7.3.1. Methods

Flu HA Assay with 2DPN Folding Card

Based on the previous 2DPN folding cards demonstrated by Fu *et al.* [68,72], we adapted the flu HA assay using mutant SA + b-HB36.5 capture into a 2DPN folding card format. Test membranes for the

2DPN were cut from nitrocellulose membrane (Millipore HFB135) using a CO₂ laser cutter. Nitrocellulose-binding mutant streptavidin (AbCam #ab51404) was patterned onto the test region of each strip at 1 mg/mL in PBS, and the spotted membranes were stored under desiccation at room temperature overnight before use. All other 2DPN folding card components were fabricated using a CO₂ laser cutter and assembled manually. The folding card was made of Mylar sheets with adhesive layers on one or both sides (Fralock #T-5501-10/1, -10/2, -4/1, or -4/2, Valencia, CA). The sample input pads were made of glass fiber (Ahlstrom #GR8975, Helsinki, Finland), and wicking pads were made of cellulose (Millipore #CFSP223000).

To run the 2DPN devices, the following assay reagents were applied to the sample input pads: (1) 20 μ L mixture with b-HB36.5 at 100 nM, recombinant HA at 100 nM (or negative control), and detection antibody (CA/Ab2, IRR #FR-505) at 100 nM; (2) 10 μ L PBST wash with biotin-BSA at 1 mg/mL; (3) 20 μ L Au-2° label (Au-goat-anti-mouse, Arista Biologicals, Inc.), and (4) 60 μ L PBST wash. The folding card was closed to initiate fluid flow and the start of the assay. Exposed adhesive layers in the folding card allowed the card to stay closed with good contact between the input pads and the test membrane. The devices were tested using test samples with 100 nM recombinant HA (A/California/04/2009 H1N1, Influenza Reagent Resource #FR-180) and no-HA negative controls. After completion of the assay (20 minutes), the folding cards were re-opened, and the devices were scanned at 600 dpi, 48-bit HDR color, $\gamma=1$.

7.3.2. Results and Discussion

Flu HA Assay with 2DPN Folding Card

Images of two influenza HA 2DPN folding card devices are shown in Figure 94, one for a negative control sample (no HA) and one for a test sample (100 nM HA). A zoomed-in image of the test line region is also provided. The assay stack is also illustrated, and the location of each reagent in the 2DPN network is indicated. These results show that we successfully demonstrated the translation of our flu HA assay using stem region binder capture, and the nitrocellulose-specific streptavidin-biotin anchoring strategy developed in chapter 4, to a 2DPN folding card format. These 2DPN devices yielded clear signal for the test samples with recombinant HA and clean negative controls. This demonstration represents the first 2DPN for flu HA detection and a key step in the development of our paper-based influenza diagnostic. While we used wet reagents for this version of the device, future work will focus on optimizing the 2DPN and including dried reagents in order to further automate device operation and reduce user steps. Additionally, the final flu diagnostic

device may not take the form of a folding card, as researchers in our group have since developed other methods for 2DPN automation. Nevertheless, this demonstration represents the first step in evolving the flu HA assay developed herein into a diagnostic device that is simple and easy to use at the point of care.

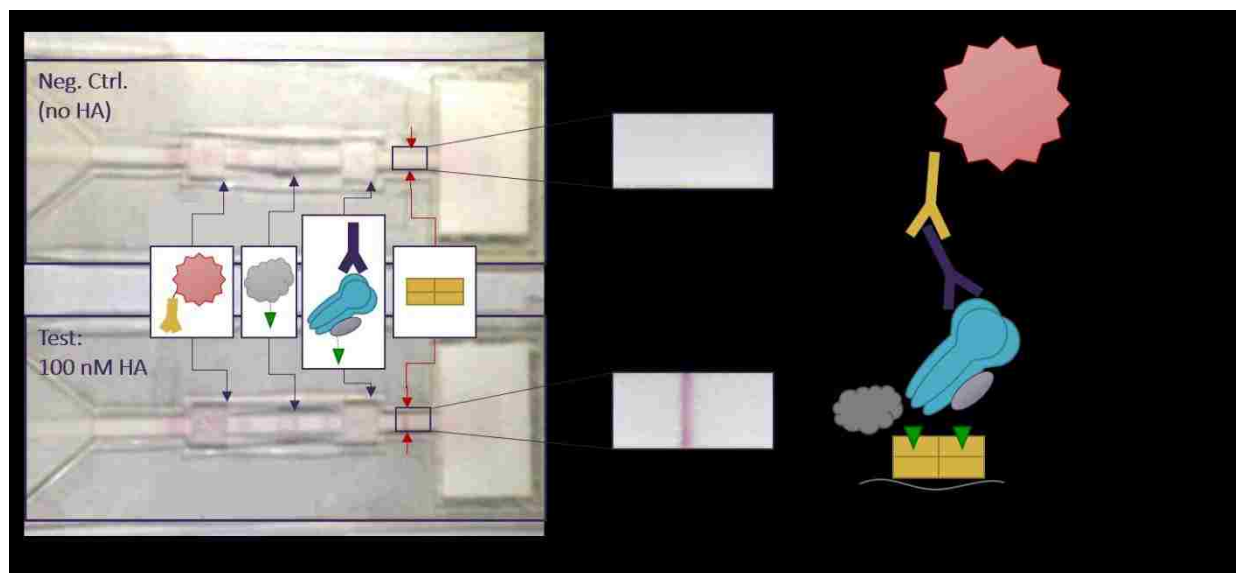


Figure 94. Demonstration of the flu HA assay in a 2DPN folding card.

The flu HA assay with biotin-HB36.5 capture anchored by mutant SA was demonstrated in a 2DPN folding card format. Two representative devices are shown, one a negative control (top) and one a test case with 100 nM HA (bottom). The assay stack is illustrated on the right, and the device components corresponding to the assay stack are illustrated on top of the folding card image. A zoomed-in version of each test line is also provided.

7.4. Demonstration of Improved Paper-Based Flu Assay

In this final section, we focus on demonstrating the improvements made to flu HA detection using the novel methods developed herein, relative to standard methods. To provide a point of comparison for our novel methods, a standard antibody-based lateral flow immunoassay for HA was developed and characterized based on its analytical sensitivity for both recombinant HA and whole influenza virus. In order to put these LODs in context, the clinically relevant range of influenza virus during infection was estimated in terms of cultured virus units and recombinant HA concentration using the method described below. Finally, the LODs of our final head region binder- and stem region binder-based flu HA assay, characterized in section 5.5, are compared to these benchmarks to assess their performance. This work was done in collaboration with PhD student Caitlin Anderson.

7.4.1. Methods

Standard Immunoassay for Flu Hemagglutinin

To determine the efficacy of our novel influenza HA assays, we compared them to a traditional antibody-based lateral flow immunoassay, illustrated in Figure 95. Since commercial lateral flow tests do not exist for HA detection (all commercial influenza rapid diagnostic tests detect the internal nucleoprotein instead [4]), we developed the standard IgG-based lateral flow strips in-house. To do so, an antibody binding pair was determined from the IgG antibodies available from the IRR for HA from A/Solomon Islands/3/2006 influenza. Of the four antibodies available, only three showed binding to HA in our paper-based system (see Figure 80). Of the three remaining choices, two of the antibodies bound to the same epitope of HA, based on competitive binding studies performed and supplied by the IRR. Of these, the strongest performing antibody was selected, which was the SI/Ab3 (IRR #FR-502) antibody that we have been using for detection in our flu binder capture systems. The only remaining antibody available to form the complementary antibody binding pair was SI/Ab4 (IRR #FR-503), which showed the weakest binding to HA in our previous test (Figure 80). However, since these were our only options, so we moved forward with this antibody pair for demonstration of the all-antibody-based assay. This limit of available antibodies highlights a major drawback of traditional immunoassays, underscoring the advantage of using designed, recombinant binders in the first place.

The capture antibody (IRR #FR-503) was patterned onto GE FF80HP nitrocellulose at 0.5 mg/mL in PBS (stock concentration) in the form of test lines, as described above. The detection antibody (IRR #FR-502) was conjugated directly to gold nanoparticles using a commercial conjugation kit (InnovaCoat Gold 40 nm Gold Particle Kit, #230-0005, InnovaBiosciences, Cambridge, United Kingdom). The assay was run through the sequential delivery of the following reagents: 1) 20 μ L HA, virus, or negative control, 2) 20 μ L PBST wash, 3) 20 μ L gold-conjugated detection antibody at OD 2.5, and 4) 20 μ L PBST wash. All reagents were diluted in a running buffer of PBST+BSA.

Recombinant HA was tested at concentrations of 100 nM, 10 nM, 1 nM, 100 pM, and 10 pM, and influenza virus was tested at concentrations of 1.25×10^8 , 1.25×10^7 , 1.25×10^6 , and 1.25×10^5 chicken embryo infectious dose (CEID₅₀/mL), with four replicates per concentration. Buffer-only

(PBST+BSA) negative controls were also tested. Note that the influenza virus concentrations

represent $\frac{1}{2}$, $\frac{1}{20}$, $\frac{1}{200}$, and $\frac{1}{2000}$ dilutions of the stock concentration, 2.5×10^8 CEID₅₀/mL. The $\frac{1}{2}$ dilution was the highest concentration that could be tested while still maintaining at least 50% running buffer in the sample. The three subsequent 10x dilutions of virus, as well as the 10x dilutions of recombinant HA, were chosen to maximize the concentration range tested with the limited amount of Au-labeled detection antibody available for this assay.

Estimation of Clinically Relevant Ranges of Virus and HA

The clinically relevant range of influenza virus during infection is reported in *Fields Virology* to be 10^3 to 10^7 tissue culture infectious dose (TCID₅₀)/mL [85]. However, our assays were performed with recombinant HA [mol/L=M], or with virus whose stock concentration was reported in chicken embryo infectious dose (CEID₅₀)/mL, yielding a mismatch in units. In order to estimate the clinically relevant levels of influenza virus and HA in terms of the units of the reagents tested, we built correlation curves from data available from the literature. Specifically, we used data from Chan *et al.* in which virus samples were quantified both in terms of culture, to yield TCID₅₀/mL, and qRT-PCR, to yield copies of M gene/mL [201]. Since there is one copy of the M gene per virion, and approximately 500 copies of HA per virion [86,88], we were able to construct a linear correlation between TCID₅₀/mL and HA concentration, as shown in Figure 96A. We then used data published by the Centers for Disease Control and Prevention (CDC), in which virus samples were reported in both concentration of virus [EID₅₀/mL] and nucleoprotein [μ g/mL] [103]. It should be noted that this data showed remarkably higher variability than the Chan *et al.* data, but nevertheless was the

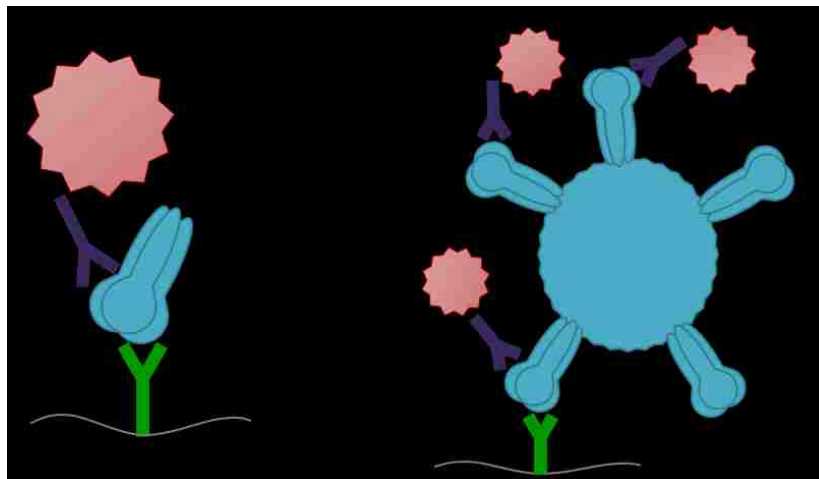


Figure 95. Traditional immunoassay for HA.

Illustrations of the standard antibody-based immunoassay used for comparison to our novel systems. (A) Antibody capture, Au-labeled antibody detection, with recombinant HA. (B) The same assay with whole virus.

best data we had available to draw an approximate correlation. This variability underscores the approximate nature of this estimation, given the high variability among biological and viral samples. Then, based on approximately 1000 nucleoproteins per virion [86,88], we were able to correlate EID₅₀/mL to number of virions, and thus EID₅₀/mL to concentration of HA. We further assumed that EID₅₀/mL is equivalent to CEID₅₀/mL, since the embryos were presumed to be from chicken, leading to the calibration curve shown in Figure 96B. Based on these correlations, we estimated the clinically relevant ranges of HA [M] and virus [CEID₅₀/mL] shown in Table 14.

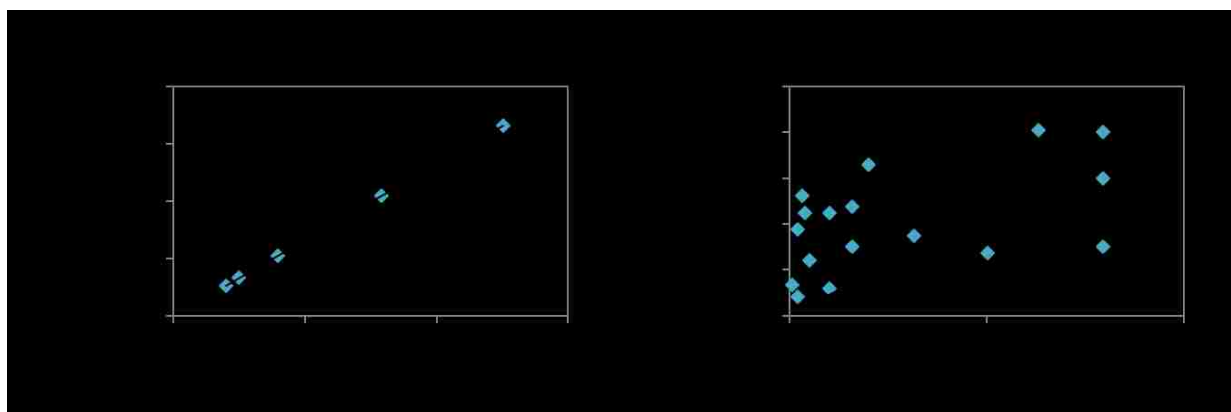


Figure 96. Correlations between different units of virus concentration.

(A) Correlation of HA concentration [M] and virus concentration [TCID₅₀/mL], based on data from Chan *et al.* [201].
 (B) Correlation of HA concentration [M] and virus concentration [CEID₅₀/mL], based on data from the CDC [103].

7.4.2. Results and Discussion

Characterization of Standard Lateral Flow Immunoassay

The standard lateral flow immunoassay for HA, using IgG capture by direct adsorption and Au-conjugated IgG detection, was evaluated for analytical sensitivity using the assay methodology described above. The results for recombinant HA detection are provided in Figure 97A, and the results for whole virus detection are given in Figure 97B. In each case, representative images of test lines at each concentration are provided, in addition to the full assay response curve. The antibody-based assay exhibited a statistical LOD of 7.6 nM for recombinant HA (95% confidence interval: [3.8 nM, 14.8 nM]), which was significantly higher (less sensitive) than both the stem region binder and head region binder assays characterized in in section 5.5 ($p < 0.05$ by Welch's *t*-test). For whole virus, the signals were very low for the concentration range tested, which led to an LOD estimation of 1.39×10^8 CEID₅₀/mL. Since this value is slightly greater than the highest concentration tested (1.25×10^8 CEID₅₀/mL), the calibration curve is ill-formed in this range; therefore, we can only say that the LOD for this Ab assay with whole virus is greater than 1.25×10^8 CEID₅₀/mL. Additionally,

the standard error of the LOD estimate was extremely high, owing to the noisy and low signal in this regime, resulting in a unproductive 95% CI of [-2, infinity]. This large confidence interval reiterates the lack of real signal in this concentration range (which was limited by the stock concentration of the virus) from which to generate an effective LOD estimate. In any case, the results clearly indicate that the antibody assay is less sensitive than the novel assays developed with flu binder capture, especially with recombinant head region binder, which produced true signal and a reliable LOD estimate for this concentration range of virus. These results are compared in detail to our novel assay systems and to the estimated clinically relevant ranges of virus and HA in Table 14.

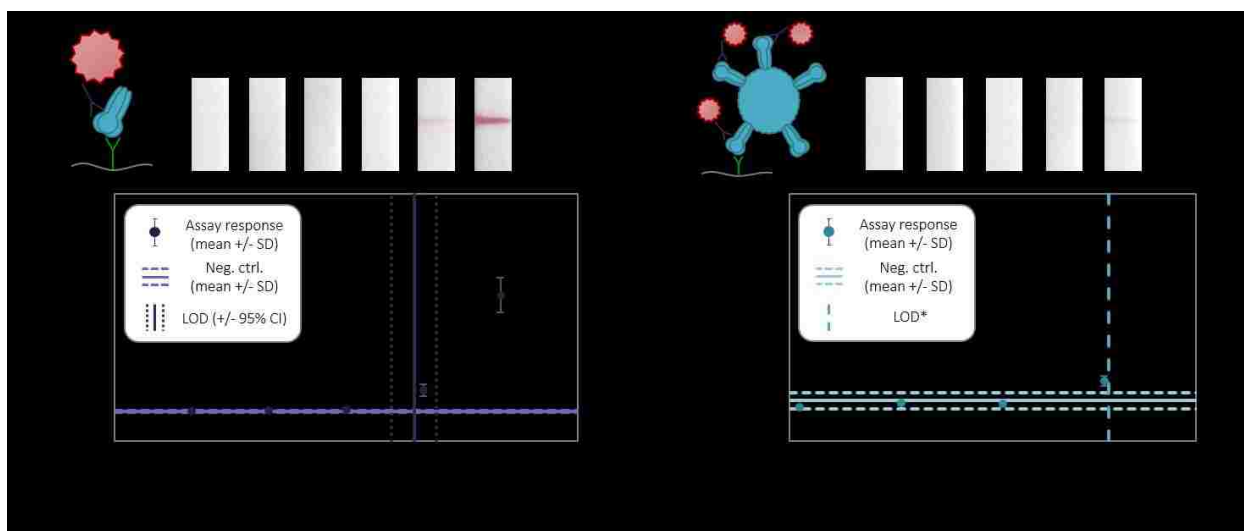


Figure 97. Analytical sensitivity of traditional immunoassay. Representative test lines and the full assay response curves are provided. Each condition was tested with n=4 replicates. (A) Assay run with recombinant HA. (B) Assay run with whole virus.

Comparison of Novel Assays Developed Herein to Standard Immunoassay

To evaluate the performance of our final flu binder-based assays, the assay results are summarized in Table 14 and compared to both the results of the traditional antibody-based assay and the estimated clinically relevant ranges of virus and HA. It is important to reiterate that these clinically relevant ranges are only rough estimations, since the exact correlations between these units of virus will differ for each sample preparation. However, these estimations help guide the interpretation of the assay results. Importantly, these results indicate that the assay with Trimer 11 head region binder capture has an LOD that is within the clinically relevant range for both the estimated HA and virus concentrations, albeit towards the high end. The traditional antibody assay, however, falls outside of the clinically relevant range for recombinant HA, and at the very high end of the range for virus (but with a large error in that estimation that could make its true LOD much

higher than the clinically relevant range). Therefore, the traditional antibody assay is unlikely to be usable clinically, while the head region binder assay shows promise for clinical utility. Additionally, the assay with biotinylated stem region binder b-HB36.5 capture anchored by mutant SA yields the best sensitivity at 14 pM for recombinant HA, which is in the low-to-mid end of the clinically relevant range. Therefore, as previously discussed, this assay also shows promise, if HA can be isolated from clinical samples.

Based on these results, both recombinant flu binder-based systems yield superior analytical sensitivity to the traditional lateral flow immunoassay using monoclonal antibodies for capture and detection. We have therefore demonstrated that the use of computationally designed, recombinant affinity proteins not only offer greater design control at a lower cost than antibodies, but that they can be used to improve the performance of paper-based assays.

Table 14. Summary of flu HA assay performance.

The LOD with 95% CI for each assay is listed and compared to the clinically relevant range of influenza. The clinically relevant range of virus in TCID₅₀/mL is known from the literature [85]. *The ranges in terms of HA [M] and virus [CEID₅₀/mL] are estimated as described in section 7.4.1.

	Clinically Relevant Range		
	Low	Mid	High
Virus [TCID ₅₀ /mL]	1 x 10 ³	1 x 10 ⁵	1 x 10 ⁷
Virus [CEID ₅₀ /mL]*	1.5 x 10 ⁴	1.5 x 10 ⁶	1.5 x 10 ⁸
HA [M]*	300 fM	30 pM	3 nM
	Flu HA Assay LODs		
	Lower 95% CI	LOD	Upper 95% CI
Mut. SA + b-HB36.5 capture, HA	8 pM	14 pM	25 pM
Trimer 11 capture, HA	358 pM	451 pM	569 pM
Trimer 11 capture, virus	1.88 x 10 ⁷ CEID ₅₀ /mL	3.54 x 10 ⁷ CEID ₅₀ /mL	6.66 x 10 ⁷ CEID ₅₀ /mL
Antibody capture, HA	3.8 nM	7.6 nM	14.8 nM
Antibody capture, virus	n/a	> 1.25 x 10 ⁸ CEID ₅₀ /mL	n/a

7.5. Conclusions

In this chapter, we have demonstrated the strides made through this thesis work toward improved flu testing. While we have not yet developed a fully integrated device for use at the point of care, we have demonstrated that the flu HA assay developed herein can be translated to a 2DPN, as first step toward this device development. Through the user assessment sessions, we also verified that the 2DPN format is reasonable for point-of-care use, at least in a clinical setting. Most importantly, we

showed that our two best flu assays developed in the previous chapters, the Trimer 11 head region binder assay and the biotinylated stem region binder assay with mutant SA anchoring, outperform a standard antibody-based lateral flow immunoassay. While we could not compare directly to commercial influenza RDTs, which detect the internal nucleoprotein, these commercial tests are reported to have LODs in the range of 10^5 to 10^7 TCID₅₀/mL [103], which is at the high end of the clinically relevant range. Therefore, our current flu HA assays appear to show similar, if not better, sensitivity than these commercial tests. This achievement has come without the use of additional assay schemes afforded by the 2DPN platform, such as the use of sample pre-processing or signal enhancement [48,68,71,72,75,80]. Therefore, as these flu HA assays are further optimized and translated into 2DPN devices, we expect the sensitivity to reach the lower end of the clinically relevant range of virus.

8. Conclusions and Future Work

8.1. Overall Summary and Conclusions

The work in this thesis was motivated by the need for improved flu testing at the point of care, in order to manage flu and flu-like illnesses more efficiently to save time, reduce healthcare costs, and ultimately improve patient outcomes. We worked toward this goal by developing understanding of, tools for, and assays using specifically designed membrane-protein and protein-protein interactions, as summarized below.

In chapter 3, we studied protein adsorption to nitrocellulose in detail. We evaluated and learned from the adsorption profiles of many commonly used proteins, such as IgG, BSA, and streptavidin. Importantly, we learned that not all proteins adsorb to nitrocellulose robustly, motivating the need for immobilization strategies other than direct adsorption. To this end we applied our adsorption knowledge to identify nitrocellulose anchor protein candidates.

In chapter 4, we developed novel strategies to immobilize recombinant affinity proteins to nitrocellulose membranes, including the use of the anchor proteins described above. This work was demonstrated using the recombinant stem region flu binder, but these strategies are valid for any type of recombinant affinity protein or otherwise chemically modifiable capture molecule. We ultimately demonstrated that the combination of the recombinant stem region flu binder with the nitrocellulose-specific streptavidin-biotin immobilization strategy can be used to achieve improved performance in a flu HA assay relative to a standard assay based on IgG capture immobilized by direct adsorption.

In chapter 5, we put our protein adsorption knowledge and immobilization strategies to use for the development of a fully functional flu HA assay for influenza virus detection. In this work, we developed various assay stacks using both the stem and head region flu binders. Using the recombinant head region flu binder, we demonstrated the detection of whole influenza virus. To our knowledge, this represents the first report of whole influenza virus detection on paper. We also demonstrated a highly sensitive assay for recombinant HA using the stem region binder, which shows promise if HA can be isolated from virus through sample preparation.

In chapter 6, we developed a novel method for the robust statistical analysis of the analytical sensitivity of bioassays. Developed in collaboration with the Department of Statistics, this method

allows for the determination of a statistically robust estimate of the limit of detection of an assay, complete with 95% confidence interval. It also provides a means for comparing the LODs of two different assays statistically to determine when a significant improvement in the sensitivity has been achieved.

Finally, in chapter 7, we used this statistical LOD analysis method to demonstrate the significant improvements made in influenza HA and virus detection using our novel flu binder-based assays, relative to a traditional antibody-based lateral flow immunoassay. We also showed that our assays detect HA and virus at clinically relevant levels, albeit with further room for improvement in order to detect the very lowest levels of virus. We also described the work that has been done to begin to translate the influenza HA assay developed herein to a ZDPN device.

While we have not explicitly demonstrated influenza subtyping, this work represents the first paper-based assay for the detection of influenza hemagglutinin, which is the first, crucial step towards subtyping. Once the right discriminatory set of flu binders are developed by the Baker lab to differentiate H1 from H3 hemagglutinin, those reagents can be swapped into the assay developed here with minimal effort. In this manner, the use of the recombinant flu binders has not only resulted in improved sensitivity, but it has also offered the possibility for additional diagnostic information that is not possible when the internal nucleoprotein is targeted, as is the case for currently available commercial influenza RDTs [4]. Given that the HA subtype (H1 vs. H3) distinguishes the two currently circulating subtypes of influenza A virus (H1N1 and H3N2) [202], being able to determine the HA subtype with a simple point-of-care test would provide valuable information for epidemiological surveillance and the clinical management of disease treatment and prognosis. However, given that the highly conserved sialic acid binding site of the HA head region is surrounded by regions with high mutation rates [85,141], future challenges may include maintaining head region binding for evolving strains of HA.

In addition to achieving a more sensitive and information-rich flu assay, the use of the recombinant affinity proteins also opens the door for companion diagnostics-therapeutics, since these flu binders have shown the potential for therapeutic use ([144] for stem region binder; head region binder activity in preparation for publication). In such a companion system, the flu binder-based diagnostic test would not only diagnose the flu, but it would also indicate which flu binder should be given for treatment, based on which binder is able to recognize the specific strain at hand most sensitively.

Overall, this work represents an important demonstration of the power of recombinant affinity proteins for diagnostics, as well as a significant step toward the development of a high-sensitivity, low-cost flu test for improved diagnosis and disease management at the point of care. This work also includes several novel achievements: (1) the first demonstration of computationally designed, recombinant affinity proteins for paper-based diagnostics, (2) the first lateral flow test based on the influenza HA protein, and (3) the first paper-based assay for whole influenza virus detection. In addition to these practical accomplishments, we also developed a wealth of general knowledge about protein immobilization to nitrocellulose and recombinant affinity protein-based assays that can be utilized for the development of future paper-based assays for other disease targets.

8.2. List of Contributions from Work

The work in this thesis has resulted in the following contributions to the literature and scientific community. †Denotes equal contribution.

Publications

- Fridley GE†, **Holstein CA**†, Oza SB†, Yager P, “The evolution of nitrocellulose as a material for bioassays,” *MRS Bulletin* 38 (4): 326-330 (Apr 2013)
- **Holstein CA**, Chevalier A, Bennett S, Anderson CE, Keniston K, Olsen C, Li B, Bales B, Moore D, Fu E, Baker D, Yager P, “Immobilizing Affinity Proteins to Nitrocellulose: A Toolbox for Paper-Based Assay Developers,” *Analytical and Bioanalytical Chemistry*, in preparation (submission June 2015)
- **Holstein CA**†, Fridley GE†, Adcock CA, Yager P, “Methods and Models to Examine Protein Adsorption to Nitrocellulose,” *Journal of Membrane Science*, in preparation (submission June 2015)
- **Holstein CA**, Griffin M, Hong J, Sampson P, Yager P, “A Statistical Method for Determining and Comparing Limits of Detection of Bioassays,” *Analytical Chemistry*, in preparation (submission June 2015)
- **Holstein CA**, Strauch E-M, Anderson CE, Bennett S, Chevalier A, Nelson J, Fu E, Baker D, Yager P, “Development of a Paper-Based Assay for Whole Influenza Virus Detection using a Computationally Designed Hemagglutinin Head Region Binder,” in preparation (submission July 2015)

Book Chapter

- Buser JR†, **Holstein CA**†, and Yager P, “Microfluidic Diagnostics for Low-Resource Settings: Improving Global Health without a Power Cord,” in *Microfluidics for Medical Applications*, 1st ed. Berg A and Segerink L, Eds. Royal Society of Chemistry, 2014, ch. 8.

Oral Presentations

- **Holstein CA**, Bennett S, Chevalier A, Baker D, Fu E, Yager P, “Paper-Based Assay for Influenza Hemagglutinin Using Computationally Designed Affinity Protein,” Biomedical Engineering Society Annual Meeting, September 2013, Seattle, WA
- **Holstein CA**, Bennett S, Strauch EM, Chevalier A, Fu E, Baker D, and Yager P, “Development of a Paper-Based Diagnostic for Influenza Detection,” IEEE EMBS Special Topic Conference: Healthcare Innovation & Point-of-Care Technologies, October 2014, Seattle, WA
- **Holstein CA**, Bennett S, Strauch EM, Chevalier A, Fu E, Baker D, and Yager P, “Paper-Based Diagnostic for Influenza A Detection,” Biomedical Engineering Society Annual Meeting, October 2014, San Antonio, TX

Poster Presentations

- Osborn JL, Marshall EA, **Holstein C**, Ball C, Lutz B, Fu E, Yager P, “A Self-Referencing Paper T-Sensor for Diffusion-Based Analyte Detection,” Fifteenth International Conference on Miniaturized Systems for Chemistry and Life Sciences (MicroTAS), October 2011, Seattle, WA
- **Holstein CA**, Keniston K, Yager P, “Paper-Microfluidic pH Gradients for Protein Analysis,” Biomedical Engineering Society Annual Meeting, October 2012, Atlanta, GA
- **Holstein CA**‡, Fridley G‡, Fu E, Yager P, “Understanding Protein Adsorption to Nitrocellulose,” Gordon Research Conference, Physics and Chemistry of Microfluidics, June 2013, Barga, Italy

8.3. Future Work

While we have made significant strides toward improved POC flu testing, several lines of work remain to further improve the performance of the flu HA assays developed herein and translate them into fully functioning diagnostic devices.

First, given that our limits of detection are still in the low-to-mid area of the estimated clinically relevant range of virus concentrations, we need to further improve the sensitivity of the flu HA assay. Some of this improvement is expected to come from the addition of more sophisticated assay schemes afforded by the 2DPN platform, such as the use of signal enhancement. In addition, it would be ideal to eliminate the need for antibody detection and move to an all-flu-binder-based assay. We have demonstrated a few all-flu-binder stacks through this work, but none are able to detect virus with high sensitivity. A promising candidate is the use of a newly developed version of the head region binder, Trimer 11.2, for detection. Specifically, Dr. Eva-Maria Strauch has created a version of T11.2 that is conjugated to horseradish peroxidase (HRP) for enzymatic-based signal

generation. Graduate student Caitlin Anderson has shown with preliminary testing that this T11.2-HRP reagent may provide both an option for an all-flu-binder assay and the more sensitive detection of virus than with the gold nanoparticle-based signal generation used herein.

Additionally, given the superior sensitivity of the assay with stem region binder capture, and the vast array of assay schemes afforded by the combination of stem and head region binders, it may be worthwhile to continue working toward the detection of isolated HA, rather than whole virus. While detecting whole virus is straightforward from a sample preparation perspective, our automated 2DPN platforms offer the ability to perform some on-board sample preparation and therefore the possibility for isolated HA detection. Moreover, lysis conditions are necessary to detect HA isolated from the host cell membrane, which may help generate the best possible sensitivity of HA detection. Practically, lysis would also be ideal in order to integrate the HA assay with the NP assay in the simplest manner possible. This work depends on determining a strategy for HA isolation, however, which may prove to be challenging. If isolated HA detection can be demonstrated, then a related line of future work would be to develop a lower-cost mimic to the mutant SA + biotin-HB36.5 system, using the protein engineering expertise of the Baker lab.

Finally, integration of this influenza HA assay with the influenza NP assay and characterization with patient samples remains the ultimate goal of this project. For this to be successful, a new version of the head region binder will need to be developed that binds to the currently circulating strain of H1N1 influenza (still essentially the A/California/04/2009 (H1N1) strain). Since the current Trimer 11 head region binder does not recognize this contemporary strain (all assay development was done with the A/Solomon Islands/03/2006 (H1N1) influenza strain, which is no longer circulating), we were unable to test our assay with any of the real patient nasal swab samples, which have been collected by collaborator Dr. Janet Englund at Seattle Children's Hospital. When this head region binder is developed, it can be swapped into the flu HA assay, which can then be characterized for clinical sensitivity and specificity using the patient samples. These clinical sensitivity and specificity results will provide the ultimate metrics of the clinical utility of our next-generation influenza diagnostic.

References

1. Hurt AC, Alexander R, Hibbert J, Deed N, Barr IG. Performance of six influenza rapid tests in detecting human influenza in clinical specimens. *J Clin Virol.* 2007;39: 132–135. doi:10.1016/j.jcv.2007.03.002
2. Centers for Disease Control and Prevention. Seasonal Influenza (Flu) - Q & A: Seasonal Influenza (Flu): The Disease [Internet]. 6 Jul 2011 [cited 31 Mar 2013]. Available: <http://www.cdc.gov/flu/about/qa/disease.htm>
3. Molinari N-AM, Ortega-Sanchez IR, Messonnier ML, Thompson WW, Wortley PM, Weintraub E, et al. The annual impact of seasonal influenza in the US: Measuring disease burden and costs. *Vaccine.* 2007;25: 5086–5096. doi:10.1016/j.vaccine.2007.03.046
4. CDC - Seasonal Influenza (Flu) - Guidance for Clinicians on the Use of Rapid Influenza Diagnostic Tests [Internet]. 13 Nov 2012 [cited 18 Apr 2013]. Available: http://www.cdc.gov/flu/professionals/diagnosis/clinician_guidance_ridt.htm
5. Yager P, Domingo GJ, Gerdes J. Point-of-Care Diagnostics for Global Health. *Annu Rev Biomed Eng.* 2008;10: 107–144. doi:10.1146/annurev.bioeng.10.061807.160524
6. Buser JR, Holstein CA, Yager P. Microfluidic Diagnostics for Low-resource Settings: Improving Global Health without a Power Cord. In: Berg A, Segerink L, editors. *Microfluidics for Medical Applications*. Cambridge: Royal Society of Chemistry; 2014. pp. 151–190. Available: <http://ebook.rsc.org/?DOI=10.1039/9781849737593-00151>
7. Squires DA. Explaining High Health Care Spending in the United States: An International Comparison of Supply, Utilization, Prices, and Quality. *Commonw Fund.* 2012;10. Available: <http://www.commonwealthfund.org/Publications/Issue-Briefs/2012/May/High-Health-Care-Spending.aspx>
8. Yager P, Edwards T, Fu E, Helton K, Nelson K, Tam MR, et al. Microfluidic diagnostic technologies for global public health. *Nature.* 2006;442: 412–418. doi:10.1038/nature05064
9. Pai NP, Vadnais C, Denkinger C, Engel N, Pai M. Point-of-Care Testing for Infectious Diseases: Diversity, Complexity, and Barriers in Low- And Middle-Income Countries. *PLoS Med.* 2012;9: e1001306. doi:10.1371/journal.pmed.1001306
10. World Health Organization. World Health Statistics [Internet]. 2011. Available: http://www.who.int/gho/publications/world_health_statistics/2011/en/index.html
11. Davis K, Stremikis K, Squires D, Schoen C. Mirror, Mirror on the Wall, 2014 Update: How the U.S. Health Care System Compares Internationally [Internet]. The Commonwealth Fund; 2014 Jun. Available: <http://www.commonwealthfund.org/publications/fund-reports/2014/jun/mirror-mirror>
12. Berwick DM, Hackbarth AD. Eliminating Waste in US Health Care. *JAMA.* 2012;307: 1513. doi:10.1001/jama.2012.362

13. Gubala V, Harris LF, Ricco AJ, Tan MX, Williams DE. Point of Care Diagnostics: Status and Future. *Anal Chem.* 2012;84: 487–515. doi:10.1021/ac2030199
14. McNERNEY R, DALEY P. Towards a point-of-care test for active tuberculosis: obstacles and opportunities. *Nat Rev Microbiol.* 2011;9: 204–213. doi:10.1038/nrmicro2521
15. Chin CD, Linder V, Sia SK. Lab-on-a-chip devices for global health: Past studies and future opportunities. *Lab Chip.* 2007;7: 41. doi:10.1039/b611455e
16. Institute of Medicine (U.S.). Best care at lower cost: the path to continuously learning health care in America [Internet]. Washington, D.C: National Academies Press; 2012. Available: <http://www.iom.edu/reports/2012/best-care-at-lower-cost-the-path-to-continuously-learning-health-care-in-america.aspx>
17. Choi S, Goryll M, Sin LYM, Wong PK, Chae J. Microfluidic-based biosensors toward point-of-care detection of nucleic acids and proteins. *Microfluid Nanofluidics.* 2010;10: 231–247. doi:10.1007/s10404-010-0638-8
18. Boehme CC, Nicol MP, Nabeta P, Michael JS, Gotuzzo E, Tahirli R, et al. Feasibility, diagnostic accuracy, and effectiveness of decentralised use of the Xpert MTB/RIF test for diagnosis of tuberculosis and multidrug resistance: a multicentre implementation study. *The Lancet.* 2011;377: 1495–1505. doi:10.1016/S0140-6736(11)60438-8
19. Cepheid. Cepheid | Xpert MTB/RIF [Internet]. 2011 [cited 2 May 2013]. Available: <http://www.cepheidinternational.com/tests-and-reagents/ce-ivd-test/xpert-mtbrif>
20. Vassall A, van Kampen S, Sohn H, Michael JS, John KR, den Boon S, et al. Rapid Diagnosis of Tuberculosis with the Xpert MTB/RIF Assay in High Burden Countries: A Cost-Effectiveness Analysis. Wilson D, editor. *PLoS Med.* 2011;8: e1001120. doi:10.1371/journal.pmed.1001120
21. Foundation for Innovative Diagnostics. FIND - Negotiated prices for Xpert® MTB/RIF and FIND country list [Internet]. Aug 2012 [cited 17 May 2013]. Available: http://www.finddiagnostics.org/about/what_we_do/successes/find-negotiated-prices/xpert_mtb_rif.html
22. Lauks IR. Microfabricated Biosensors and Microanalytical Systems for Blood Analysis. *Acc Chem Res.* 1998;31: 317–324. doi:10.1021/ar9700670
23. Grand Challenges in Global Health. A Point-of-Care Diagnostic System for the Developing World [Internet]. 2005 [cited 19 Apr 2013]. Available: <http://www.grandchallenges.org/MeasureHealthStatus/Challenges/DiagnosticTools/Pages/PointofCare.aspx>
24. Lafleur L, Stevens D, McKenzie K, Ramachandran S, Spicar-Mihalic P, Singhal M, et al. Progress toward multiplexed sample-to-result detection in low resource settings using microfluidic immunoassay cards. *Lab Chip.* 2012; doi:10.1039/c2lc20751f
25. Stevens DY, Petri CR, Osborn JL, Spicar-Mihalic P, McKenzie KG, Yager P. Enabling a microfluidic immunoassay for the developing world by integration of on-card dry reagent storage. *Lab Chip.* 2008;8: 2038–2045. doi:10.1039/b811158h

26. Micronics. PanNAT Molecular Diagnostic System [Internet]. 2013 [cited 19 Apr 2013]. Available: <http://www.micronics.net/products/diagnostic-products/PanNAT>
27. Chin CD, Laksanasopin T, Cheung YK, Steinmiller D, Linder V, Parsa H, et al. Microfluidics-based diagnostics of infectious diseases in the developing world. *Nat Med*. 2011;17: 1015–1019. doi:10.1038/nm.2408
28. Chin CD, Cheung YK, Laksanasopin T, Modena MM, Chin SY, Sridhara AA, et al. Mobile Device for Disease Diagnosis and Data Tracking in Resource-Limited Settings. *Clin Chem*. 2013;59: 629–640. doi:10.1373/clinchem.2012.199596
29. Laksanasopin T, Guo TW, Nayak S, Sridhara AA, Xie S, Olowookere OO, et al. A smartphone dongle for diagnosis of infectious diseases at the point of care. *Sci Transl Med*. 2015;7: 273re1–273re1. doi:10.1126/scitranslmed.aaa0056
30. Rosen S. Market Trends in Lateral Flow Immunoassays. In: Wong RC, Tse HY, editors. *Lateral Flow Immunoassay*. New York, NY: Humana Press; 2009. pp. 35–49.
31. Fridley GE, Holstein CA, Oza SB, Yager P. The evolution of nitrocellulose as a material for bioassays. *MRS Bull*. 2013;38: 326–330. doi:10.1557/mrs.2013.60
32. Chard T. Pregnancy tests: a review. *Hum Reprod Oxf Engl*. 1992;7: 701–710.
33. O'Farrell B. Evolution of Lateral Flow-Based Immunoassay Systems. In: Wong RC, Tse HY, editors. *Lateral Flow Immunoassay*. New York, NY: Humana Press; 2009. pp. 1–33.
34. Bonner AB, Monroe KW, Talley LI, Klasner AE, Kimberlin DW. Impact of the rapid diagnosis of influenza on physician decision-making and patient management in the pediatric emergency department: results of a randomized, prospective, controlled trial. *Pediatrics*. 2003;112: 363–367.
35. Posthuma-Trumpie GA, Korf J, van Amerongen A. Lateral flow (immuno)assay: its strengths, weaknesses, opportunities and threats. A literature survey. *Anal Bioanal Chem*. 2009;393: 569–582. doi:10.1007/s00216-008-2287-2
36. U.S. Food and Drug Administration. First Rapid Home-Use HIV Kit Approved for Self-Testing [Internet]. 2014 Sep. Available: <http://www.fda.gov/ForConsumers/ConsumerUpdates/ucm310545.htm>
37. Yetisen AK, Akram MS, Lowe CR. Paper-based microfluidic point-of-care diagnostic devices. *Lab Chip*. 2013;13: 2210. doi:10.1039/c3lc50169h
38. Byrnes S, Thiessen G, Fu E. Progress in the development of paper-based diagnostics for low-resource point-of-care settings. *Bioanalysis*. 2013;5: 2821–2836. doi:10.4155/bio.13.243
39. Rolland JP, Mourey DA. Paper as a novel material platform for devices. *MRS Bull*. 2013;38: 299–305. doi:10.1557/mrs.2013.58
40. Li X, Ballerini DR, Shen W. A perspective on paper-based microfluidics: Current status and future trends. *Biomicrofluidics*. 2012;6: 011301. doi:10.1063/1.3687398

41. Osborn JL. Novel Paper Networks for Point-of-Care Sample Preparation and Indirect IgM Detection. University of Washington. 2011.
42. Martinez AW, Phillips ST, Whitesides GM, Carrilho E. Diagnostics for the developing world: microfluidic paper-based analytical devices. *Anal Chem*. 2010;82: 3–10. doi:10.1021/ac9013989
43. Washburn EW. The Dynamics of Capillary Flow. *Phys Rev*. 1921;17: 273–283. doi:10.1103/PhysRev.17.273
44. USGS Water-Science School. Capillary action [Internet]. 10 Jan 2013 [cited 8 May 2013]. Available: <http://ga.water.usgs.gov/edu/capillaryaction.html>
45. Peiris A, Stein B. Capillary Action - UC Davis ChemWiki [Internet]. 2010 [cited 8 May 2013]. Available: http://chemwiki.ucdavis.edu/Physical_Chemistry/Physical_Properties_of_Matter/Intermolecular_Forces/Cohesive_And_Adhesive_Forces/Capillary_Action
46. Bell JM, Cameron FK. The Flow of Liquids Through Capillary Spaces. *J Phys Chem*. 1906;10: 658–674. doi:10.1021/j150080a005
47. Mendez S, Fenton EM, Gallegos GR, Petsev DN, Sibbett SS, Stone HA, et al. Imbibition in Porous Membranes of Complex Shape: Quasi-stationary Flow in Thin Rectangular Segments. *Langmuir*. 2010;26: 1380–1385. doi:10.1021/la902470b
48. Fu E, Ramsey SA, Kauffman P, Lutz B, Yager P. Transport in two-dimensional paper networks. *Microfluid Nanofluidics*. 2010;10: 29–35. doi:10.1007/s10404-010-0643-y
49. Lutz BR, Trinh P, Ball C, Fu E, Yager P. Two-dimensional paper networks: programmable fluidic disconnects for multi-step processes in shaped paper. *Lab Chip*. 2011;11: 4274. doi:10.1039/c1lc20758j
50. Darcy H. *Les Fontaines Publiques de la Ville de Dijon*. Paris: Dalmont; 1856.
51. Brown GO. Henry Darcy and the making of a law. *Water Resour Res*. 2002;38: 11–1–11–12. doi:10.1029/2001WR000727
52. Dullien FAL. *Porous Media: Fluid Transport and Pore Structure*. New York, NY: Academic Press, Inc.; 1979.
53. Millipore. *Rapid Lateral Flow Test Strips: Considerations for Product Development*. Millipore Corporation; 2008.
54. Bird RB, Stewart WE, Lightfoot EN. *Transport Phenomena*. 2nd ed. John Wiley & Sons; 2002.
55. Purcell EM. Life at low Reynolds number. *Am J Phys*. 1977;45: 3. doi:10.1119/1.10903
56. Osborn JL, Lutz B, Fu E, Kauffman P, Stevens DY, Yager P. Microfluidics without pumps: reinventing the T-sensor and H-filter in paper networks. *Lab Chip*. 2010;10: 2659. doi:10.1039/c004821f

57. Martinez AW, Phillips ST, Butte MJ, Whitesides GM. Patterned Paper as a Platform for Inexpensive, Low-Volume, Portable Bioassays. *Angew Chem Int Ed.* 2007;46: 1318–1320. doi:10.1002/anie.200603817
58. Martinez AW, Phillips ST, Whitesides GM. Three-dimensional microfluidic devices fabricated in layered paper and tape. *Proc Natl Acad Sci.* 2008;105: 19606–19611. doi:10.1073/pnas.0810903105
59. Carrilho E, Martinez AW, Whitesides GM. Understanding Wax Printing: A Simple Micropatterning Process for Paper-Based Microfluidics. *Anal Chem.* 2009;81: 7091–7095. doi:10.1021/ac901071p
60. Martinez AW, Phillips ST, Nie Z, Cheng C-M, Carrilho E, Wiley BJ, et al. Programmable diagnostic devices made from paper and tape. *Lab Chip.* 2010;10: 2499–2504. doi:10.1021/ac901071p
61. Schilling KM, Jauregui D, Martinez AW. Paper and toner three-dimensional fluidic devices: programming fluid flow to improve point-of-care diagnostics. *Lab Chip.* 2013;13: 628. doi:10.1039/c2lc40984d
62. Thom NK, Yeung K, Pillion MB, Phillips ST. “Fluidic batteries” as low-cost sources of power in paper-based microfluidic devices. *Lab Chip.* 2012; doi:10.1039/c2lc40126f
63. Mentele MM, Cunningham J, Koehler K, Volckens J, Henry CS. Microfluidic Paper-Based Analytical Device for Particulate Metals. *Anal Chem.* 2012; 120426083304003. doi:10.1021/ac300309c
64. Pollock NR, Rolland JP, Kumar S, Beattie PD, Jain S, Noubary F, et al. A Paper-Based Multiplexed Transaminase Test for Low-Cost, Point-of-Care Liver Function Testing. *Sci Transl Med.* 2012;4: 152ra129–152ra129. doi:10.1126/scitranslmed.3003981
65. Diagnostics For All. Projects - Liver Function [Internet]. 2013 [cited 22 Apr 2015]. Available: <http://www.dfa.org/projects/liver-function.php>
66. Phillips ST, Lewis GG. Advances in materials that enable quantitative point-of-care assays. *MRS Bull.* 2013;38: 315–319. doi:10.1557/mrs.2013.57
67. Maxwell EJ, Mazzeo AD, Whitesides GM. Paper-based electroanalytical devices for accessible diagnostic testing. *MRS Bull.* 2013;38: 309–314. doi:10.1557/mrs.2013.56
68. Fu E, Liang T, Spicar-Mihalic P, Houghtaling J, Ramachandran S, Yager P. Two-Dimensional Paper Network Format That Enables Simple Multistep Assays for Use in Low-Resource Settings in the Context of Malaria Antigen Detection. *Anal Chem.* 2012;84: 4574–4579. doi:10.1021/ac300689s
69. Spicar-Mihalic P, Toley B, Houghtaling J, Liang T, Yager P, Fu E. CO₂ laser cutting and ablative etching for the fabrication of paper-based devices. *J Micromechanics Microengineering.* 2013;23: 067003. doi:10.1088/0960-1317/23/6/067003
70. Fu E, Lutz B, Kauffman P, Yager P. Controlled reagent transport in disposable 2D paper networks. *Lab Chip.* 2010;10: 918–920. doi:10.1039/b919614e

71. Fu E, Kauffman P, Lutz B, Yager P. Chemical signal amplification in two-dimensional paper networks. *Sens Actuators B Chem.* 2010;149: 325–328. doi:10.1016/j.snb.2010.06.024
72. Fu E, Liang T, Houghtaling J, Ramachandran S, Ramsey SA, Lutz B, et al. Enhanced sensitivity of lateral flow tests using a two-dimensional paper network format. *Anal Chem.* 2011;83: 7941–7946. doi:10.1021/ac201950g
73. Kauffman P, Fu E, Lutz B, Yager P. Visualization and measurement of flow in two-dimensional paper networks. *Lab Chip.* 2010;10: 2614. doi:10.1039/c004766j
74. Ramachandran S, Fu E, Lutz B, Yager P. Long-term dry storage of an enzyme-based reagent system for ELISA in point-of-care devices. *The Analyst.* 2014;139: 1456. doi:10.1039/c3an02296j
75. Fridley GE, Le HQ, Fu E, Yager P. Controlled release of dry reagents in porous media for tunable temporal and spatial distribution upon rehydration. *Lab Chip.* 2012;12: 4321. doi:10.1039/c2lc40785j
76. Fridley GE, Le H, Yager P. Highly Sensitive Immunoassay Based on Controlled Rehydration of Patterned Reagents in a 2-Dimensional Paper Network. *Anal Chem.* 2014;86: 6447–6453. doi:10.1021/ac500872j
77. Lutz B, Liang T, Fu E, Ramachandran S, Kauffman P, Yager P. Dissolvable fluidic time delays for programming multi-step assays in instrument-free paper diagnostics. *Lab Chip.* 2013;13: 2840. doi:10.1039/c3lc50178g
78. Houghtaling J, Liang T, Thiessen G, Fu E. Dissolvable Bridges for Manipulating Fluid Volumes in Paper Networks. *Anal Chem.* 2013;85: 11201–11204. doi:10.1021/ac4022677
79. Toley BJ, McKenzie B, Liang T, Buser JR, Yager P, Fu E. Tunable-Delay Shunts for Paper Microfluidic Devices. *Anal Chem.* 2013;85: 11545–11552. doi:10.1021/ac4030939
80. Toley BJ, Wang JA, Gupta M, Buser JR, Lafleur LK, Lutz BR, et al. A versatile valving toolkit for automating fluidic operations in paper microfluidic devices. *Lab Chip.* 2015;15: 1432–1444. doi:10.1039/C4LC01155D
81. Rohrman BA, Richards-Kortum RR. A paper and plastic device for performing recombinase polymerase amplification of HIV DNA. *Lab Chip.* 2012;12: 3082. doi:10.1039/c2lc40423k
82. Apilux A, Ukita Y, Chikae M, Chailapakul O, Takamura Y. Development of automated paper-based devices for sequential multistep sandwich enzyme-linked immunosorbent assays using inkjet printing. *Lab Chip.* 2013;13: 126. doi:10.1039/c2lc40690j
83. Chen H, Cogswell J, Anagnostopoulos C, Faghri M. A fluidic diode, valves, and a sequential-loading circuit fabricated on layered paper. *Lab Chip.* 2012;12: 2909. doi:10.1039/c2lc20970e
84. Wright PF, Webster RG. Orthomyxoviruses. In: Knipe DM, Howley PM, editors. *Fields Virology.* 4th ed. Philadelphia, PA: Lippincott Williams and Wilkins; 2001. pp. 1533–1579.

85. Wright PF, Neumann G, Kawaoka Y. Orthomyxoviruses. In: Knipe DM, Howley PM, editors. *Fields Virology*. 5th ed. Philadelphia, PA: Lippincott Williams and Wilkins; 2007. pp. 1691–1740.
86. Palese P, Shaw G. Orthomyxoviridae: The Viruses and Their Replication. In: Knipe DM, Howley PM, editors. *Fields Virology*. Philadelphia, PA: Lippincott Williams and Wilkins; 2007. pp. 1647–1689.
87. Elsevier Health Sciences. Rapid Reference to Influenza [Internet]. 2012 [cited 9 Apr 2013]. Available: <http://www.rapidreferenceinfluenza.com/resource-center>
88. Lamb RA. The Influenza Virus RNA Segments and Their Encoded Proteins. In: Palese P, Kingsbury DW, editors. *Genetics of Influenza Viruses*. Austria: Springer-Verlag/Wien; 1983. pp. 21–69.
89. Fouchier RAM, Munster V, Wallensten A, Bestebroer TM, Herfst S, Smith D, et al. Characterization of a Novel Influenza A Virus Hemagglutinin Subtype (H16) Obtained from Black-Headed Gulls. *J Virol*. 2005;79: 2814–2822. doi:10.1128/JVI.79.5.2814-2822.2005
90. Tong S, Li Y, Rivaller P, Conrardy C, Castillo DAA, Chen L-M, et al. A distinct lineage of influenza A virus from bats. *Proc Natl Acad Sci*. 2012; doi:10.1073/pnas.1116200109
91. Tong S, Zhu X, Li Y, Shi M, Zhang J, Bourgeois M, et al. New World Bats Harbor Diverse Influenza A Viruses. Subbarao K, editor. *PLoS Pathog*. 2013;9: e1003657. doi:10.1371/journal.ppat.1003657
92. Garcia-Sastre A. The neuraminidase of bat influenza viruses is not a neuraminidase. *Proc Natl Acad Sci*. 2012;109: 18635–18636. doi:10.1073/pnas.1215857109
93. Wu Y, Wu Y, Tefsen B, Shi Y, Gao GF. Bat-derived influenza-like viruses H17N10 and H18N11. *Trends Microbiol*. 2014;22: 183–191. doi:10.1016/j.tim.2014.01.010
94. Centers for Disease Control and Prevention. Estimates of Deaths Associated with Seasonal Influenza --- United States, 1976--2007. *Morb Mortal Wkly Rep*. 2010;59: 1057–1062.
95. World Health Organization. Influenza (Seasonal) [Internet]. Apr 2009 [cited 13 May 2013]. Available: <http://www.who.int/mediacentre/factsheets/fs211/en/index.html>
96. Centers for Disease Control and Prevention. CDC Reports Flu Hit Younger People Particularly Hard This Season [Internet]. 20 Feb 2014 [cited 30 Mar 2014]. Available: <http://www.cdc.gov/media/releases/2014/p0220-flu-report.html>
97. World Health Organization. WHO Risk Assessment: Human infections with influenza A(H7N9) virus [Internet]. 2013 Apr. Available: http://www.who.int/influenza/human_animal_interface/influenza_h7n9/RiskAssessment_H7N9_13Apr13.pdf
98. World Health Organization. WHO | Avian influenza A(H7N9) virus [Internet]. 2015 [cited 22 Apr 2015]. Available: http://www.who.int/influenza/human_animal_interface/influenza_h7n9/en/

99. Centers for Disease Control and Prevention. Seasonal Influenza (Flu) - Antiviral Medications: Summary for Clinicians [Internet]. 22 Dec 2012 [cited 31 Mar 2013]. Available: <http://www.cdc.gov/flu/professionals/antivirals/summary-clinicians.htm>
100. Mahony JB. Detection of Respiratory Viruses by Molecular Methods. *Clin Microbiol Rev.* 2008;21: 716–747. doi:10.1128/CMR.00037-07
101. Jannetto PJ, Buchan BW, Vaughan KA, Ledford JS, Anderson DK, Henley DC, et al. Real-Time Detection of Influenza A, Influenza B, and Respiratory Syncytial Virus A and B in Respiratory Specimens by Use of Nanoparticle Probes. *J Clin Microbiol.* 2010;48: 3997–4002. doi:10.1128/JCM.01118-10
102. Centers for Disease Control and Prevention. CDC - Seasonal Influenza (Flu) - Guidance for Clinicians on the Use of RT-PCR and Other Molecular Assays for Diagnosis of Influenza Virus Infection [Internet]. 25 May 2012 [cited 13 May 2013]. Available: <http://www.cdc.gov/flu/professionals/diagnosis/molecular-assays.htm>
103. Centers for Disease Control and Prevention. Evaluation of 11 Commercially Available Rapid Influenza Diagnostic Tests -- United States, 2011-2012. *Morb Mortal Wkly Rep.* 2012;61: 873–876.
104. U.S. Food and Drug Administration. CLIA - Clinical Laboratory Improvement Amendments - Waived Influenza RDTs [Internet]. 1 Apr 2013 [cited 18 Apr 2013]. Available: http://www.accessdata.fda.gov/scripts/cdrh/cfdocs/cfCLIA/Results.cfm?start_search=1&Test_System_Name=influenza&Qualifier=&Analyte_Name=&Document_Number=&Clia_Analyte_Specialty=&Clia_Complexity=Waived&Effective_Date_FROM=&Effective_Date_TO=&san=&PAGENUM=10&SortColumn=DATE%5FEFFECTIVE%20DESC
105. U.S. Food and Drug Administration. IVD Regulatory Assistance > CLIA Categorization Criteria [Internet]. 20 Mar 2009 [cited 18 Apr 2013]. Available: <http://www.fda.gov/MedicalDevices/DeviceRegulationandGuidance/IVDRegulatoryAssistance/ucm124208.htm>
106. Wong RC. Regulatory Issues in the Development and Marketing of Lateral Flow Immunoassays. In: Wong RC, Tse HY, editors. *Lateral Flow Immunoassay*. New York, NY: Humana Press; 2009. pp. 205–217.
107. Petrozzino JJ, Smith C, Atkinson MJ. Rapid Diagnostic Testing for Seasonal Influenza: An Evidence-Based Review and Comparison with Unaided Clinical Diagnosis. *J Emerg Med.* 2010;39: 476–490.e1. doi:10.1016/j.jemermed.2009.11.031
108. Chartrand C. Accuracy of Rapid Influenza Diagnostic Tests: A Meta-analysis. *Ann Intern Med.* 2012;156: 500. doi:10.7326/0003-4819-156-7-201204030-00403
109. Cellulose - Wikipedia, the free encyclopedia [Internet]. [cited 14 May 2013]. Available: <http://en.wikipedia.org/wiki/Cellulose>
110. Nitrocellulose - Wikipedia, the free encyclopedia [Internet]. [cited 14 May 2013]. Available: <http://en.wikipedia.org/wiki/Nitrocellulose>

111. Tonkinson JL, Stillman BA. Nitrocellulose: A Tried and True Polymer Finds Utility as a Post-Genomic Substrate. *Front Biosci.* 2002;7: c1–12.
112. De la Ossa MÁF, Torre M, García-Ruiz C. Determination of nitrocellulose by capillary electrophoresis with laser-induced fluorescence detection. *Anal Chim Acta.* 2012;745: 149–155. doi:10.1016/j.aca.2012.07.032
113. Martin RS, Colombi A. Christian Friedrich Schönbein (1799-1868): From the Perilous Explosive Guncotton to the Salutary Dialysis Membranes. *Am J Nephrol.* 1992;12: 196–198. doi:10.1159/000168445
114. Falkowitz AL, Piech FE. Cellulose Lacquers - Nitrocellulose Lacquers for Aircraft. *Ind Eng Chem.* 1956;48: 1326–1326. doi:10.1021/ie50560a606
115. Hofmann HE, Reid EW. Formulation of Nitrocellulose Lacquers. *Ind Eng Chem.* 1928;20: 687–694. doi:10.1021/ie50223a007
116. Theisen E. The History of Nitrocellulose as a Film Base. *SMPTE Motion Imaging J.* 1933;20: 259–262. doi:10.5594/J10153
117. Bechhold H. Kolloidstudien mit der Filtrationsmethode. *Z Für Elektrotechnik Elektrochem.* 1907;13: 527–533. doi:10.1002/bbpc.19070133207
118. Ferry JD. Ultrafilter Membranes and Ultrafiltration. *Chem Rev.* 1936;18: 373–455. doi:10.1021/cr60061a001
119. Baker RW. Membrane technology and applications. Chichester, England: John Wiley & Sons; 2004.
120. Zsigmondy R, Bachmann W. Über neue Filter. *Z Für Anorg Allg Chem.* 1918;103: 119–128. doi:10.1002/zaac.19181030107
121. Mansfield M. Nitrocellulose Membranes for Lateral Flow Immunoassays: A Technical Treatise. In: Wong RC, Tse HY, editors. *Lateral Flow Immunoassay.* New York, NY: Humana Press; 2009. pp. 95–113.
122. Nygaard AP, Hall BD. A method for the detection of RNA-DNA complexes. *Biochem Biophys Res Commun.* 1963;12: 98–104.
123. Gillespie D, Spiegelman S. A quantitative assay for DNA-RNA hybrids with DNA immobilized on a membrane. *J Mol Biol.* 1965;12: 829–842. doi:10.1016/S0022-2836(65)80331-X
124. Flavell RA, Birfelder EJ, Sanders JPM, Borst P. DNA-DNA Hybridization on Nitrocellulose Filters. 1. General Considerations and Non-Ideal Kinetics. *Eur J Biochem.* 1974;47: 535–543. doi:10.1111/j.1432-1033.1974.tb03722.x
125. Southern EM. Detection of specific sequences among DNA fragments separated by gel electrophoresis. *J Mol Biol.* 1975;98: 503–517. doi:10.1016/S0022-2836(75)80083-0

126. Alwine JC, Kemp DJ, Stark GR. Method for detection of specific RNAs in agarose gels by transfer to diazobenzyloxymethyl-paper and hybridization with DNA probes. *Proc Natl Acad Sci U S A.* 1977;74: 5350–5354.
127. Towbin H. Electrophoretic Transfer of Proteins from Polyacrylamide Gels to Nitrocellulose Sheets: Procedure and Some Applications. *Proc Natl Acad Sci.* 1979;76: 4350–4354. doi:10.1073/pnas.76.9.4350
128. Burnette WN. “Western Blotting”: Electrophoretic transfer of proteins from sodium dodecyl sulfate-polyacrylamide gels to unmodified nitrocellulose and radiographic detection with antibody and radioiodinated protein A. *Anal Biochem.* 1981;112: 195–203. doi:10.1016/0003-2697(81)90281-5
129. Přistoupil TI, Kramlová M, Štěrbíková J. On the mechanism of adsorption of proteins to nitrocellulose in membrane chromatography. *J Chromatogr A.* 1969;42: 367–375. doi:10.1016/S0021-9673(01)80636-1
130. Tovey ER, Baldo BA. Protein binding to nitrocellulose, nylon and PVDF membranes in immunoassays and electroblotting. *J Biochem Biophys Methods.* 1989;19: 169–183.
131. Janeway C. *Immunobiology : The Immune System in Health and Disease.* [Internet]. 5th ed. New York: Garland Science; 2001. Available: <http://www.ncbi.nlm.nih.gov/books/NBK10757/>
132. Hage DS, editor. *Handbook of Affinity Chromatography.* 2nd ed. Boca Raton, FL: CRC Press, Taylor & Francis Group; 2006.
133. Goding JW. Antibody production by hybridomas. *J Immunol Methods.* 1980;39: 285–308. doi:10.1016/0022-1759(80)90230-6
134. Binz HK, Amstutz P, Plückthun A. Engineering novel binding proteins from nonimmunoglobulin domains. *Nat Biotechnol.* 2005;23: 1257–1268. doi:10.1038/nbt1127
135. Klein JS, Gnanaprasagam PNP, Galimidi RP, Foglesong CP, West AP, Bjorkman PJ. Examination of the contributions of size and avidity to the neutralization mechanisms of the anti-HIV antibodies b12 and 4E10. *Proc Natl Acad Sci.* 2009;106: 7385–7390. doi:10.1073/pnas.0811427106
136. Nygren P-Å, Skerra A. Binding proteins from alternative scaffolds. *J Immunol Methods.* 2004;290: 3–28. doi:10.1016/j.jim.2004.04.006
137. Chao G, Lau WL, Hackel BJ, Sazinsky SL, Lippow SM, Wittrup KD. Isolating and engineering human antibodies using yeast surface display. *Nat Protoc.* 2006;1: 755–768. doi:10.1038/nprot.2006.94
138. Famulok M, Mayer G. Aptamer Modules as Sensors and Detectors. *Acc Chem Res.* 2011;44: 1349–1358. doi:10.1021/ar2000293
139. Vermasvuori R. Production of Recombinant Proteins and Monoclonal Antibodies – Techno-Economical Evaluation of the Production Methods [Internet]. Helsinki University of Technology. 2009. Available: <http://lib.tkk.fi/Lic/2009/urn100121.pdf>

140. Centers for Disease Control and Prevention. Images of Influenza Viruses | CDC [Internet]. 15 Aug 2014 [cited 25 Apr 2015]. Available: <http://www.cdc.gov/flu/images.htm>
141. Weis W, Brown JH, Cusack S, Paulson JC, Skehel JJ, Wiley DC. Structure of the influenza virus haemagglutinin complexed with its receptor, sialic acid. *Nature*. 1988;333: 426–431. doi:10.1038/333426a0
142. Fleishman SJ, Whitehead TA, Ekiert DC, Dreyfus C, Corn JE, Strauch E-M, et al. Computational Design of Proteins Targeting the Conserved Stem Region of Influenza Hemagglutinin. *Science*. 2011;332: 816–821. doi:10.1126/science.1202617
143. Stevenson CEM, Burton N, Costa MMR, Nath U, Dixon RA, Coen ES, et al. Crystal structure of the MYB domain of the RAD transcription factor from *Antirrhinum majus*. *Proteins Struct Funct Bioinforma*. 2006;65: 1041–1045. doi:10.1002/prot.21136
144. Whitehead TA, Chevalier A, Song Y, Dreyfus C, Fleishman SJ, De Mattos C, et al. Optimization of affinity, specificity and function of designed influenza inhibitors using deep sequencing. *Nat Biotechnol*. 2012;30: 543–548. doi:10.1038/nbt.2214
145. Hopp TP, Prickett KS, Price VL, Libby RT, March CJ, Pat Cerretti D, et al. A Short Polypeptide Marker Sequence Useful for Recombinant Protein Identification and Purification. *Bio/Technology*. 1988;6: 1204–1210. doi:10.1038/nbt1088-1204
146. American Chemical Society, American Chemical Society. *Proteins at interfaces: physicochemical and biochemical studies*. Washington, DC: American Chemical Society; 1987.
147. American Chemical Society, American Chemical Society. *Proteins at interfaces II: fundamentals and applications*. Washington, DC: American Chemical Society; 1995.
148. *Proteins at Interfaces (Conference)*, American Chemical Society. *Proteins at Interfaces III: state of the art*.
149. Van Oss CJ, Good RJ, Chaudhury MK. Mechanism of DNA (Southern) and protein (Western) blotting on cellulose nitrate and other membranes. *J Chromatogr*. 1987;391: 53–65.
150. Hoffman WL, Jump AA. Tween 20 removes antibodies and other proteins from nitrocellulose. *J Immunol Methods*. 1986;94: 191–196.
151. Sicard C, Brennan JD. Bioactive paper: Biomolecule immobilization methods and applications in environmental monitoring. *MRS Bull*. 2013;38: 331–334. doi:10.1557/mrs.2013.61
152. Wilchek M, Bayer EA, Livnah O. Essentials of biorecognition: The (strept)avidin–biotin system as a model for protein–protein and protein–ligand interaction. *Immunol Lett*. 2006;103: 27–32. doi:10.1016/j.imlet.2005.10.022
153. Hussack G, Luo Y, Veldhuis L, Hall JC, Tanha J, MacKenzie R. Multivalent Anchoring and Oriented Display of Single-Domain Antibodies on Cellulose. *Sensors*. 2009;9: 5351–5367. doi:10.3390/s90705351

154. Shoseyov O, Shani Z, Levy I. Carbohydrate Binding Modules: Biochemical Properties and Novel Applications. *Microbiol Mol Biol Rev.* 2006;70: 283–295. doi:10.1128/MMBR.00028-05
155. Wu P, Castner DG, Grainger DW. Diagnostic devices as biomaterials: a review of nucleic acid and protein microarray surface performance issues. *J Biomater Sci Polym Ed.* 2008;19: 725–753. doi:10.1163/156856208784522092
156. Rusmini F, Zhong Z, Feijen J. Protein Immobilization Strategies for Protein Biochips. *Biomacromolecules.* 2007;8: 1775–1789. doi:10.1021/bm061197b
157. Jonkheijm P, Weinrich D, Schröder H, Niemeyer CM, Waldmann H. Chemical Strategies for Generating Protein Biochips. *Angew Chem Int Ed.* 2008;47: 9618–9647. doi:10.1002/anie.200801711
158. Metkar SS, Mahajan SK, Sainis JK. Modified procedure for nonspecific protein staining on nitrocellulose paper using Coomassie brilliant blue R-250. *Anal Biochem.* 1995;227: 389–391. doi:10.1006/abio.1995.1297
159. Deegan RD, Bakajin O, Dupont TF, Huber G, Nagel SR, Witten TA. Capillary flow as the cause of ring stains from dried liquid drops. *Nature.* 1997;389: 827–829. doi:10.1038/39827
160. Fridley GE. Methods and models to control and predict behavior of two dimensional paper networks for diagnostics. University of Washington. 2014.
161. Holstein CA, Fridley GE, Adcock CA, Yager P. Methods and Models to Examine Protein Adsorption to Nitrocellulose [In preparation]. 2015.
162. McClellan SJ, Franses EI. Adsorption of bovine serum albumin at solid/aqueous interfaces. *Colloids Surf Physicochem Eng Asp.* 2005;260: 265–275. doi:10.1016/j.colsurfa.2005.03.017
163. Bradford MM. A rapid and sensitive method for the quantitation of microgram quantities of protein utilizing the principle of protein-dye binding. *Anal Biochem.* 1976;72: 248–254. doi:10.1016/0003-2697(76)90527-3
164. Di Risio S, Yan N. Adsorption and inactivation behavior of horseradish peroxidase on cellulosic fiber surfaces. *J Colloid Interface Sci.* 2009;338: 410–419. doi:10.1016/j.jcis.2009.07.005
165. Kim K, Kang S. Adsorption properties of bovine serum albumin on porous polymer microgels. *Korea Polym J.* 1998;6: 235–240.
166. Hou W-C, Moghadam BY, Westerhoff P, Posner JD. Distribution of Fullerene Nanomaterials between Water and Model Biological Membranes. *Langmuir.* 2011;27: 11899–11905. doi:10.1021/la2017837
167. Hou W-C, Moghadam BY, Corredor C, Westerhoff P, Posner JD. Distribution of Functionalized Gold Nanoparticles between Water and Lipid Bilayers as Model Cell Membranes. *Environ Sci Technol.* 2012;46: 1869–1876. doi:10.1021/es203661k
168. Skopp J. Derivation of the Freundlich Adsorption Isotherm from Kinetics. *J Chem Educ.* 2009;86: 1341. doi:10.1021/ed086p1341

169. Klein D, Kern R, Sokol R. A method for quantification and correction of proteins after transfer to immobilization membranes. *Biochem Mol Biol Int.* 1995;36: 59–66.
170. Barbosa LRS, Ortore MG, Spinozzi F, Mariani P, Bernstorff S, Itri R. The Importance of Protein-Protein Interactions on the pH-Induced Conformational Changes of Bovine Serum Albumin: A Small-Angle X-Ray Scattering Study. *Biophys J.* 2010;98: 147–157. doi:10.1016/j.bpj.2009.09.056
171. Ma C, Yeung ES. Single Molecule Imaging of Protein Molecules in Nanopores. *Anal Chem.* 2010;82: 478–482. doi:10.1021/ac902487c
172. Norde W, Horbett TA, Brash JL. Proteins at Interfaces III: Introductory Overview. In: Horbett T, Brash JL, Norde W, editors. *Proteins at Interfaces III State of the Art 2012.* Washington, DC: American Chemical Society; 2012. pp. 1–34. Available: <http://pubs.acs.org/doi/abs/10.1021/bk-2012-1120.ch001>
173. Vinu A, Murugesan V, Tangermann O, Hartmann M. Adsorption of Cytochrome c on Mesoporous Molecular Sieves: Influence of pH, Pore Diameter, and Aluminum Incorporation. *Chem Mater.* 2004;16: 3056–3065. doi:10.1021/cm049718u
174. McIlvaine TC. A Buffer Solution for Colorimetric Comparison. *J Biol Chem.* 1921;49: 183–186.
175. Thermo Scientific. Avidin-Biotin Interaction [Internet]. 2013 [cited 29 Apr 2013]. Available: <http://www.piercenet.com/browse.cfm?fldID=4A957146-5056-8A76-4E97-81995432210B>
176. Beynon R. Buffers for pH control (c) Rob Beynon, University of Liverpool [Internet]. 9 Jul 2006 [cited 16 May 2013]. Available: <http://www.liv.ac.uk/buffers/buffercalc.html>
177. Koga N, Tatsumi-Koga R, Liu G, Xiao R, Acton TB, Montelione GT, et al. Principles for designing ideal protein structures. *Nature.* 2012;491: 222–227. doi:10.1038/nature11600
178. Huang P-S, Oberdorfer G, Xu C, Pei XY, Nannenga BL, Rogers JM, et al. High thermodynamic stability of parametrically designed helical bundles. *Science.* 2014;346: 481–485. doi:10.1126/science.1257481
179. Li B, Olsen CE, Moore DR. Porous membranes having a polymeric coating and methods for their preparation and use [Internet]. US20130171368 A1. Available: <http://www.google.com/patents/US20130171368>
180. Dithiothreitol - Wikipedia, the free encyclopedia [Internet]. 14 Mar 2013 [cited 5 May 2013]. Available: <http://en.wikipedia.org/wiki/Dithiothreitol>
181. TCEP - Wikipedia, the free encyclopedia [Internet]. 16 Mar 2013 [cited 5 May 2013]. Available: <http://en.wikipedia.org/wiki/TCEP>
182. Avidity. Avidity Patented AviTag™ Technology [Internet]. [cited 16 May 2013]. Available: <https://www.avidity.com/>
183. Beckett D, Kovaleva E, Schatz PJ. A minimal peptide substrate in biotin holoenzyme synthetase-catalyzed biotinylation. *Protein Sci.* 2008;8: 921–929. doi:10.1110/ps.8.4.921

184. Fire E, Gutman O, Roth MG, Henis YI. Dynamic or Stable Interactions of Influenza Hemagglutinin Mutants with Coated Pits. *J Biol Chem*. 1995;270: 21075–21081. doi:10.1074/jbc.270.36.21075
185. Lee BW, Bey RF, Baarsch MJ, Emery DA. Subtype specific ELISA for the detection of Antibodies against influenza A H1N1 and H3N2 in swine. *J Virol Methods*. 1993;45: 121–136. doi:10.1016/0166-0934(93)90097-B
186. Markets and Markets. In Vitro Diagnostic (IVD) Market, Technique & Applications - Forecast to 2017 [Internet]. 2013 Jul. Available: <http://www.marketsandmarkets.com/Market-Reports/ivd-in-vitro-diagnostics-market-703.html>
187. PubMed search: Assay, 2012 [Internet]. [cited 24 Feb 2015]. Available: <http://www.ncbi.nlm.nih.gov/pubmed/?term=%28assay%5BTtitle%2FAbstract%5D%29+AND+%28%222012%2F1%2F1%22%5BDate+-+Publication%5D+%3A+%222012%2F31%2F12%22%5BDate+-+Publication%5D%29>
188. Currie LA. Nomenclature in evaluation of analytical methods including detection and quantification capabilities (IUPAC Recommendations 1995). *Pure Appl Chem*. 1995;67: 1699–1723. doi:10.1351/pac199567101699
189. Tholen DW, Linnet K, Kondratovich M, Armbruster DA, Garrett PE, Jones RL, et al. Protocols for determination of limits of detection and limits of quantitation: approved guideline (NCCLS document EP17-A). Wayne, Pa.: NCCLS; 2004.
190. Armbruster DA, Pry T. Limit of blank, limit of detection and limit of quantitation. *Clin Biochem Rev Aust Assoc Clin Biochem*. 2008;29 Suppl 1: S49–52.
191. Faber NM. The limit of detection is not the analyte level for deciding between “detected” and “not detected.” *Accreditation Qual Assur*. 2008;13: 277–278. doi:10.1007/s00769-007-0351-9
192. Lavagnini I, Magno F. A statistical overview on univariate calibration, inverse regression, and detection limits: Application to gas chromatography/mass spectrometry technique. *Mass Spectrom Rev*. 2007;26: 1–18. doi:10.1002/mas.20100
193. Findlay JWA, Dillard RF. Appropriate calibration curve fitting in ligand binding assays. *AAPS J*. 2007;9: E260–E267. doi:10.1208/aapsj0902029
194. Gottschalk PG, Dunn JR. The five-parameter logistic: A characterization and comparison with the four-parameter logistic. *Anal Biochem*. 2005;343: 54–65. doi:10.1016/j.ab.2005.04.035
195. Davidian M, Giltinan DM. *Nonlinear Models for Repeated Measurement Data*. Chapman and Hall/CRC Press; 1995.
196. Fong Y, Wakefield J, De Rosa S, Frahm N. A Robust Bayesian Random Effects Model for Nonlinear Calibration Problems. *Biometrics*. 2012;68: 1103–1112. doi:10.1111/j.1541-0420.2012.01762.x
197. Oppenheimer L, Capizzi TP, Weppelman RM, Mehta H. Determining the lowest limit of reliable assay measurement. *Anal Chem*. 1983;55: 638–643. doi:10.1021/ac00255a013

198. Garden JS, Mitchell DG, Mills WN. Nonconstant variance regression techniques for calibration-curve-based analysis. *Anal Chem.* 1980;52: 2310–2315. doi:10.1021/ac50064a017
199. Welch BL. The Generalization of “Students”s’ Problem When Several Different Population Variances are Involved. *Biometrika.* 1947;34: 28–35. doi:10.1093/biomet/34.1-2.28
200. Satterthwaite FE. An Approximate Distribution of Estimates of Variance Components. *Biom Bull.* 1946;2: 110–114.
201. Chan KH, Lai ST, Poon LLM, Guan Y, Yuen KY, Peiris JSM. Analytical sensitivity of rapid influenza antigen detection tests for swine-origin influenza virus (H1N1). *J Clin Virol.* 2009;45: 205–207. doi:10.1016/j.jcv.2009.05.034
202. Centers for Disease Control and Prevention. Seasonal Influenza: Flu Basics [Internet]. 23 Feb 2015 [cited 10 Apr 2015]. Available: <http://www.cdc.gov/flu/about/disease/index.htm>

Appendix A: List of Abbreviations

Abbreviation	Description
2DPN	Two-dimensional paper network
AA	Amino acids
BSA	Bovine serum albumin
CA2009	A/California/04/2009 (H1N1) influenza
CBB	Coomassie Brilliant Blue
CEID ₅₀	Chicken egg infective dose
CLIA	Clinical Laboratory Improvement Amendments
Da	Dalton; 1 Da = 1 g/mol
DFA	Direct fluorescence antibody
DNA	Deoxyribonucleic acid
ELISA	Enzyme-linked immunosorbent assay
FBS	Fetal bovine serum
FDA	U.S. Food and Drug Administration
FITC	Fluorescein isothiocyanate
Flu	Influenza
GDP	Gross domestic product
GE GRC	General Electric Global Research Center
GMA	Glycidyl methacrylate
GUI	Graphical user interface
HA	Hemagglutinin
HBS	HEPES-buffered saline
HIV	Human immunodeficiency virus
HRP	Horseradish peroxidase
IgG	Immunoglobulin G
LF	Lateral flow
LFT	Lateral flow test
LOD	Limit of detection
MW	Molecular weight
NA	Neuraminidase
NAAT	Nucleic acid amplification test
NC	Nitrocellulose
NHS	<i>N</i> -hydroxysuccinimide
NP	Nucleoprotein
NTA	Nitrilotriacetic acid
OD	Optical density
OG	Octylglucoside
PBS	Phosphate-buffered saline
PBSS	PBS plus 0.02% or 0.1% (w/v) SDS
PBST	PBS plus 0.1% (v/v) Tween-20
PBST+BSA	PBST plus 1% (w/v) BSA
PCR	Polymerase chain reaction

PDB	Protein Data Bank
PDMS	Polydimethylsiloxane
PEG	Polyethylene glycol
pI	Isoelectric point
POC	Point-of-care
PVDF	Polyvinylidene fluoride
qRT-PCR	Real-time qualitative reverse transcription PCR
RDT	Rapid diagnostic test
RNA	Ribonucleic acid
RNP	Ribonucleoprotein
SA	Streptavidin
SC1918	A/South Carolina/1/1918 (H1N1) influenza
SD	Standard deviation
SDS	Sodium dodecyl sulfate
SE	Standard error
SPR	Surface plasmon resonance
T11	Trimer 11 head region flu binder
TB	Tuberculosis
TCA	Trichloroacetic acid
TCID ₅₀	Tissue culture infective dose
T _m	Melting temperature
μPAD	Microfluidic paper analytical device
v/v	Volume by volume
w/v	Weight by volume

Appendix B: MATLAB Program *quantifyColorimetricSignal.m*

B.1. Description

Introduction

This MATLAB program was designed to expedite the quantification of colorimetric signal from paper-based assays (although could be used for any pixel intensity quantification needs in general). The program is run by the user through a few command-line prompts and a graphical user interface (GUI). The program is designed to make the quantification process semi-automated, while still retaining the flexibility to allow the program to be used for devices of any shape or size. The program requires a MATLAB license, as well as MATLAB's Image Processing toolbox.

Image Requirements

This program should be capable of analyzing images of any common image type (*.TIF, *.JPG, *.PNG, etc.), although only *.TIF files have been tested extensively. The program will automatically determine the type (grayscale/RGB) and bit-depth of the image. However, the user must know what color channel they would like to use for analysis (e.g. grayscale or green channel) and if that makes sense for their image.

Basic Use of the Script

To run the program, open MATLAB, navigate to your directory of choice, and ensure that the file *quantifyColorimetricSignal.m* is in your current working directory. Then, complete the following steps.

Step 1: Run the program

Run the program by typing the following command in the Command Window:

```
myData = quantifyColorimetricSignal
```

Note that 'myData' can be replaced with whatever name you would like to give to the output results.

```
Command Window
fx >> LFchallenge_NoFlow = quantifyColorimetricSignal
```

Step 2: Enter input options

The program starts by prompting the user for five input options, listed in the table below. Answer each prompt in the Command Window. After the user input options are entered, the main GUI opens in a new window.

```
Command Window

Enter the image file name: LFchallenge_NoFlow.tif

Enter the number of spots to quantify: 24

Which quantification method would you like to use?
  1. Average grayscale pixel intensity
  2. Average red channel pixel intensity
  3. Average green channel pixel intensity
  4. Average blue channel pixel intensity
  5. Average grayscale pixel intensity for
     negative images (e.g. fluorescence)
Enter the number corresponding to your choice: 3

Do you want to enter spot names or load spot names from a previous session?
  1. Enter spot names
  2. Load spot names
Enter the number corresponding to your choice: 1

Do you want to draw ROIs or load pre-drawn ROIs?
  1. Draw ROIs
  2. Load ROIs
Enter the number corresponding to your choice: 1

Now draw your regions of interest.
Press enter when done.
fx |
```

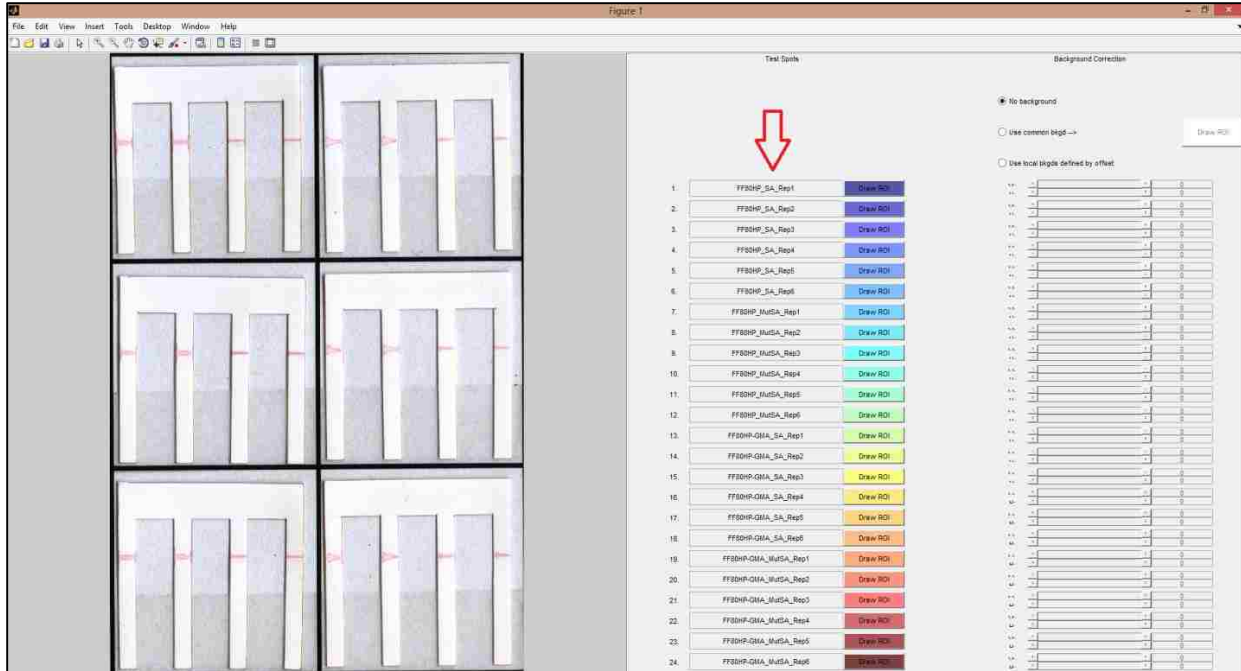
List of input options for running program to quantify signal intensity.

List of the five input options required to run the MATLAB program *quantifyColorimetricSignal.m*. Input examples and notes for each option are included.

Input Option	Example User Input	Notes
Image file name	LFchallenge_NoFlow.tif	Must include the file extension as part of the file name
Number of “spots” or regions of interest to be quantified	24	There is technically no limit on the number of spots that can be quantified in a single session; however, the GUI usually starts getting crowded after 20 or 30 spots, depending on your screen size
Quantification method	3 (Average green channel pixel intensity)	There are currently 5 options: Average grayscale pixel intensity Average red channel pixel intensity Average green channel pixel intensity Average blue channel pixel intensity Average grayscale pixel intensity for negative images (e.g. fluorescence) Choose whichever option makes sense for your image.
Enter or load spot names	1	For most cases, choose option 1 to enter in names for each test region. In the case of batch analysis, for which you are loading a closely related image with the same spot names, choose option 2 to load previously entered spot names
Draw or load regions of interest (ROIs)	1	For most cases, choose option 1 to draw an ROI for each test region. In the case of batch analysis, for which you are loading a closely related image with the same spot locations, choose option 2 to load previously drawn ROIs

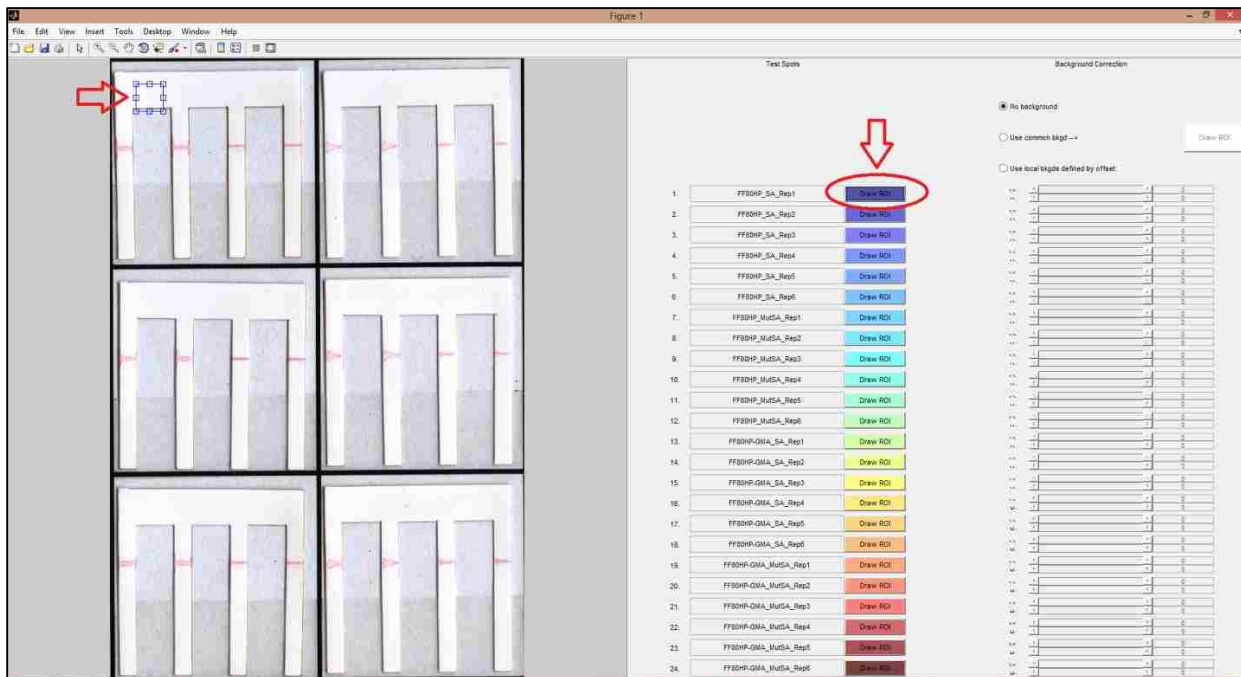
Step 3: Enter spot names

Begin your analysis by entering in a name for each spot to be quantified in the GUI.



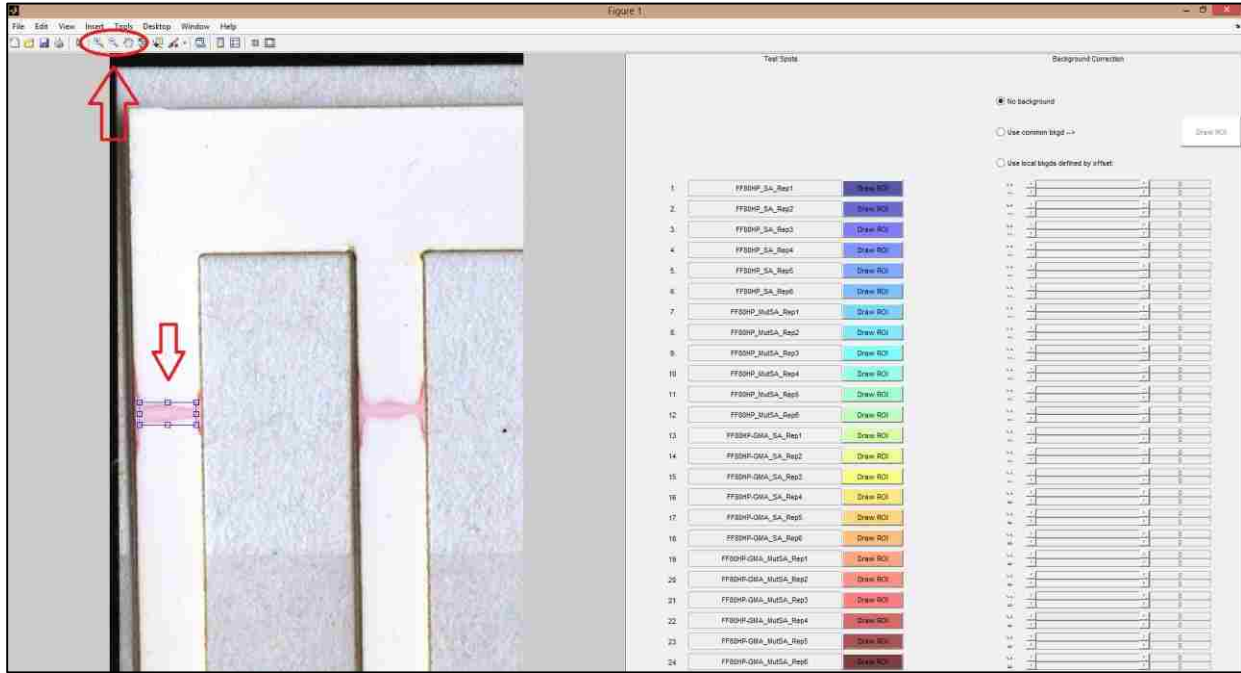
Step 4: Draw the first ROI

Next, click the first "Draw ROI" button to draw a region of interest for your first test spot. A default-sized ROI will appear near the top left corner of the image.



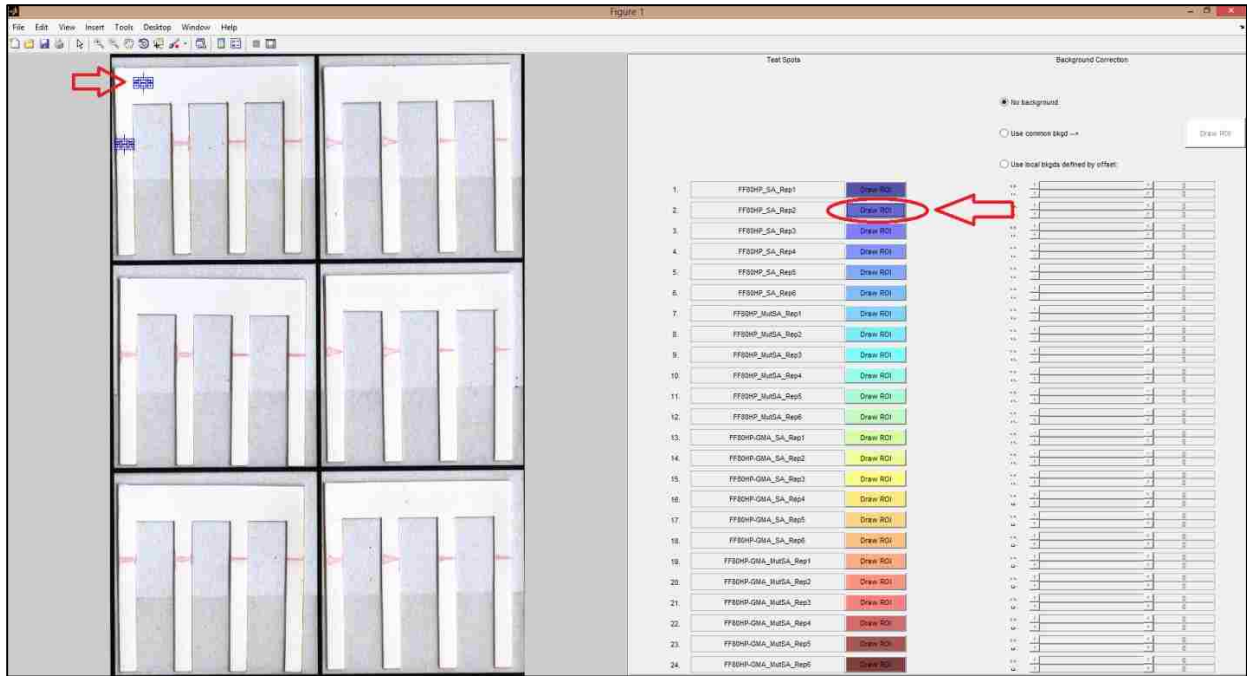
Step 5: Adjust the ROI

Drag and resize the ROI to match the spot you wish to quantify. You can use the zoom and pan features of the image viewer during this process.



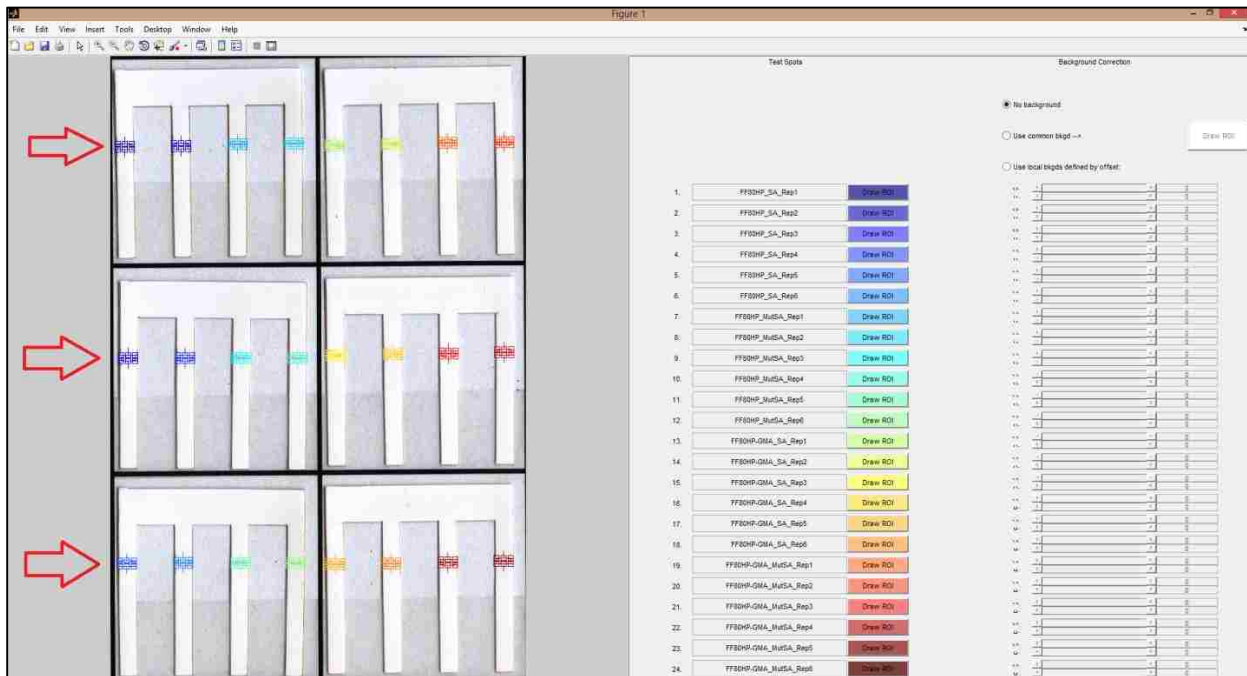
Step 6: Draw the next ROI

Click the next “Draw ROI” button to draw the region of interest for your next test spot. This ROI (and all subsequent ROIs) will automatically assume the same dimensions as the first ROI (although can be resized if desired).



Step 7: Repeat steps 5-6 until all ROIs have been drawn

Follow steps 5-6 to draw ROIs for all remaining test spots.



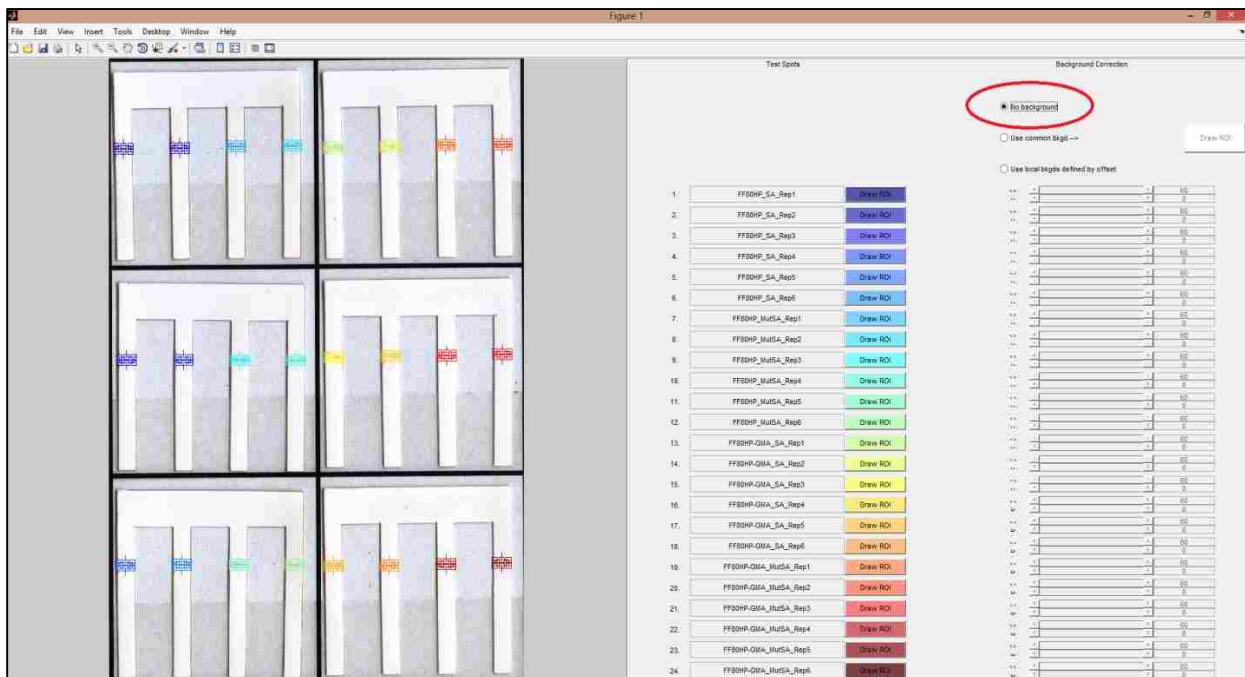
Step 8: Select option for background correction

Choose one of three options for the type of background correction to be used:

1. **No background:** No background subtraction will be performed; the raw pixel intensity of the i^{th} test region ($I_{\text{raw},i}$) will simply be inverted and scaled from 0 (white) to 1 (dark), as follows:

$$I_{\text{corrected},i} = \frac{I_{\text{raw},i} - I_{\text{max}}}{0 - I_{\text{max}}}$$

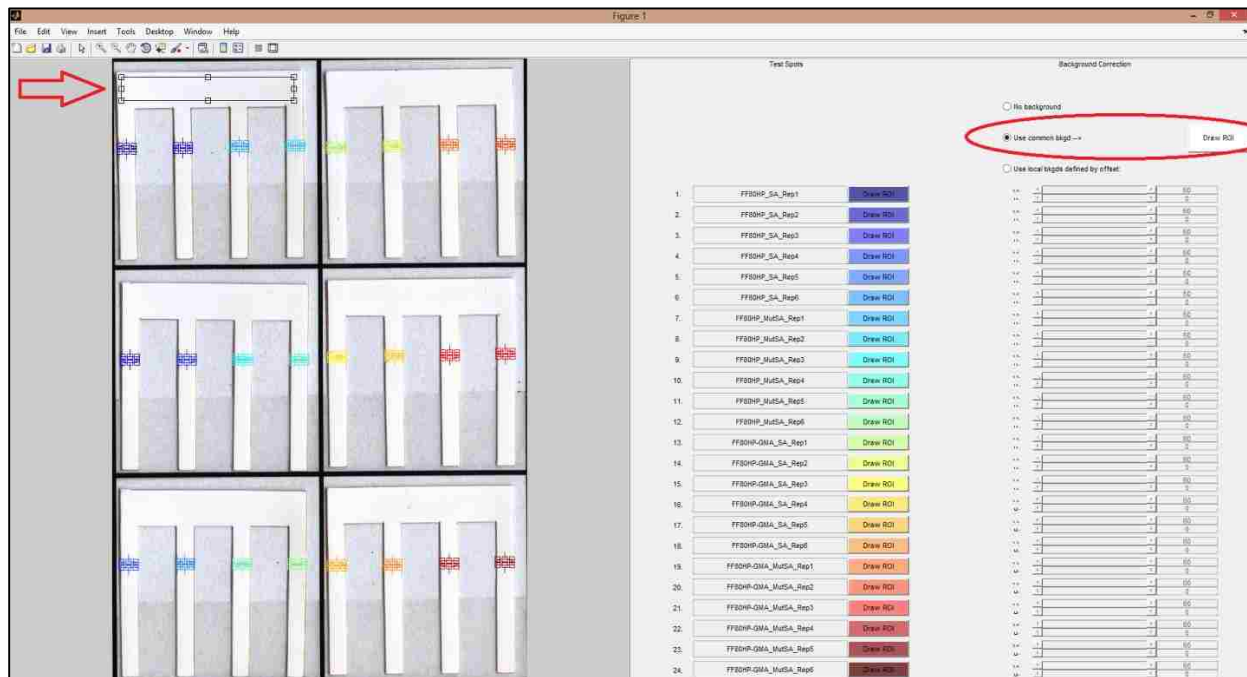
where 0 represents the lowest possible pixel intensity (i.e. black), and I_{max} is the maximum pixel intensity (i.e. white) for the given bit-depth, e.g. 255 for an 8-bit image.



2. **Use common background:** The raw pixel intensity of the i^{th} test region ($I_{raw,i}$) will be corrected using the pixel intensity of the chosen common background region ($I_{background}$) and inverted and scaled from 0 (white) to 1 (dark), as follows:

$$I_{corrected,i} = \frac{I_{raw,i} - I_{background}}{0 - I_{background}}$$

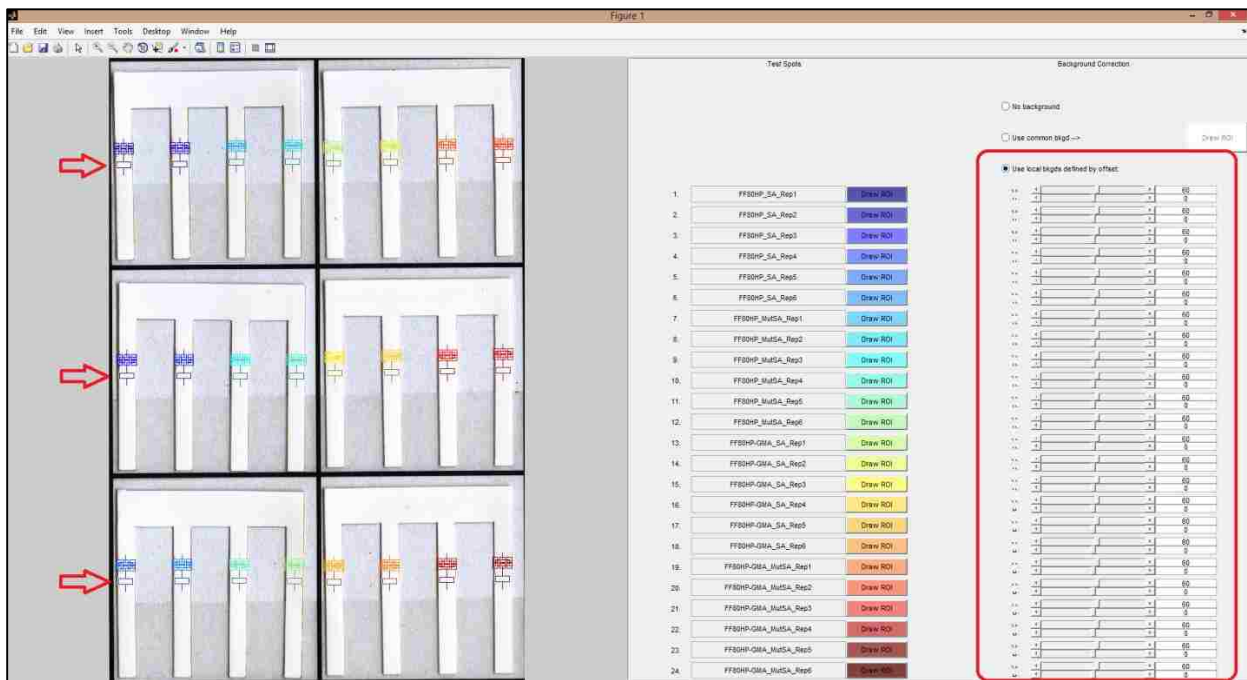
where 0 represents the lowest possible pixel intensity (i.e. black). Here, the common background ROI is drawn by the user.



3. **Use local backgrounds defined by offset:** The raw pixel intensity of the i^{th} test region ($I_{raw,i}$) will be corrected using the pixel intensity of corresponding i^{th} background region ($I_{background,i}$) and inverted and scaled from 0 (white) to 1 (dark), as follows:

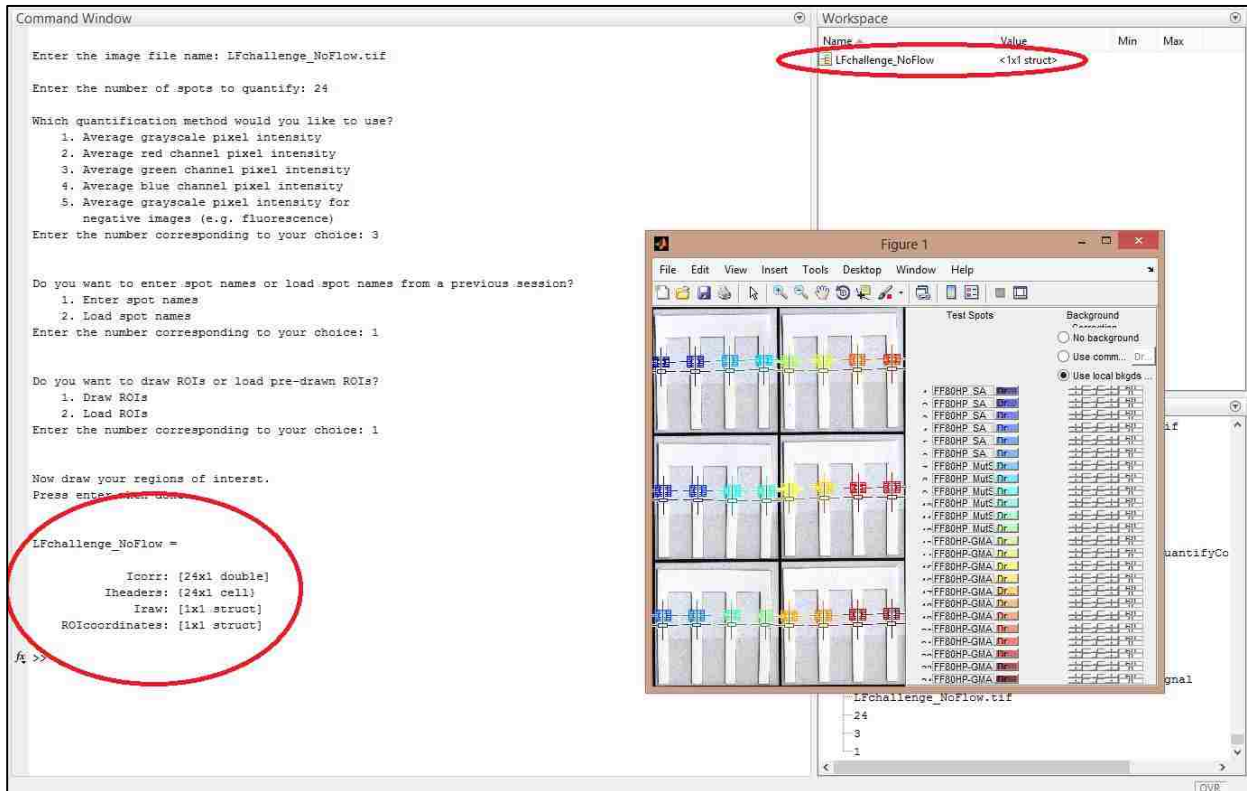
$$I_{corrected,i} = \frac{I_{raw,i} - I_{background,i}}{0 - I_{background,i}}$$

where 0 represents the lowest possible pixel intensity (i.e. black). Here each local background ROI is defined by a vertical and/or horizontal offset from the test ROI. The dimensions of each background ROI are exactly equal to the dimensions of the corresponding test ROI and cannot be resized. ***This local background correction is typically recommended for most test strips.***



Step 9: Complete quantification

After all ROIs have been set in the GUI, leave the GUI window open, but click back in the Command Window and hit enter to complete the quantification process. Your data structure 'myData' will now appear in your Workspace, and some details about this output variable will be displayed in the Command Window. After this step, you can close the GUI window.



Step 10: Save data as a *.mat file

Save your data (i.e. the variables in your Workspace) to a *.mat file to retain the data in a MATLAB-usable form for future use. To do so, type the following command:

```
save myDatasetName.mat
```

This will create a file under this name in your Current Folder.

Current Folder

Name

- Old Code
- Tutorial
- 20110121_GE_D1_FinalScan.tif
- 20110218_InvitrogenBlock_SourcePads.tif
- 20110707_DengueRDTs_FocusDyCtrls.tif
- 20111228_FHB80.4Vis_FITCantiFLAG_100ugmL_0p1sExp.png
- 20131109_MuSCs_MIP09_Eluorescence_GMA.tif
- 20130312_LFchallengeData.mat**
- LFchallenge_NoFlow.tif
- LFchallenge_PBST.tif
- MATLAB_SpotQuant_Screenshot_20121220.png
- MATLABTutorial_QuantifyColorimetricSignal.docx
- myTestData.mat
- PATHExp.tif
- PATHExp_20121220.mat
- ProteinSpotTest-10minDeStain_Unblocked_0.0025percentCBB.tif
- quantifyColorimetricSignal.m
- quantTest_20120520.mat
- quantTest_20120720.mat
- quantTest_20120802.mat
- quantTest_20130207.mat
- Thumbs.db
- ~\$TLABTutorial_QuantifyColorimetricSignal.docx
- ~WRL0003.tmp

LFchallenge_NoFlow.tif (TF File)

No details available

Command Window

```

Enter the image file name: LFchallenge_NoFlow.tif

Enter the number of spots to quantify: 24

Which quantification method would you like to use?
1. Average grayscale pixel intensity
2. Average red channel pixel intensity
3. Average green channel pixel intensity
4. Average blue channel pixel intensity
5. Average grayscale pixel intensity for
   negative images (e.g. fluorescence)
Enter the number corresponding to your choice: 3

Do you want to enter spot names or load spot names from a previous session?
1. Enter spot names
2. Load spot names
Enter the number corresponding to your choice: 1

Do you want to draw ROIs or load pre-drawn ROIs?
1. Draw ROIs
2. Load ROIs
Enter the number corresponding to your choice: 1

Now draw your regions of interest.
Press enter when done.

LFchallenge_NoFlow =

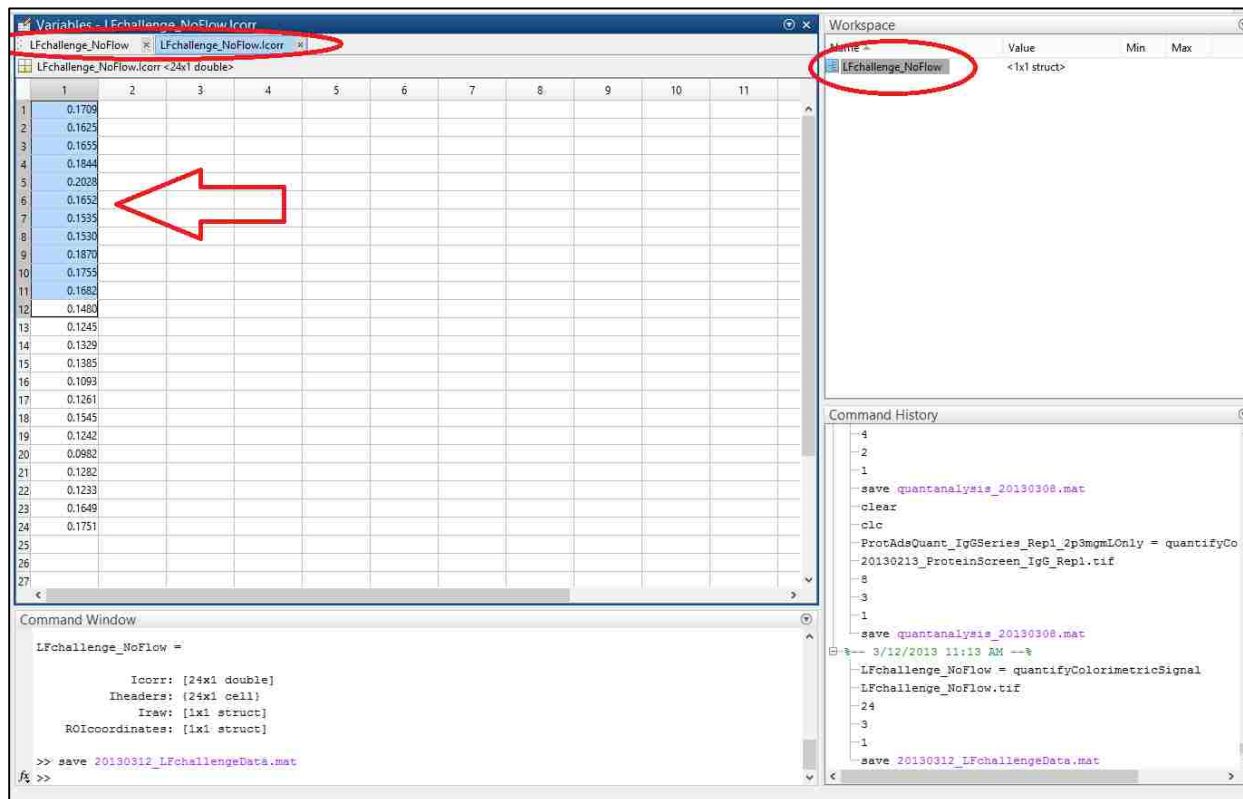
        Icorr: [24x1 double]
        Iheaders: (24x1 cell)
        Iraw: [1x1 struct]
        ROIcoordinates: [1x1 struct]

>> save 20130312_LFchallengeData.mat

```

Step 11: Export data if desired

At this point, you can analyze the data however you would like. If you would like to export your data to Excel for analysis, the simplest way is to double-click on your 'myData' variable in your Workspace, then double-click and view the normalized (and potentially background-corrected) pixel intensities (I_{corr}) in the data viewer. You can then copy the data from any or all cells and paste into an Excel file for curation and analysis.



Loading Data from Previous Session

It is sometimes desirable to perform a quantification session using spot names and/or ROIs loaded from a previous session. For example, I may want to analyze a similar set of devices, but for a different experimental condition. To do so, use the following steps.

Step 1*: Run the program

Use the same command as before, this time assigning a different name to your output variable:

```
myData_Set2 = quantifyColorimetricSignal
```

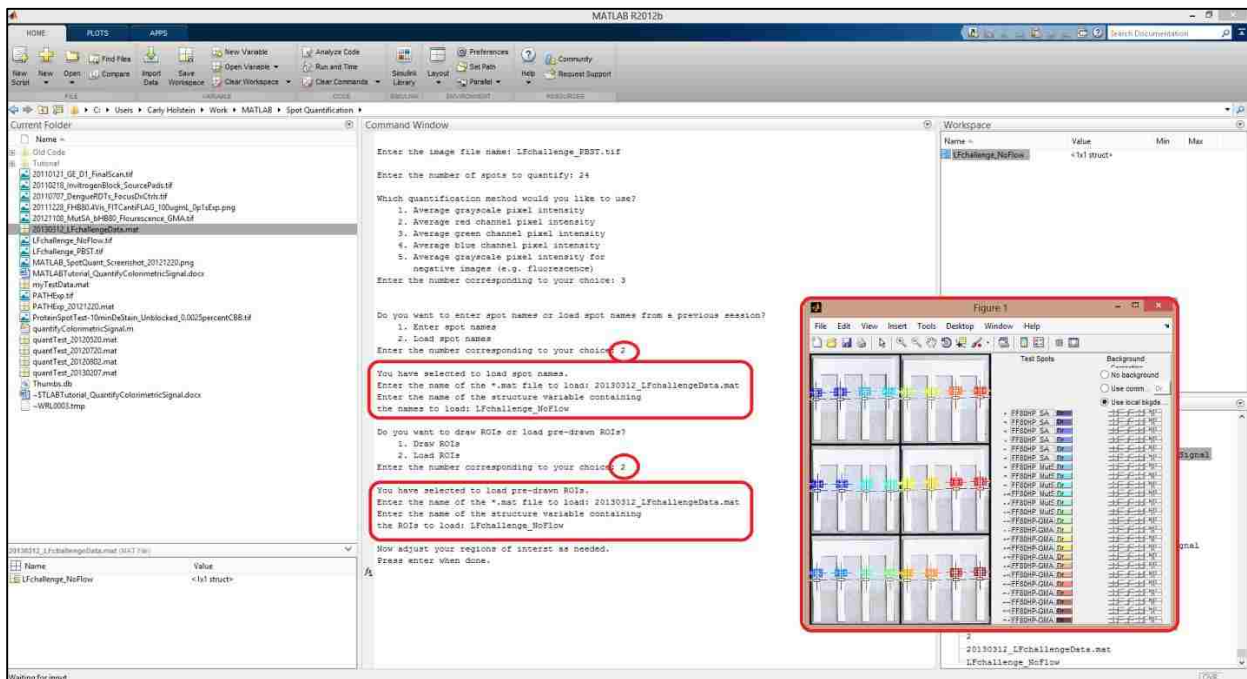
```

Command Window
>> LFchallenge_PBST = quantifyColorimetricSignal

```

Step 2*: Enter input options

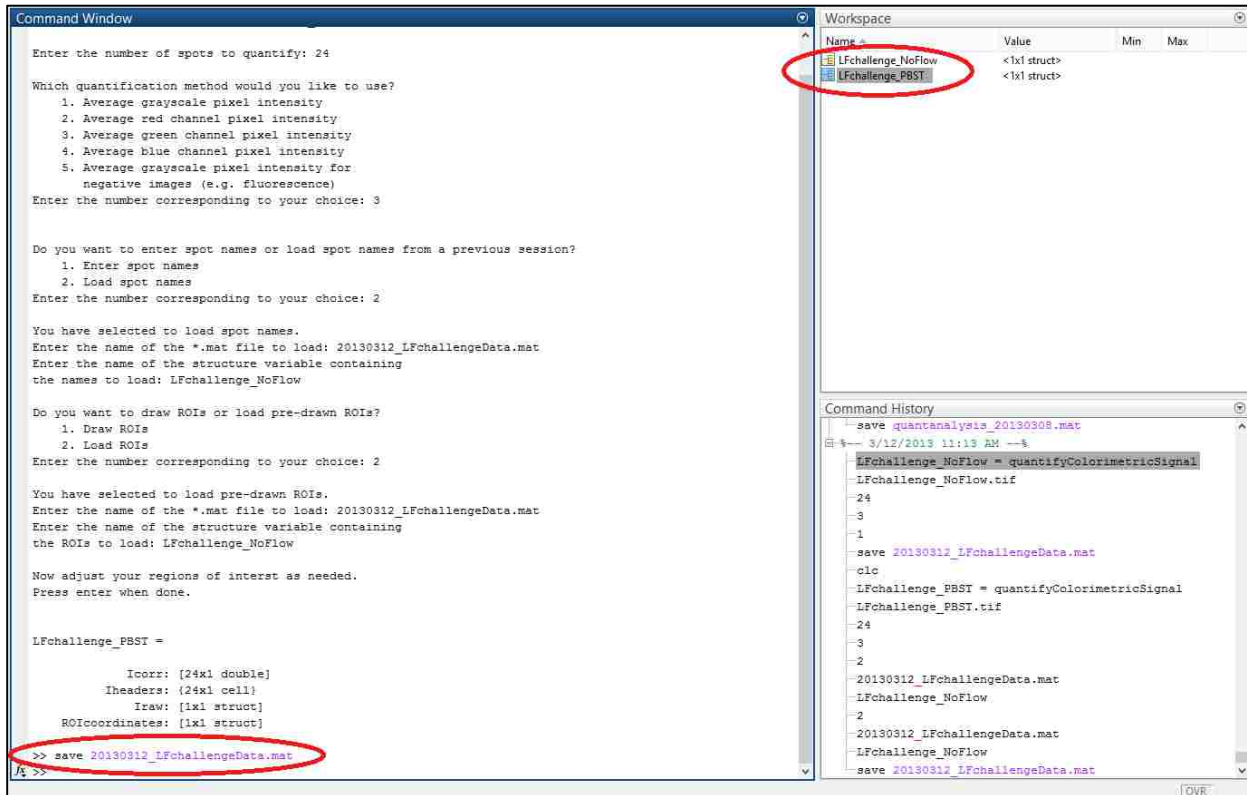
As before, enter the input options when prompted. This time, be sure to select option '2' to load previously used sample names and ROIs for those respective prompts. When prompted, enter the name of the *.mat file (i.e. *myDatasetName.mat*) and structure variable (i.e. *myData*) in which your previous data is stored. Now, when the GUI loads, it will already contain the same sample names and ROIs as used previously, which can save you significant time when performing batch analysis. Note that you can still change the sample names and adjust the ROIs as desired.



Steps 3-11*: Same as above

At this point, you can follow the same steps 3-11, as written above. After quantification is complete, you will have a new variable *myData_Set2* in your workspace. Be sure to re-save your Workspace to save your data. If you are saving under the same *.mat file used previously, ensure that your

previous variables are loaded in your Workspace before you save; otherwise, you will overwrite the *.mat file and will contain only the new variable.



B.2. Code

```
function myData = quantifyColorimetricSignal
```

```

% USAGE: myData = quantifyColorimetricSignal
% RETURNS 'myData' structure variable with four fields:
% 1. Icorr, the background-corrected signal
% 2. Iheaders, the user-entered names corresponding to each test
spot
% 3. Iraw, the raw signal of both the test spots and background
spot(s)
% 4. ROIcoordinates, the coordinates of both the test and background
regions of interest (ROIs)
% Copyright Carly Holstein, University of Washington, 2011
% Last update: 30 October 2013
  
```

```
clear all; close all; clc;
```

```

%-- Declare Global Variables --%
global h; %for handles
global sampleNames;
  
```

```

global approxROI;
global cmap;

%-- Get Initial Info --%
imageName = input('\nEnter the image file name: ','s');

nSamples = input('\nEnter the number of spots to quantify: ','s');
nSamples = str2num(nSamples);

quantOptions = [1,2,3,4,5]; %Change this to reflect available options
fprintf('\n%s','Which quantification method would you like to use?');
fprintf('\n\t%s','1. Average grayscale pixel intensity');
fprintf('\n\t%s','2. Average red channel pixel intensity');
fprintf('\n\t%s','3. Average green channel pixel intensity');
fprintf('\n\t%s','4. Average blue channel pixel intensity');
fprintf('\n\t%s','5. Average grayscale pixel intensity for');
fprintf('\n\t%s\n','   negative images (e.g. fluorescence)');
quantChoice = input('Enter the number corresponding to your choice:
','s');
quantChoice = str2num(quantChoice);
fprintf('\n');
while all(quantChoice~=quantOptions) %Error check
    fprintf('%s','Not a valid selection. ');
    quantChoice = input('\nPlease enter the integer number
corresponding to your choice: ','s');
    quantChoice = str2num(quantChoice);
    fprintf('\n');
end

loadNameOptions = [1,2];
fprintf('\n%s','Do you want to enter spot names or load spot names
from a previous session?');
fprintf('\n\t%s','1. Enter spot names');
fprintf('\n\t%s\n','2. Load spot names');
loadNameChoice = input('Enter the number corresponding to your choice:
','s');
loadNameChoice = str2num(loadNameChoice);
fprintf('\n');
while all(loadNameChoice~=loadNameOptions) %Error check
    fprintf('%s','Not a valid selection. ');
    loadNameChoice = input('\nPlease enter the integer number
corresponding to your choice: ','s');
    loadNameChoice = str2num(loadNameChoice);
    fprintf('\n');
end

if loadNameChoice==2
    %Load sample names
    fprintf('%s\n','You have selected to load spot names. ');
    namesToLoad_matfile = input('Enter the name of the *.mat file to
load: ','s');

```



```

namesToLoad_struct = input('Enter the name of the structure
variable containing\nthe names to load: ','s');
load(namesToLoad_matfile,namesToLoad_struct);
namesToLoad = eval(strcat(namesToLoad_struct, '.Iheaders'));
while(size(namesToLoad,1)~= nSamples) %Error Check
    fprintf('\n%s', 'Not a valid selection. Number of spot names
must equal number of spots entered above');
    namesToLoad_matfile = input('Enter the name of the *.mat file
to load: ','s');
    namesToLoad_struct = input('Enter the name of the structure
variable containing the names to load: ','s');
    load(namesToLoad_matfile,namesToLoad_struct);
    namesToLoad = eval(strcat(namesToLoad_struct, '.Iheaders'));
end
end

ROIOptions = [1,2];
fprintf('\n%s', 'Do you want to draw ROIs or load pre-drawn ROIs?');
fprintf('\n\t%s', '1. Draw ROIs');
fprintf('\n\t%s\n', '2. Load ROIs');
ROIChoice = input('Enter the number corresponding to your choice:
','s');
ROIChoice = str2num(ROIChoice);
fprintf('\n');
while all(ROIChoice~=ROIOptions) %Error check
    fprintf('%s', 'Not a valid selection. ');
    ROIChoice = input('\nPlease enter the integer number corresponding
to your choice: ','s');
    ROIChoice = str2num(ROIChoice);
    fprintf('\n');
end

%- Load Pre-Drawn ROI Information, If Applicable -%
if ROIChoice==2
    %Load ROI data
    fprintf('%s\n', 'You have selected to load pre-drawn ROIs. ');
    ROIsToLoad_matfile = input('Enter the name of the *.mat file to
load: ','s');
    ROIsToLoad_struct = input('Enter the name of the structure
variable containing\nthe ROIs to load: ','s');
    load(ROIsToLoad_matfile,ROIsToLoad_struct);
    ROIsToLoad = eval(strcat(ROIsToLoad_struct, '.ROIcoordinates'));
    while(size(ROIsToLoad.sample,1)~= nSamples) %Error Check
        fprintf('\n%s', 'Not a valid selection. Number of spot ROIs
must equal number of spots entered above');
        ROIsToLoad_matfile = input('Enter the name of the *.mat file
to load: ','s');
        ROIsToLoad_struct = input('Enter the name of the structure
variable containing\nthe ROIs to load: ','s');
        load(ROIsToLoad_matfile,ROIsToLoad_struct);

```

```

        ROIsToLoad =
eval(strcat(ROIsToLoad_struct, '.ROIcoordinates'));
    end
end

%-- Initialize Necessary Variables --%

if loadNameChoice==2
    sampleNames = namesToLoad;
else
    sampleNames = cell(nSamples,1); %for storing names of spots
end

signal_corr = zeros(nSamples,1); %column vec to store final bkgd-
corrected signals

signal_raw.sample = zeros(nSamples,1);

%-- Open Analysis Figure --%
h.fig1 = figure(1);

%- Draw Image -%
h.axes1 = axes('Parent',h.fig1,'Position',[0,0,0.5,1]);
testim = imread(imageName);
[imagesize.ypix imagesize.xpix] = size(testim);
h.im = imshow(testim,'Parent',h.axes1);

%- Draw UI Panel -%
h.uipanel = uipanel('Parent',h.fig1,'Position',[0.5,0,0.5,1]);
cmap = jet(nSamples);
cmapdim = rgb2hsv(cmap);
cmapdim(:,2) = cmapdim(:,2)*0.5;
cmapdim = hsv2rgb(cmapdim);

%Header text for 'Test Spots'
h.SampleTitle = uicontrol('Style','text',...
    'Parent',h.uipanel,...
    'Units','normalized',...
    'Position',[0.1,0.95,0.3,0.05],...
    'String','Test Spots');

%Header test for 'Background Correction'
h.BkgdTtitle = uicontrol('Style','text',...
    'Parent',h.uipanel,...
    'Units','normalized',...
    'Position',[0.6,0.95,0.3,0.05],...
    'String','Background Correction');

```

```

    %Radio buttons for background selection
h.BkgdSelectionButtons = uibuttongroup('Parent',h.uipanel,...
    'Units','normalized',...
    'Position',[0.6,0.8,0.4,0.15],...
    'BorderType','none',...
    'SelectionChangeFcn',@changeBkgdSelection);
h.BkgdButton1 = uicontrol('Style','Radio',...
    'Parent',h.BkgdSelectionButtons,...
    'Units','normalized',...
    'Position',[0,0.67,1,0.33],...
    'String','No background');
h.BkgdButton2 = uicontrol('Style','Radio',...
    'Parent',h.BkgdSelectionButtons,...
    'Units','normalized',...
    'Position',[0,0.33,0.75,0.33],...
    'String','Use common bkgd -->');
h.BkgdButton3 = uicontrol('Style','Radio',...
    'Parent',h.BkgdSelectionButtons,...
    'Units','normalized',...
    'Position',[0,0,1,0.33],...
    'String','Use local bkgds defined by offset:');

    %Push button to draw ROI for background
h.BkgdROIButton = uicontrol('Style','pushbutton',...
    'Parent',h.BkgdSelectionButtons,...
    'Units','normalized',...
    'Position',[0.75,0.33,0.25,0.33],...
    'String','Draw ROI',...
    'BackgroundColor',[1 1 1],...
    'Enable','off',...
    'Callback',{@drawBkgdROI});

h.SampleNameLabel = zeros(nSamples,1);
h.SampleName = zeros(nSamples,1);
% h.SampleROIButton = zeros(nSamples,1); <--- DELETE
h.BkgdCheckbox = zeros(nSamples,1);
h.BkgdVertOSText = zeros(nSamples,1);
h.BkgdHorzOSText = zeros(nSamples,1);
h.BkgdVertOSSlider = zeros(nSamples,1);
h.BkgdHorzOSSlider = zeros(nSamples,1);
h.BkgdVertOSnumbox = zeros(nSamples,1);
h.BkgdHorzOSnumbox = zeros(nSamples,1);
h.BkgdCommonROIrect = [];
for i=1:nSamples
    fldname = sprintf('%s%d','sample',i);
    h.SampleROIrect.(fldname) = [];
    h.BkgdROIrect.(fldname) = [];
end

sampleRowStart = 0.8; %relative height

```

```

sampleRowHeight = sampleRowStart/nSamples;
for i=1:nSamples
    %Label for each sample text box
    h.SampleNameLabel(i) = uicontrol('Style','text',...
        'Parent',h.uipanel,...
        'Units','normalized',...
        'Position',[0.05,sampleRowStart-
i*sampleRowHeight+0.3*sampleRowHeight,0.05,0.4*sampleRowHeight],...
        'String',sprintf('%d%c',i,'.')); %e.g.: '2.'

    %Editable text box for each sample
    if loadNameChoice==2
        currentNameString = sampleNames{i};
    else
        currentNameString = [];
    end
    h.SampleName(i) = uicontrol('Style','edit',...
        'Parent',h.uipanel,...
        'Units','normalized',...
        'Position',[0.1,sampleRowStart-
i*sampleRowHeight+0.1*sampleRowHeight,0.25,0.8*sampleRowHeight],...
        'String',currentNameString,...
        'Callback',{@setNames,i});

    %Push button to draw ROI for each sample
    h.SampleROIButton(i) = uicontrol('Style','pushbutton',...
        'Parent',h.uipanel,...
        'Units','normalized',...
        'Position',[0.35,sampleRowStart-
i*sampleRowHeight+0.1*sampleRowHeight,0.1,0.8*sampleRowHeight],...
        'String','Draw ROI',...
        'BackgroundColor',cmapdim(i,:),...
        'Callback',{@drawSampleROI,i});

    %Label for vertical offset slider
    h.BkgdVertOStext(i) = uicontrol('Style','text',...
        'Parent',h.uipanel,...
        'Units','normalized',...
        'Position',[0.6,sampleRowStart-
i*sampleRowHeight+0.6*sampleRowHeight,0.05,0.2*sampleRowHeight],...
        'String','V: ');

    %Label for horizontal offset slider
    h.BkgdHorzOStext(i) = uicontrol('Style','text',...
        'Parent',h.uipanel,...
        'Units','normalized',...
        'Position',[0.6,sampleRowStart-
i*sampleRowHeight+0.2*sampleRowHeight,0.05,0.2*sampleRowHeight],...
        'String','H: ');

    %Slider for vertical offset of background ROI

```

```

maxvalvert = round(0.3*imagesize.ypix);
minvalvert = round(-0.3*imagesize.ypix);
rangevert = maxvalvert - minvalvert;
h.BkgdVertOSslider(i) = uicontrol('Style','slider',...
    'Parent',h.uipanel,...
    'Units','normalized',...
    'Position',[0.65,sampleRowStart-
i*sampleRowHeight+0.5*sampleRowHeight,0.2,0.4*sampleRowHeight],...
    'Max',maxvalvert,...
    'Min',minvalvert,...
    'Value',0,...
    'SliderStep',[1/rangevert 10/rangevert],...
    'Enable','off',...
    'Callback',{@setVertOSslider,i});

    %Slider for horizontal offset of background ROI
maxvalhorz = round(0.3*imagesize.xpix);
minvalhorz = round(-0.3*imagesize.xpix);
rangehorz = maxvalhorz - minvalhorz;
h.BkgdHorzOSslider(i) = uicontrol('Style','slider',...
    'Parent',h.uipanel,...
    'Units','normalized',...
    'Position',[0.65,sampleRowStart-
i*sampleRowHeight+0.1*sampleRowHeight,0.2,0.4*sampleRowHeight],...
    'Max',maxvalhorz,...
    'Min',minvalhorz,...
    'Value',0,...
    'SliderStep',[1/rangehorz 10/rangehorz],...
    'Enable','off',...
    'Callback',{@setHorzOSslider,i});

    %Editable textbox for vertical offset of background ROI
h.BkgdVertOSnumbox(i) = uicontrol('Style','edit',...
    'Parent',h.uipanel,...
    'Units','normalized',...
    'Position',[0.85,sampleRowStart-
i*sampleRowHeight+0.5*sampleRowHeight,0.1,0.4*sampleRowHeight],...
    'String','0',...
    'Enable','off',...
    'Callback',{@setVertOSbox,i});

    %Editable textbox for horizontal offset of background ROI
h.BkgdHorzOSnumbox(i) = uicontrol('Style','edit',...
    'Parent',h.uipanel,...
    'Units','normalized',...
    'Position',[0.85,sampleRowStart-
i*sampleRowHeight+0.1*sampleRowHeight,0.1,0.4*sampleRowHeight],...
    'String','0',...
    'Enable','off',...
    'Callback',{@setHorzOSbox,i});
end

```

```

%- Load Pre-Drawn ROIs, If Applicable -%
if ROIChoice==2
    %Draw sample ROIs and set GUI items accordingly
    for i=1:nSamples
        loadSampleROI(i,ROIsToLoad.sample(i,:));
    end

    %Draw background ROIs and set GUI items accordingly
    if ischar(ROIsToLoad.bkgd) %i.e. 'No background correction used'
        %no no bkgd
        set(h.BkgdSelectionButtons,'SelectedObject',h.BkgdButton1);
    elseif size(ROIsToLoad.bkgd,1)==1
        %set common bkgd
        set(h.BkgdSelectionButtons,'SelectedObject',h.BkgdButton2);
        loadBkgdROI(ROIsToLoad.bkgd);
    else
        %set local bkgds
        set(h.BkgdSelectionButtons,'SelectedObject',h.BkgdButton3);
        for i=1:nSamples

loadLocalBkgdROI(i,ROIsToLoad.bkgd(i,:),ROIsToLoad.sample(i,:));
            end
        end

        %Prompt user
        input('\nNow adjust your regions of interest as needed. \nPress
enter when done.\n');
    else
        %Prompt user
        input('\nNow draw your regions of interest. \nPress enter when
done.\n');
    end

%-- Get ROI Dimensions --%
approxROI.sample = zeros(nSamples,4); %one row per sample, 4 cols for
ROI: x-pos,y-pos,width,height
approxROI.headers = {'x-pos','y-pos','width','height'};
bkgdChoice = get(h.BkgdSelectionButtons,'SelectedObject'); %handle for
selected background option

switch bkgdChoice
    case h.BkgdButton3 %Local background for each sample ROI
        %initialize
        approxROI.bkgd = zeros(nSamples,4); %one row per sample, 4
cols for ROI: x-pos,y-pos,width,height
        signal_raw.bkgd = zeros(nSamples,1);
        %will fill in values in loop below

    case h.BkgdButton2 %Common background for all sample ROIs

```

```

        approxROI.bkgd = getPosition(h.BkgdCommonROIrect); %4 cols for
ROI: x-pos,y-pos,width,height
        signal_raw.bkgd = zeros(1,1);

        otherwise %No background used
            approxROI.bkgd = 'No background correction used';
            signal_raw.bkgd = [];
end

for i=1:nSamples
    fldname = sprintf('%s%d', 'sample', i);
    approxROI.sample(i,:) = getPosition(h.SampleROIrect.(fldname));

    if bkgdChoice == h.BkgdButton3 %Local bkgds
        approxROI.bkgd(i,:) = getPosition(h.BkgdROIrect.(fldname));
    end
end

%-- Calculate Background-Corrected Signal, Icorr --%
for i=1:nSamples

    %Get sample ROI
    xpos = round(approxROI.sample(i,1));
    ypos = round(approxROI.sample(i,2));
    wd    = round(approxROI.sample(i,3));
    ht    = round(approxROI.sample(i,4));
    ROI_sample = testim(ypos:ypos+ht,xpos:xpos+wd,:);

    %Get background ROI
    switch bkgdChoice
        case h.BkgdButton3 %Local background for each sample ROI
            xpos = round(approxROI.bkgd(i,1));
            ypos = round(approxROI.bkgd(i,2));
            wd    = round(approxROI.bkgd(i,3));
            ht    = round(approxROI.bkgd(i,4));
            ROI_bkgd = testim(ypos:ypos+ht,xpos:xpos+wd,:);

        case h.BkgdButton2 %Common background for all sample ROIs
            xpos = round(approxROI.bkgd(1));
            ypos = round(approxROI.bkgd(2));
            wd    = round(approxROI.bkgd(3));
            ht    = round(approxROI.bkgd(4));
            ROI_bkgd = testim(ypos:ypos+ht,xpos:xpos+wd,:);

        otherwise
            %No background; normalize to max pixel value for file type
            ROI_bkgd = [];
    end

    %Call quantification algorithm

```

```

        %Assign handle to desired quantification function
switch quantChoice
    case 1
        calculateSignal = @calcAvgGrayPixIntensity; %average
grayscale intensity
    case 2
        calculateSignal = @calcAvgRPixIntensity; %average red
channel intensity
    case 3
        calculateSignal = @calcAvgGPixIntensity; %average green
channel intensity
    case 4
        calculateSignal = @calcAvgBPixIntensity; %average blue
channel intensity
    case 5
        calculateSignal = @calcAvgNegGrayPixIntensity; %average
grayscale intensity for negative image
end

    %Determine format of output
if bkgdChoice == h.BkgdButton1 %no background ROI
    [signal_corr(i),signal_raw.sample(i)] =
calculateSignal(ROI_sample,ROI_bkgd);
else
    [signal_corr(i),signal_raw.sample(i),signal_raw.bkgd(i)] =
calculateSignal(ROI_sample,ROI_bkgd);
end

end

%-- Return Vars --%

    %Note: all variables now returned automacially as fields of the
output structure
    %Icorr = signal_corr; %background-corrected signal
    %Iheaders = sampleNames; %user-entered names for each test spot
    %Iraw = signal_raw; %contains uncorrected sample and bkgd signals
    %ROIcoordinates = approxROI %contails sample and bkgd ROIs

myData.Icorr = signal_corr;
myData.Iheaders = sampleNames;
myData.Iraw = signal_raw;
myData.ROIcoordinates = approxROI;

end %end main function

%----- SUBFUNCTIONS -----%

```



```

function [Icorr, varargout] =
calcAvgGrayPixIntensity(sampleROI,bkgdROI)
% This function is an option for the signal quantification algorithm.
It
% simply calculates the average grayscale pixel intensity of the ROI
% selected by the user and performs a background correction.
%
% USAGE: [Icorr, (Iraw.sample), (Iraw.bkgd)] =
calcAvgGrayPixIntensity(sampleROI,bkgdROI)

%Calculate raw sample intensities
Iraw.sample = mean(mean(rgb2gray(sampleROI)));

%Calculate raw bkgd intensities, or get max pixel value
if isempty(bkgdROI)==0 %if bkgd ROI given
    Iraw.bkgd = mean(mean(rgb2gray(bkgdROI)));
else %no background correction - normalize to max pixel value
    imageclass = class(sampleROI);
    Iraw.bkgd = double(intmax(imageclass));
end

%Calculate normalized intensity
Idark = 0;
Icorr = (Iraw.sample - Iraw.bkgd)/(Idark - Iraw.bkgd);

%Return vars
if nargout > 1
    varargout{1} = Iraw.sample;

    if nargout > 2
        if isempty(bkgdROI)==0 %if bkgd provided
            varargout{2} = Iraw.bkgd;
        else
            varargout{2} = [];
        end
    end
end
end

function [Icorr, varargout] = calcAvgRPixIntensity(sampleROI,bkgdROI)
% This function is an option for the signal quantification algorithm.
It
% simply calculates the average red channel pixel intensity of the ROI
% selected by the user and performs a background correction.
%
% USAGE: [Icorr, (Iraw.sample), (Iraw.bkgd)] =
calcAvgRPixIntensity(sampleROI,bkgdROI)

%Calculate raw sample intensities
Iraw.sample = mean(mean(sampleROI(:, :, 1)));

```

```

%Calculate raw bkgd intensities, or get max pixel value
if isempty(bkgdROI)==0 %if bkgd ROI given
    Iraw.bkgd = mean(mean(bkgdROI(:, :, 1)));
else %no background correction - normalize to max pixel value
    imageclass = class(sampleROI);
    Iraw.bkgd = double(intmax(imageclass));
end

%Calculate normalized intensity
Idark = 0;
Icorr = (Iraw.sample - Iraw.bkgd)/(Idark - Iraw.bkgd);

%Return vars
if nargout > 1
    varargout{1} = Iraw.sample;

    if nargout > 2
        if isempty(bkgdROI)==0 %if bkgd provided
            varargout{2} = Iraw.bkgd;
        else
            varargout{2} = [];
        end
    end
end
end

end

function [Icorr, varargout] = calcAvgGPixIntensity(sampleROI,bkgdROI)
% This function is an option for the signal quantification algorithm.
It
% simply calculates the average green channel pixel intensity of the
ROI
% selected by the user and performs a background correction.
%
% USAGE: [Icorr, (Iraw.sample), (Iraw.bkgd)] =
calcAvgGPixIntensity(sampleROI,bkgdROI)

%Calculate raw sample intensities
Iraw.sample = mean(mean(sampleROI(:, :, 2)));

%Calculate raw bkgd intensities, or get max pixel value
if isempty(bkgdROI)==0 %if bkgd ROI given
    Iraw.bkgd = mean(mean(bkgdROI(:, :, 2)));
else %no background correction - normalize to max pixel value
    imageclass = class(sampleROI);
    Iraw.bkgd = double(intmax(imageclass));
end

%Calculate normalized intensity
Idark = 0;

```

```

Icorr = (Iraw.sample - Iraw.bkgd)/(Idark - Iraw.bkgd);

%Return vars
if nargout > 1
    varargout{1} = Iraw.sample;

    if nargout > 2
        if isempty(bkgdROI)==0 %if bkgd provided
            varargout{2} = Iraw.bkgd;
        else
            varargout{2} = [];
        end
    end
end
end

end

function [Icorr, varargout] = calcAvgBPixIntensity(sampleROI,bkgdROI)
% This function is an option for the signal quantification algorithm.
It
% simply calculates the average blue channel pixel intensity of the
ROI
% selected by the user and performs a background correction.
%
% USAGE: [Icorr, (Iraw.sample), (Iraw.bkgd)] =
calcAvgBPixIntensity(sampleROI,bkgdROI)

%Calculate raw sample intensities
Iraw.sample = mean(mean(sampleROI(:, :, 3)));

%Calculate raw bkgd intensities, or get max pixel value
if isempty(bkgdROI)==0 %if bkgd ROI given
    Iraw.bkgd = mean(mean(bkgdROI(:, :, 3)));
else %no background correction - normalize to max pixel value
    imageclass = class(sampleROI);
    Iraw.bkgd = double(intmax(imageclass));
end

%Calculate normalized intensity
Idark = 0;
Icorr = (Iraw.sample - Iraw.bkgd)/(Idark - Iraw.bkgd);

%Return vars
if nargout > 1
    varargout{1} = Iraw.sample;

    if nargout > 2
        if isempty(bkgdROI)==0 %if bkgd provided
            varargout{2} = Iraw.bkgd;
        else
            varargout{2} = [];
        end
    end
end
end

```

```

        end
    end
end

end

function [Icorr, varargout] =
calcAvgNegGrayPixIntensity(sampleROI,bkgdROI)
% This function is an option for the signal quantification algorithm.
% It
% simply calculates the average grayscale pixel intensity for a
% negative
% image of the ROI selected by the user and performs a background
% correction.
%
% USAGE: [Icorr, (Iraw.sample), (Iraw.bkgd)] =
calcAvgNegGrayPixIntensity(sampleROI,bkgdROI)

    %Calculate raw sample intensities
    Iraw.sample = mean(mean(rgb2gray(sampleROI)));

    %Calculate raw bkgd intensities, or use dark pixel value
    if isempty(bkgdROI)==0 %if bkgd ROI given
        Iraw.bkgd = mean(mean(rgb2gray(bkgdROI)));
    else %no background correction - normalize to black pixel value
        Iraw.bkgd = 0;
    end

    %Get max pixel value corresponding to brightest signal possible
    (white)
    imageclass = class(sampleROI);
    Ibright = double(intmax(imageclass));

    %Calculate normalized intensity
    Icorr = (Iraw.sample - Iraw.bkgd)/(Ibright - Iraw.bkgd);

    %Return vars
    if nargout > 1
        varargout{1} = Iraw.sample;

        if nargout > 2
            if isempty(bkgdROI)==0 %if bkgd provided
                varargout{2} = Iraw.bkgd;
            else
                varargout{2} = [];
            end
        end
    end
end
end
end

```

```

function setNames(hObj,event,i)
% Called when user enters sample concentration ('name') values
    global sampleNames;
    sampleNames{i} = get(hObj,'String'); %name for given test spot
end

function loadSampleROI(i,coords)
% Called when user chooses to load pre-drawn ROIs
    global h;
    global cmap;

    fldname = sprintf('%s%d','sample',i);
    if isempty(h.SampleROIRect.(fldname))==0 %if there already is a
rect, clear it first
        delete(h.SampleROIRect.(fldname));
        h.SampleROIRect.(fldname) = [];
    end

    xpos = coords(1);
    ypos = coords(2);
    wd = coords(3);
    ht = coords(4);

    %If local bkgds enabled, enable textboxes and sliders for defining
bkgd offsets
    if strcmp(get(h.BkgdSelectionButtons,'SelectedObject'),'Use local
bkgds defined by offset:') == 1
        set(h.BkgdVertOSnumbox(i),'Enable','on');
        set(h.BkgdVertOSSlider(i),'Enable','on');
        set(h.BkgdHorzOSnumbox(i),'Enable','on');
        set(h.BkgdHorzOSSlider(i),'Enable','on');
    end

    h.SampleROIRect.(fldname) = imrect(h.axes1,[xpos ypos wd ht]);
%make new rect
    setColor(h.SampleROIRect.(fldname),cmap(i,:))

end

function loadBkgdROI(coords)
% Called when user chooses to load a pre-drawn common background ROI
    global h;

    if isempty(h.BkgdCommonROIrect)==0 %if there already is a rect,
clear it first
        delete(h.BkgdCommonROIrect);
        h.BkgdROIrect = [];
    end

    %Update GUI Selections
    %enable bkgd ROI button:

```

```

set(h.BkgdROIButton, 'Enable', 'on');

for i=1:n
    %disable bkgd text boxes and sliders
    set(h.BkgdVertOSnumbox(i), 'Enable', 'off');
    set(h.BkgdVertOSSlider(i), 'Enable', 'off');
    set(h.BkgdHorzOSnumbox(i), 'Enable', 'off');
    set(h.BkgdHorzOSSlider(i), 'Enable', 'off');

    %delete bkgd ROIs, if they exist
    fldname = sprintf('%s%d', 'sample', i);
    if isempty(h.BkgdROIrect.(fldname))==0 %if there is a rect
        delete(h.BkgdROIrect.(fldname));
        h.BkgdROIrect.(fldname) = [];
    end
end

%Draw ROI
xpos = coords(1);
ypos = coords(2);
wd = coords(3);
ht = coords(4);

h.BkgdCommonROIrect = imrect(h.axes1, [xpos ypos wd ht]); %make new
rect
setColor(h.BkgdCommonROIrect, [0 0 0]); %black

end

function loadLocalBkgdROI(i, bkgdcoords, samplecoords)
% Called when user chooses to load pre-drawn local background ROIs
global h;
global cmap;

cmapdark = rgb2hsv(cmap);
cmapdark(:,3) = cmapdark(:,3)*0.5;
cmapdark = hsv2rgb(cmapdark);
fldname = sprintf('%s%d', 'sample', i);

%get background and sample ROI coordinates for comparison
xpos_bkgd = bkgdcoords(1);
ypos_bkgd = bkgdcoords(2);
wd_bkgd = bkgdcoords(3);
ht_bkgd = bkgdcoords(4);
xpos_sample = samplecoords(1);
ypos_sample = samplecoords(2);
vertOffset = ypos_bkgd - ypos_sample;
horzOffset = xpos_bkgd - xpos_sample;

%enable sliders
set(h.BkgdVertOSSlider(i), 'Enable', 'on');

```

```

set(h.BkgdHorzOSSlider(i), 'Enable', 'on');
set(h.BkgdVertOSSlider(i), 'Value', vertOffset);
set(h.BkgdHorzOSSlider(i), 'Value', horzOffset);

%enable textboxes
set(h.BkgdVertOSnumbox(i), 'Enable', 'on');
set(h.BkgdHorzOSnumbox(i), 'Enable', 'on');
set(h.BkgdVertOSnumbox(i), 'String', num2str(vertOffset));
set(h.BkgdHorzOSnumbox(i), 'String', num2str(horzOffset));

%draw rectangle
h.BkgdROIrect.(fldname) = imrect(h.axes1,[xpos_bkgd ypos_bkgd
wd_bkgd ht_bkgd]); %make new rect
setColor(h.BkgdROIrect.(fldname), cmapdark(i, :));
setResizable(h.BkgdROIrect.(fldname), 0); %not resizable

end

function drawSampleROI(hObj, event, i)
% Called when user pushes button to draw an approximate ROI
global h;
global cmap;

fldname = sprintf('%s%d', 'sample', i);
if isempty(h.SampleROIrect.(fldname))==0 %if there already is a
rect, clear it first
delete(h.SampleROIrect.(fldname));
h.SampleROIrect.(fldname) = [];
end

if isempty(h.SampleROIrect.sample1)==0 %if 1st rectangle exists
already, make other rects the same size
rect1pos = getPosition(h.SampleROIrect.sample1);
xpos = 100;
ypos = 100;
wd = rect1pos(3);
ht = rect1pos(4);
else %otherwise use arbitrary size and position
xpos = 100;
ypos = 100;
wd = 100;
ht = 100;
end

%If local bkgds enabled, enable textboxes and sliders for defining
bkgd offsets
if strcmp(get(h.BkgdSelectionButtons, 'SelectedObject'), 'Use local
bkgds defined by offset:') == 1
set(h.BkgdVertOSnumbox(i), 'Enable', 'on');
set(h.BkgdVertOSSlider(i), 'Enable', 'on');
set(h.BkgdHorzOSnumbox(i), 'Enable', 'on');

```

```

        set(h.BkgdHorzOSSlider(i), 'Enable', 'on');
    end

    h.SampleROIRect.(fldname) = imrect(h.axes1,[xpos ypos wd ht]);
    %make new rect
    setColor(h.SampleROIRect.(fldname), cmap(i,:))

end

function drawBkgdROI(hObj,event)
% Called when user pushes button to draw common background ROI
    global h;

    if isempty(h.BkgdCommonROIRect)==0 %if there already is a rect,
clear it first
        delete(h.BkgdCommonROIRect);
        h.BkgdROIRect = [];
    end

    if isempty(h.SampleROIRect.sample1)==0 %if 1st sample rectangle
exists already, make bkgd rect the same size
        rectlpos = getPosition(h.SampleROIRect.sample1);
        wd = rectlpos(3);
        ht = rectlpos(4);
    else %otherwise use arbitrary size
        wd = 100;
        ht = 100;
    end

    h.BkgdCommonROIRect = imrect(h.axes1,[100 100 wd ht]); %make new
rect
    setColor(h.BkgdCommonROIRect,[0 0 0]); %black

end

function changeBkgdSelection(hObj,event)
% Called when user changes radio button selection for background type
% 'event' contains fields:
% - 'EventName', 'SelectionChanged'
% - 'OldValue', handle of previous object selected
% - 'NewValue', handle of currently selected object

    global h;
    n = length(h.BkgdCheckbox);

    if event.NewValue == h.BkgdButton1 %No background
        %disable bkgd ROI button:
        set(h.BkgdROIButton, 'Enable', 'off');
    end

```



```

%delete common bkgd ROI, if it exists
if isempty(h.BkgdCommonROIrect)==0 %if there is a rect
    delete(h.BkgdCommonROIrect);
    h.BkgdROIrect = [];
end

for i=1:n
    %delete bkgd ROIs, if they exist
    fldname = sprintf('%s%d','sample',i);
    if isempty(h.BkgdROIrect.(fldname))==0 %if there is a rect
        delete(h.BkgdROIrect.(fldname));
        h.BkgdROIrect.(fldname) = [];
    end

    %disable bkgd text boxes and sliders
    set(h.BkgdVertOSnumbox(i),'Enable','off');
    set(h.BkgdVertOSSlider(i),'Enable','off');
    set(h.BkgdHorzOSnumbox(i),'Enable','off');
    set(h.BkgdHorzOSSlider(i),'Enable','off');
end
end

if event.NewValue == h.BkgdButton2 %Use common background
    %enable bkgd ROI button:
    set(h.BkgdROIbutton,'Enable','on');

    for i=1:n
        %delete bkgd ROIs, if they exist
        fldname = sprintf('%s%d','sample',i);
        if isempty(h.BkgdROIrect.(fldname))==0 %if there is a rect
            delete(h.BkgdROIrect.(fldname));
            h.BkgdROIrect.(fldname) = [];
        end

        %disable bkgd text boxes and sliders
        set(h.BkgdVertOSnumbox(i),'Enable','off');
        set(h.BkgdVertOSSlider(i),'Enable','off');
        set(h.BkgdHorzOSnumbox(i),'Enable','off');
        set(h.BkgdHorzOSSlider(i),'Enable','off');
    end
end

if event.NewValue == h.BkgdButton3 %Use local backgrounds
    %disable bkgd ROI button:
    set(h.BkgdROIbutton,'Enable','off');

    %delete common bkgd ROI, if it exists
    if isempty(h.BkgdCommonROIrect)==0 %if there is a rect
        delete(h.BkgdCommonROIrect);
        h.BkgdROIrect = [];
    end
end

```

```

    %Draw background ROIs and enable sliders and text boxes if
sample ROI already exists
    global h;
    global cmap;

    cmapdark = rgb2hsv(cmap);
    cmapdark(:,3) = cmapdark(:,3)*0.5;
    cmapdark = hsv2rgb(cmapdark);

    for i=1:n
        fldname = sprintf('%s%d','sample',i);

        if isempty(h.SampleROIrect.(fldname))==0 %if sample rect
exists
            %enable offset text and sliders
            set(h.BkgdVertOSnumbox(i),'Enable','on');
            set(h.BkgdVertOSSlider(i),'Enable','on');
            set(h.BkgdHorzOSnumbox(i),'Enable','on');
            set(h.BkgdHorzOSSlider(i),'Enable','on');
            set(h.BkgdVertOSSlider(i),'Value',0);
            set(h.BkgdHorzOSSlider(i),'Value',0);
            set(h.BkgdVertOSnumbox(i),'String','0');
            set(h.BkgdHorzOSnumbox(i),'String','0');

            %draw rectangles
            rectpos = getPosition(h.SampleROIrect.(fldname));
%make same size as sample rect
            xp = rectpos(1);
            yp = rectpos(2);
            wd = rectpos(3);
            ht = rectpos(4);
            h.BkgdROIrect.(fldname) = imrect(h.axes1,[xp yp wd
ht]); %make new rect
            setColor(h.BkgdROIrect.(fldname),cmapdark(i,:));
            setResizable(h.BkgdROIrect.(fldname),0); %not
resizeable
        else
            %draw rectangles of arbitrary size if sample rect
doesn not exist
            xp = 100;
            yp = 100;
            wd = 100;
            ht = 100;
            h.BkgdROIrect.(fldname) = imrect(h.axes1,[xp yp wd
ht]); %make new rect
            setColor(h.BkgdROIrect.(fldname),cmapdark(i,:));
            setResizable(h.BkgdROIrect.(fldname),0); %not
resizeable
        end
    end
end

```

```

    end

end

function setVertOSslider(hObj,event,i)
% Called when vertical offset of background ROI is changed by slider
global h;

%get value
vertOSvalue = get(hObj,'Value');

%update textbox value
set(h.BkgdVertOSnumbox(i),'String',num2str(vertOSvalue));

%get horizontal offset for reference
horzOSvalue = get(h.BkgdHorzOSslider(i),'Value');

%adjust background ROI position
fldname = sprintf('%s%d','sample',i);
ROIpos = getPosition(h.SampleROIrect.(fldname)); %sample ROI
position
xp = ROIpos(1)+horzOSvalue;
yp = ROIpos(2)+vertOSvalue;
wd = ROIpos(3);
ht = ROIpos(4);
setPosition(h.BkgdROIrect.(fldname),[xp yp wd ht]);

end

function setHorzOSslider(hObj,event,i)
% Called when horizontal offset of background ROI is changed by slider
global h;

%get value
horzOSvalue = get(hObj,'Value');

%update textbox value
set(h.BkgdHorzOSnumbox(i),'String',num2str(horzOSvalue));

%get vertical offset for reference
vertOSvalue = get(h.BkgdVertOSslider(i),'Value');

%adjust background ROI position
fldname = sprintf('%s%d','sample',i);
ROIpos = getPosition(h.SampleROIrect.(fldname)); %sample ROI
position
xp = ROIpos(1)+horzOSvalue;
yp = ROIpos(2)+vertOSvalue;

```

```

    wd = ROIpos(3);
    ht = ROIpos(4);
    setPosition(h.BkgdROIrect.(fldname), [xp yp wd ht]);

end

function setVertOSbox(hObj,event,i)
% Called when vertical offset of background ROI is changed by textbox
    global h;

    %get value
    vertOSvalue = str2num(get(hObj,'String'));

    %update slider value
    set(h.BkgdVertOSslider(i), 'Value', vertOSvalue);

    %get horizontal offset for reference
    horzOSvalue = get(h.BkgdHorzOSslider(i), 'Value');

    %adjust background ROI position
    fldname = sprintf('%s%d', 'sample', i);
    ROIpos = getPosition(h.SampleROIrect.(fldname)); %sample ROI
position
    xp = ROIpos(1)+horzOSvalue;
    yp = ROIpos(2)+vertOSvalue;
    wd = ROIpos(3);
    ht = ROIpos(4);
    setPosition(h.BkgdROIrect.(fldname), [xp yp wd ht]);

end

function setHorzOSbox(hObj,event,i)
% Called when horizontal offset of background ROI is changed by
textbox
    global h;

    %get value
    horzOSvalue = str2num(get(hObj,'String'));

    %update slider value
    set(h.BkgdHorzOSslider(i), 'Value', horzOSvalue);

    %get vertical offset for reference
    vertOSvalue = get(h.BkgdVertOSslider(i), 'Value');

    %adjust background ROI position
    fldname = sprintf('%s%d', 'sample', i);

```

```
ROIpos = getPosition(h.SampleROIrect.(fldname)); %sample ROI
position
xp = ROIpos(1)+horzOSvalue;
yp = ROIpos(2)+vertOSvalue;
wd = ROIpos(3);
ht = ROIpos(4);
setPosition(h.BkgdROIrect.(fldname),[xp yp wd ht]);

end
```

Appendix C: MATLAB Program *analyzeProteinSpots.m*

C.1. Description

The MATLAB program *analyzeProteinSpots.m* is used to quantify both the size and intensity of circular proteins spots, primarily for analyzing protein adsorption. The size of the protein spot and its relative pixel intensity reflect the speed and robustness of adsorption, respectively.

I built the algorithm as a MATLAB script called *analyzeProteinSpots.m*. I based the graphical user interface (GUI) and basic region-of-interest (ROI) on my previously developed MATLAB script for quantifying pixel intensity in rectangular ROIs (i.e. for test lines), *quantifyColorimetricSignal.m*. Here, we instead wanted to quantify protein spots, which are typically elliptical in shape. I therefore adapted edge-finding and ellipse-detection algorithms developed by others to automatically identify and quantify the protein spot in each ROI. The ROIs, however, are still drawn manually (with some automated help to ensure equally sized ROIs) in order to maximize the flexibility of the program for different sizes and arrangements of ROIs. The six steps performed by my program are summarized in the table below.

#	Step
1	Draw box around region of interest (approximate)
2	Convert ROI to one-channel (or grayscale) image
3	Find edges based on derivative of pixel intensity (built-in function in MATLAB, using 'Prewitt' method)
4	Fit edges with ellipse (by least squares; MATLAB user-provided function)
5	Return size of ellipse
6	Calculate average pixel intensity inside ellipse

The protein spot analysis program is illustrated below with a set of three example protein spots: BSA spotted at 5 mg/mL, 2.5 mg/mL, and 0.5 mg/mL.

Step 1, the user-defined selection of ROIs in the GUI, is shown in below.

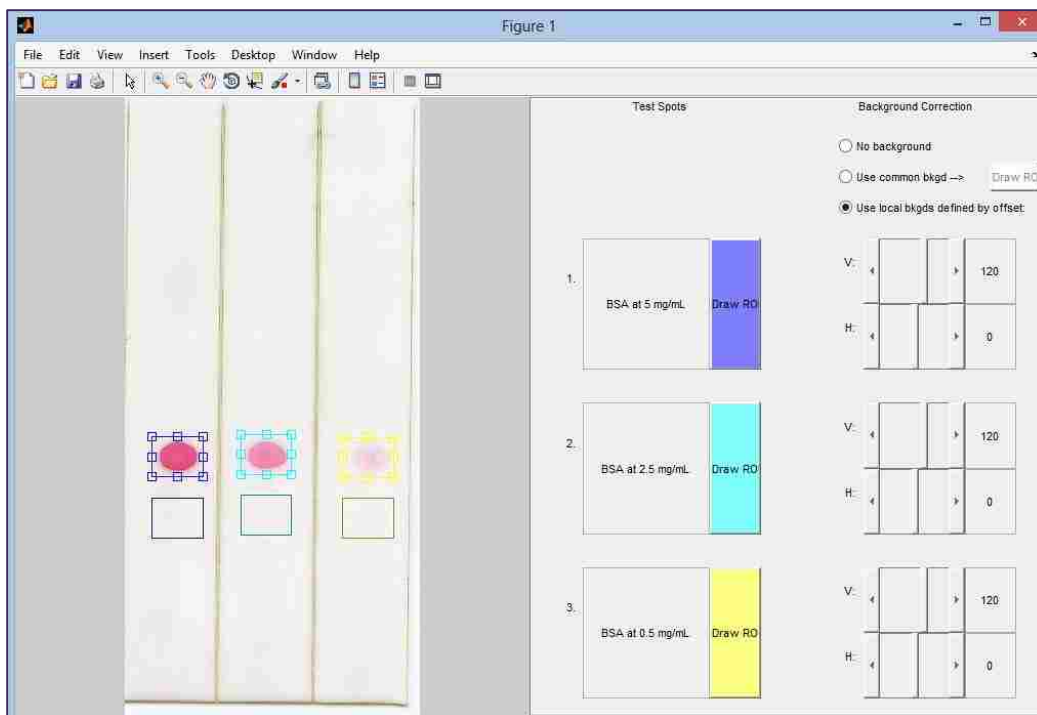


Image of the GUI being used to select the ROIs for each of the three spots tested.

Steps 2-4 are illustrated in the figure below, which includes a comparison of the original spots the green-channel-only versions of the spots, overlaid with the results of the edge detection (blue circles) and ellipse of best fit (green line). This ellipse of best fit is used to determine the size of the spot (area of the ellipse).

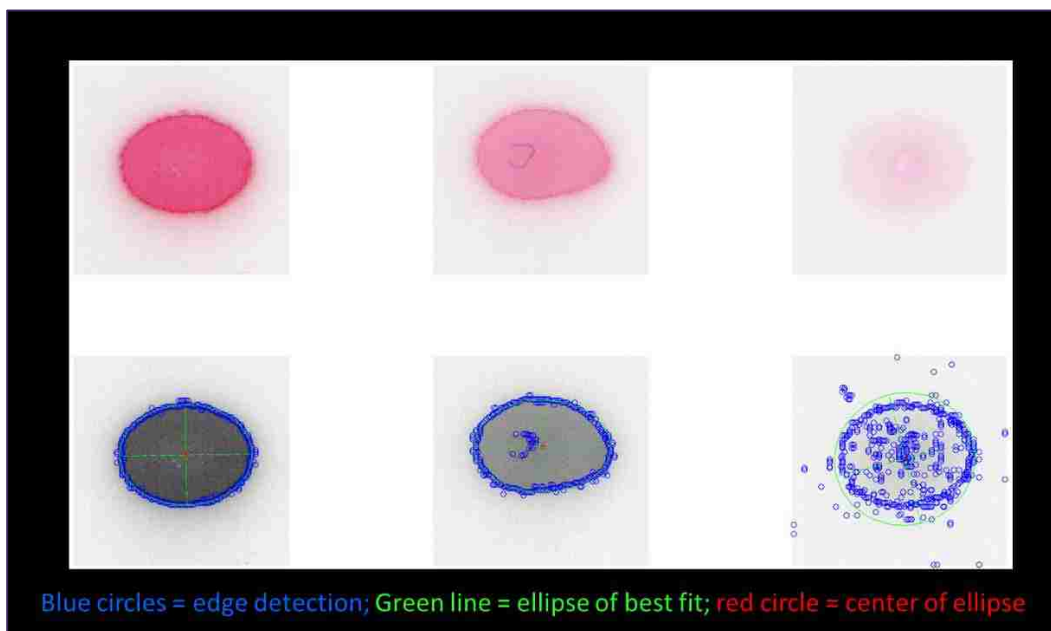


Illustration of the edge-detection and ellipse-fitting portions of the algorithm, performed on the green-channel versions of the protein spot images.

Finally, in order to calculate the average pixel intensity inside the ellipse, we need to create a mask or binary version of the ellipse to determine which pixels are inside and which are outside the ellipse. This mask is shown in the figure below, in addition to the previous steps already highlighted in detail.

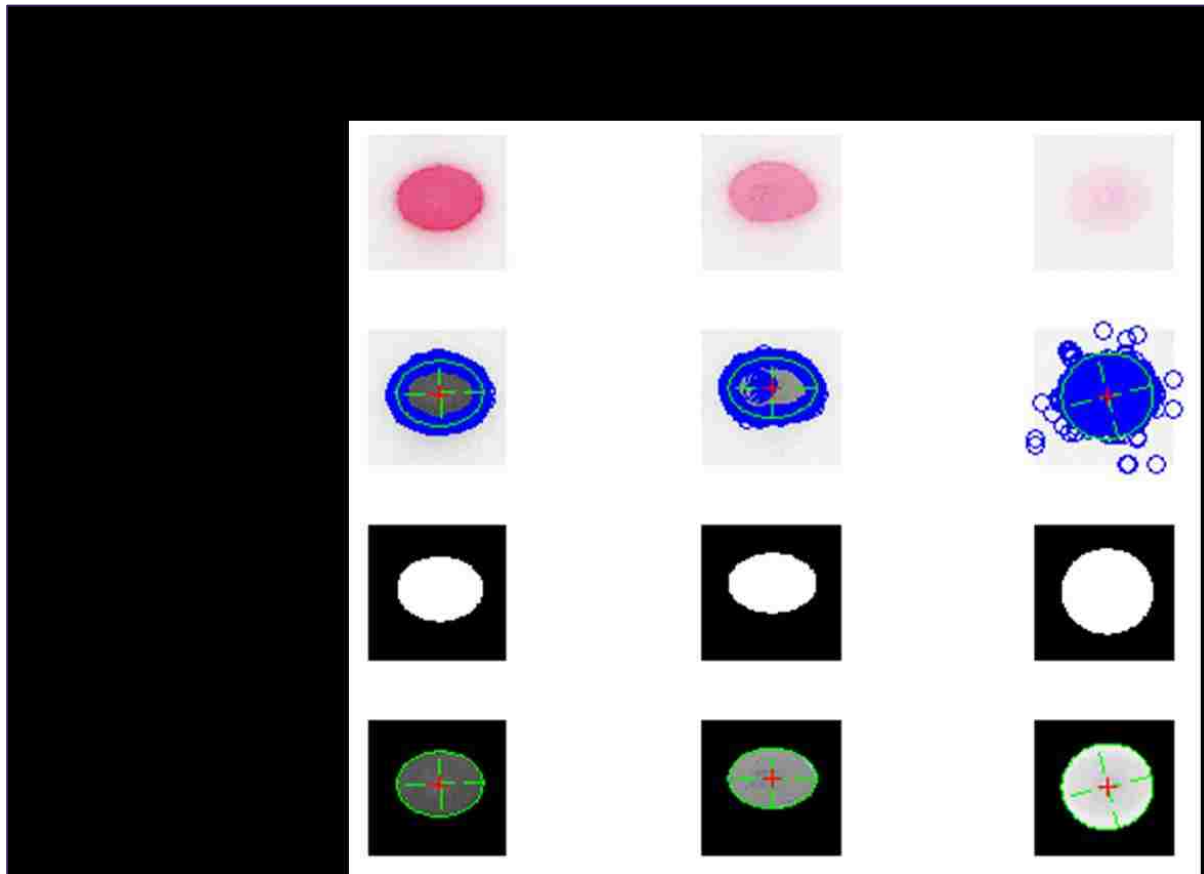
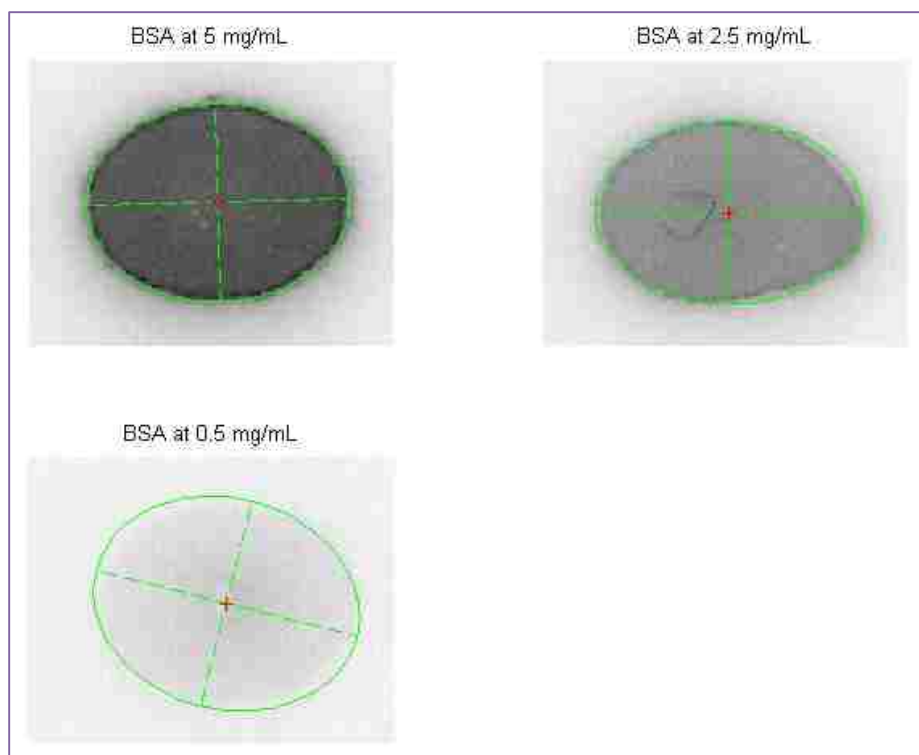


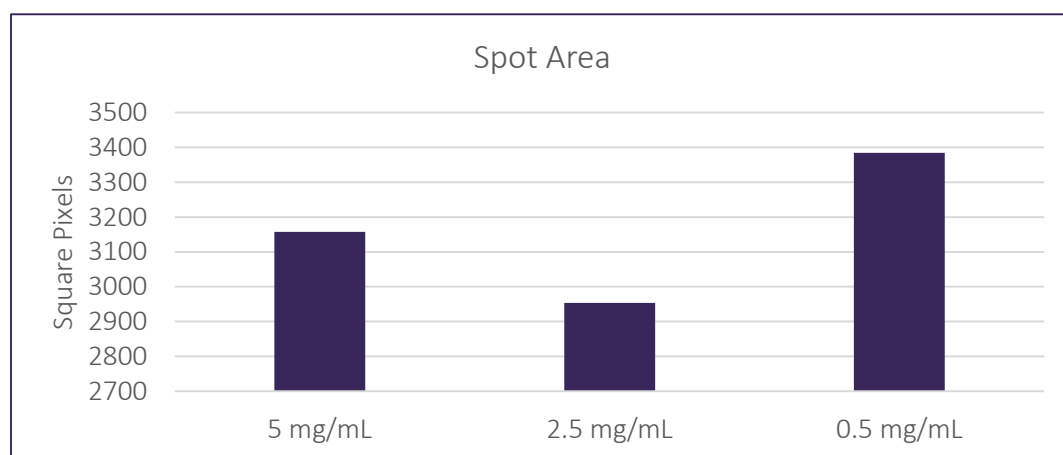
Illustration of the ellipse mask creation step (in addition to the previous steps), which is used to determine which pixels to include in the quantification of the average pixel intensity of the spot.

The resulting fits from this program are overlaid with the original protein spots (shown in green-channel only) in the figure below.

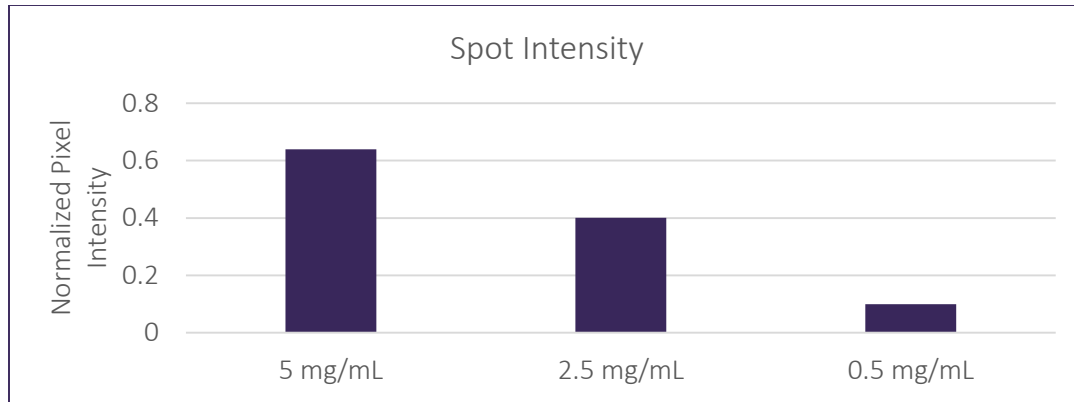


The resulting ellipse fits for the three protein spots tested (green channel images shown).

The corresponding spot areas (of the ellipses of best fit) and the background-subtracted, normalized average green-channel pixel intensities inside each ellipse are plotted in the figures below. These results show that the algorithm can successfully identify and quantify protein spots, although the accuracy of the ellipse-finding functionality is slightly diminished when the spot intensity is very low, such as is the case for the 0.5 mg/mL BSA spot.



The resulting spot areas, determined by the area of each ellipse of best fit.



The resulting average background-subtracted, normalized green-channel pixel intensity inside the best-fit ellipse for each spot.

Overall, this protein spot analysis program works well for the identification and quantification of protein spots in lateral flow challenge and protein spot analysis experiments.

C.2. Code

```
function myData = analyzeProteinSpots

% USAGE: myData = analyzeProteinSpots
% RETURNS 'myData' structure variable with four fields:
% 1. Icorr, the background-corrected signal
% 2. Iheaders, the user-entered names corresponding to each test spot
% 3. Iraw, the raw signal of both the test spots and background spot(s)
% 4. ROIcoordinates, the coordinates of both the test and background
%     regions of interest (ROIs)
% 5. Fits to spots (lliceses)
% 6. Spot diamters
% 7. Spot areas
% Copyright Carly Holstein, University of Washington, 2011
% Last update: 2 April 2014

clear all; close all; clc;

%-- Declare Global Variables --%
global h; %for handles
global sampleNames;
global approxROI;
global cmap;

%-- Get Initial Info --%
imageName = input('\nEnter the image file name: ','s');

nSamples = input('\nEnter the number of spots to quantify: ','s');
nSamples = str2num(nSamples);

spotOptions = [1]; %Change this to reflect available options
fprintf('\n%s','Which spot size quantification would you like to use?');
fprintf('\n\t%s\n','1. Best-fit ellipse');
```

```

% fprintf('\n\t%s','2. Best-fit circle'); % NOT AVAILABLE YET
% fprintf('\n\t%s\n','3. Pixel distribution profile'); % NOT AVAILABLE YET
spotChoice = input('Enter the number corresponding to your choice: ','s');
spotChoice = str2num(spotChoice);
fprintf('\n');
while all(spotChoice~=spotOptions) %Error check
    fprintf('%s','Not a valid selection. ');
    spotChoice = input('\nPlease enter the integer number corresponding to
your choice: ','s');
    spotChoice = str2num(spotChoice);
    fprintf('\n');
end

quantOptions = [1,2,3,4,5]; %Change this to reflect available options
fprintf('\n%s','Which pixel intensity quantification method would you like to
use? ');
fprintf('\n\t%s','1. Average grayscale pixel intensity');
fprintf('\n\t%s','2. Average red channel pixel intensity');
fprintf('\n\t%s','3. Average green channel pixel intensity');
fprintf('\n\t%s','4. Average blue channel pixel intensity');
fprintf('\n\t%s','5. Average grayscale pixel intensity for');
fprintf('\n\t%s\n','    negative images (e.g. fluorescence)');
quantChoice = input('Enter the number corresponding to your choice: ','s');
quantChoice = str2num(quantChoice);
fprintf('\n');
while all(quantChoice~=quantOptions) %Error check
    fprintf('%s','Not a valid selection. ');
    quantChoice = input('\nPlease enter the integer number corresponding to
your choice: ','s');
    quantChoice = str2num(quantChoice);
    fprintf('\n');
end

loadNameOptions = [1,2];
fprintf('\n%s','Do you want to enter spot names or load spot names from a
previous session? ');
fprintf('\n\t%s','1. Enter spot names');
fprintf('\n\t%s\n','2. Load spot names');
loadNameChoice = input('Enter the number corresponding to your choice:
','s');
loadNameChoice = str2num(loadNameChoice);
fprintf('\n');
while all(loadNameChoice~=loadNameOptions) %Error check
    fprintf('%s','Not a valid selection. ');
    loadNameChoice = input('\nPlease enter the integer number corresponding
to your choice: ','s');
    loadNameChoice = str2num(loadNameChoice);
    fprintf('\n');
end

if loadNameChoice==2
    %Load sample names
    fprintf('%s\n','You have selected to load spot names. ');
    namesToLoad_matfile = input('Enter the name of the *.mat file to load:
','s');

```

```

namesToLoad_struct = input('Enter the name of the structure variable
containing\nthe names to load: ','s');
load(namesToLoad_matfile,namesToLoad_struct);
namesToLoad = eval(strcat(namesToLoad_struct, '.Iheaders'));
while(size(namesToLoad,1)~= nSamples) %Error Check
    fprintf('\n%s', 'Not a valid selection. Number of spot names must
equal number of spots entered above');
namesToLoad_matfile = input('Enter the name of the *.mat file to
load: ','s');
namesToLoad_struct = input('Enter the name of the structure variable
containing the names to load: ','s');
load(namesToLoad_matfile,namesToLoad_struct);
namesToLoad = eval(strcat(namesToLoad_struct, '.Iheaders'));
end
end

ROIOptions = [1,2];
fprintf('\n%s', 'Do you want to draw ROIs or load pre-drawn ROIs?');
fprintf('\n\t%s', '1. Draw ROIs');
fprintf('\n\t%s\n', '2. Load ROIs');
ROIChoice = input('Enter the number corresponding to your choice: ','s');
ROIChoice = str2num(ROIChoice);
fprintf('\n');
while all(ROIChoice~=ROIOptions) %Error check
    fprintf('%s', 'Not a valid selection. ');
    ROIChoice = input('\nPlease enter the integer number corresponding to
your choice: ','s');
    ROIChoice = str2num(ROIChoice);
    fprintf('\n');
end

%- Load Pre-Drawn ROI Information, If Applicable -%
if ROIChoice==2
    %Load ROI data
    fprintf('%s\n', 'You have selected to load pre-drawn ROIs. ');
    ROIsToLoad_matfile = input('Enter the name of the *.mat file to load:
','s');
    ROIsToLoad_struct = input('Enter the name of the structure variable
containing\nthe ROIs to load: ','s');
    load(ROIsToLoad_matfile,ROIsToLoad_struct);
    ROIsToLoad = eval(strcat(ROIsToLoad_struct, '.ROIcoordinates'));
    while(size(ROIsToLoad.sample,1)~= nSamples) %Error Check
        fprintf('\n%s', 'Not a valid selection. Number of spot ROIs must equal
number of spots entered above');
        ROIsToLoad_matfile = input('Enter the name of the *.mat file to load:
','s');
        ROIsToLoad_struct = input('Enter the name of the structure variable
containing\nthe ROIs to load: ','s');
        load(ROIsToLoad_matfile,ROIsToLoad_struct);
        ROIsToLoad = eval(strcat(ROIsToLoad_struct, '.ROIcoordinates'));
    end
end

%-- Initialize Necessary Variables --%

```

```

if loadNameChoice==2
    sampleNames = namesToLoad;
else
    sampleNames = cell(nSamples,1); %for storing names of spots
end

signal_corr = zeros(nSamples,1); %column vec to store final bkgd-corrected
signals

signal_raw.sample = zeros(nSamples,1); %column vec to store raw spot signals

% spotFitInfo = zeros(nSamples,1); %column array of structures to store
parameters from spot fitting
spotFitInfo = struct([]);
spotArea = zeros(nSamples,1); %column vec to store spot areas

if spotChoice == 2 %for circle
    spotDiameter = zeros(nSamples,1); %column vec to store spot diameters
else %for ellipse or two-way pixel distribution
    spotDiameter = zeros(nSamples,2); %column vec to store spot diameters, a
and b
end

%-- Open Analysis Figure --%
h.fig1 = figure(1);

%- Draw Image -%
h.axes1 = axes('Parent',h.fig1,'Position',[0,0,0.5,1]);
testim = imread(imageName);
[imagesize.ypix imagesize.xpix] = size(testim);
h.im = imshow(testim,'Parent',h.axes1);

%- Draw UI Panel -%
h.uipanel = uipanel('Parent',h.fig1,'Position',[0.5,0,0.5,1]);
cmap = jet(nSamples);
cmapdim = rgb2hsv(cmap);
cmapdim(:,2) = cmapdim(:,2)*0.5;
cmapdim = hsv2rgb(cmapdim);

%Header text for 'Test Spots'
h.SampleTitle = uicontrol('Style','text',...
    'Parent',h.uipanel,...
    'Units','normalized',...
    'Position',[0.1,0.95,0.3,0.05],...
    'String','Test Spots');

%Header test for 'Background Correction'
h.BkgdTitle = uicontrol('Style','text',...
    'Parent',h.uipanel,...
    'Units','normalized',...
    'Position',[0.6,0.95,0.3,0.05],...
    'String','Background Correction');

%Radio buttons for background selection

```

```

h.BkgdSelectionButtons = uibuttongroup('Parent',h.uipanel,...
    'Units','normalized',...
    'Position',[0.6,0.8,0.4,0.15],...
    'BorderType','none',...
    'SelectionChangeFcn',@changeBkgdSelection);
h.BkgdButton1 = uicontrol('Style','Radio',...
    'Parent',h.BkgdSelectionButtons,...
    'Units','normalized',...
    'Position',[0,0.67,1,0.33],...
    'String','No background');
h.BkgdButton2 = uicontrol('Style','Radio',...
    'Parent',h.BkgdSelectionButtons,...
    'Units','normalized',...
    'Position',[0,0.33,0.75,0.33],...
    'String','Use common bkgd -->');
h.BkgdButton3 = uicontrol('Style','Radio',...
    'Parent',h.BkgdSelectionButtons,...
    'Units','normalized',...
    'Position',[0,0,1,0.33],...
    'String','Use local bkgds defined by offset:');

    %Push button to draw ROI for background
h.BkgdROIButton = uicontrol('Style','pushbutton',...
    'Parent',h.BkgdSelectionButtons,...
    'Units','normalized',...
    'Position',[0.75,0.33,0.25,0.33],...
    'String','Draw ROI',...
    'BackgroundColor',[1 1 1],...
    'Enable','off',...
    'Callback',{@drawBkgdROI});

h.SampleNameLabel = zeros(nSamples,1);
h.SampleName = zeros(nSamples,1);
h.BkgdCheckbox = zeros(nSamples,1);
h.BkgdVertOSText = zeros(nSamples,1);
h.BkgdHorzOSText = zeros(nSamples,1);
h.BkgdVertOSslider = zeros(nSamples,1);
h.BkgdHorzOSslider = zeros(nSamples,1);
h.BkgdVertOSnumbox = zeros(nSamples,1);
h.BkgdHorzOSnumbox = zeros(nSamples,1);
h.BkgdCommonROIrect = [];
for i=1:nSamples
    fldname = sprintf('%s%d','sample',i);
    h.SampleROIrect.(fldname) = [];
    h.BkgdROIrect.(fldname) = [];
end

sampleRowStart = 0.8; %relative height
sampleRowHeight = sampleRowStart/nSamples;
for i=1:nSamples
    %Label for each sample text box
    h.SampleNameLabel(i) = uicontrol('Style','text',...
        'Parent',h.uipanel,...
        'Units','normalized',...

```

```

        'Position',[0.05,sampleRowStart-
i*sampleRowHeight+0.3*sampleRowHeight,0.05,0.4*sampleRowHeight],...
        'String',sprintf('%d%c',i, '.')); %e.g.: '2.'

    %Editable text box for each sample
    if loadNameChoice==2
        currentNameString = sampleNames{i};
    else
        currentNameString = [];
    end
    h.SampleName(i) = uicontrol('Style','edit',...
        'Parent',h.uipanel,...
        'Units','normalized',...
        'Position',[0.1,sampleRowStart-
i*sampleRowHeight+0.1*sampleRowHeight,0.25,0.8*sampleRowHeight],...
        'String',currentNameString,...
        'Callback',{@setNames,i});

    %Push button to draw ROI for each sample
    h.SampleROIButton(i) = uicontrol('Style','pushbutton',...
        'Parent',h.uipanel,...
        'Units','normalized',...
        'Position',[0.35,sampleRowStart-
i*sampleRowHeight+0.1*sampleRowHeight,0.1,0.8*sampleRowHeight],...
        'String','Draw ROI',...
        'BackgroundColor',cmapdim(i,:),...
        'Callback',{@drawSampleROI,i});

    %Label for vertical offset slider
    h.BkgdVertOSText(i) = uicontrol('Style','text',...
        'Parent',h.uipanel,...
        'Units','normalized',...
        'Position',[0.6,sampleRowStart-
i*sampleRowHeight+0.6*sampleRowHeight,0.05,0.2*sampleRowHeight],...
        'String','V: ');

    %Label for horizontal offset slider
    h.BkgdHorzOSText(i) = uicontrol('Style','text',...
        'Parent',h.uipanel,...
        'Units','normalized',...
        'Position',[0.6,sampleRowStart-
i*sampleRowHeight+0.2*sampleRowHeight,0.05,0.2*sampleRowHeight],...
        'String','H: ');

    %Slider for vertical offset of background ROI
    maxvalvert = round(0.3*imagesize.ypix);
    minvalvert = round(-0.3*imagesize.ypix);
    rangevert = maxvalvert - minvalvert;
    h.BkgdVertOSSlider(i) = uicontrol('Style','slider',...
        'Parent',h.uipanel,...
        'Units','normalized',...
        'Position',[0.65,sampleRowStart-
i*sampleRowHeight+0.5*sampleRowHeight,0.2,0.4*sampleRowHeight],...
        'Max',maxvalvert,...
        'Min',minvalvert,...
        'Value',0,...

```

```

        'SliderStep',[1/rangevert 10/rangevert],...
        'Enable','off',...
        'Callback',{@setVertOSslider,i});

    %Slider for horizontal offset of background ROI
    maxvalhorz = round(0.3*imagesize.xpix);
    minvalhorz = round(-0.3*imagesize.xpix);
    rangehorz = maxvalhorz - minvalhorz;
    h.BkgdHorzOSslider(i) = uicontrol('Style','slider',...
        'Parent',h.uipanel,...
        'Units','normalized',...
        'Position',[0.65,sampleRowStart-
i*sampleRowHeight+0.1*sampleRowHeight,0.2,0.4*sampleRowHeight],...
        'Max',maxvalhorz,...
        'Min',minvalhorz,...
        'Value',0,...
        'SliderStep',[1/rangehorz 10/rangehorz],...
        'Enable','off',...
        'Callback',{@setHorzOSslider,i});

    %Editable textbox for vertical offset of background ROI
    h.BkgdVertOSnumbox(i) = uicontrol('Style','edit',...
        'Parent',h.uipanel,...
        'Units','normalized',...
        'Position',[0.85,sampleRowStart-
i*sampleRowHeight+0.5*sampleRowHeight,0.1,0.4*sampleRowHeight],...
        'String','0',...
        'Enable','off',...
        'Callback',{@setVertOSbox,i});

    %Editable textbox for horizontal offset of background ROI
    h.BkgdHorzOSnumbox(i) = uicontrol('Style','edit',...
        'Parent',h.uipanel,...
        'Units','normalized',...
        'Position',[0.85,sampleRowStart-
i*sampleRowHeight+0.1*sampleRowHeight,0.1,0.4*sampleRowHeight],...
        'String','0',...
        'Enable','off',...
        'Callback',{@setHorzOSbox,i});
end

%- Load Pre-Drawn ROIs, If Applicable -%
if ROIChoice==2
    %Draw sample ROIs and set GUI items accordingly
    for i=1:nSamples
        loadSampleROI(i,ROIsToLoad.sample(i,:));
    end

    %Draw background ROIs and set GUI items accordingly
    if ischar(ROIsToLoad.bkgd) %i.e. 'No background correction used'
        %no no bkgd
        set(h.BkgdSelectionButtons,'SelectedObject',h.BkgdButton1);
    elseif size(ROIsToLoad.bkgd,1)==1
        %set common bkgd
        set(h.BkgdSelectionButtons,'SelectedObject',h.BkgdButton2);
        loadBkgdROI(ROIsToLoad.bkgd);
    end
end

```



```

else
    %set local bkgds
    set(h.BkgdSelectionButtons,'SelectedObject',h.BkgdButton3);
    for i=1:nSamples
        loadLocalBkgdROI(i,ROIsToLoad.bkgd(i,:),ROIsToLoad.sample(i,:));
    end
end

%Prompt user
input('\nNow adjust your regions of interest as needed. \nPress enter when
done.\n');
else
    %Prompt user
    input('\nNow draw your regions of interest. \nPress enter when done.\n');
end

%-- Get ROI Dimensions --%
approxROI.sample = zeros(nSamples,4); %one row per sample, 4 cols for ROI: x-
pos,y-pos,width,height
approxROI.headers = {'x-pos','y-pos','width','height'};
bkgdChoice = get(h.BkgdSelectionButtons,'SelectedObject'); %handle for
selected background option

switch bkgdChoice
    case h.BkgdButton3 %Local background for each sample ROI
        %initialize
        approxROI.bkgd = zeros(nSamples,4); %one row per sample, 4 cols for
ROI: x-pos,y-pos,width,height
        signal_raw.bkgd = zeros(nSamples,1);
        %will fill in values in loop below

    case h.BkgdButton2 %Common background for all sample ROIs
        approxROI.bkgd = getPosition(h.BkgdCommonROIrect); %4 cols for ROI:
x-pos,y-pos,width,height
        signal_raw.bkgd = zeros(1,1);

    otherwise %No background used
        approxROI.bkgd = 'No background correction used';
        signal_raw.bkgd = [];
end

for i=1:nSamples
    fldname = sprintf('%s%d','sample',i);
    approxROI.sample(i,:) = getPosition(h.SampleROIrect.(fldname));

    if bkgdChoice == h.BkgdButton3 %Local bkgds
        approxROI.bkgd(i,:) = getPosition(h.BkgdROIrect.(fldname));
    end
end

%-- PERFORM SPOT ANALYSIS --%
figure;
subplot_col = ceil(sqrt(nSamples));

```

```

subplot_row = ceil(nSamples/subplot_col);
for i=1:nSamples

    %- Find Spot -%

    %Get sample ROI
    xpos = round(approxROI.sample(i,1));
    ypos = round(approxROI.sample(i,2));
    wd   = round(approxROI.sample(i,3));
    ht   = round(approxROI.sample(i,4));
    ROI_sample = testim(ypos:ypos+ht,xpos:xpos+wd,:);

    %Take desired channel or grayscale
    switch quantChoice
        case 1 %Grayscale
            ROI_sample_SingleCh = rgb2gray(ROI_sample);
        case 2 %Red channel
            ROI_sample_SingleCh = ROI_sample(:,:,1);
        case 3 %Green channel
            ROI_sample_SingleCh = ROI_sample(:,:,2);
        case 4 %Blue channel
            ROI_sample_SingleCh = ROI_sample(:,:,3);
        case 5 %Inverse grayscale (for fluorescence images)
            ROI_sample_SingleCh = rgb2gray(ROI_sample); %Inversion gets
applied during background correction
    end

    %Use chosen method to find spot
    switch spotChoice
        case 1 %Fit with ellipse

            %Get best-fit ellipse
            [a,b,xfit,yfit,xc,yc,A_line,B_line,ellipseFitResults] =
getEllipseFit(ROI_sample_SingleCh);

            %Calculate average pixel intensity inside ellipse
            inEllipse = ellipseFitResults.inEllipse;
            pixInt = mean(ROI_sample_SingleCh(inEllipse));

            %Plot ellipse and fit
            subplot(subplot_row,subplot_col,i);
            imshow(ROI_sample_SingleCh);
            hold on;
            plot(xfit,yfit,'g-');
            plot(A_line(1,:),A_line(2),'g--');
            plot(B_line(1,:),B_line(2),'g--');
            plot(xc,yc,'r+');
            title(sampleNames{i});

            %Report spot metrics
            if i==1
                spotFitInfo = ellipseFitResults;
            else
                [spotFitInfo(i)] = ellipseFitResults;
            end
        end
    end
end

```

```

        [spotDiameter(i,:)] = 2*[a,b];
        [spotArea(i)] = pi*a*b;
        [signal_raw.sample(i)] = pixInt;

    case 2 %Fit with circle %NOT AVAILABLE YET

        case 3 %Pixel distribution profile (like plot profile in ImageJ) %NOT
AVAILABLE YET

end

%- Calculate Background-Corrected Signal, Icorr -%

%Get background ROI
switch bkgdChoice
    case h.BkgdButton3 %Local background for each sample ROI
        xpos = round(approxROI.bkgd(i,1));
        ypos = round(approxROI.bkgd(i,2));
        wd  = round(approxROI.bkgd(i,3));
        ht  = round(approxROI.bkgd(i,4));
        ROI_bkgd = testim(ypos:ypos+ht,xpos:xpos+wd,:);

    case h.BkgdButton2 %Common background for all sample ROIs
        xpos = round(approxROI.bkgd(1));
        ypos = round(approxROI.bkgd(2));
        wd  = round(approxROI.bkgd(3));
        ht  = round(approxROI.bkgd(4));
        ROI_bkgd = testim(ypos:ypos+ht,xpos:xpos+wd,:);

    otherwise
        %No background; normalize to max pixel value for file type
        ROI_bkgd = [];
end

%Call quantification algorithm
%Assign handle to desired quantification function
switch quantChoice
    case 1
        calculateSignal = @calcAvgGrayPixIntensity; %average grayscale
intensity
    case 2
        calculateSignal = @calcAvgRPixIntensity; %average red channel
intensity
    case 3
        calculateSignal = @calcAvgGPixIntensity; %average green channel
intensity
    case 4
        calculateSignal = @calcAvgBPixIntensity; %average blue channel
intensity
    case 5
        calculateSignal = @calcAvgNegGrayPixIntensity; %average grayscale
intensity for negative image
end

```

```

    %Report raw background signal(s) only if background option selected
    if bkgdChoice == h.BkgdButton1 %no background ROI
        [signal_corr(i)] = calculateSignal(signal_raw.sample(i),ROI_bkgd);
    else
        [signal_corr(i),signal_raw.bkgd(i)] =
calculateSignal(signal_raw.sample(i),ROI_bkgd);
    end

end

%-- Return Vars --%

%Note: all variables now returned automacially as fields of the output
structure
    %Icorr = signal_corr; %background-corrected signal
    %Iheaders = sampleNames; %user-entered names for each test spot
    %Iraw = signal_raw; %contains uncorrected sample and bkgd signals
    %ROIcoordinates = approxROI %contails sample and bkgd ROIs
    %spotFits = spotFitInfo;
    %spotDiameter = spotDiameter;
    %spotArea = spotArea;

myData.Icorr = signal_corr;
myData.Iheaders = sampleNames;
myData.Iraw = signal_raw;
myData.ROIcoordinates = approxROI;
myData.spotFits = spotFitInfo;
myData.spotDiameter = spotDiameter;
myData.spotArea = spotArea;

end %end main function

%----- SUBFUNCTIONS -----%

function [A,B,X_fit,Y_fit,XC,YC,A_line,B_line,ellipse_fit_results] =
getEllipseFit(im)

%im is grayscale or single-channel image (uint9, uint16, etc.)
%XC is center of ellipse, x-coord.
%YC is center of ellipse, y-coord.
%A is major radius of ellipse
%B is minor radius of ellipse

%-- Find edges based on built-in derivative detection
[edges_BW,thresh] = edge(im,'prewitt'); %'sobel' or 'prewitt' methods are
best

%-- Find (x,y) pairs for edge
[row,col] = size(edges_BW);
edgeInd_lin = find(edges_BW);
[Y,X] = ind2sub([row col],edgeInd_lin);

```

```

%-- Solve for ellipse of best-fit *USING CODE FROM OHAD GAL (C) 2003*
ellipse_fit_results = fit_ellipse(X,Y);
XC = ellipse_fit_results.X0_in;
YC = ellipse_fit_results.Y0_in;
A = ellipse_fit_results.a;
B = ellipse_fit_results.b;
theta = linspace(0,2*pi,100);
x_fit = ellipse_fit_results.X0 + ellipse_fit_results.a*cos(theta);
y_fit = ellipse_fit_results.Y0 + ellipse_fit_results.b*sin(theta);
rotated_fit = ellipse_fit_results.R*[x_fit;y_fit];
X_fit = rotated_fit(1,:);
Y_fit = rotated_fit(2,:);
A_line = ellipse_fit_results.R*[
ellipse_fit_results.X0+ellipse_fit_results.a*[-1 1]; [ellipse_fit_results.Y0
ellipse_fit_results.Y0] ];
B_line = ellipse_fit_results.R*[ [ellipse_fit_results.X0
ellipse_fit_results.X0]; ellipse_fit_results.Y0+ellipse_fit_results.b*[-1 1]
];

%-- Calculate average pixel intensity inside ellipse
%Make mask, return boolean 'inEllipse'
[row,col] = size(im);
[xmat, ymat] = meshgrid(1:col,1:row);
inEllipse = ((xmat-XC).^2)./(A^2) + ((ymat-YC).^2)./(B^2) <= 1;
ellipse_fit_results.inEllipse = inEllipse;

```

end

```

function [Icorr, varargout] = calcAvgGrayPixIntensity(sampleSignal,bkgdROI)
% This function is an option for the signal quantification algorithm. It
% simply calculates the average grayscale pixel intensity of the ROI
% selected by the user and performs a background correction.
%
% USAGE: [Icorr, (Iraw.bkgd)] =
calcAvgGrayPixIntensity(sampleRawSignal,bkgdROI)

%Calculate raw bkgd intensities, or get max pixel value
if isempty(bkgdROI)==0 %if bkgd ROI given
    Iraw.bkgd = mean(mean(rgb2gray(bkgdROI)));
else %no background correction - normalize to max pixel value
    imageclass = class(bkgdROI);
    Iraw.bkgd = double(intmax(imageclass));
end

%Calculate normalized intensity
Idark = 0;
Icorr = (sampleSignal - Iraw.bkgd)/(Idark - Iraw.bkgd);

%Return vars
if nargin > 1
    if isempty(bkgdROI)==0 %if bkgd provided
        varargout{1} = Iraw.bkgd;
    else
        varargout{1} = [];
    end
end

```

```

        end
    end

end

function [Icorr, varargout] = calcAvgRPixIntensity(sampleSignal,bkgdROI)
% This function is an option for the signal quantification algorithm. It
% simply calculates the average red channel pixel intensity of the ROI
% selected by the user and performs a background correction.
%
% USAGE: [Icorr, (Iraw.bkgd)] = calcAvgRPixIntensity(sampleRawSignal,bkgdROI)

%Calculate raw bkgd intensities, or get max pixel value
if isempty(bkgdROI)==0 %if bkgd ROI given
    Iraw.bkgd = mean(mean(bkgdROI(:,:,1)));
else %no background correction - normalize to max pixel value
    imageclass = class(bkgdROI);
    Iraw.bkgd = double(intmax(imageclass));
end

%Calculate normalized intensity
Idark = 0;
Icorr = (sampleSignal - Iraw.bkgd)/(Idark - Iraw.bkgd);

%Return vars
if nargout > 1
    if isempty(bkgdROI)==0 %if bkgd provided
        varargout{1} = Iraw.bkgd;
    else
        varargout{1} = [];
    end
end
end

end

function [Icorr, varargout] = calcAvgGPixIntensity(sampleSignal,bkgdROI)
% This function is an option for the signal quantification algorithm. It
% simply calculates the average green channel pixel intensity of the ROI
% selected by the user and performs a background correction.
%
% USAGE: [Icorr, (Iraw.bkgd)] = calcAvgGPixIntensity(sampleRawSignal,bkgdROI)

%Calculate raw bkgd intensities, or get max pixel value
if isempty(bkgdROI)==0 %if bkgd ROI given
    Iraw.bkgd = mean(mean(bkgdROI(:,:,2)));
else %no background correction - normalize to max pixel value
    imageclass = class(bkgdROI);
    Iraw.bkgd = double(intmax(imageclass));
end

%Calculate normalized intensity
Idark = 0;
Icorr = (sampleSignal - Iraw.bkgd)/(Idark - Iraw.bkgd);

```

```

%Return vars
if nargin > 1
    if isempty(bkgdROI)==0 %if bkgd provided
        varargout{1} = Iraw.bkgd;
    else
        varargout{1} = [];
    end
end
end

end

function [Icorr, varargout] = calcAvgBPixIntensity(sampleSignal,bkgdROI)
% This function is an option for the signal quantification algorithm. It
% simply calculates the average blue channel pixel intensity of the ROI
% selected by the user and performs a background correction.
%
% USAGE: [Icorr, (Iraw.bkgd)] = calcAvgBPixIntensity(sampleRawSignal,bkgdROI)

%Calculate raw bkgd intensities, or get max pixel value
if isempty(bkgdROI)==0 %if bkgd ROI given
    Iraw.bkgd = mean(mean(bkgdROI(:,:,3)));
else %no background correction - normalize to max pixel value
    imageclass = class(bkgdROI);
    Iraw.bkgd = double(intmax(imageclass));
end

%Calculate normalized intensity
Idark = 0;
Icorr = (sampleSignal - Iraw.bkgd)/(Idark - Iraw.bkgd);

%Return vars
if nargin > 1
    if isempty(bkgdROI)==0 %if bkgd provided
        varargout{1} = Iraw.bkgd;
    else
        varargout{1} = [];
    end
end
end

end

function [Icorr, varargout] =
calcAvgNegGrayPixIntensity(sampleSignal,bkgdROI)
% This function is an option for the signal quantification algorithm. It
% simply calculates the average grayscale pixel intensity for a negative
% image of the ROI selected by the user and performs a background correction.
%
% USAGE: [Icorr, (Iraw.bkgd)] =
calcAvgNegGrayPixIntensity(sampleRawSignal,bkgdROI)

%Calculate raw bkgd intensities, or use dark pixel value
if isempty(bkgdROI)==0 %if bkgd ROI given
    Iraw.bkgd = mean(mean(rgb2gray(bkgdROI)));
else %no background correction - normalize to black pixel value

```

```

        Iraw.bkgd = 0;
    end

    %Get max pixel value corresponding to brightest signal possible (white)
    imageclass = class(bkgdROI);
    Ibright = double(intmax(imageclass));

    %Calculate normalized intensity
    Icorr = (sampleSignal - Iraw.bkgd)/(Ibright - Iraw.bkgd);

    %Return vars
    if nargin > 1
        if isempty(bkgdROI)==0 %if bkgd provided
            varargout{1} = Iraw.bkgd;
        else
            varargout{1} = [];
        end
    end
end

end

function setNames(hObj,event,i)
% Called when user enters sample concentration ('name') values
global sampleNames;
sampleNames{i} = get(hObj,'String'); %name for given test spot
end

function loadSampleROI(i,coords)
% Called when user chooses to load pre-drawn ROIs
global h;
global cmap;

fldname = sprintf('%s%d','sample',i);
if isempty(h.SampleROIRect.(fldname))==0 %if there already is a rect,
clear it first
    delete(h.SampleROIRect.(fldname));
    h.SampleROIRect.(fldname) = [];
end

xpos = coords(1);
ypos = coords(2);
wd = coords(3);
ht = coords(4);

%If local bkgds enabled, enable textboxes and sliders for defining bkgd
offsets
if strcmp(get(h.BkgdSelectionButtons,'SelectedObject'),'Use local bkgds
defined by offset:') == 1
    set(h.BkgdVertOSnumbox(i),'Enable','on');
    set(h.BkgdVertOSSlider(i),'Enable','on');
    set(h.BkgdHorzOSnumbox(i),'Enable','on');
    set(h.BkgdHorzOSSlider(i),'Enable','on');
end
end

```



```

    h.SampleROIrect.(fldname) = imrect(h.axes1,[xpos ypos wd ht]); %make new
rect
    setColor(h.SampleROIrect.(fldname), cmap(i,:))

end

function loadBkgdROI(coords)
% Called when user chooses to load a pre-drawn common background ROI
    global h;

    if isempty(h.BkgdCommonROIrect)==0 %if there already is a rect, clear it
first
        delete(h.BkgdCommonROIrect);
        h.BkgdROIrect = [];
    end

    %Update GUI Selections
    %enable bkgd ROI button:
    set(h.BkgdROIbutton, 'Enable', 'on');

    for i=1:n
        %disable bkgd text boxes and sliders
        set(h.BkgdVertOSnumbox(i), 'Enable', 'off');
        set(h.BkgdVertOSSlider(i), 'Enable', 'off');
        set(h.BkgdHorzOSnumbox(i), 'Enable', 'off');
        set(h.BkgdHorzOSSlider(i), 'Enable', 'off');

        %delete bkgd ROIs, if they exist
        fldname = sprintf('%s%d', 'sample', i);
        if isempty(h.BkgdROIrect.(fldname))==0 %if there is a rect
            delete(h.BkgdROIrect.(fldname));
            h.BkgdROIrect.(fldname) = [];
        end
    end

    end

    %Draw ROI
    xpos = coords(1);
    ypos = coords(2);
    wd = coords(3);
    ht = coords(4);

    h.BkgdCommonROIrect = imrect(h.axes1,[xpos ypos wd ht]); %make new rect
    setColor(h.BkgdCommonROIrect,[0 0 0]); %black

end

function loadLocalBkgdROI(i,bkgdcoords,samplecoords)
% Called when user chooses to load pre-drawn local background ROIs
    global h;
    global cmap;

    cmapdark = rgb2hsv(cmap);
    cmapdark(:,3) = cmapdark(:,3)*0.5;
    cmapdark = hsv2rgb(cmapdark);
    fldname = sprintf('%s%d', 'sample', i);

```

```

%get background and sample ROI coordinates for comparison
xpos_bkgd = bkgdcoords(1);
ypos_bkgd = bkgdcoords(2);
wd_bkgd = bkgdcoords(3);
ht_bkgd = bkgdcoords(4);
xpos_sample = samplecoords(1);
ypos_sample = samplecoords(2);
vertOffset = ypos_bkgd - ypos_sample;
horzOffset = xpos_bkgd - xpos_sample;

%enable sliders
set(h.BkgdVertOSslider(i), 'Enable', 'on');
set(h.BkgdHorzOSslider(i), 'Enable', 'on');
set(h.BkgdVertOSslider(i), 'Value', vertOffset);
set(h.BkgdHorzOSslider(i), 'Value', horzOffset);

%enable textboxes
set(h.BkgdVertOSnumbox(i), 'Enable', 'on');
set(h.BkgdHorzOSnumbox(i), 'Enable', 'on');
set(h.BkgdVertOSnumbox(i), 'String', num2str(vertOffset));
set(h.BkgdHorzOSnumbox(i), 'String', num2str(horzOffset));

%draw rectangle
h.BkgdROIrect.(fldname) = imrect(h.axes1, [xpos_bkgd ypos_bkgd wd_bkgd
ht_bkgd]); %make new rect
setColor(h.BkgdROIrect.(fldname), cmapdark(i, :));
setResizable(h.BkgdROIrect.(fldname), 0); %not resizable

end

function drawSampleROI(hObj, event, i)
% Called when user pushes button to draw an approximate ROI
    global h;
    global cmap;

    fldname = sprintf('%s%d', 'sample', i);
    if isempty(h.SampleROIrect.(fldname)) == 0 %if there already is a rect,
clear it first
        delete(h.SampleROIrect.(fldname));
        h.SampleROIrect.(fldname) = [];
    end

    if isempty(h.SampleROIrect.sample1) == 0 %if 1st rectangle exists already,
make other rects the same size
        rect1pos = getPosition(h.SampleROIrect.sample1);
        xpos = 100;
        ypos = 100;
        wd = rect1pos(3);
        ht = rect1pos(4);
    else %otherwise use arbitrary size and position
        xpos = 100;
        ypos = 100;
        wd = 100;
        ht = 100;
    end
end

```

```

end

%If local bkgds enabled, enable textboxes and sliders for defining bkgd
offsets
if strcmp(get(h.BkgdSelectionButtons,'SelectedObject'),'Use local bkgds
defined by offset:') == 1
    set(h.BkgdVertOSnumbox(i),'Enable','on');
    set(h.BkgdVertOSSlider(i),'Enable','on');
    set(h.BkgdHorzOSnumbox(i),'Enable','on');
    set(h.BkgdHorzOSSlider(i),'Enable','on');
end

h.SampleROIrect.(fldname) = imrect(h.axes1,[xpos ypos wd ht]); %make new
rect
setColor(h.SampleROIrect.(fldname),cmap(i,:))

end

function drawBkgdROI(hObj,event)
% Called when user pushes button to draw common background ROI
global h;

if isempty(h.BkgdCommonROIrect)==0 %if there already is a rect, clear it
first
    delete(h.BkgdCommonROIrect);
    h.BkgdROIrect = [];
end

if isempty(h.SampleROIrect.sample1)==0 %if 1st sample rectangle exists
already, make bkgd rect the same size
    rectlpos = getPosition(h.SampleROIrect.sample1);
    wd = rectlpos(3);
    ht = rectlpos(4);
else %otherwise use arbitrary size
    wd = 100;
    ht = 100;
end

h.BkgdCommonROIrect = imrect(h.axes1,[100 100 wd ht]); %make new rect
setColor(h.BkgdCommonROIrect,[0 0 0]); %black

end

function changeBkgdSelection(hObj,event)
% Called when user changes radio button selection for background type
% 'event' contains fields:
% - 'EventName', 'SelectionChanged'
% - 'OldValue', handle of previous object selected
% - 'NewValue', handle of currently selected object

global h;
n = length(h.BkgdCheckbox);

```

```

if event.NewValue == h.BkgdButton1 %No background
    %disable bkgd ROI button:
    set(h.BkgdROIButton, 'Enable', 'off');

    %delete common bkgd ROI, if it exists
    if isempty(h.BkgdCommonROIrect)==0 %if there is a rect
        delete(h.BkgdCommonROIrect);
        h.BkgdROIrect = [];
    end

    for i=1:n
        %delete bkgd ROIs, if they exist
        fldname = sprintf('%s%d', 'sample', i);
        if isempty(h.BkgdROIrect.(fldname))==0 %if there is a rect
            delete(h.BkgdROIrect.(fldname));
            h.BkgdROIrect.(fldname) = [];
        end

        %disable bkgd text boxes and sliders
        set(h.BkgdVertOSnumbox(i), 'Enable', 'off');
        set(h.BkgdVertOSSlider(i), 'Enable', 'off');
        set(h.BkgdHorzOSnumbox(i), 'Enable', 'off');
        set(h.BkgdHorzOSSlider(i), 'Enable', 'off');
    end
end

if event.NewValue == h.BkgdButton2 %Use common background
    %enable bkgd ROI button:
    set(h.BkgdROIButton, 'Enable', 'on');

    for i=1:n
        %delete bkgd ROIs, if they exist
        fldname = sprintf('%s%d', 'sample', i);
        if isempty(h.BkgdROIrect.(fldname))==0 %if there is a rect
            delete(h.BkgdROIrect.(fldname));
            h.BkgdROIrect.(fldname) = [];
        end

        %disable bkgd text boxes and sliders
        set(h.BkgdVertOSnumbox(i), 'Enable', 'off');
        set(h.BkgdVertOSSlider(i), 'Enable', 'off');
        set(h.BkgdHorzOSnumbox(i), 'Enable', 'off');
        set(h.BkgdHorzOSSlider(i), 'Enable', 'off');
    end
end

if event.NewValue == h.BkgdButton3 %Use local backgrounds
    %disable bkgd ROI button:
    set(h.BkgdROIButton, 'Enable', 'off');

    %delete common bkgd ROI, if it exists
    if isempty(h.BkgdCommonROIrect)==0 %if there is a rect
        delete(h.BkgdCommonROIrect);
        h.BkgdROIrect = [];
    end
end

```

```

%Draw background ROIs and enable sliders and text boxes if sample ROI
already exists
global h;
global cmap;

cmapdark = rgb2hsv(cmap);
cmapdark(:,3) = cmapdark(:,3)*0.5;
cmapdark = hsv2rgb(cmapdark);

for i=1:n
    fldname = sprintf('%s%d','sample',i);

    if isempty(h.SampleROIrect.(fldname))==0 %if sample rect exists
        %enable offset text and sliders
        set(h.BkgdVertOSnumbox(i),'Enable','on');
        set(h.BkgdVertOSSlider(i),'Enable','on');
        set(h.BkgdHorzOSnumbox(i),'Enable','on');
        set(h.BkgdHorzOSSlider(i),'Enable','on');
        set(h.BkgdVertOSSlider(i),'Value',0);
        set(h.BkgdHorzOSSlider(i),'Value',0);
        set(h.BkgdVertOSnumbox(i),'String','0');
        set(h.BkgdHorzOSnumbox(i),'String','0');

        %draw rectangles
        rectpos = getPosition(h.SampleROIrect.(fldname)); %make same
size as sample rect
        xp = rectpos(1);
        yp = rectpos(2);
        wd = rectpos(3);
        ht = rectpos(4);
        h.BkgdROIrect.(fldname) = imrect(h.axes1,[xp yp wd ht]);
%make new rect
        setColor(h.BkgdROIrect.(fldname),cmapdark(i,:));
        setResizable(h.BkgdROIrect.(fldname),0); %not resizable
    else
        %draw rectangles of arbitrary size if sample rect doesn not
exist
        xp = 100;
        yp = 100;
        wd = 100;
        ht = 100;
        h.BkgdROIrect.(fldname) = imrect(h.axes1,[xp yp wd ht]);
%make new rect
        setColor(h.BkgdROIrect.(fldname),cmapdark(i,:));
        setResizable(h.BkgdROIrect.(fldname),0); %not resizable
    end
end
end
end

function setVertOSSlider(hObject,event,i)
% Called when vertical offset of background ROI is changed by slider

```

```

global h;

%get value
vertOSvalue = get(hObj, 'Value');

%update textbox value
set(h.BkgdVertOSnumbox(i), 'String', num2str(vertOSvalue));

%get horizontal offset for reference
horzOSvalue = get(h.BkgdHorzOSslider(i), 'Value');

%adjust background ROI position
fldname = sprintf('%s%d', 'sample', i);
ROIpos = getPosition(h.SampleROIrect.(fldname)); %sample ROI position
xp = ROIpos(1)+horzOSvalue;
yp = ROIpos(2)+vertOSvalue;
wd = ROIpos(3);
ht = ROIpos(4);
setPosition(h.BkgdROIrect.(fldname), [xp yp wd ht]);

end

function setHorzOSslider(hObj, event, i)
% Called when horizontal offset of background ROI is changed by slider
global h;

%get value
horzOSvalue = get(hObj, 'Value');

%update textbox value
set(h.BkgdHorzOSnumbox(i), 'String', num2str(horzOSvalue));

%get vertical offset for reference
vertOSvalue = get(h.BkgdVertOSslider(i), 'Value');

%adjust background ROI position
fldname = sprintf('%s%d', 'sample', i);
ROIpos = getPosition(h.SampleROIrect.(fldname)); %sample ROI position
xp = ROIpos(1)+horzOSvalue;
yp = ROIpos(2)+vertOSvalue;
wd = ROIpos(3);
ht = ROIpos(4);
setPosition(h.BkgdROIrect.(fldname), [xp yp wd ht]);

end

function setVertOSbox(hObj, event, i)
% Called when vertical offset of background ROI is changed by textbox
global h;

%get value
vertOSvalue = str2num(get(hObj, 'String'));

```

```

%update slider value
set(h.BkgdVertOSslider(i), 'Value', vertOSvalue);

%get horizontal offset for reference
horzOSvalue = get(h.BkgdHorzOSslider(i), 'Value');

%adjust background ROI position
fldname = sprintf('%s%d', 'sample', i);
ROIpos = getPosition(h.SampleROIrect.(fldname)); %sample ROI position
xp = ROIpos(1)+horzOSvalue;
yp = ROIpos(2)+vertOSvalue;
wd = ROIpos(3);
ht = ROIpos(4);
setPosition(h.BkgdROIrect.(fldname), [xp yp wd ht]);

end

function setHorzOSbox(hObj, event, i)
% Called when horizontal offset of background ROI is changed by textbox
global h;

%get value
horzOSvalue = str2num(get(hObj, 'String'));

%update slider value
set(h.BkgdHorzOSslider(i), 'Value', horzOSvalue);

%get vertical offset for reference
vertOSvalue = get(h.BkgdVertOSslider(i), 'Value');

%adjust background ROI position
fldname = sprintf('%s%d', 'sample', i);
ROIpos = getPosition(h.SampleROIrect.(fldname)); %sample ROI position
xp = ROIpos(1)+horzOSvalue;
yp = ROIpos(2)+vertOSvalue;
wd = ROIpos(3);
ht = ROIpos(4);
setPosition(h.BkgdROIrect.(fldname), [xp yp wd ht]);

end

function ellipse_t = fit_ellipse( x,y,axis_handle )
%
% fit_ellipse - finds the best fit to an ellipse for the given set of points.
% By Ohad Gal (c) 2003
% Modified by Carly Holstein (c) 2013
%
% Format:    ellipse_t = fit_ellipse( x,y,axis_handle )
%
% Input:    x,y          - a set of points in 2 column vectors. AT LEAST 5
points are needed !

```

```

%          axis_handle - optional. a handle to an axis, at which the
estimated ellipse
%          will be drawn along with it's axes
%
% Output:  ellipse_t - structure that defines the best fit to an ellipse
%          a          - sub axis (radius) of the X axis of the
non-tilt ellipse
%          b          - sub axis (radius) of the Y axis of the
non-tilt ellipse
%          phi        - orientation in radians of the ellipse
(tilt)
%          X0         - center at the X axis of the non-tilt
ellipse
%          Y0         - center at the Y axis of the non-tilt
ellipse
%          X0_in      - center at the X axis of the tilted
ellipse
%          Y0_in      - center at the Y axis of the tilted
ellipse
%          long_axis  - size of the long axis of the ellipse
%          short_axis - size of the short axis of the ellipse
%          status     - status of detection of an ellipse
%          R          - rotation matrix
%          ellipseCoeffs - [A, B, C, D, E, F]
%          ellipseCoeffs_orig - [A, B, C, D, E, F] %Before
rotation removed
%
% Note:    if an ellipse was not detected (but a parabola or hyperbola),
then an empty structure is returned

% initialize
orientation_tolerance = 1e-3;

% empty warning stack
warning( '' );

% prepare vectors, must be column vectors
x = x(:);
y = y(:);

% remove bias of the ellipse - to make matrix inversion more accurate. (will
be added later on).
mean_x = mean(x);
mean_y = mean(y);
x = x-mean_x;
y = y-mean_y;

% the estimation for the conic equation of the ellipse
X = [x.^2, x.*y, y.^2, x, y ];
a = sum(X)/(X'*X);

% check for warnings
if ~isempty( lastwarn )
    disp( 'stopped because of a warning regarding matrix inversion' );
    ellipse_t = [];
    return

```



```

end

% extract parameters from the conic equation
[a,b,c,d,e] = deal( a(1),a(2),a(3),a(4),a(5) );
a_orig = a;
b_orig = b;
c_orig = c;
d_orig = d;
e_orig = e;

% remove the orientation from the ellipse
if ( min(abs(b/a),abs(b/c)) > orientation_tolerance )

    orientation_rad = 1/2 * atan( b/(c-a) );
    cos_phi = cos( orientation_rad );
    sin_phi = sin( orientation_rad );
    [a,b,c,d,e] = deal(...
        a*cos_phi^2 - b*cos_phi*sin_phi + c*sin_phi^2,...
        0,...
        a*sin_phi^2 + b*cos_phi*sin_phi + c*cos_phi^2,...
        d*cos_phi - e*sin_phi,...
        d*sin_phi + e*cos_phi );
    [mean_x,mean_y] = deal( ...
        cos_phi*mean_x - sin_phi*mean_y,...
        sin_phi*mean_x + cos_phi*mean_y );
else
    orientation_rad = 0;
    cos_phi = cos( orientation_rad );
    sin_phi = sin( orientation_rad );
end

% check if conic equation represents an ellipse
test = a*c;
switch (1)
case (test>0), status = '';
case (test==0), status = 'Parabola found'; warning( 'fit_ellipse: Did not
locate an ellipse' );
case (test<0), status = 'Hyperbola found'; warning( 'fit_ellipse: Did not
locate an ellipse' );
end

% if we found an ellipse return it's data
if (test>0)

    % make sure coefficients are positive as required
    if (a<0), [a,c,d,e] = deal( -a,-c,-d,-e ); end

    % final ellipse parameters
    X0      = mean_x - d/2/a;
    Y0      = mean_y - e/2/c;
    F       = 1 + (d^2)/(4*a) + (e^2)/(4*c);
    [a,b]   = deal( sqrt( F/a ),sqrt( F/c ) );
    long_axis = 2*max(a,b);
    short_axis = 2*min(a,b);

```

```

    % rotate the axes backwards to find the center point of the original
    TILTED ellipse
    R      = [ cos_phi sin_phi; -sin_phi cos_phi ];
    P_in   = R * [X0;Y0];
    X0_in  = P_in(1);
    Y0_in  = P_in(2);

    % pack ellipse into a structure
    ellipse_t = struct( ...
        'a',a,...
        'b',b,...
        'phi',orientation_rad,...
        'X0',X0,...
        'Y0',Y0,...
        'X0_in',X0_in,...
        'Y0_in',Y0_in,...
        'long_axis',long_axis,...
        'short_axis',short_axis,...
        'status','',...
        'R',R,...
        'ellipseCoeffs',[a,b,c,d,e,F],...
        'ellipseCoeffs_orig',[a_orig,b_orig,c_orig,d_orig,e_orig,F]);
else
    % report an empty structure
    ellipse_t = struct( ...
        'a',[],...
        'b',[],...
        'phi',[],...
        'X0',[],...
        'Y0',[],...
        'X0_in',[],...
        'Y0_in',[],...
        'long_axis',[],...
        'short_axis',[],...
        'status',status,...
        'R',[],...
        'ellipseCoeffs',[],...
        'ellipseCoeffs_orig',[]);
end

% check if we need to plot an ellipse with it's axes.
if (margin>2) & ~isempty( axis_handle ) & (test>0)

    % rotation matrix to rotate the axes with respect to an angle phi
    R = [ cos_phi sin_phi; -sin_phi cos_phi ];

    % the axes
    ver_line      = [ [X0 X0]; Y0+b*[-1 1] ];
    horz_line     = [ X0+a*[-1 1]; [Y0 Y0] ];
    new_ver_line  = R*ver_line;
    new_horz_line = R*horz_line;

    % the ellipse
    theta_r      = linspace(0,2*pi);
    ellipse_x_r  = X0 + a*cos( theta_r );
    ellipse_y_r  = Y0 + b*sin( theta_r );

```

```
rotated_ellipse = R * [ellipse_x_r;ellipse_y_r];

% draw
hold_state = get( axis_handle, 'NextPlot' );
set( axis_handle, 'NextPlot', 'add' );
plot( new_ver_line(1,:),new_ver_line(2,:), 'r' );
plot( new_horz_line(1,:),new_horz_line(2,:), 'r' );
plot( rotated_ellipse(1,:),rotated_ellipse(2,:), 'r' );
set( axis_handle, 'NextPlot', hold_state );
end
end
```

Appendix D: MATLAB Program *LODanalysis.m*

D.1. Description

The MATLAB program *LODanalysis.m* is used to calculate an estimate of the limit of detection of a bioassay, complete with 95% confidence interval. This method is described in detail in chapter 6.

D.2. Code

```
%Perform statistical LOD analysis
%Final LOD analysis method
% Originally developed June-July 2014, Carly Holstein
% Updated April 2015 based on recommended revisions from Maryclare Griffin
(Statistics Consulting Group) and adaption by Carly Holstein
%Copyright Carly Holstein, University of Washington, 2014
%Last updated: April 24, 2015

function LODanalysis(rawDataInputFileName,resultsOutputFileName)

%USAGE: LODanalysis(rawDataInputFileName,resultsOutputFileName)
% rawDataInputFileName: string variable containing name of *.mat file
% that contains raw data. Raw data file must contain the following
% variables:
%     pixInt: Structure variable containing two fields:
%         test: n x m array of pixel intensities for the test data
%         where n = number of test concentrations
%         m = number of replicates per concentration
%     negCtrl: 1 x m array of pixel intensities for the negative
controls
%         where m = number of replicates of the negative control
%     testConc: n x 1 array of the concentrations of analyte tested,
%     corresponding to the data in the 'test' field of 'pixInt'
% resultsOutputFileName: string variable containing name of *.mat file
% to which the results will be saved.

load(rawDataInputFileName);

%-- Prepare Data For Analysis --%

%Transform C to log(C+2) to enable analysis, combine test and negative
control data
[numConcentrations, numRepsTest] = size(pixInt.test);
testConc_logplus2 = log10(testConc+2); %Log10 of (test concentrations+2)
allTestData_testConc_logplus2 = repmat(testConc_logplus2,numRepsTest,1);
allTestData_pixInt = reshape(pixInt.test,numConcentrations*numRepsTest,[]);

numReps_negCtrl = length(pixInt.negCtrl);
negConc = zeros(numReps_negCtrl,1); %Negative control concentration = 0
negConc_logplus2 = log10(negConc+2); %Log10 of (0+2)
```

```

allData_testConc_logplus2 = [allTestData_testConc_logplus2;
negConc_logplus2];
allData_pixInt = [allTestData_pixInt; pixInt.negCtrl'];

numReps_Total = (numRepsTest*numConcentrations) + numReps_negCtrl;

%Calculate variances [Not used here, but could be used for weighting fit, if
n>10
pixIntVar.test = var(pixInt.test,0,2); %returns column vector of variances
for each test concentration
pixIntVar.negCtrl = var(pixInt.negCtrl); %variance for negative controls
allTestData_pixIntVar =
reshape( repmat(pixIntVar.test,numRepsTest,1), numConcentrations*numRepsTest, []
);
negConc_pixIntVar = pixIntVar.negCtrl*ones(numReps_negCtrl,1);
allData_pixIntVar = [allTestData_pixIntVar; negConc_pixIntVar];
allData_pixInt_InverseVar = 1./allData_pixIntVar;

%-- Perform 4PL Fit --%
[xData, yData] = prepareCurveData(allData_testConc_logplus2, allData_pixInt);
%Fit using all data points
ft = fitype( '((a-d)/(1+((x/c)^b))+d', 'independent', 'x', 'dependent', 'y'
); %4PL curve
opts = fitoptions( 'Method', 'NonlinearLeastSquares' );
opts.Display = 'Off';
opts.Lower = [-10 0 0 0]; %lower bounds on [a b c d] %Only a can be nonzero,
but restrict to -10 to speed fitting
opts.StartPoint = [1 1 1 1]; %starting points for [a b c d]
opts.Upper = [10 Inf Inf 10]; %upper bounds on [a b c d]
%opts.Weights = allData_pixInt_InverseVar; %weight by inverse variance [Not
using; not recommended for n<10]
[fitresult, gof] = fit( xData, yData, ft, opts );

%-- Calculate Upper Limit of the Negative Controls, Lc --%
mu_c = mean(pixInt.negCtrl); %mean signal of the negative controls
SD_c = std(pixInt.negCtrl); %standard deviation of the negative controls
df_c = length(pixInt.negCtrl)-1; %degrees of freedom for negative controls =
n-1
alpha = 0.05; %alpha value = desired probability of false positive
t_c = tinv(1-alpha,df_c); %t-multiplier for given alpha and df
Lc = mu_c + t_c*SD_c; %Limit of the negative controls based on SD

%-- Calculate Pooled SD of Test Concentrations, Determine Ld in Signal Space
--%
var_test_pooled = sum(pixIntVar.test)/length(pixIntVar.test); %pooled
variance for all test concentrations (assumes equal reps per concentration)
SD_test = sqrt(var_test_pooled); %standard deviation of the pooled test data
(assumes homoscedasticity)
df_test = numConcentrations*(numRepsTest-1); %degrees of freedom for test
data = nCon*(nReps-1) (per stats consulting)
beta = 0.05; %beta value = desired probability of false negative
t_test = tinv(1-beta,df_test); %t-multiplier for given alpha and df

```

```

Ld = Lc + t_test*SD_test; %Limit of detection in signal space based on SD

%-- Calculate LOD in Concentration Space, Based on Calibration Curve --%

%Calculate LOD from fit
logplus2_LOD = fitresult.c*(( (fitresult.a-fitresult.d)/(Ld-fitresult.d) -
1)^(1/fitresult.b));
LOD = 10^logplus2_LOD - 2;

%-- Calculate SE and 95% CI of LOD based on Covariance Matrix of Fit --%

% Save paramaters for subfunctions
fitpars = [fitresult.d fitresult.a fitresult.b fitresult.c];

% Step 1: Obtain Estimate of Asymptotic Variance-Covariance Matrix for 4PL
parameters
% - Calculate Gradient of the Likelihood Function Used to Obtain NLS Fit
fitgrad = gradfun(fitpars, transpose(allData_testConc_logplus2));
% - Calculate Estimate of Meaurement Error Variance
sigsq = gof.sse/(length(allData_testConc_logplus2) - 4);
% - Calculate Hessian for Likelihood Function Used to Obtain NLS Fit
fithessian =
transpose(fitgrad)*(1/sigsq)*eye(length(allData_testConc_logplus2))*fitgrad;
% - Calculate Estimate of Asymptotic Variance-Covariance Matrix for 4PL
Parameters
fitcov = inv(fithessian);

% Step 2: Apply Delta-Method to Obtain Estimate of log(LOD + 2) SE
% - Calculate Derivative of 4PL Function With Respect to 4PL Parameters at
4PL Parameter Estimates
gradinv = gradfuninv(fitpars, Ld);
% - Calculate Derivative of Inverse 4PL Function With Respect to Signal at Ld
dfitinv = dfitfuninv(Ld, fitpars);
% - Calculate Estimate of Asymptotic Variance of log(LOD + 2)
logplus2_LOD_asympvariance = transpose(gradinv)*fitcov*gradinv +
dfitinv^2*sigsq/4; %asymptotic variance
% - Take Square Root to Get log(LOD + 2) SE
logplus2_LOD_SE = sqrt(logplus2_LOD_asympvariance); %although sqrt(var) = SD,
here we have asymptotic variance, and sqrt(asymp var) = SE
logplus2_LOD_SD = logplus2_LOD_SE*sqrt(numReps_Total); %SD not used here, but
useful value to have for data
logplus2_LOD_var = logplus2_LOD_SD^2; %Variance not used here, but useful
value to have for data

logplus2_LOD_lower95 = norminv(0.025,logplus2_LOD,logplus2_LOD_SE);
logplus2_LOD_upper95 = norminv(0.975,logplus2_LOD,logplus2_LOD_SE);

LOD_lower95 = 10^logplus2_LOD_lower95 - 2;
LOD_upper95 = 10^logplus2_LOD_upper95 - 2;

%-- Plot Results --%

```

```

figure('Name','LOD Analysis');
hTestConc =
plot(allTestData_testConc_logplus2,allTestData_pixInt,'b.','MarkerSize',10);
hold on;
hNegCtrl = plot(negConc_logplus2,pixInt.negCtrl,'bo');

fitData_x =
linspace(min(allData_testConc_logplus2),max(allData_testConc_logplus2),100);
fitData_y = ((fitresult.a-
fitresult.d)./(1+((fitData_x./fitresult.c).^fitresult.b)))+fitresult.d;
h4PLFit = plot(fitData_x,fitData_y,'r-');

predictedInterval = predint(fitresult,fitData_x,0.95,'functional','off');
%Prediction interval of fit, 95% confidence, functional interval, non-
simultaneous
h4PL95CI = plot(fitData_x,predictedInterval,'r--'); %95% prediction interval

hLc = plot([fitData_x(1),fitData_x(end)],[Lc Lc],'c-'); %Lc line (horizontal)
hLd = plot([fitData_x(1),fitData_x(end)],[Ld Ld],'g-'); %Ld line (horizontal)
hLOD = plot([logplus2_LOD,logplus2_LOD],[fitData_y(1),fitData_y(end)],'m-');
%LOD line (vertical)
hLODlower95 =
plot([logplus2_LOD_lower95,logplus2_LOD_lower95],[fitData_y(1),fitData_y(end)
],'m--'); %LOD, lower 95% confidence interval line (vertical)
hLODupper95 =
plot([logplus2_LOD_upper95,logplus2_LOD_upper95],[fitData_y(1),fitData_y(end)
],'m--'); %LOD, upper 95% confidence interval line (vertical)
hLegend =
legend([hTestConc,hNegCtrl,h4PLFit,h4PL95CI(1),hLc,hLd,hLOD,hLODlower95],'Tes
t Concentrations','Negative Controls','4PL fit','4PL fit 95%
CI','L_C','L_D','LOD','LOD 95% CI');
set(hLegend,'Location','NorthWest','FontName','Calibri Light','FontSize',12);

xlabel('HA Concentration (pM)');
%xlabel('Virus Concentration (CEID50/mL)');
ylabel('Normalized Pixel Intensity');

xtickvalues = sort([testConc; 0]);
xtickvalues_logplus2 = log10(xtickvalues+2);
set(gca,'XTick',xtickvalues_logplus2);
set(gca,'XTickLabel',xtickvalues);
set(gca,'FontName','Calibri Light','FontSize',12);

save(resultsOutputFileName);

end

%-- SUBFUNCTIONS --%
%Written by Maryclare Griffin to find covariance matrix in order to
%calculate SE and CI of LOD, based on variance in the 4PL fit

function y = gradfun(pars, x)
% Gives derivatives of 4PL function with respect to each 4PL parameter

c = pars(1);

```

```

d = pars(2);
b = pars(3);
e = pars(4);
dc = 1 - 1./(1 + exp(b*(log(x) - log(e))));
dd = 1./(1 + exp(b*(log(x) - log(e))));
db = -1*(d - c)*(log(x) - log(e)).*exp(b*(log(x) - log(e)))./(1 +
exp(b*(log(x) - log(e))))).^2;
de = ((d - c)*b*exp(b*(log(x) - log(e)))/e)./(1 + exp(b*(log(x) -
log(e))))).^2;
y = [dc; dd; db; de];
y = transpose(y);

```

end

```

function y = gradfuninv(pars, x)
% Gives derivatives of inverse 4PL function with respect to each 4PL
parameter

```

```

c = pars(1);
d = pars(2);
b = pars(3);
e = pars(4);
dc = -1*(e*((d - x)./(x - c)).^(1/b))./(b*(c - x));
dd = e*((x - d)./(c - x)).^(1/b)./(b*(d - x));
db = -1*e*((x - d)./(c - x)).^(1/b).*log((x - d)./(c - x))/(b^2);
de = ((d - x)./(x - c)).^(1/b);
y = [dc; dd; db; de];

```

end

```

function y = dfitfuninv(x, pars)
% Gives derivative of inverse 4PL function with respect to signal

```

```

c = pars(1);
d = pars(2);
b = pars(3);
e = pars(4);
y = (e*(c - d)*((x - d)./(c - x)).^(1/b - 1))./(b*(c - x).^2);

```

end

Appendix E: MATLAB Program *LODcomparison.m*

E.1. Description

The MATLAB program *LODcomparison.m* is used for the comparison limits of detection by Welch's *t*-test. This simple calculation is described in detail in chapter 6 (see Eqn 40 through Eqn 42).

E.2. Code

```
%Perform Welch's t-test to compare two LOD estimates using mean & SE
estimates
%Intended for use after LODanalysis.m
%Copyright Carly Holstein, University of Washington, 2015
%Last updated: April 24, 2015

function results = LODcomparison(assay1,assay2)

%USAGE: LODcomparison(Assay1TTestInputs,Assay2TTestInputs)
% Assay1TTestInputs: structure variable containing three fields:
%     mu: mean of LOD estimate
%     se: standard error of LOD estimate ( = SD/sqrt(n) )
%     n: total number of replicates
% Assay2TTestInputs: structure variable containing three fields:
%     mu: mean of LOD estimate
%     se: standard error of LOD estimate ( = SD/sqrt(n) )
%     n: total number of replicates
% Returns structure variable with five fields:
%     tstat: t-statistic for comparison
%     df: degrees of freedom left over after LOD analysis
%     dfwelch: degrees of freed for Welch's t-test
%     p: p-value based on t-statistic and dfwelch
%     significant: returns 'yes' for p < 0.05, 'no' otherwise

results.tstat = ( assay1.mu - assay2.mu ) / ( sqrt( assay1.se^2 + assay2.se^2
) );
results.df = max(assay1.n,assay2.n)-4; %Four degrees of freedom already used
for determining 4PL parameters
results.dfwelch = ( ( assay1.se^2 + assay2.se^2 )^2 ) / (
(assay1.se^4)/(results.df) + (assay2.se^4)/(results.df) );
results.p = 1 - (tcdf(abs(results.tstat),results.dfwelch) - tcdf(-
1*abs(results.tstat),results.dfwelch));
if results.p < 0.05
    results.significant = 'yes';
else
    results.significant = 'no';
end

end
```